Development of an apparatus for time resolved measurement of OH and HO$_2$, with application to atmospherically relevant reactions.

Thomas Henry Speak

Submitted in accordance with the requirements for the degree of
Doctor of Philosophy

The University of Leeds

School of Chemistry

December 2019

The candidate confirms that the work submitted is his own, except where work which has formed part of jointly authored publications has been included. The contribution of the candidate and the other authors to this work has been explicitly indicated below. The candidate confirms that appropriate credit has been given within the thesis where reference has been made to the work of others.

The description of the instrument for HO_2 detection in the experimental section (Chapter 2), the description of the characterization of which forms part of chapter 3, and the example application of this instrument to n-butanol oxidation; are derived from work included in:

"A New Instrument for Time Resolved Measurement of HO_2 Radicals", Speak, T. H. and Blitz, M. A. and Stone, D. and Seakins, P. W., Atmospheric Measurement Techniques Discussions, 2019

Within this, all the experimental work was carried out by and data was collected by T. Speak, the figures and first draft were produced by T.Speak. D. Stone provided input into experimental design and analysis of transport effects. M. Blitz and P. Seakins led the project and completed the manuscript.

Acknowledgments:

Firstly, I would like to thank my supervisor, Professor Paul Seakins, for giving me this opportunity to work at Leeds, and for all of his advice over the past four years. In particular though I must also thank my co-supervisor Dr. Mark Blitz whose experimental expertise and ability to keep lasers running have helped me throughout my PhD (and without whom Dainton Lab would be a far less productive workplace). I would also like to thank all of my past and present colleagues in both the Dainton Lab and B36 for their help and assistance, especially Diogo De Jesus Medeiros without whom the computational calculations and data analysis that follow later would have been far more taxing.

Secondly, I must thank those colleagues who have made a regular feature in keeping me at least partially sane, and without whom this work would not have been possible, Dr. Kevin Douglass, Dr. Dan Stone. I will be eternally grateful for the support you have both given me over the last 4 years especially being there when I needed you most.

I would like to thank Alex Brennan and Nic West for letting me and Freja continually talk over them for at least an hour a day whilst feigning some general interest in our conversations. I should probably extend that thanks to all my other friends that I have made over the last few years at Leeds during both my Undergrad degree and my PhD. I must also include Claire Wright, who has taken on the challenge of reading my work and has helped me to mold the words I write into something that resembles sentences. An achievement anyone who read something I produced in high school, college or even my first year here might not have believed possible.

A special thanks my Family who have always been there to support me and guide me. To my parents for the help and support inspiration that started me on the track towards studying science in the first place, and showing me the importance of focus, hard work and graft. Thanks to my grandparents who showed me the vital skill of being able to bodge a good enough solution to a problem, when the prefect tools or solution isn't available, which was often required, and for the endless supplies of support and cakes. Finally to my brothers for always providing me a ready source of motivation, and without whom my competitiveness and refusal to quit might have not been high enough to actually write this.

Abstract:

The primary focus of this work has been to develop and characterize an instrument for the time resolved (millisecond timescale) measurement of OH and HO_2, to monitor reactions occurring under high pressures (500 – 4000 mbar), and over a wide range of temperatures (290 – 700 K). This instrument was then used in conjunction with PTR-TOF-MS and conventional slow-flow reactors to study the OH initiated oxidation of a range of nitrogen containing compounds.

Chapter 3 describes the development of this system and its characterization. Of particular importance to later work, it was noted that measuring the temperature of a flowing gas with a thermocouple could be highly inaccurate. Following this observation, chemical thermometers (e.g. the reaction of OH and methane) were instead used to assign the temperature at which reactions were occurring in the high-pressure system (and this was later extended to conventional slow-flow systems). HO_2 detection was carried out indirectly via titration with NO to form OH, which was then detected by LIF. Efficient and selective titration of HO_2 could only be achieved beyond the breakdown of the jet in the low-pressure detection cell, and as such, time resolution of the HO_2 signal was reduced compared with the OH measurements. However, HO_2 yield could be achieved with high accuracy and precision. This was validated for the reaction of OH with methanol under high (6×10^{18} cm^{-3}) and low oxygen ($<1 \times 10^{16}$ cm^{-3}) conditions; where the measured yields of 87 ± 5 % at low oxygen, and 99 ± 2 % at high oxygen were in excellent agreement with the expected yields of 85 ± 8 % and 100 % from McCaulley *et al.*.[1]

In chapter 4, this apparatus was applied to study the OH initiated oxidation of n-butanol (a potential 'drop in' biofuel); where, the measurement of OH recycling, and HO_2 yields allowed for the assignment of α and β branching fractions. The measured branching ratios were $\beta = 0.24 \pm 0.04$ (616 – 640 K), and $\alpha = (0.57 \pm 0.06)$ at 293 K, and (0.54 ± 0.04) at 616 K. Understanding the ratio of the α and β branching fractions for OH abstraction from n-butanol is important in modelling its ignition delay time, with α leading to the formation of HO_2 a chain inhibiting reaction.

Chapter 5 and 6 describe the study of the OH initiated oxidation of methyl formamide (MF), dimethyl formamide (DMF), tertiary butyl amine (tBA), and methyl propane diamine (diamine). In chapter 5, the temperature dependence of the OH oxidation of dimethyl formamide was studied, and particular emphasis was placed on the

source of OH recycling that becomes prevalent above 450 K. The overall temperature dependence of OH and DMF was assigned as $k_{OH+DMF} = (1.317 \pm 0.117) \times 10^{-11} (\frac{T}{298})^{-0.5} e^{37.16/RT}$, with an ambient temperature value of $k_{298\,K} = (1.30 \pm 0.12) \times 10^{-11}$ cm^3 molecule^{-1} s^{-1}. High level computational calculations (CCSD(T)/CBS//mp2/6-311++g(3df,3pd)) were carried out to generate potential energy surfaces for the abstraction reactions and the subsequent R + O$_2$ surfaces.

The results of both the experimental and computational work carried out, indicated that the majority abstraction over all temperatures was from the aldehydic position. This is of atmospheric significance as it is a route to the formation of a nitrogen centred radical, which can lead to the formation of dimethyl nitramine and dimethyl nitrosamine. Nitramines and nitrosamines are potent carcinogenic compounds.

Chapter 7 used the reaction of OH and isoprene to illustrate potential differences in the chemistry observed when the reaction was carried under different experimental conditions, where the reactions were monitored using PTR-TOF-MS. The well-defined ambient temperature rate coefficient of OH and isoprene allowed it to be used as a reference compound for a relative rate study of OH and 1,3,5- tri methyl benzene (TMB) which was carried out in EUPHORE and HIRAC giving $k_{OH+TMB} = (5.77 \pm 0.05) \times 10^{-11}$ cm^3 molecule^{-1} s^{-1}. From reactions carried out in EUPHORE, an ambient pressure quartz reactor, and the high pressure system (at 1000 mbar) the combined yield of methacrolein and methyl vinyl ketone was shown to be > 70 % in good agreement with that observed by Sprengnether *et al.* (72 $\pm$ 7 %).(2) In addition, from the reactions carried out in HIRAC, an ambient pressure quartz reactor, and the high pressure system the yield of m/z 83 was assigned as 3 – 7 % at room temperature and was identified as the product of the abstraction, not of 3-MF (3-methyl furan). The homogenous pathway to 3-MF is not well known, and at room temperature when the reaction were carried out in the high-pressure reactor, and the quartz reactor secondary OH chemistry and heterogeneous routes were minimized.

1.   MCCAULLEY, J., N. KELLY, M. GOLDE and F. KAUFMAN. Kinetic studies of the reactions of F and OH with CH$_3$OH, The Journal of Physical Chemistry, 1989, **93**(3), pp.1014-1018.
2.   SPRENGNETHER, M., K.L. DEMERJIAN, N.M. DONAHUE and J.G. ANDERSON. Product analysis of the OH oxidation of isoprene and 1,3-butadiene in the presence of NO. *Journal of Geophysical Research: Atmospheres*, 2002, **107**(D15), pp.ACH 8-1-ACH 8-13.

Table of contents:

1 Contents

4 Application of the system for OH and HO_2 measurement to butanol oxidation

5 An experimental and computational study of the OH initiated oxidation of DMF

Table of Figures:

Table of tables:

Table of schemes:

List of abbreviations:

3-MF – 3 –methyl furan

AMP - 2-amino-2- methyl-1-propanol $(CH_3)_2C(CH_2OH)NH_2$

BBO – barium borate crystal

C_2H_4 – Ethylene

C_2H_6 – Ethane

CE – 'collision energy'

CH_3OH – Methanol

CRDS – Cavity ring down spectroscopy

CSE – chemically significant eigenvalue

cw – continuous wave

DCM – (Dicyanomethylene)-2-methyl-6-(4-dimethylaminostyryl)-4H-pyran

Diamine - N-methyl-propan-1,3-diamine $CH_3NCH_2CH_2CH_2NH_2$

di-HPCARP – Dihydroperoxy-carbonyl peroxy radicals

DMF – N,N'-dimethylformamide

EUPHORE – EUropean PHOtochemical REactor

FAGE – Fluorescence assay by gas expansion

FC – Frank-Condon overlap factor

FFR – Field free region

FTIR – Fourier transformed infra-red spectroscopy

GC-FID – Gas chromatography flame ionization detection

GC-MS – Gas chromatography mass spectrometry

GD – glow discharge

H_2O_2 – hydrogen peroxide

HeNe – Helium neon laser

HIRAC – Highly Instrumented Reactor for Atmospheric Chemistry

HO_2 – Hydroperoxy radical

HOx – collective for oxides of hydrogen

HPALD – Hydroxy peroxy aldehydes (here C_5 HPALDs formed from isoprene)

id – Internal diameter

IERE – internal energy relaxation eigenvalue

IR – Infra –red

KDP – mono-potassium phosphate crystal

KHP – keto hydroperoxides

LASER – light amplification by stimulated emission of radiation

LIF – laser induced fluorescence (also SLIF – saturated LIF)

LOD – Limit of detection

LOQ – Limit of quantification

M – generic collider

m/z – Mass to charge ratio

MCP – multi channel plate (detector)

ME – master equation

MESMER – master equation solver for multi-energy well reactions

MF – Methyl formamide (HC(O)N(CH$_3$)H)

MFC – mass flow controler

MVK – methyl vinyl ketone CH$_3$C(O)CHCH$_2$

NO – nitric oxide

NO$_2$ – nitrogen dioxide

NOx – collective for oxides of nitrogen

OH – Hydroxyl radical

OOQOOH –hydroperoxy alkyl peroxy radicals

OVOCS – Oxidated Volatile Organic Compounds

PES – Potential energy surface

PMT – Photo Multiplier Tube

PTR-TOF-MS – Proton transfer reaction – time of flight – mass spectrometry

QOOH –hydroperoxy alkyl radicals

QY – Quantum yield (also FQY – fluorescence quantum yield)

R – alkyl radical

RCCI – Reaction controlled compression ignition engine

Re – Reynolds number

RET – Rotational energy transfer

RF – radio frequency

RH – general fuel

RO – alkoxy radical

RO$_2$ – Alkyl peroxy (peroxy) radical

RRK – Rice, Ramsperger, Kassel theory (also RRKM – includes the work of Marcus)

SCCM – standard centimeters cubed per minute

SD – source drift region

SIFT-MS – Selective Ion Flow Tube Mass Spectrometry

SLM – standard liters per minute (dm^3 min^{-1} $atmosphere^{-1}$)

TBA – Tertiary butyl amine ($(CH_3)_3CNH_2$ ($tBuNH_2$))

tBuOOH – Tertiary butyl hydroperoxide

TMB – 1,3,5-trimethyl benzene (mesitylene)

UV – ultra violet

Variac – Variable autotransformer

VET – vibrational energy transfer

VOC – volatile organic compound

YAG – Yttrium aluminium garnet cyrstal, also Nd:YAG – neodymium doped YAG

1 General introduction

Tropospheric VOC oxidation and low temperature combustion (< 1000K) systems are both dominated by OH initiated oxidation. The HO_2 yield formed following the initial OH reaction can be important when modelling ignition delay times or ozone forming potentials. Measuring OH kinetics and HO_2 yields under high oxygen concentrations, at high pressures (500 – 4000 mbar), and over a wide range of temperatures (300 – 800 K) can provide important insights into the development of both novel biofuels and understanding the atmospheric impact of many VOCs. The ability to detect OH and HO_2 by conventional methods can become complex under the conditions applicable to low temperature oxidation and atmospheric chemistry. Radical precursors, humidity and products can provide interferences to absorption methods, and high temperatures and pressures make LIF measurements less sensitive.

This thesis will focus in particular on the development of the Leeds high-pressure system for time resolved OH and HO_2 measurement, and the application of this to amine and amide oxidation. Amines and amides have been the subject of only limited previous studies. Increased biomass burning, agricultural emissions and increased application of amines in new roles (e.g. in carbon capture and storage) requires a better understanding of their OH initiated oxidation, especially to the potential environmental risks associated with amine and amide oxidation.

1.1 OH initiated oxidation

1.1.1 Tropospheric chemistry and the HOx cycle
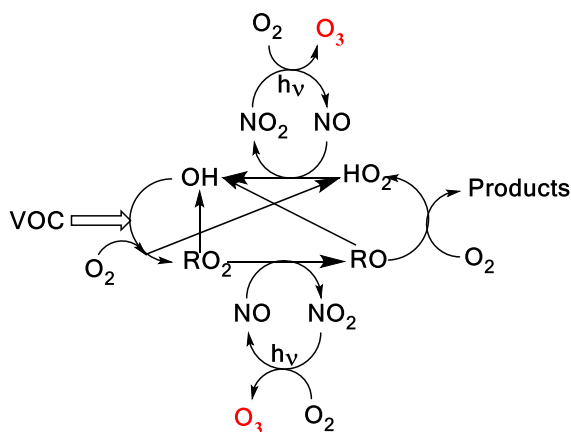
Scheme 1.1 A simplified tropospheric HOx cycle showing the importance of these short-lived radical species both to the chemical removal of VOCs and the formation of ozone.

In the atmosphere HO_2 and OH radicals (OH + HO_2 = HOx) are closely coupled via several reactions as shown in Scheme 1.1. The short lifetimes of HOx radicals mean that concentrations are determined by chemical production and removal and not by transport processes, making them ideal candidates as test species for our understanding of atmospheric chemical mechanisms (1-3).

The primary atmospheric OH source is via the photolysis of ozone, where the $O(^1D)$ radicals formed react with water to generate OH radicals (R1.1a,b). OH radicals are the dominant daytime oxidant, removing the majority of volatile organic compounds (VOCs) in the troposphere.(4)

$$O_3 \xrightarrow{+h\nu} O(\ ^1D) + O_2; \ \ O(\ ^1D) + \ H_2O \rightarrow \ 2\ OH \ \ \text{(R1.1a \& R1.1b)}$$
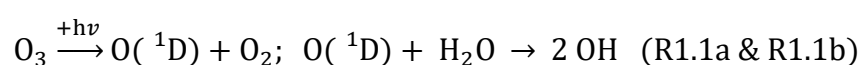
For saturated hydrocarbons (RH) such as methane or ethane, the OH reaction (R1.2) is via abstraction of a proton to leave an alkyl radical (R); in the case of unsaturated hydrocarbons (ethylene, isoprene) OH addition to the double bond is the primary OH reaction. OH addition reactions are pressure dependent, as the excess energy from the nascent adduct must be removed by collisions with a third body (M).

$$RH + OH \rightarrow R + H_2O \ \ \ \ \ \text{(R1.2)}$$

$$C_2H_4 + OH \rightarrow CH_2CH_2OH^* \xrightarrow{M} CH_2CH_2OH \ \ \text{(R1.3)}$$
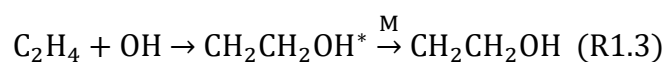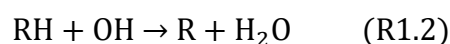
Under tropospheric conditions ($[O_2]$ = 5.7 × 10^{18} cm^{-3}), the reaction with OH is generally followed by addition of oxygen to form peroxy radicals (RO_2). The chemistry that follows depends greatly on the NOx (oxides of nitrogen) concentrations. In polluted areas with high NO concentrations, the reaction of RO_2 with NO will generate alkoxy radicals (RO) and NO_2 (R1.5) In low NOx environments (remote, clean regions) the reaction with other peroxy radicals can dominate their atmospheric removal.

$$R + O_2 \rightarrow RO_2 \ \ \ \ \ \text{(R1.4)}$$

$$RO_2 + NO \ \ \rightarrow NO_2 \ + RO \ \ \ \text{(R1.5)}$$

$$RO_2 + RO_2 \rightarrow O_2 \ + 2RO \ \ \ \ \text{(R1.6)}$$
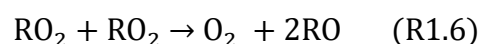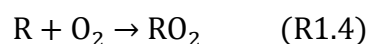
For RO_2s formed from atmospheric VOCs, such as methylperoxy (CH_3O_2), self-reaction with CH_3OO or cross-reactions with HO_2 lead to the formation of organic peroxides or organic acids. These channels act as radical termination processes except,

for the case of carbonyl based RO_2s where the cross reaction with HO_2 can be a chain propagation step by regenerating OH. (5-8)

For terpene derived RO_2s, often both RO_2-RO_2 (R6), RO_2-HO_2, and RO_2-NO (R5) reactions will lead to alkoxy radical formation.(9) For many alkoxy radicals e.g. methoxy or ethoxy radicals, the subsequent reaction is with oxygen to form a carbonyl and HO_2. In all but the cleanest environments, the subsequent reaction will be of HO_2 with NO to regenerate OH and form NO_2. Photolysis of the NO_2 formed from tropospheric HOx cycles, is the principle source of ground level ozone where the $O(^3P)$ formed reacts with O_2 to form ozone (O_3). This whole sequence is described as the HOx cycle and is summarized as Scheme 1.1.

1.1.2 Low-temperature combustion

The importance of OH and HO_2 chemistry is not limited to atmospheric processes; both OH and HO_2 are key intermediates in low temperature (500 – 1000 K) combustion processes, particularly those involving oxygenated fuels (10). The mechanisms of low temperature combustion are of particular interest in the development of new engine technologies such as reactively controlled compression ignition (RCCI) (11) and are closely linked to atmospheric oxidation mechanisms as both occur through radical-chain oxidation dominated by OH reactions.

The exact source of the initiating radicals in low-temperature combustion is less well understood; however, following the initial radical generation low temperature combustion follow similar cycles to tropospheric HOx oxidation. In low-temperature combustion, OH propagation occurs where, following interception of the R radical, the RO_2 isomerizes to form a alkyl hydro peroxy radical (QOOH), reaction 1.7a; this process is often in competition with HO_2 formation which is a chain inhibition step, reaction 8.

$$R + O_2 \rightarrow RO_2 \rightarrow QOOH \rightarrow OH + Products \qquad (R1.7a)$$

$$R + O_2 \rightarrow HO_2 + Products \qquad (R1.8)$$

For fuel combustion to occur, the radical initially generated must lead to chain branching. In low-temperature combustion, this is linked to the formation of hydroperoxyalkylperoxy radicals (OOQOOH) following the interception of QOOH radicals by oxygen. When OOQOOH radicals decompose to form OH and ketohydroperoxides (KHP) these can further decompose to produce additional OH

3

radicals. This increase in the number of radicals leads to chain branching in low temperature combustion, reaction 1.7b. (12)

$$RO_2 \rightarrow QOOH + O_2 \rightarrow OOQOOH \rightarrow OH + KHP \rightarrow OH + Products \qquad (R1.7b)$$
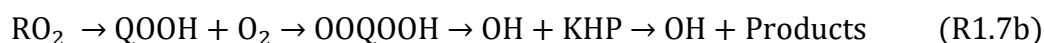
For many fuels, such as dimethyl ether (DME), the ability to measure QOOH radicals is limited due to their typically low concentrations and lifetimes. Understanding the chemistry of the formation of QOOH radicals and their subsequent decomposition, and interception by oxygen is also complex, an example potential energy surface is given as Figure 1.1. The QOOH radicals tend to be higher in energy than the RO_2 radicals with a low barrier to QOOH decomposition.(13) These factors combine to lead to a low population of the QOOH well; in addition, the competition between QOOH interception and QOOH decomposition is hard to experimentally separate when both processes lead to OH reformation.
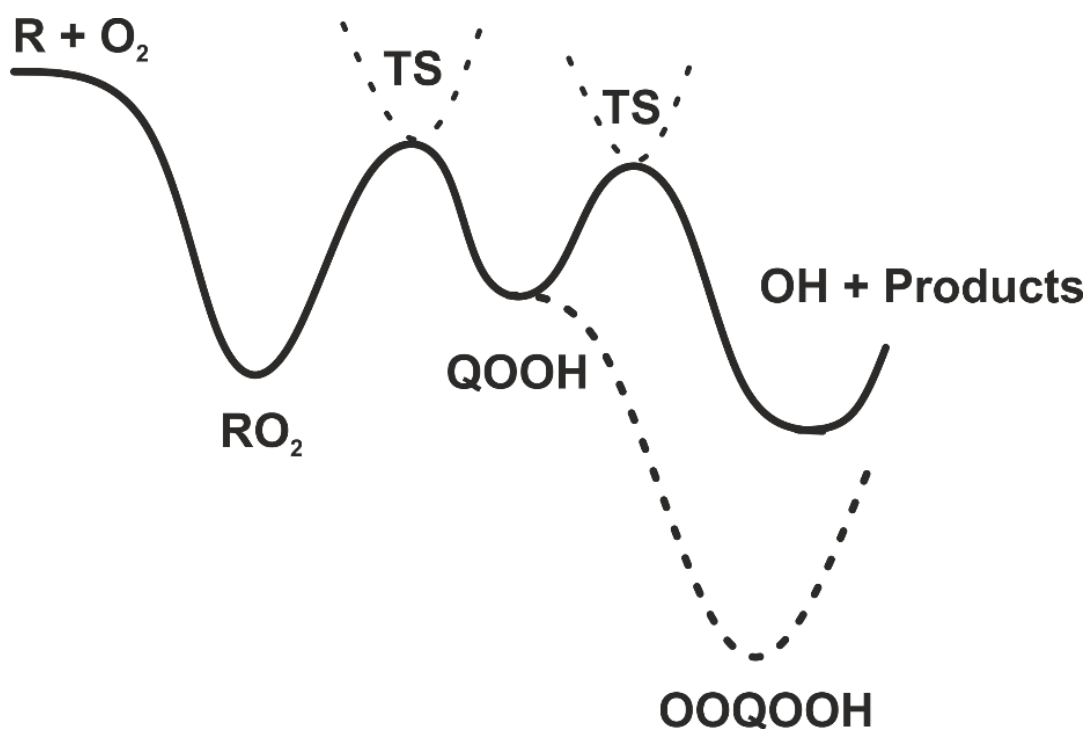
Figure 1.1 A general PES for the R+O₂ surface for a fuel, where interception by oxygen to form a OOQOOH species is shown as a dashed well.

Therefore, the ability to measure both OH kinetics and perform product analysis becomes important when attempting to elucidate the chemical pathways that lead to OH regeneration. In addition, where HO_2 formation is an inhibition step, for example butanol

oxidation (Chapter 4), the respective OH to HO_2 yield can be important in determining the ignition delay time for the fuel. (14)

1.1.3 Amine and amide oxidation.

Amines, amides, and other nitrogen containing compounds can be emitted into the atmosphere from a wide variety of sources. In particular through agricultural emissions, biomass burning and industrial releases. In the effort to move towards a low carbon economy there will be a general increase in biomass burning, and if amine based carbon capture and storage is introduced on a wide scale then this will become a significant source of nitrogen containing organic emissions. There have currently only been a limited number of studies, examining the OH initiated oxidation of nitrogen containing compounds, and further work is required to better understand the implications of increased emissions.

Although, OH initiated amine and amide oxidation has been the subject of fewer studies than the equivalent oxygenates, studies of a range of nitrogen containing compounds have been carried out. These have included studying the OH removal rates for several simple amines (15-19) and more complex amines such as ethanolamines, nicotine, and pipirazine. (20-25) Work has also been carried out on a range of simple amides including formamides and acetamides.(26-30) The majority of these studies have however been carried out under ambient conditions or over a small temperature range (260 - 350 K).

Ambient temperature studies allow for the modeling of the atmospheric chemistry that would follow release of compounds to the atmosphere, from biomass decomposition, livestock or from industry. However, there is the potential for both the site of the initial OH reaction and any subsequent product formation pathways to change with temperature. Nitrogen containing compounds make up a significant fraction of the fuel sources during biomass burning, and a disposal method for degraded amine wash solutions from carbon capture and storage is *via* incineration; to model the impact of these it is important to study amine and amide oxidation as a function of temperature.

R
 \
  N−NO
 /
R'

nitrosamine

R
 \
  N−NO$_2$
 /
R'

nitramine

Scheme 1.2 The structure of nitramines and nitrosamines.

Current UK government subsidies are leading major power stations to utilize biomass burning, as are many smaller facilities around the country; internationally this is part of governments' push to reduce reliance on fossil fuels and reduce the carbon emissions to meet the targets set for 2020. (31) The long term implications related to the increased combustion of biomass for power generation and related to forest fires, both controlled and uncontrolled, the plumes of which can contain many harmful chemicals including nitramines and nitrosamines (the structures of which are shown in Scheme 1.2), are not yet fully understood.(32)
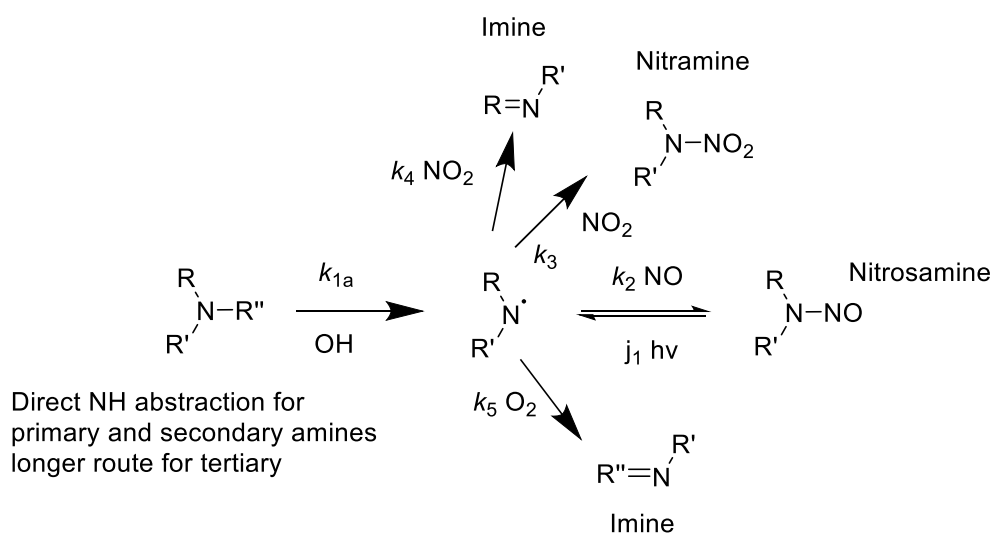
Scheme 1.3 A general scheme for the OH initiated oxidation of simple amines.

Production of nitrosamines or nitramines is of particular importance to health due to the potential toxicity of these classes of molecules (33). The formation of nitramines and nitrosamines is the product of the reaction of nitrogen centered radicals with NO and NO$_2$, Scheme 1.3. The reaction of nitrogen centered radicals with oxygen to form products is slow even with the relatively high oxygen concentration (5.7 × 10^{18} cm^{-3}) present in the atmosphere.(34, 35) Therefore, in environments such as downwind of power stations or forest fires with moderate to high NOx levels, the reaction with NO or NO$_2$ can then be faster than the reaction oxygen leading to potentially high yields of nitramines and nitrosamines.(36, 37)

Where the reaction with oxygen occurs, the product of the oxidation of a nitrogen centered radical is in general an imine. In addition, following formation of a primary nitrosamine, a further reaction with oxygen leads to the formation of an imine, HO_2 and NO, Scheme 1.3.(38) Imine formation in the atmosphere has been suggested as a route to both N_2O and cyanide formation.(39) N_2O is a particularly potent greenhouse gas, and the environmental and human health impact of cyanide formation could be significant these potential pathways for methylamine taken from Schade and Crutzen (39) are given as Scheme 1.4.

Scheme 1.4 The potential routes for the OH initiated oxidation of methylamine given in Schade and Crutzen.(39) Routes in black have been observed experimentally, those in red were not observed to occur.

The ability to measure accurate OH removal rates for a variety of amines and amides can be non-trivial. This is due to difficulties in delivering consistent known concentrations of the compounds, especially in the presence of radical precursors. This is partially due to many amides and amines having low vapour-pressures, and they can react with metal surfaces leading to uncertainties in the added concentrations in direct kinetic studies. Amines are basic, and many radical precursors such as peroxides tend to have lower pHs and as such can undergo acid base reactions during delivery that result in reduced concentrations of the compound when the radical oxidation is initiated. Further to this point, thermal stability issues can affect some amines and amides and this can lead to uncertainties in the concentrations delivered.

Where low vapour pressures are the major cause of uncertainty in the delivered concentration, UV absorption can be used to measure the concentration *in situ*. This method was used successfully in the work of Onel *et al.* to measure the OH removal rates of several ethanolamines. (20, 22) The method chosen for the work to be described later for delivery of low vapour pressure compounds was to sample the ambient vapour

pressure in a backing gas of nitrogen, with the backing pressure of nitrogen kept above that of the majority flow to which it would be added.

Where experiments were carried out in a novel high-pressure reactor for fast gas kinetic measurements and HO_2 yield detection, the output flow could be sampled by PTR-TOF-MS. By sampling the exit gas, it was possible to ensure that a constant new concentration had been reached when changing VOC flow, and to provide end-product analysis. In addition, the ability to monitor the output allowed for the observation of reactions between the compound added and radical precursors, and to ascertain when pyrolysis of the compound of interest became significant. It was therefore decided that this instrument could be used to study a range of nitrogen containing compounds, and expand the temperature range for those that had been the subject of only ambient temperature measurements.

1.2 Radical detection

As has been described in section 1.1, when considering atmospheric and combustion chemistry radical species (OH, HO_2, RO_2, RO, QOOH) are of critical importance to understanding the reactive removal of stable species. While it is possible to ascertain the bimolecular removal rate of VOCs through the relative rate method (section 1.3) and to measure the products formed from the reactions of radicals with stable molecules, to fully understanding the radical chemistry it is important to be able to detect them. In particular detecting the concentration of OH and HO_2 in the atmosphere can provide a key test species to evaluate the output of atmospheric chemistry models. To adequately model the combustion chemistry of new fuels, it is important to be able to measure both yields and the formation and loss kinetics of OH and HO_2.

A variety of methods exists for detecting radicals, which includes laser-induced fluorescence (LIF), absorption, and mass spectrometry. The discussion of radical detection to follow will focus on LIF, as this is the principle technique that has been employed in the work that follows in chapters 2 – 6.

1.2.1 Laser Induced Fluorescence (LIF)

Laser induced fluorescence (LIF) is a spectroscopic method where the spontaneous emission of light at a particular range of wavelengths (fluorescence) from an electronically excited species is monitored, following excitation through the absorption of

laser light, shown in Figure 1.2.(40) LIF is highly species selective, indeed even isotopomer selective (same number of each isotope of each element, but differing in position), because a single highly structured transition is probed, in general for small molecules this is an individual rotational line within a vibronic transition. The advantage this holds over broad band sources lies in the specificity of probing individual transitions, and the reduced line width of the laser light.
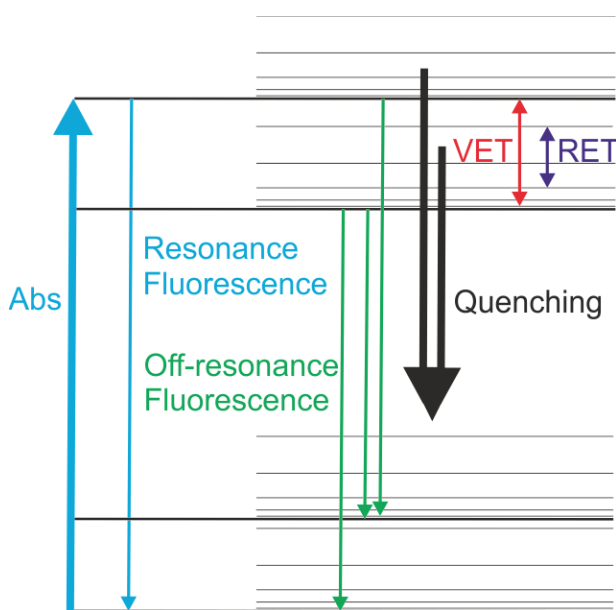
Figure 1.2   A simplified image of the processes that can occur in molecular LIF. Vibrational energy transfer (VET) and rotational energy transfer (RET), allow for the redistribution of energy within the excited species and are facilitated through collisions.

LIF can in theory be used to study any species that does not undergo complete dissociation following the electronic excitation, provided that the fluorescence quantum yield (QY) is sufficient compared to the background scatter generated from the probe light. LIF can be carried out where the lower state is not the ground state but an excited state, allowing the monitoring of vibrationally hot molecules, and allows the monitoring of the distribution of energy within products formed from a reaction.(41)

Atomic LIF has much greater sensitivity than LIF for molecules,(42, 43) in general atomic LIF requires much greater electronic excitation energies at very short wavelengths (e.g. 130 nm for O atoms).(44) Where LIF is used for studying small molecules, it is most effective for molecules with low lying electronic levels, where excitation does not significantly change the bonding of the molecule. For molecules that meet this criterion, the Franck-Condon factor should be significant and fragmentation of the excited species

should be minimal. Where excitation leads to fragmentation, for instance for methyl radicals, LIF is not possible,(45) however photo fragmentation laser induced fluorescence can occur.(46)

Two photon absorptions (226 nm for O atoms)(47) LIF is also possible although the absolute signal will be much lower as two photon processes are quadratically dependent on laser power. Two photon LIF can allow measurements to be made where either background signals would saturate detection for conventional LIF, or where the fluorescence quantum yield is low.(48)

For measurement of many atomic species, however, laser induced fluorescence is not used in practice because of a lack of laser sources with sufficient probe power at the low wavelengths required. In many cases, resonance lamps are used; where resonance lamps are used for fluorescence detection, the principles are the same as for continuous wave (cw) laser induced fluorescence.

The sensitivity of LIF depends on the absorption and emission spectra of the species being probed, for larger molecules absorption and emission spectra have broader lines and lower fluorescence quantum yields (FQY); lower FQY can lead to a reduction in sensitivity if background signals are not also reduced. Temperature can also reduce the sensitivity of LIF where spectral broadening and population of a larger range of rotational levels occurs at higher temperatures.(42) The sensitivity of LIF is also dependent on the rate of non-radiative process, vibrational relaxation and collisional quenching; in general, this makes LIF most effective when measuring at low effective pressures. The FAGE (fluorescence assay by gas expansion) technique that will be discussed in more detail later can be utilized to reduce quenching effects, and if the LIF probing occurs in the jet-expanded gas greater sensitivity is possible, benefiting both from the cooling, and reduced collision frequency that free expansion provides.

For molecular LIF, fluorescence from the upper electronic state can occur to several vibrational levels within the lower electronic state, and vibrational energy transfer (VET) can lead to fluorescence from lower vibrational levels in the upper state than that originally populated. Figure 1.2 shows a simplified picture of molecular LIF. In general, the absolute sensitivity of LIF is greatest where fluorescence and excitation are at the same wavelength (resonant) as the Franck-Condon overlap is large, where excitation is at a lower wavelength than fluorescence (off resonant), the reduced sensitivity can be offset

by the reduced background signal possible from the ability to filter out scattered probe light.

LIF is in general significantly more sensitive than absorption techniques, for low concentrations detection by absorption techniques it is hard to distinguish a small change from the large incident intensity. For LIF, the fluorescence signal is proportional to the probe power and concentration of the ground state of the species being probed.(48) Unlike absorption techniques, LIF is not an absolute measurement of the concentration, and so where absolute concentrations are required, a calibration must be performed. For LIF measurements, the calibration to calculate concentrations is a large source of the experimental uncertainty.(45) For larger molecular species the fluorescence quantum yields decreases (48) and as such LIF can become rapidly impractical for species larger than ethoxy radicals when used for kinetic measurements. Although, for some large radicals LIF has still been a used for radical detection for example t-butoxy radicals.(49-51)

Although not an absolute measurement, LIF is a highly versatile technique for monitoring changes in the concentration of species of interest. The versatility of LIF techniques comes from the ability to use tuneable lasers to selectively probe many different molecular or atomic species. It is even possible using multiple imaging optics and multiple probe lasers to simultaneously monitor the time evolution of different species.

In general, when used with pulsed laser photolysis (PLP) a pulsed probe laser is also used, and a single LIF time point is generally collected per photolysis event. By then varying the delay between photolysis and probe a decay profile can be built up, Figure 1.3. In absorption based experiments an entire decay is measured per photolysis event, this leads to absorption methods being more efficient at recovering profiles; LIF being less efficient but more sensitive than absorption techniques allowing lower radical concentrations to be detected but more photolysis events are required. Where high repetition rate probe lasers (multi kHz) or continuous wave probe lasers are used, entire decays can be collected for a single photolysis event in a similar manner to absorption methods.
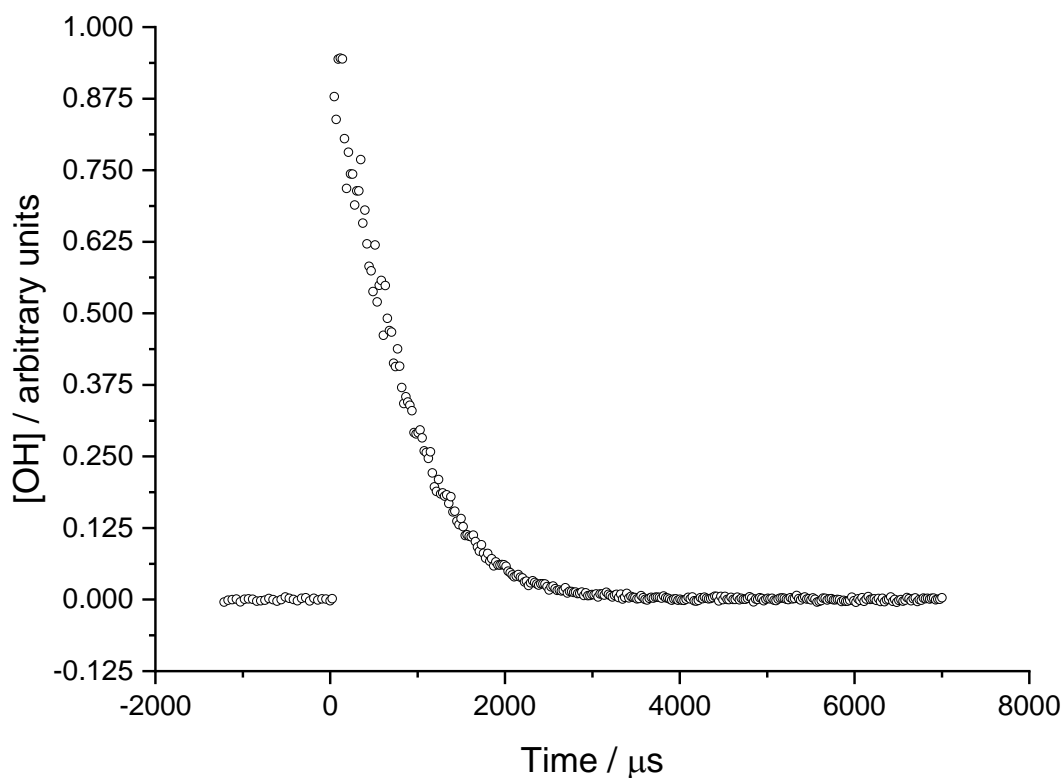
Figure 1.3. An example of a trace from a PLP LIF experiment, where the timing is the delay between the photolysis laser and the probe laser with time zero being when photolysis occurs. By scanning a range of delays, a full decay profile can be collected.

1.2.2 Quenching

Quenching is a non-radiative, non-reactive inter molecular loss process for an excited molecule, where energy is transferred to the quencher and then from the quencher to the surroundings. (52) There are several mechanisms by which quenching can occur through collisions: electron transfer, energy transfer, paramagnetic effects and through the presence of heavy atoms.(53, 54)

In electron transfer, a reaction initially occurs where an electron is transferred leading to the formation of a pair of ions. In this transfer reaction, the activated neutral loses energy and becomes a deactivated ion. If the ions undergo a second reaction to return to neutral species then this process can be considered as quenching of the excited molecule.(53) Where simultaneous exchange of electrons occurs this can be considered direct energy transfer between the excited molecule and the quencher. For both electron exchange and electron transfer, the quencher and excited molecules must be spatially close to each other (requires collision) and have orbitals close in energy to allow efficient quenching to occur. A longer-range energy transfer process can occur, where dipole-

12

dipole interactions allow deactivation of an electron in the excited species to initiate excitation of an electron in the quencher, this process is often called resonance energy transfer or Forster resonance energy transfer.(54) There is a distance dependence on the efficiency of dipole-dipole quenching but over a significantly longer range when compared to the reduction in efficiency where direct orbital overlap is required. (53, 55)

The presence of heavy atoms and or paramagnetic species can also have an impact on the quenching observed. For heavy atoms this is due to the greater ease with which heavy atoms can undergo spin forbidden processes, facilitating transitions between triplet and singlet states in the excited molecule.(53) For paramagnetic effects the permanent magnetic moment of the paramagnetic molecule or ion allows enhance spin orbit coupling. In a manner similar to heavy atoms, this allows for an increased rate of spin forbidden processes. Oxygen is a paramagnetic molecule and as such as a quencher will exhibit this effect, for oxygen this may occur in addition to collisional quenching electron transfer and or electron exchange occurring.(56) This is of particular importance both when studying under atmospheric conditions and to combustion systems, where oxygen is present at high concentrations.

In the gas phase collisional quenching is in general the dominant process, and where the bath gas is a molecule (e.g. N_2, O_2), as opposed to a noble gas (Ar, He etc). vibrational energy transfer can occur.(57) Where more complex molecules such as methane (CH_4) are present, the vibrational transfer process can become more significant.(58) Where rotational and vibrational energy transfer occurs quenching can become a more efficient process and as such quenching rates can be increased by orders of magnitude.(59)

Quenching rates depend on both the concentration of the quencher and the quenching efficiency. Where electronic levels are widely spaced and vibrational and rotational energy transfer is not possible, the quenching efficiency is low e.g. for helium. For molecules that have many vibrational degrees of freedom (CH_4) or where paramagnetic effects are present (O_2), the quenching efficiency can be dramatically increased.(57-61) Reactions carried out in this work used nitrogen as bath gas with oxygen as a smaller fraction of the total flow (1-20 %).

Where the rates of quenching processes are significant (high pressures of nitrogen or oxygen bath gases), *in situ* LIF measurements can still be made by using 'saturated' LIF

(SLIF).(62-65) In conventional (linear) LIF there is a linear response of LIF signal on probe power, this relies on the assumption of minimal depletion of the population of the lower state. At high probe intensities, when this assumption is no longer valid, the absorption is described as being saturated, and there is a non-linear response of signal with increasing probe power.(48) Where the absorption has been saturated, the population of the excited state is still proportional to the lower state population, but is no longer proportional to the absorption coefficient.
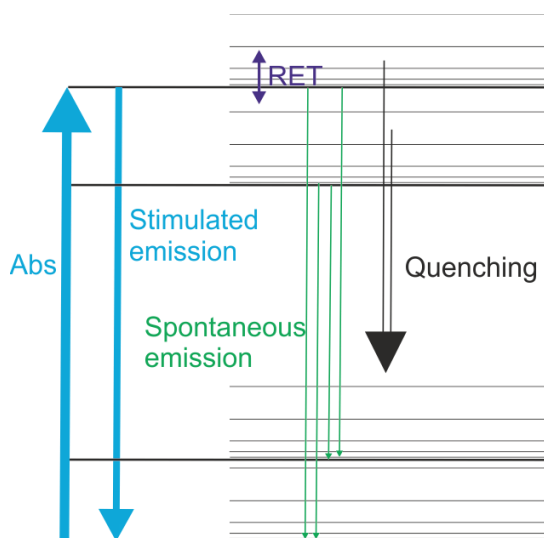
Figure 1.4 An energy level diagram for SLIF. At high probe energies absorption can become saturated and stimulated emission can become the dominant loss process for the excited electronic state, this allows LIF measurements to be made even when quenching rates are fast. For non-saturated LIF (Figure 1.2) stimulated emission is a minor process and the competition between quenching and spontaneous emission dominates.

At high pressures, loss processes from the higher state can be simplified to spontaneous emission, quenching and stimulated emission. LIF sensitivity generally decreases where quenching rates are in competition with the rate of spontaneous emission; at higher probe energies stimulated emission of photons becomes the dominant source of fluorescence. Once the absorption has become 'saturated', further increases in probe power will provide larger increases in the rate of stimulated emission than in absorption. With sufficiently large probe power, once absorption of a photon has occurred the dominant loss process from the excited state will be stimulated emission, shown in Figure 1.4. Where stimulated emission is the dominant loss processes from the excited electronic state, the fluorescence quantum yield depends on the probe power, as

a result it is possible to carry out LIF studies at high pressures inaccessible to conventional LIF detection. (> 100 bar)(64)

The requirement for high probe energies for saturated LIF can lead to complications from two photon processes and increased scattered light. As the measurements rely on stimulated emission the collected fluorescence has the same wavelength as the probe light so scattered light cannot be filtered out which can lead to saturation effects on the detector. In addition, analysis can be further complicated by a requirement to understand the rotational energy transfer processes (62-64, 66) and if non-uniform saturation is present.(64)

Another technique for making LIF measurements from the atmosphere was developed, instead of making LIF measurements at high pressures, the high-pressure system is pinhole sampled and the gas is jet expanded into a low-pressure cell.(67) This technique is called FAGE (fluorescence assay by gas expansion) The LIF signal in the low-pressure cell is still proportional to the concentration in the higher-pressure system. Where accurate calibrations can be performed, FAGE LIF to make accurate assignment of radical concentrations.(68)

The ability to couple FAGE LIF cells to flow tubes has been utilized to make kinetic OH measurements sampling high-pressure (> 500 mbar) reactors.(69-75) If a small flow of NO is added before the probe laser samples, HO_2 can be partially titrated to OH and an indirect measurement of HO_2 concentrations can be made using OH LIF. (69, 72, 73)

Where LIF detection was performed in the jet-expanded gas,(74) fast radical kinetics on the microsecond timescale could be measured with high accuracy and precision.(76) This was possible when the timescale for transport from the high-pressure reactor and the timescale over which the reaction was measured were well separated.(74) By performing LIF in the jet expanded gas itself, the sensitivity of LIF was increased due to the cooling effect free expansion generates (30 K in the jet versus 300 K in the high pressure reactor) and due to a high number density in the expansion comparable to the collision frequency. Where OH kinetic measurements were made at higher pressures in this work (>300 Torr), OH LIF detection was made using the FAGE method.(69)

1.2.3 OH and HO$_2$ detection

As discussed in sections 1.1.1 and 1.1.2, monitoring OH and HO$_2$ concentrations under the elevated temperatures and high pressures of combustion processes and under the high oxygen concentrations present in the atmosphere (5×10^{18} cm^{-3}) is of interest. In low-temperature combustion, HO$_2$ formation is a chain inhibition process, with OH reformation a chain propagating or chain branching process. The ratio of chain branching to chain inhibition processes is often the controlling factor in modelling ignition delay times (14). High temperatures and concentrations of oxygen may be required to convert atmospheric processes, which take several 10s of seconds at ambient temperatures (and hence may be influenced by surface chemistry or secondary reactions) to the millisecond or microsecond timescale where they can be studied by flash photolysis techniques without such interferences (76).

When experiments are carried out in conventional quasi-static (low-pressure) reaction cells, laser induced fluorescence (LIF) detection of OH radicals is possible, and LIF provides a highly sensitive detection method. HO$_2$ formation can be assigned by carrying experiments out in the absence and presence of a small concentration of NO and measuring the degree of OH recycling that occurs.(15) LIF only provides a relative signal and in order to derive absolute concentrations it is necessary to calibrate the signal. In addition, at elevated temperatures and pressure LIF detection becomes less sensitive.

Direct measurements of HO$_2$ rely on absorption techniques, and important kinetic information on HO$_2$ reactivity has been determined mainly using UV absorption spectroscopy. This can be achieved either with conventional absorption techniques (including multipass optics to enhance the path length) or in the IR with cavity ring down spectroscopy (CRDS) (77, 78). However, the HO$_2$ UV absorption spectrum (200 - 260 nm) is broad and featureless (79), and as such, overlaps with the UV absorptions of many other species present in atmospheric degradation pathways or combustion systems (particularly H$_2$O$_2$ and RO$_2$). To utilize the selectivity of the structured IR spectra, absorption methods have been developed in both the mid and near-IR (NIR) (80). Mid-IR absorption features for HO$_2$ provide sufficient absorption cross-sections for study (81) but suffer from severe pressure broadening, reducing sensitivity under the conditions relevant to atmospheric and combustion systems (82). Detection in the NIR has similar advantages in terms of a structured spectrum providing greater selectivity; the weaker absorption cross-sections are compensated by the higher powers and ease of use of NIR

laser sources (83). However, pressure broadening and interference from H_2O absorptions can make these measurements difficult at even low concentrations of water (10^{14} molecule cm^{-3}).

In the atmosphere and in chamber studies, OH can be detected by a sensitive but non-absolute method laser induced fluorescence. HO_2 can be indirectly measured using the same technique via conversion to OH, with detection of OH via laser induced fluorescence (LIF) (1, 67, 84, 85) or conversion to $H_2^{34}SO_4$ (reactions 1.9 – 1.11) with subsequent detection of the acid via mass spectrometry (86, 87).

$$OH + SO_2 \rightarrow HSO_3 \qquad (R1.9)$$

$$HSO_3 + O_2 \rightarrow SO_3 + HO_2 \qquad (R1.10)$$

$$H_2O + SO_3 \rightarrow H_2SO_4 \qquad (R1.11)$$

In the LIF method, also known as Fluorescence Assay by Gaseous Expansion (FAGE (67)), which is the technique that will be a focus of the work to come, OH can be directly detected by LIF following expansion from a high pressure system into a low pressure detection cell. Where HO_2 is detected, a flow of NO is introduced which reacts with HO_2 (R1.12):

$$HO_2 + NO \rightarrow OH + NO_2 \qquad (R1.12)$$

The resulting OH is then monitored. The high sensitivity with which OH can be detected gives HO_2 detection limits in the 10^8 molecule cm^{-3} range for 5 – 10 s averaging, however, to extract concentrations, both OH detection methods require calibration (68). For chamber measurements of HO_2, comparisons with direct CRDS measurements have verified the reliability of the calibration process (78).

As stated earlier, in general LIF becomes less sensitive at higher temperatures (due to distribution of population over more rotational levels) and O_2 concentrations (due to quenching). Sampling into the low-pressure region reduces both the effect of collisional quenching and temperature on the sensitivity of LIF detection, although there is a reduction in the number density of the HOx species in the expansion. The principle of coupling a LIF based FAGE cell for OH and HO_2 detection to a higher pressure reactor has been utilized by Nehr *et al.* where adaptions were made to the Jülich OH lifetime instrument (73). The instrument to be discussed later in this work (Chapter 3) shifts the timescale over which the OH measurements can be made. Changes in OH radical

concentration being measured with microsecond resolution, allowing fast gas phase radical reactions to be measured in addition to HO_2 yield measurements.

1.3 Kinetic measurements

In general, all kinetic measurement techniques involve comparing the concentration at a given reaction time $[A]_t$ to the concentration at a previous time (usually time zero $[A]_0$), the fraction remaining at time t is proportional to the removal rate. For bimolecular reactions (A+B), the rate of reaction is proportional to the rate coefficient (k_{B+A}) and the concentration of the two species ($[A]$, $[B]$), this is shown as Equation 1.1.

$$\frac{d[A]}{d[t]} = -k_{B+A}[A][B] \qquad Equation\ 1.1$$

By integrating equation 1 between time zero and a given time, t, Equation 1.2a is generated and this can be rearranged as Equation 1.2b. In this form, if the ratio of the concentrations of one species is known and the absolute concentration of the second species is also known then the bimolecular rate coefficient can be assigned.

$$ln[A]_t - ln[A]_0 = -k_{B+A} \int_0^t [B]\, dt \quad Equation\ 1.2a$$

$$ln\frac{[A]_0}{[A]_t} = k_{B+A} \int_0^t [B]\, dt \qquad Equation\ 1.2b$$

In direct kinetic measurements, one method commonly used to define the bimolecular rate coefficient is the pseudo first order assumption; this method has been used widely in the work carried out later in chapters 4, 5, 6. If a large excess of one reactant is used, such that its concentration changes minimally during the reaction, d[B]/dt $\approx$0, then the reaction is considered to be pseudo first order with respect to the deficient reactant equations 1.3a and 1.3b. Under these conditions the pseudo first order rate coefficient (k_{obs}) can be assigned from the relative change in the concentration of the deficient reactant. That only a relative change is required means that raw changes in signal response from techniques such as LIF, GC-FID or mass spectra can be used to assign the rate coefficient without any absolute calibration.

$$\frac{d[A]}{dt} = -k_{obs} \times [A] \qquad Equation\ 1.3a$$

$$k_{obs} = k_{bimolecular} \times [B] \qquad Equation\ 1.3b$$

The reaction is then studied with varied concentrations of the excess reagent. By plotting the observed rate coefficients against the concentration of the excess reagent ([B]) the gradient of this plot is the bimolecular rate coefficient, Figure 1.5. Where pseudo first order conditions cannot be maintained then the decay of both species will be non-exponential, and the resulting kinetics can be difficult to deconvolute and requires measuring the loss of both species simultaneously.
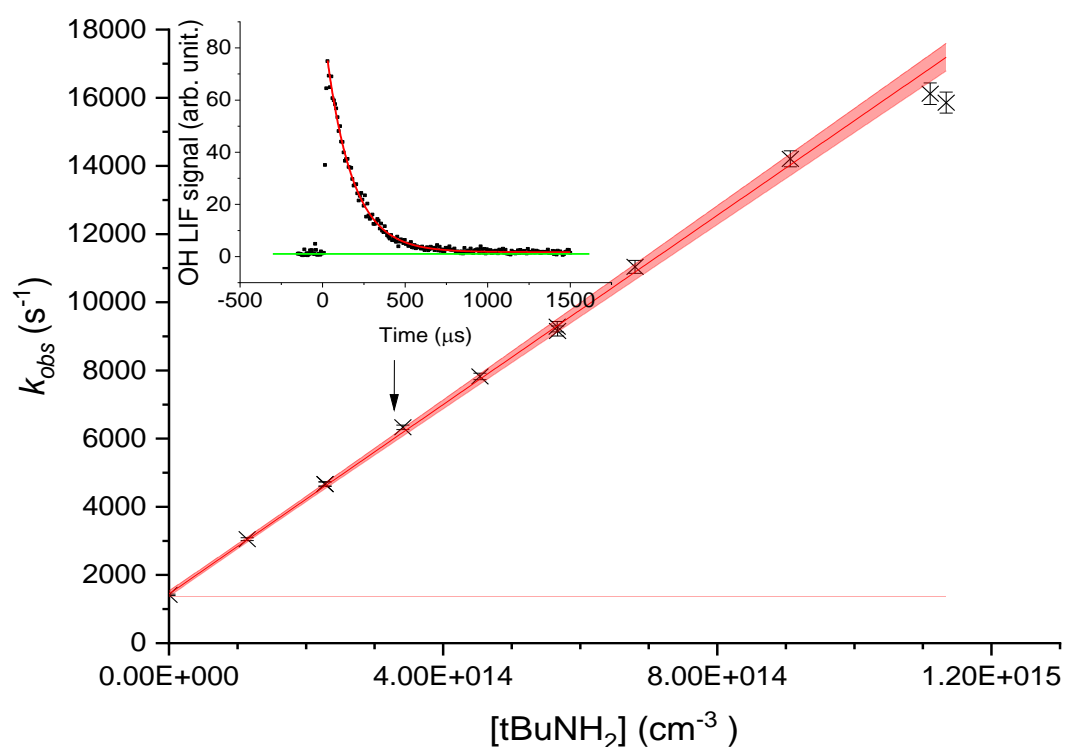
Figure 1.5 A plot of pseudo first order rate coefficient (k_{obs}) against excess reagent concentration ([RH]) generally referred to as a bimolecular plot. The gradient of the liner portion of this plot is the bimolecular rate coefficient.

Instead of directly measuring bimolecular removal rate coefficients by monitoring the concentrations of the two species that are reacting, it is possible to measure them indirectly through the relative rate method. The relative rate method compares the time resolved loss of a reagent of interest (R) compared to the loss of a reference species (S) (which has a well-defined bimolecular rate coefficient) to allow for the calculation of the unknown bimolecular rate coefficient. This method is well established and has been used to define rate coefficients for many important atmospheric reactions; one significant advantage of this method is that it can allow for the precise measurement of rate coefficients even where the concentration of the reactants cannot be defined well.

$$ln\frac{[R]_0}{[R]_t} = \frac{k_{R+X}}{k_{S+X}}ln\frac{[S]_0}{[S]_t} \qquad \textit{Equation 1.4}$$

By substituting both the compound of interest, R, and the standard, S, into Equation 1.2b two equations are formed. When the equation for the reference compound is further substituted into the equation for the compound of interest and rearranged Equation 1.4 is formed. From Equation 1.4 a plot, Figure 1.6, of $ln([R]_0/[R]_t)$ versus $ln([S]_0/[S]_t)$ will have a gradient that is the ratio of the rate coefficients. This is the principle by which relative rate experiments work and this has been an important tool for measuring kinetics especially for slow reactions where performing direct kinetic measurements were complex, this method has been used to study the reaction of OH and TMB in chapter 7.
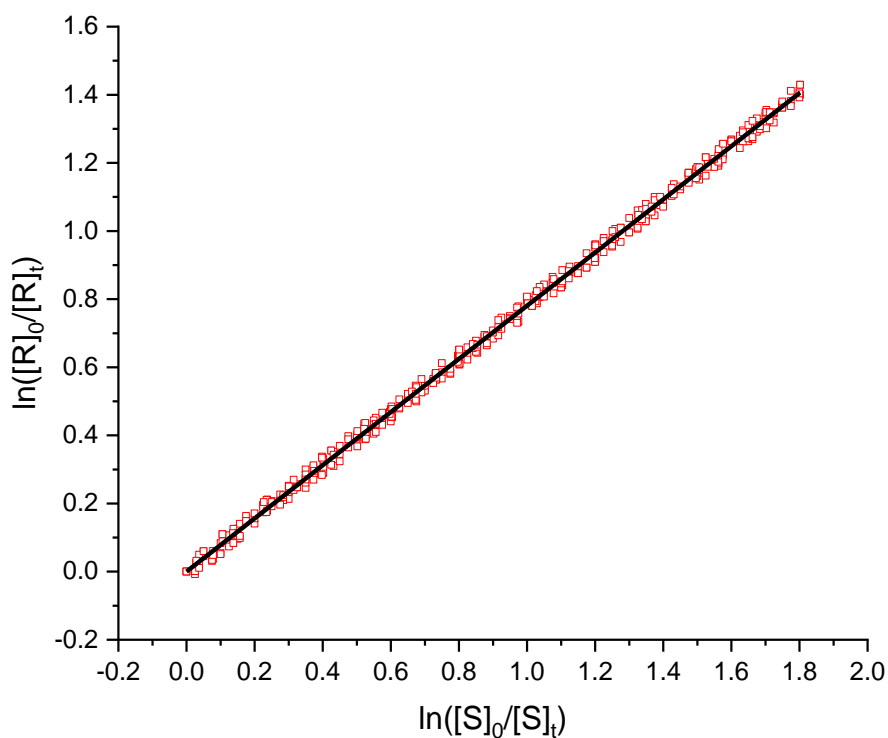
Figure 1.6 A relative rate plot the gradient of this plot is the ratio of the bimolecular rate coefficients.Where the rate coefficient for a reactive species (R) and the reference compound (S) is well known the unknown bimolecular rate coefficient can be defined.

The situation as defined above is for an ideal experiment where the only losses from the system are the reaction of the reference and compound of interest with the reactive species. In practice this can be an oversimplification that will lead to erroneous bimolecular rate coefficients being assigned. Dilution, wall losses, photolysis and reaction

with precursors can all increase the losses of reference and compounds of interest. Where these loss processes are not small with respect to reactive losses they need to be explicitly accounted for.
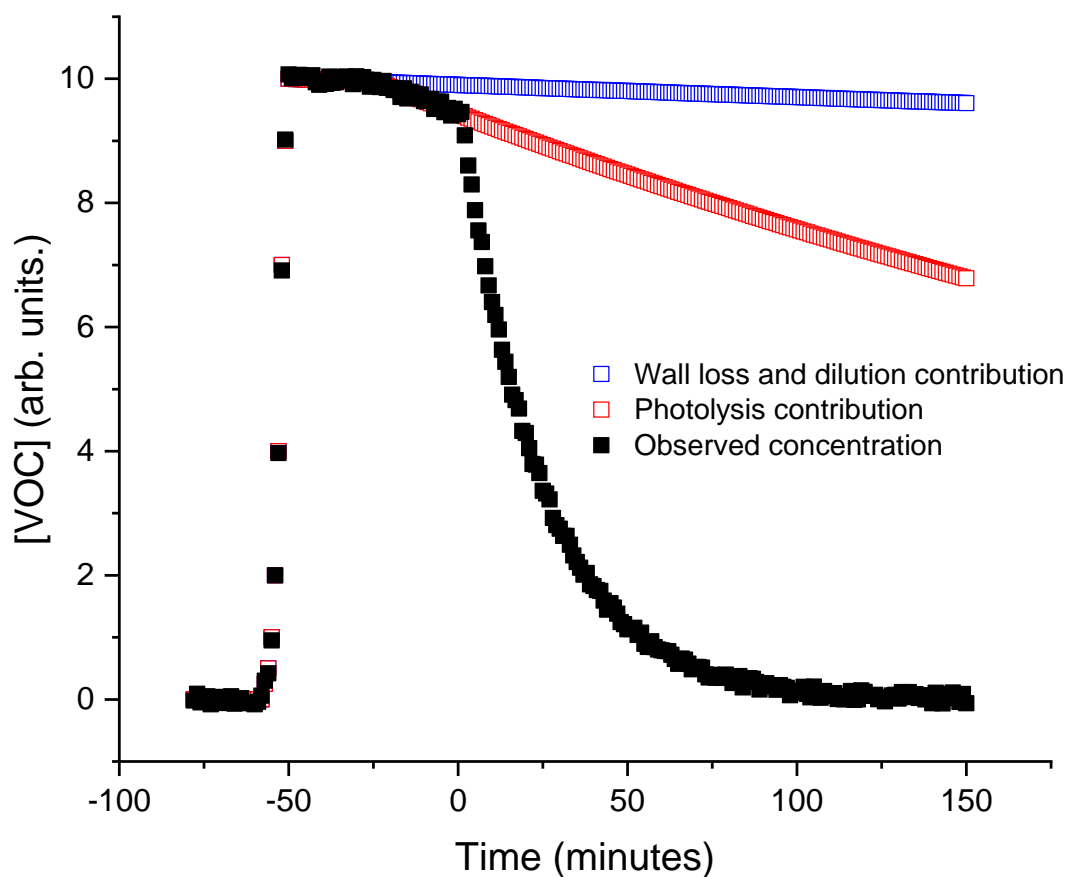
Figure 1.7 Examples of the concentration profiles that would be seen for a VOC during a photo-oxidation experiment where the VOC is lost through wall losses, dilution and photolysis in addition to reaction, with the contribution from wall loss is shown as blue square and photolysis of the VOC as red squares.

Dilution can be accounted for in several ways, one common method is including an unreactive and highly volatile tracer; the decrease in the tracer concentration can then be used to map the expected dilution effect on the more reactive compounds. Alternatively, if constant replenishment of the backing gas is maintained and the reactants are well mixed then the concentration can be adjusted appropriately using the fraction replaced to define the expected dilution losses.

Wall losses can be assigned by monitoring the changes in concentration observed in the absence of precursors and photolysis occurring. Where this is carried out the observed decrease will include both wall losses and dilution losses. Photolysis of the reactants can be accounted for in the same manner where the photolysis source is turned on for a period in the absence of the precursor and the losses of the reference and reagent of study are monitored. Again, this can be applied to additionally assign reaction with the precursor by monitoring the change in observed signals when the precursor is added in the absence of photolysis.

A corrected concentration at each time point $[A]_c$ can then be calculated, red squares in Figure 1.7, for each species and when this is substituted for the concentration at time zero in the relative rate plot the slope gives the ratio of the bimolecular rate coefficients. For relative rate measurements performed in chambers with large surface to volume ratios where wall loss rates are low, if the compounds being studied (reactant of study and reference compounds) do not photolyze significantly the gradients of both plots (corrected and uncorrected relative rate plots) should differ minimally and corrections can be neglected.

For relative rate analysis, the detection method for the species being studied and the reference do not have to generate exact concentrations, so long as the signal response is linear in concentration. Several common techniques used in relative rate experiments are FTIR (Fourier-transform infrared spectroscopy), gas chromatography (GC), mass-spectrometry (MS), cavity ring down spectroscopy (CRDS), and laser induced fluorescence (LIF).(88) Where relative rate experiments were carried out in this work the principle detection method chosen was chemical ionization by proton transfer reactions with ions measured by time of flight mass spectrometry (PTR-TOF-MS).

1.4 Pressure dependence and chemical activation

As was briefly mentioned in section 1.1.1, it is possible for reactions to display pressure dependence, whereby up to a limit increases in pressure lead to increases in observed rate coefficient, an example of a highly pressure dependent reaction is that of OH with ethylene.(89) There are two main classes of pressure dependent reactions: unimolecular dissociations, and addition reactions, which are depicted in Figure 1.8. In addition reactions, the energy released through the formation of a new bond must be lost to form a stable product molecule, and this is achieved through collisions with the bath gas, Reaction 1.13a. For unimolecular dissociations, the pressure dependence derives

from collisions between the reactant and the bath gas providing the energy to allow the reaction to proceed, Reaction 1.13b.

$$A + B \Leftrightarrow AB^* \xrightarrow{[M]} AB \qquad (R1.13a)$$

$$AB \xLeftrightarrow{[M]} AB^* \rightarrow A + B \qquad (R1.13b)$$
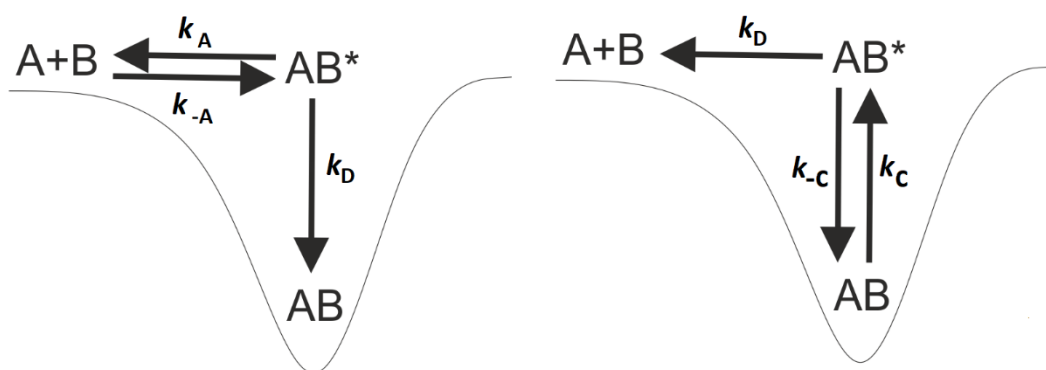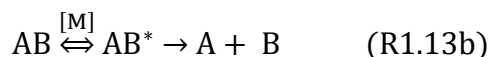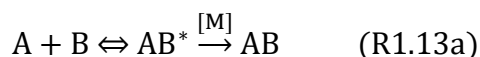
Figure 1.8 Pictorial representations of the Lindemann model of pressure dependent reactions.The LHS shows a bimolecular association reaction and the RHS depicts a unimolecular decomposition reaction.

The description above is a summary of the first qualitative explanation for the presence of pressure dependence in unimolecular reactions and is known as the Lindemann mechanism, named after its proposer. The Lindemann mechanism is a hard sphere model and separates unimolecular decomposition reactions into three distinct processes: activating collisions with the bath gas, M, (k_c), deactivating collisions (k_{-c}), and dissociation of the activated species (k_d). Now if AB* is sufficiently reactive then after a short induction time the loss rate of AB* should match the formation rate and the concentration [AB*] can be considered to be at a steady state, Equation 1.5.

$$k_c[AB][M] = k_{-c}[AB^*] + k_d[AB^*] \qquad Equation \ 1.5$$

Now from Equation 5 it can be seen that the rate of formation of products is dependent on the steady state concentration of AB* and the rate coefficient for dissociation. By rearranging Equation 1.5 for the concentration of AB* and substituting into the product formation rate equation, Equation 1.6 can be generated.

$$\frac{d[product]}{dt} = \left(\frac{k_d k_c}{k_d + k_{-c}[M]} \right)[AB][M] \quad Equation \ 1.6$$

A summary examination of Equation 1.6 produces two different regions of behavior the high and low pressure limits. At the high-pressure limit the k_{-c}[M] term dominates the denominator, deactivation is the primary loss of AB* and further increases in pressure will not increase the observed formation rate. At the low-pressure limit then dissociation is the primary loss of AB*, k_d dominates the denominator and the observed product formation rate is directly proportional to the number of collisions.

$$k_{AB} = \frac{[M]}{\frac{1}{k^0} + \frac{[M]}{k^\infty}} \qquad \textit{Equation 1.7}$$
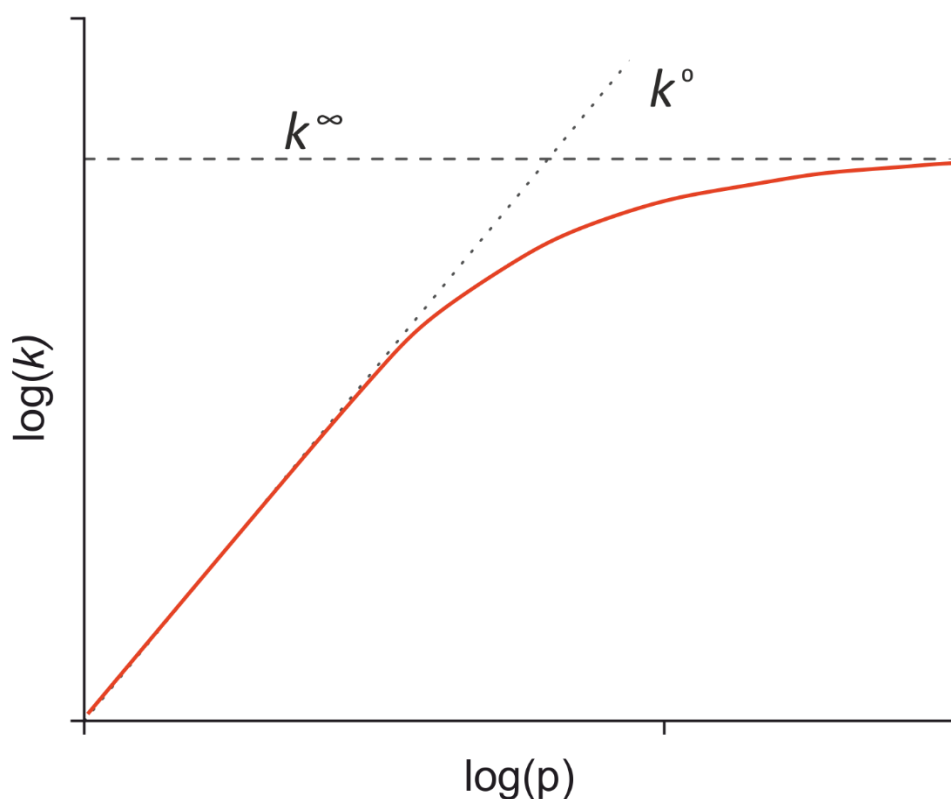
Figure 1.9 A representation of the pressure fall off curve (red line) for a pressure dependent reactionwhere the low-pressure limit, k^0, is depicted by a dotted line and the high-pressure limit, k^∞, by a dashed line.

A general way of describing this low and high-pressure behavior of the Lindemann mechanism to allow for a description over a range of pressures can be given as Equation 1.7, and is represented as Figure 1.9. In Equation 1.7 k^0 is the low pressure limit rate coefficient and $k\infty$ is the high pressure limit value. This allows for a qualitative description of unimolecular dissociation processes it cannot reproduce the experimentally observed pressure fall off curves. The lack of quantitative accuracy comes from the

assumptions intrinsic to Lindemann theory, molecules are not hard spheres and the total energy of polyatomic molecules is distributed between translational, rotational, and vibrational modes.

The failure of Lindemann theory to account for the vibrational contribution to activation rate leads to a systematic underestimation of the activation rate. A systematic underestimation of k_c leads to the incorrect onset of the pressure fall off curve. The presence of different types of barrier to reaction (tight versus loose transition states) is also negated in the Lindemann model. Some reactions pass through transition states that require constrained molecular geometries to occur.

For association reactions, Reaction 1.13b, the activated species AB* will again be at equilibrium. Here, the equilibrium is between adduct formation (k_a), deactivation (k_d) to form the product, AB, and dissociation back to reactants (k_{-a}), A + B, Equation 1.8. Treating this system in the same manner as the unimolecular decomposition again yields two pressure limit behaviors. At the high-pressure limit (k^∞) the deactivation of AB* can be treated as instantaneous and the rate of product formation is dependent only on the rate of the initial activated complex formation, Equation 1.9. Under low-pressure conditions (k^0), Equation 1.10, there is an equilibrium between the rate of adduct formation and loss. In the low-pressure regime third order kinetics will be observed where the rate of adduct formation scales with pressure.

$$\frac{d[product]}{dt} = \left(\frac{k_d k_a}{k_{-a} + k_d[\text{M}]}\right)[\text{A}][\text{B}][\text{M}] \quad Equation\ 1.8$$

$$k^\infty = k_d[\text{A}][\text{B}] \qquad Equation\ 1.9$$

$$k^0 = \left(\frac{k_d k_a}{k_{-a}}\right)[\text{A}][\text{B}][\text{M}] \quad Equation\ 1.10$$

Again, as with the unimolecular decomposition description, Lindemann theory neglect the contribution of the vibrational modes to deactivation of AB*. This leads to a failure to adequately describe the fall off region adequately. There were several subsequent important modification to Lindemann theory that provided improved results in describing the high-pressure limit. The first of these was the inclusion of internal vibrational modes in the hypothetical molecules. When applied to unimolecular decompositions, this modified theory (Lindemann-Hinshelwood) led to an increase in k_a, while k_{-a} remained the same, and k_d decreased. While, this theory qualitatively improved

the description of the high-pressure limit it still failed to quantitatively describe the shape of the pressure fall off curve.

A significant improvement that better described such systems was developed by Rice Ramsperger and Kassel (RRK). In RRK theory it is assumed that for reactions to occur it is not merely sufficient for the excited complex AB* to be formed but that this must then pass through a particular geometry $AB^{\#}$ for a reaction to occur. In this model, depicted in Figure 1.10, it is assumed that energy transfer processes are fast with respect to reactions, and that AB* and $AB^{\#}$ have the same energy. In AB*, the energy is randomly distributed across the molecule; whereas, in $AB^{\#}$ the required energy is localized to the reactive mode. This model can accurately predict the shape and occurrence of the fall off region where the effective number of oscillators as opposed to the total number of oscillators is included.
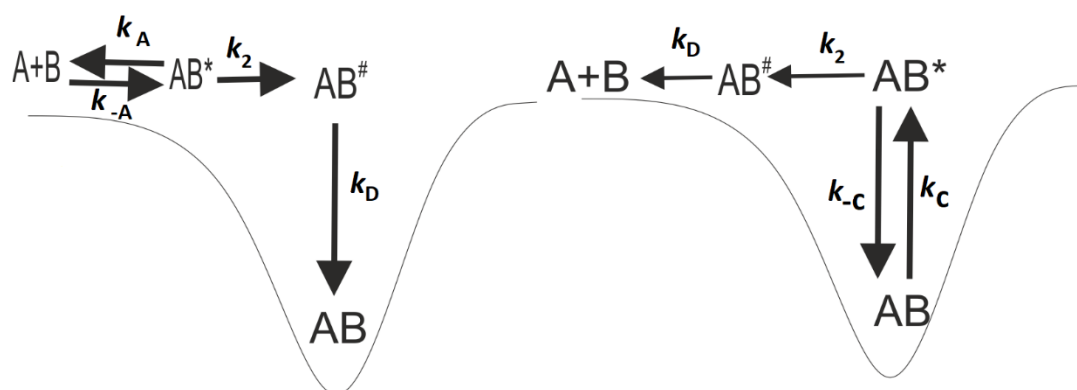
Figure 1.10 Depicts RRK theoryof association reactions (LHS) and unimolecular decompositions (RHS) modify the Lindemann-Hinshelwood scheme to include $AB^{\#}$ a species with the same energy as AB*, where the energy is localised to the reactive mode.

RRKM (Rice, Ramsperger, Kassel and Marcus) was a further addition post Lindeman theory to calculate pressure dependent rate coefficients. Marcus combined the Eyring equation with RRK theory to calculate micro-canonical rate coefficients (calculated as a function of energy). And identified the restricted geometry of the excited complex ($AB^{\#}$) was the transition state, this is shown in Figure 1.11, where the vibrational levels of AB are shown and AB* is identified as rovibrationally excited AB.

RRKM theory as with transition state theory assumes all transfer across the transition state is permanent. RRKM calculates micro canonical rate coefficients, $k(E)$, and $k(E)$ is dependent on: the transition frequency, the probability of AB* to form $AB^{\#}$.
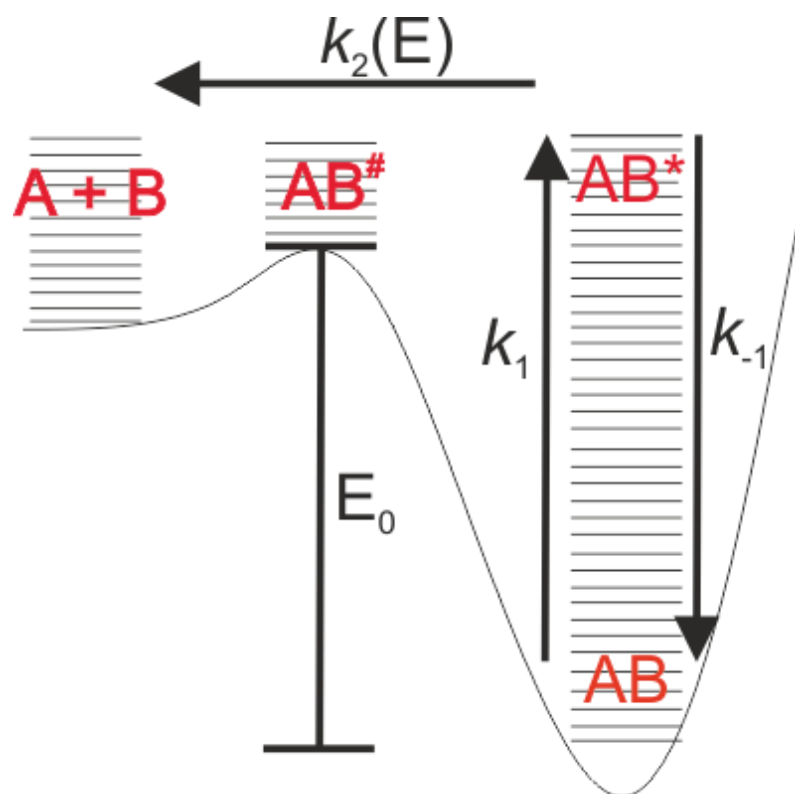
Figure 1.11 RRKM theory couples the Eyring equation to RRK theory, and identifies AB# in RRK theory as the transition state. This method can allow micro-canonical rate coefficients to be calculated.

In its simplest form RRKM theory evaluates the probability of AB^* to form $AB^{\#}$ from the density of states for molecules, $\rho(E)$, and the sum of states for the transition state, $W(E')$, which can be calculated from their frequencies.(90) This then allows the calculation of energy resolved rate coefficients for unimolecular reactions, Equation 1.11. In Equation 1.11 E' is the energy above the barrier to reaction in the activated complex (E' = E - E_0), and h is Plancks constant. Full RRKM theory should treat both angular momentum (J) and total energy (E) but in the form used in MESMER (which will be described in detail in section 1.61 to follow) this is simplified to only treat E.

$$k(E) = \frac{W(E')}{h\rho(E)} \qquad\qquad \textit{Equation } 1.11$$

1.5 Computational chemistry calculations

Computational chemistry can be used to calculate properties of poly atomic species, including: energies, structures and vibrational frequencies. This can be important for modelling chemical reactions, especially when the properties of short-lived species are

required that cannot be studied experimental. There are three main classes of computational calculations: ab-initio methods, which are based only on physical constants and quantum mechanics; semi-empirical methods, which also contain some empirical parameters; and density functional theory methods. The computational calculations carried out in this work were mainly carried out with three different methods: two were ab-initio post Hartree-Fock methods, CCSD(T) and MP2, and one was a density functional theory method, M06-2X.

1.5.1 Computational methods

Hartree-Fock theory assumes that electrons are non-interacting to allow approximate wavefunctions to be calculated and generate 'Hartree -Fock' equations which are approximate solutions to the Schrödinger equation. The wavefunction generated is formed by combining various input 'basis' functions which will be described in more detail later. The variational principle can then be applied to iteratively find the minimum energy that describes that particular geometry. (91-93) A significant crude approximation within HF theory is that electrons only feel the average effect of all the other electrons (they feel the mean field of all the particles), this approximation is included to avoid the N-body problem but leads to significant inaccuracies in the resultant energies. Several methods have been developed to account for the effect that the instantaneous position of one electron has on the other electrons in the system (electron correlation). The two principle post HF methods used in this work both use Moller-Plesset perturbation theory (MP); (94) MP theory assumes that the correction to account for electron correlation is some small perturbation of the HF energy. (95, 96) The perturbations to the HF energy are accounted for as a power series and are described as the correlation potential. The first meaningful correction to the HF calculations is achieved from the inclusion of the second order term (MP2), with higher order corrections (MP3, MP4) providing improved results but with much increased computational cost. (97, 98) MP2 was used as one of the methods of choice to optimize structures and calculate frequencies in Chapter 5.

Coupled cluster theory generates multi electron wavefunction from more basic molecular orbitals and accounts for electron correlation using an exponential cluster operator (T). (99, 100) The base molecular orbitals are often HF orbitals generated from a underlying calculation, however, this does not have to be the case and other orbitals can be used. The cluster operator (T) is a linear combination of excited determinants, and a variety of excitations can be included i.e. single (S), double (D), triple (T) and even

quadruple (Q) excitations. When this method is called the abbreviation CCSD denotes a couple cluster equation with single and double excitations included and CCSDT also includes triple excitations. Often the full treatment of the triples is computationally prohibitive and in these cases an estimation of the triples contribution can be calculated non-iteratively and where this is performed it is shown in brackets, as CCSD(T). (101) The non-iterative approximation to the triples contribution is calculated using many body perturbation theory. CCSD(T) with a sufficiently large basis set was the principle method used to calculate accurate single point energies in the calculations performed in Chapter 5.

Density functional theory (DFT, more correctly density functional approximations) describes a suite of methods that are designed to determine the electronic properties of a system by using functionals (functions of functions) of the electron density. (102-104) The high level DFT functionals commonly used in modern calculations contain approximations to model electron correlation and electron exchange. DFT can struggle to accurately model dispersion forces and to combat this, many methods include explicit descriptions of these interactions. In Gaussian (09), it is possible to select both the exchange and correlation functional or call single functionals either hybrid or standalone; (105) it is often also possible to add empirical dispersion explicitly to the functionals that have been called to better account for this effect. (106) Where DFT methods are used in Gaussian 09 (105) it is often important to consider the accuracy of the numerical integration grid used in the calculation, with results carried out with an ultrafine integration grid usually being more reliable. DFT methods in general provide acceptably accurate geometries and vibrations with a much lower computational cost, compared with post HF methods such as MP2. (107-109)

The principle DFT functional used in Chapters 5 and 6 was M06-2X a high-level hybrid functional from the Minnesota family of functionals, where this is used with tight convergence criteria and with a ultrafine integration grid the energies, structures and properties derived are usually reliable. The use of M06-2X is not recommended where structures contain a multi reference character, and it should be noted where M06-2X has been used to describe processes with multi reference character such as bond breaking of a singlet molecule (i.e. HO-OH bond breaking) it has been shown to produce erroneous behaviour. For the systems calculated with M06-2X in chapters 5 and 6 these occurred entirely on a doublet surface.

1.5.2 Basis sets

To generate the wavefunction that describes the electrons in a chemical system, a set of orbitals are required into which the electrons can be placed. In most computational calculations this is achieved by combining several atomic orbitals, which are mixed together in the overall wavefunction, with coefficients for each orbital being varied to find the minimum energy. (104) The set of orbitals chosen to represent each atom are referred to as the basis set. The basis sets used in computational calculations usually involve the linear combination of atomic orbitals (LCAO) to form the molecular orbitals; basis sets are classified by the basis functions that they are formed from. The atomic orbitals used can be represented numerically, or by Slater, and Gaussian type functions.

The basis functions chosen for most computational calculations are formed from a linear combination of several Gaussian functions. This method is chosen as Gaussian orbitals can be more efficiently treated in higher level calculations than more descriptions of the accurate atomic orbitals. Within a basis set the list of basis functions representing atomic orbitals are described as the contracted basis functions; and the underlying component functions of these (often Gaussian functions) are described as the primitive functions. An example breakdown of the contracted basis sets and their primitive component functions is given as Table 1-1.

Table 1-1 Several common basis sets showing both the contracted and underlying primitive functions.

Basis set	H	C,F (1st row atoms)
cc-pVDZ	$(4s1p)/[2s1p]$	$(9s4p1d)/[3s2p1d]$
cc-pVTZ	$(5s2p1d)/[3s2p1d]$	$(10s5p2d2f1g)/[4s3p2d1f]$
cc-pVQZ	$(6s3p2d1f)/[4s3p2d1f]$	$(12s6p3d2f1g)/[5s4p3d2f1g]$
cc-pV5Z	$(8s4p3d2f1g)/[5s4p3d2f1g]$	$(14s8p4d3f2g1h)/[6s5p4d3f2g1h]$
aug-cc-pVDZ	$+(1s1p)/[1s1p]$	$+(1s1p1d)/[1s1p1d]$
aug-cc-pVTZ	$+(1s1p1d)/[1s1p1d]$	$+(1s1p1d1f)/[1s1p1d1f]$
aug-cc-pVQZ	$+(1s1p1d1f)/[1s1p1d1f]$	$+(1s1p1d1f1g)/[1s1p1d1f1g]$
aug-cc-pV5Z	$+(1s1p1d1f1g)/[1s1p1d1f1g]$	$+(1s1p1d1f1g1h)/[1s1p1d1f1g1h]$
6-31G*	(4s)/[2s]	(10s4p1d)/[3s2sp1d]
6-31G**	(4s1p)/[2s1p]	(10s4p1d)/[3s2sp1d]
6-31+G**	No diffuse functions added	$+(1sp)/[1sp]$

As sated early basis sets are classified by their component functions, the simplest representation that can be used in calculations are referred to as a minimal basis set. A minimal basis set is formed from the minimum number of functions that can describe the electrons in the system. A minimal basis sets use fixed size atomic orbitals for instance

STO-3G uses functions that mimic slater type atomic orbitals, formed from three gaussian hence 3G. Higher level basis sets that have different sized orbitals to describe the valence electrons are referred to by the number of atomic orbitals used to describe these i.e. double zeta basis sets use two types of atomic orbital and triple zeta use three.

Improvements to the description of the bonding involved can be achieved by the inclusion of polarization and diffuse functions. Diffuse functions are larger versions of the normal function, that allow orbitals to occupy a greater area of space, and the addition of these functions to a basis set is often referred to as augmentation (aug). (110) Polarization functions allow the contracted functions to change their shape, this is achieved by adding in orbitals with higher angular momentum than the orbitals required to describe the ground state. The inclusion of polarization functions in basis sets of the Pople type is discretionary but within some basis sets i.e. correlation consistent (CC) types these are often compulsorily included.

For the work carried out in chapters 5 and 6 the basis sets used were either Pople type split valence type or correlation consistent basis sets. In general the Pople type basis set used was 6-311++g(3df,3pd) here the 6 refers to the description of the core electrons which have 6 gaussian functions to describe them, 311 refers to the valence orbitals which have 3 different contracted functions to describe them each made up of different primitive functions (with 3, 1 and 1 primitives in the contracted functions). (111, 112) The inclusion of diffuse functions on both heavy atoms and hydrogens is depicted by ++ and (3df, 3pd) depicts the explicit inclusion of 3 d and f functions on heavy atoms and 3 p and d functions on hydrogens.

Correlation consistent basis sets are designed to be used with methods that correct for electro correlation. In addition, families of correlation consistent basis sets are designed that can be accurately extrapolated to estimate the basis set limit. The basis set limit is where the inclusion of further contracted functions into the basis set would provide no improvement in the energy calculated. (113) The correlation consistent basis sets used in this work were of the cc-pVXZ form where X refers to the zeta of the basis set. These were used with two forms of augmentation, fully augmented (aug), and partially augmented (jun). (114) Full augmentation (aug) involves the inclusion of a diffuse function for every atom and for every level of angular momentum already present in the basis functions. Partial augmentation is any augmentation greater than minimal augmentation (diffuse functions on the heavy atoms for the occupied orbitals) but less

than full augmentation. The chosen partial augmentation (jun) removes two sets of diffuse subshells from full augmentation, where one set of diffuse subshell is removed this is referred to as jul.

1.5.3 Calculating properties

As has been described computational calculations minimise the wavefunction for a particular geometry, the first derivative of the energy at a particular geometry provides the gradients away from that point. These gradients can be used to optimize the geometry, allowing the equilibrium structures of the species to be calculated. The second derivative of the energy provides the forces acting on a structure, these forces allow the calculation of the frequencies (vibrations). It is possible to optimize structures, calculate frequencies and calculate energies with different levels of calculations to minimize computational costs. The energies, structures and vibrations of important points on a potential energy surface can then be used to model the chemical processes that occur on the surface.

1.6 Master equation calculations

The methods described so far treat all collisions as strong collisions i.e. either fully activated or deactivated. This model is not entirely sufficient to describe many chemical systems. Work on further parameterizing such processes was carried out which led to the Troe parameterization of a modified strong collision theory model (115,116), where some proportion of collisions are treated as inelastic resulting in no energy exchange. However, to extract more information, to better extrapolate temperature and pressure dependent systems beyond the limits of the current experimental regimes, a more chemically accurate theoretical approach was required. One such method is via a so called master equation calculation, in complete master equation analysis energy transfer between and reactions from all states of AB are considered.

$$\frac{\partial \rho i(t)}{\partial t} = \omega \qquad Equation \ 1.12$$

The time evolution of the population of each state (ρ_i) has three terms that define its change in population:

- One for the increase in population due to collisions with other populated states with an energy E' ($\omega \sum_{E'} P_{ij} \rho_j(t)$), which depends on both the probability of energy transfer between the states (P_{ij}) and the population of the other state (ρ_j).

- One for the removal of species through collisions ($\omega\rho_i(t)$) which depends on the population of the state itself (ρ_i).

- One for the reactive loss of the species ($k_{2i}\rho_i(t)$) which depends on the population of the state and the state specific rate coefficient.

When all of these processes are considered then this can be summarized as Equation 1.12. Full master equation analysis would be highly computationally expensive even for simple systems and as such approximate methods are often used, one such approach is the energy-grained method, which is used in MESMER.

1.6.1 MESMER analysis

Where a chemical system is at thermal equilibrium, thermal relaxation is fast compared with reactions, it has been established that these systems can be modelled if an accurate potential energy surface (PES) is treated with canonical transition state theory. (117) Yet this assumption is not true for all chemical system (often including intramolecular isomerization reactions), where the timescale for thermalisation and reactions are comparable, in these situations it is possible to treat the system using an energy grained master equation (EGME).

Energy grained master equations couple collisional energy transfer to energy resolved rate coefficients and bundle groups of similar energies together to form so called 'energy grains'. Movement between the energy grains is facilitated by collisions with the bath gas with these collisions treated as stochastic events. Micro canonical (energy dependent) rates for the individual species can then be calculated in a manner that is not computationally prohibitive. These then allow for the calculation of phenomenological rate coefficients for the non-equilibrium systems. MESMER (master equation solver for multi energy well reactions) is a software that can be used to solve such ME where multiple unimolecular wells are connected. The microcannonical rate coefficients in the MESMER simulations were calculated using RRKM (Rice, Ramsperger, Kassel and Marcus) theory. Mesmer simulations were carried out for the oxidation of dimethyl formamide (chapter 5) and for tertiary butyl amine (chapter 6).

MESMER treats only a one dimensional ME where the angular momentum is averaged and only the total energy of the system is treated as the variable. (118) Although strictly the angular momentum should be treated as a variable, for fitting the experimental

data in this work the errors, in the measured eigenvalues and the *ab initio* calculations, were likely more significant.
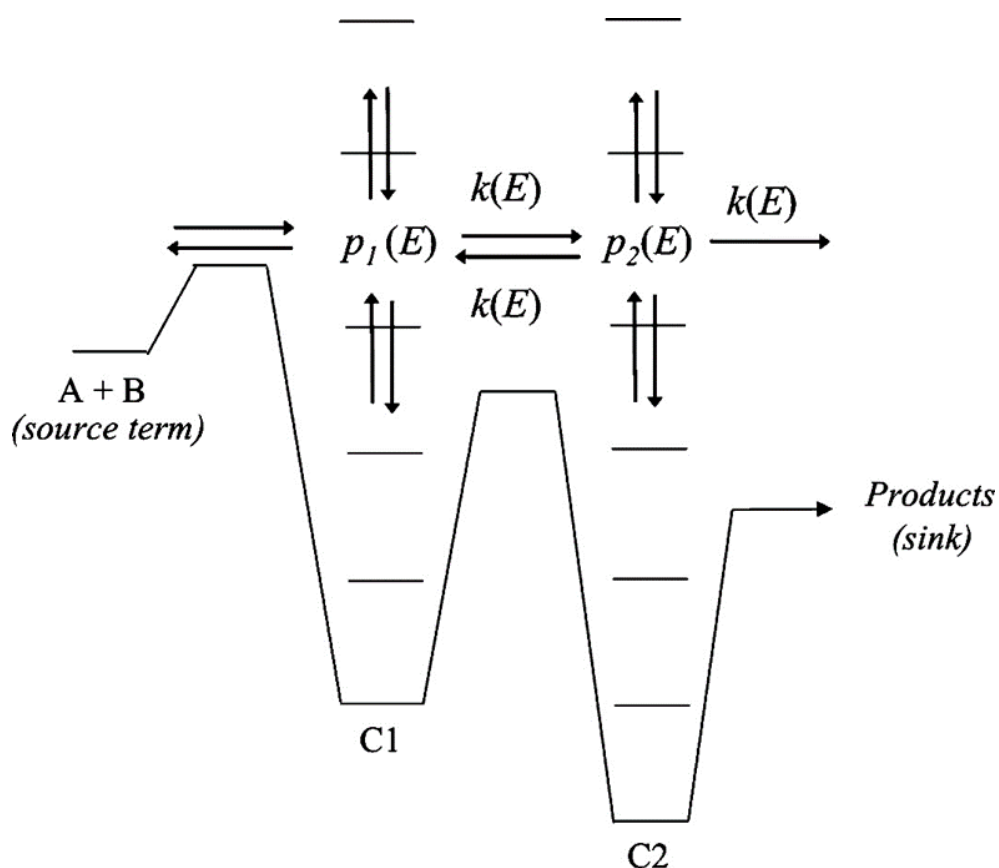
Figure 1.12: A representation of an energy grained master equation model, with two wells and three barriers, with an infinite sink for product formation. Taken from (92).

For MESMER inputs, stationary points with zero point corrected energies, vibrations, rotations, and bath gas specific energy transfer parameters were required. The energies, vibrations were taken from the outputs of high-level computational calculations for all the stationary points on the PES. Where needed, reasonable estimates for energy transfer parameters were used, and these were floated in a linked manner where appropriate.

As shown in Figure 1.12, the population change for each energy grain at a given time is a product of multiple different terms. In a simplified way, one term is due to the increase in population of a grain due to collisions, the second from the decrease in population of the energy grain due to collisions, a term due to increase in population of a grain due to reactions, and a final term denotes reactive loss from the grain. The sum of the population of each well can therefore be given as time resolved output; in the

MESMER output file these are the species time profiles, an example is given as Figure 1.13. The results of the micro canonical rate calculations can also be evaluated as a selection of the calculated eigenvalues for the system, which could then be compared to experimental measurements. Mesmer analysis of the recycling of OH radicals in the high temperature (> 450 K) oxidation of dimethyl formamide is described in chapter 5.
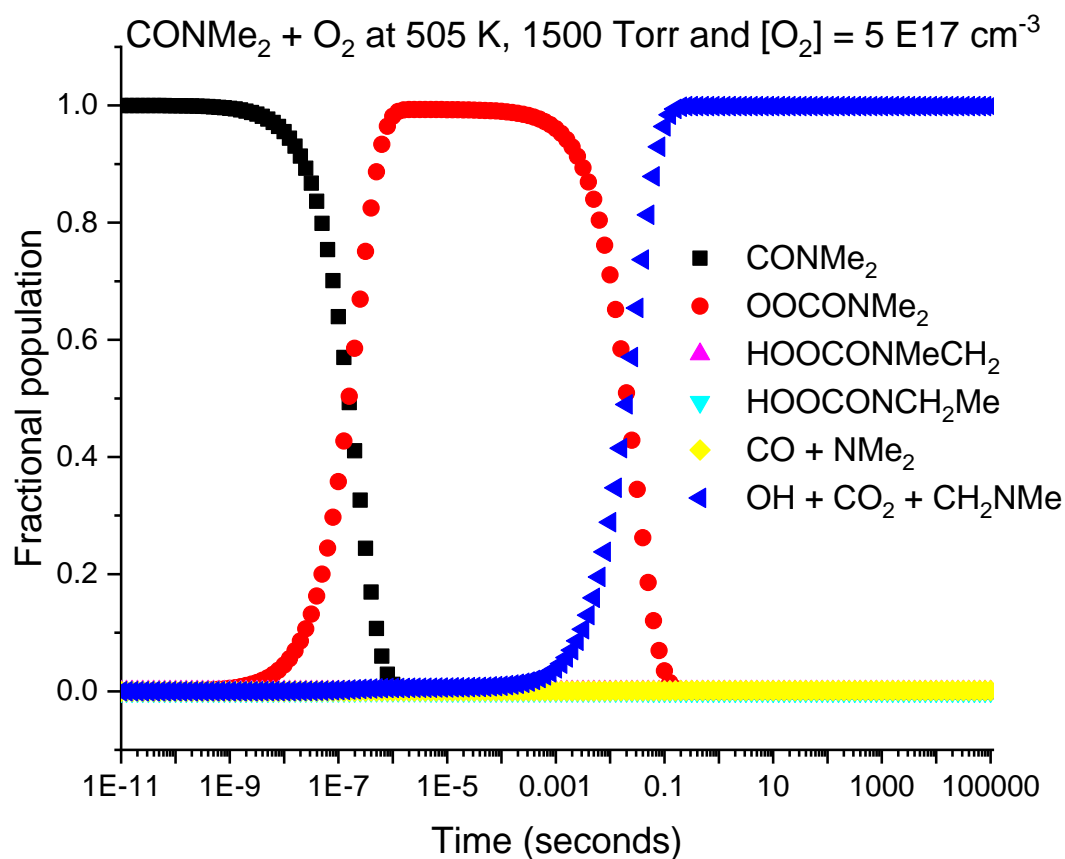
Figure 1.13 An example species time profile generated at 500 K, 1500 Torr, and with 5 × 10^{17} cm^{-3} O_2, from the R+O_2 surface formed following abstraction from the aldehydic position of dimethyl formamide.

Another method for analysing the output from the master equation calculations is referred to as 'Bartis-Widom' analysis. 'Bartis-Widom' analysis separates the chemical kinetics from the collisional relaxation kinetics, and uses this to analyse the output of the full ME calculation. For most of the master equation calculations performed using MESMER, the information that is of highest interest is the rate of chemical transformation between the wells on a surface.

If the chemical kinetic system alone (neglecting collisional relaxation) is treated as a set of coupled differential equations (in the same manner as in the full energy grained

ME) then diagonalization of this matrix will again produce a set of chemically significant eigenvalues (CSEs). In theory if there is good separation between collisional relaxation and chemical kinetics, then the CSEs obtained from this diagonalization and that of the full energy grained ME should be equivalent. The matrix being diagonalized is however much smaller through the negation of the additional energy transfer processes. The matrix used in the 'Bartis-Widom' analysis is only n×n, where n is the number of distinct species on the PES.

Where the CSEs and the internal energy relaxation eigenvalues (IEREs) are sufficiently separated, then numerical integration of the 'Bartis-Widom' phenomological rate coefficients should reproduce the species time profiles (which are the result of the full ME treatment). This provided an important check for consistency when 'Bartis-Widom' rate coefficients were used, as an integral part of a method to link master equation simulations to experimental data.

1.6.2 Direct trace fitting

In addition to assigning the output parameters of analytical fits to particular derived solutions from master equation calculations, work was also performed where the results from rate analysis of the results of master equation calculations were numerically integrated along with other assigned rate coefficients. The results of these numerically integrated reaction schemes were compared directly with the experimental traces, this was carried out using a MATLAB program developed by this group, that could write to MESMER input files, execute these MESMER calculations and then read in the resulting rate coefficients, in a manner well described in the work of D. Medeiros. (119)

A simplified description of how this was carried out will now be given, for a more complete description see the work of D. Medeiros.(119) The Matlab code initially read in the experimental traces and fitted a multi-exponential decay to them; these provided a 'good fit' to the traces where each trace could then be weighted against the bi-exponential fit to allow fair comparison of each individual fit. This treatment ensured that the weight of each trace to the overall fit of the final analysis was not swayed unfairly by their relative signal heights or scatter.

The program then wrote any parameters that were floated in the master equation calculations to the MESMER input files, called the execution of these input files and read in the resultant 'Bartis Widom' rate coefficients for all the experimental conditions. These 'MESMER' rate coefficients were then coupled with any other processes that has been

described in the program. The resulting simultaneous equations for the species were numerically integrated, the OH profiles that this produced for each trace were compared to the experimental data. The program then minimized the resulting differences using a Marquardt algorithm to minimise the total normalized χ squared, by varying the floated parameters. Where the normalized χ squared for a trace is the χ squared generated from the model fit to the data, divided by the χ squared generated by the bi-exponential fit to the same trace. In this manner all traces have an equivalent weight in the global analysis independent of the absolute signal height and degree of scatter. The test statistic χ squared is a measure of the goodness of a fit, and sums the squared difference between the modelled and observed values divided by the modelled value; a χ squared value of zero represents a perfect fit where all points lie on the modelled curve.

One advantage of this analysis method was that it provided the ability to couple the output of multiple master equation calculations at vastly reduced computational expense for the same accuracy, if transfer between the unlinked surfaces did not require the description of capture of a non-thermalized population. Coupled with this reduced computational cost, it was possible to add in additional competing loss processes in a manner that would be non-trivial to include into the master equation simulation itself, which allowed for a more complete description of the experimental processes than had been possible in the pure MESMER data fitting exercises. Direct trace analysis coupled to MESMER simulations is used extensively in chapter 5 to examine the oxidation of dimethyl formamide.

1.7 Summary

The design of a new instrument for the time resolved measurement of OH and HO_2 from a variable pressure (300 – 3000 Torr) and variable temperature reactor (290 – 750 K) provides the ability to study many reactions important to combustion or the atmosphere. Conditions that can hinder other traditional methods of measuring OH and HO_2 both through quenching effects, temperature effects(for LIF detection) and through interferences from other absorbing species (for absorption techniques). Coupling this system to a PTR-TOF-MS system can allow for further end-product analysis that can aid in the assignment of branching ratios, and the understanding of complex mechanisms.

The study of the OH initiated oxidation of a range of nitrogen containing compounds is of atmospheric importance both through their potential to form products with significant environmental implications, and the lack of detailed studies over a wide

range of temperatures. High-temperature oxidation of many nitrogen-containing compounds occurs in biomass burning and disposal of CCS wash solutions by incineration both of which may become more significant near to human habitation in the move towards lower global CO_2 emissions.

Where reaction rates are both temperature and pressure dependent, and where there is competition between pathways following an initial reaction, a detailed understanding of the potential energy surface can aid in data analysis. This can be carried out by directly coupling experimental and calculated eigenvalues from master equation simulations for chemical processes of interest. Even greater understanding can sometimes be achieved by numerically integrating reaction schemes and coupling the rate constants in these schemes to the results of master equation simulations in an iterative manner.

1.8 References

1. STONE, D., L.K. WHALLEY and D.E. HEARD. Tropospheric OH and HO_2 radicals: field measurements and model comparisons. *Chemical Society Reviews*, 2012, **41**(19), pp.6348-6404.
2. MONKS, P.S. Gas-phase radical chemistry in the troposphere. *Chemical Society Reviews*, 2005, **34**(5), pp.376-395.
3. STOCKWELL, W.R., C.V. LAWSON, E. SAUNDERS and W.S. GOLIFF. A Review of Tropospheric Atmospheric Chemistry and Gas-Phase Chemical Mechanisms for Air Quality Modeling. *Atmosphere*, 2012, **3**(1), p.1.
4. WAYNE, R.P., *Chemistry of atmospheres.* 3rd ed. Clarendon Press, Oxford, 2000.
5. LE CRÂNE, J.-P., M.-T. RAYEZ, J.-C. RAYEZ and E. VILLENAVE. A reinvestigation of the kinetics and the mechanism of the $CH3C(O)O_2$ + HO_2 reaction using both experimental and theoretical approaches. *Physical Chemistry Chemical Physics*, 2006, **8**(18), pp.2163-2171.
6. DILLON, T.J. and J.N. CROWLEY. Direct detection of OH formation in the reactions of HO_2 with $CH_3C(O)O_2$ and other substituted peroxy radicals. *Atmos. Chem. Phys.*, 2008, **8**(16), pp.4877-4889.
7. TOMAS, A., E. VILLENAVE and R. LESCLAUX. Reactions of the HO_2 Radical with CH_3CHO and $CH_3C(O)O_2$ in the Gas Phase. *The Journal of Physical Chemistry A*, 2001, **105**(14), pp.3505-3514.
8. WINIBERG, F.A.F., T.J. DILLON, S.C. ORR, C.B.M. GROß, I. BEJAN, C.A. BRUMBY, M.J. EVANS, S.C. SMITH, D.E. HEARD and P.W. SEAKINS. Direct measurements of OH and other product yields from the HO_2 + $CH_3C(O)O_2$ reaction. *Atmos. Chem. Phys.*, 2016, **16**(6), pp.4023-4042.
9. IYER, S., H. REIMAN, K.H. MØLLER, M.P. RISSANEN, H.G. KJAERGAARD and T. KURTÉN. Computational Investigation of RO_2 + HO_2 and RO_2 + RO_2 Reactions of Monoterpene Derived First-Generation Peroxy Radicals Leading to Radical Recycling. *The Journal of Physical Chemistry A*, 2018, **122**(49), pp.9542-9552.
10. ZADOR, J., C.A. TAATJES and R.X. FERNANDES. Kinetics of elementary reactions in low-temperature autoignition chemistry. *Progress in Energy and Combustion Science*, 2011, **37**(4), pp.371-421.
11. REITZ, R.D. and G. DURAISAMY. Review of high efficiency and clean reactivity controlled compression ignition (RCCI) combustion in internal combustion engines. *Progress in Energy and Combustion Science*, 2015, **46**, pp.12-71.
12. WANG, Z.D., L.D. ZHANG, K. MOSHAMMER, D.M. POPOLAN-VAIDA, V.S.B. SHANKAR, A. LUCASSEN, C. HEMKEN, C.A. TAATJES, S.R. LEONE, K. KOHSE-HOINGHAUS, N. HANSEN, P. DAGAUT and S.M. SARATHY. Additional chain-branching pathways in the low-temperature oxidation of branched alkanes. *Combustion and Flame*, 2016, **164**, pp.386-396.
13. GOLDSMITH, C.F., W.H. GREEN and S.J. KLIPPENSTEIN. Role of O_2 + QOOH in Low-Temperature Ignition of Propane. 1. Temperature and Pressure Dependent Rate Coefficients. *Journal of Physical Chemistry A*, 2012, **116**(13), pp.3325-3346.
14. AGBRO, E., A.S. TOMLIN, M. LAWES, S. PARK and S.M. SARATHY. The influence of n-butanol blending on the ignition delay times of gasoline and its surrogate at high pressures. *Fuel*, 2017, **187**, pp.211-219.
15. ONEL, L., M. BLITZ, M. DRYDEN, L. THONGER and P. SEAKINS. Branching Ratios in Reactions of OH Radicals with Methylamine,

Dimethylamine, and Ethylamine. *Environmental Science & Technology*, 2014, **48**(16), pp.9935-9942.

16. KOCH, R., H.U. KRÜGER, M. ELEND, W.U. PALM and C. ZETZSCH. Rate constants for the gas-phase reaction of OH with amines: tert-Butyl amine, 2,2,2-Trifluoroethyl amine, and 1,4-Diazabicyclo[2.2.2] octane. *International Journal of Chemical Kinetics*, 1996, **28**(11), pp.807-815.

17. ALI, M.A. and J.R. BARKER. Comparison of Three Isoelectronic Multiple-Well Reaction Systems: OH + CH₂O, OH + CH₂CH₂, and OH + CH₂NH. *Journal of Physical Chemistry A*, 2015, **119**(28), pp.7578-7592.

18. CARL, S.A. and J.N. CROWLEY. Sequential Two (Blue) Photon Absorption by NO₂ in the Presence of H₂ as a Source of OH in Pulsed Photolysis Kinetic Studies: Rate Constants for Reaction of OH with CH₃NH₂, (CH₃)₂NH, (CH₃)₃N, and C₂H₅NH₂ at 295 K. *The Journal of Physical Chemistry A*, 1998, **102**(42), pp.8131-8141.

19. ONEL, L., L. THONGER, M.A. BLITZ, P.W. SEAKINS, A.J.C. BUNKAN, M. SOLIMANNEJAD and C.J. NIELSEN. Gas-Phase Reactions of OH with Methyl Amines in the Presence or Absence of Molecular Oxygen. An Experimental and Theoretical Study. *Journal of Physical Chemistry A*, 2013, **117**(41), pp.10736-10745.

20. ONEL, L., M.A. BLITZ, J. BREEN, A.R. RICKARD and P.W. SEAKINS. Branching ratios for the reactions of OH with ethanol amines used in carbon capture and the potential impact on carcinogen formation in the emission plume from a carbon capture plant. *Physical Chemistry Chemical Physics*, 2015, **17**(38), pp.25342-25353.

21. NIELSEN, C.J., B. D'ANNA, C. DYE, M. GRAUS, M. KARL, S. KING, M.M. MAGUTO, M. MULLER, N. SCHMIDBAUER, Y. STENSTROM, A. WISTHALER and S. PEDERSEN. Atmospheric chemistry of 2-aminoethanol (MEA). *In:* J. GALE, C. HENDRIKS and W. TURKENBERG, eds. *10th International Conference on Greenhouse Gas Control Technologies.* Amsterdam: Elsevier Science Bv, 2011, pp.2245-2252.

22. ONEL, L., M.A. BLITZ and P.W. SEAKINS. Direct Determination of the Rate Coefficient for the Reaction of OH Radicals with Monoethanol Amine (MEA) from 296 to 510 K. *Journal of Physical Chemistry Letters*, 2012, **3**(7), pp.853-856.

23. ONEL, L., M. DRYDEN, M.A. BLITZ and P.W. SEAKINS. Atmospheric Oxidation of Piperazine by OH has a Low Potential To Form Carcinogenic Compounds. *Environmental Science & Technology Letters*, 2014, **1**(9), pp.367-371.

24. BORDUAS, N., J.G. MURPHY, C. WANG, G. DA SILVA and J.P.D. ABBATT. Gas Phase Oxidation of Nicotine by OH Radicals: Kinetics, Mechanisms, and Formation of HNCO. *Environmental Science & Technology Letters*, 2016, **3**(9), pp.327-331.

25. KARL, M., C. DYE, N. SCHMIDBAUER, A. WISTHALER, T. MIKOVINY, B. D'ANNA, M. MÜLLER, E. BORRÁS, E. CLEMENTE, A. MUÑOZ, R. PORRAS, M. RÓDENAS, M. VÁZQUEZ and T. BRAUERS. Study of OH-initiated degradation of 2-aminoethanol. *Atmos. Chem. Phys.*, 2012, **12**(4), pp.1881-1901.

26. BUNKAN, A.J.C., J. HETZLER, T. MIKOVINY, A. WISTHALER, C.J. NIELSEN and M. OLZMANN. The reactions of N-methylformamide and N,N-dimethylformamide with OH and their photo-oxidation under atmospheric conditions: experimental and theoretical studies. *Physical Chemistry Chemical Physics*, 2015, **17**(10), pp.7046-7059.

27. BARNES, I., G. SOLIGNAC, A. MELLOUKI and K.H. BECKER. Aspects of the Atmospheric Chemistry of Amides. *Chemphyschem*, 2010, **11**(18), pp.3844-3857.

28. BORDUAS, N., G. DA SILVA, J.G. MURPHY and J.P.D. ABBATT. Experimental and Theoretical Understanding of the Gas Phase Oxidation of Atmospheric Amides with OH Radicals: Kinetics, Products, and Mechanisms. *The Journal of Physical Chemistry A*, 2015, **119**(19), pp.4298-4308.

29. BUNKAN, A.J.C., T. MIKOVINY, C.J. NIELSEN, A. WISTHALER and L. ZHU. Experimental and Theoretical Study of the OH-Initiated Photo-oxidation of Formamide. *The Journal of Physical Chemistry A*, 2016, **120**(8), pp.1222-1230.

30. SOLIGNAC, G., A. MELLOUKI, G. LE BRAS, I. BARNES and T. BENTER. Kinetics of the OH and Cl reactions with N-methylformamide, N,N-dimethylformamide and N,N-dimethylacetamide. *Journal of Photochemistry and Photobiology A: Chemistry*, 2005, **176**(1–3), pp.136-142.

31. CHANGE, D.O.E.C. D.O.E.C. CHANGE. *Third progress report on the promotion and use of energy from renewable sources for the United Kingdom.* Low carbon technologies, 3. UK Government Publications, 2016.

32. CRITERIA, U.S.E.P.A., S.S. OFFICE, N.E.R. CENTER, U.S.E.P.A.O.O. RESEARCH and DEVELOPMENT. *Scientific and technical assessment report on nitrosamines.* U.S. Environmental Protection Agency, Office of Research and Development, 1977.

33. WAGNER, E.D., J. OSIOL, W.A. MITCH and M.J. PLEWA. Comparative in Vitro Toxicity of Nitrosamines and Nitramines Associated with Amine-based Carbon Capture and Storage. *Environmental Science & Technology*, 2014, **48**(14), pp.8203-8211.

34. GROSJEAN, D. Atmospheric chemistry of toxic contaminants. 6. Nitrosamines: dialkyl nitrosamines and nitrosomorpholine. *Journal of the Air & Waste Management Association*, 1991, **41**(3), pp.306-311.

35. LINDLEY, C.R.C., J.G. CALVERT and J.H. SHAW. Rate studies of the reactions of the $(CH_3)_2N$ radical with O_2, NO, and NO_2. *Chemical Physics Letters*, 1979, **67**(1), pp.57-62.

36. GE, X., A.S. WEXLER and S.L. CLEGG. Atmospheric amines – Part I. A review. *Atmospheric Environment*, 2011, **45**(3), pp.524-546.

37. MANZOOR, S., A. KORRE, S. DURUCAN and A. SIMPERLER. Atmospheric Chemistry Modelling of Amine Emissions from Post Combustion CO_2 Capture Technology. *Energy Procedia*, 2014, **63**, pp.822-829.

38. TANG, Y., M. HANRATH and C.J. NIELSEN. Do primary nitrosamines form and exist in the gas phase? A computational study of CH3NHNO and $(CH_3)_2$NNO. *Physical Chemistry Chemical Physics*, 2012, **14**(47), pp.16365-16370.

39. SCHADE, G.W. and P.J. CRUTZEN. Emission of aliphatic amines from animal husbandry and their reactions: Potential source of N_2O and HCN. *Journal of Atmospheric Chemistry*, 1995, **22**(3), pp.319-346.

40. TANGO, W.J., J.K. LINK and R.N. ZARE. Spectroscopy of K_2 Using Laser-Induced Fluorescence. 1968, **49**(10), pp.4264-4268.

41. ZARE, R.N. and P.J. DAGDIGIAN. Tunable Laser Fluorescence Method for Product State Analysis. 1974, **185**(4153), pp.739-747.

42. ANDREWS, D.L., P. BELTON, C. CREASER, M. CUDBY, S. KETTLE, M. MCCOUSTRA, F. MELLON, D. POWELL, N. SHEPPARD and J. SODEAU. *Perspectives in modern chemical spectroscopy.* 1 ed. Springer-Verlag Berlin Heidelberg, 1990.

43. ANDREWS, D.L. *Lasers in chemistry.* 3rd ed. Springer, Berlin, Heidelberg: Springer Verlag, 1997.

44. DÖBELE, H., M. HÖRL, M. RÖWEKAMP and B.J.A.P.B. REIMANN. Detection of atomic oxygen by laser-induced fluorescence spectroscopy at 130 nm. 1986, **39**(2), pp.91-95.

45. PILLING, M.J. and P.W. SEAKINS. *Reaction kinetics.* Oxford University Press, 1996.

46. LI, B., X. LI, M. YAO and Z. LI. Methyl Radical Imaging in Methane–Air Flames Using Laser Photofragmentation-Induced Fluorescence. 2015, **69**(10), pp.1152-1156.

47. DYER, M.J., L.D. PFEFFERLE and D.R. CROSLEY. Laser-induced fluorescence measurement of oxygen atoms above a catalytic combustor surface. *Applied Optics*, 1990, **29**(1), pp.111-118.

48. PILLING, M.J. and I.W. SMITH. *Modern gas kinetics.* Blackwell Scientific Publications, 1987.

49. BLITZ, M., M. J. PILLING, S. H. ROBERTSON and P. W. SEAKINS. Direct studies on the decomposition of the tert-butoxy radical and its reaction with NO. *Physical Chemistry Chemical Physics*, 1999, **1**(1), pp.73-80.

50. LOTZ, C. and R. ZELLNER. Fluorescence excitation spectrum of the tert-butoxy radical and kinetics of its reactions with NO and NO_2. *Physical Chemistry Chemical Physics*, 2000, **2**(10), pp.2353-2360.

51. WANG, C., L.G. SHEMESH, W. DENG, M.D. LILIEN and T.S. DIBBLE. Laser-Induced Fluorescence Excitation Spectra of tert-Butoxy and 2-Butoxy Radicals. *The Journal of Physical Chemistry A*, 1999, **103**(41), pp.8207-8212.

52. LAKOWICZ, J.R. Quenching of Fluorescence. *In:* J.R. LAKOWICZ, ed. *Principles of Fluorescence Spectroscopy.* Boston, MA: Springer US, 2006, pp.277-330.

53. SUPPAN, P. The energy of light: excited molecules. *In:* P. SUPPAN, ed. *Chemistry and light.* Royal Society of Chemistry, 1994, pp.27-86.

54. LAKOWICZ, J.R. Mechanisms and Dynamics of Fluorescence Quenching. *In:* J.R. LAKOWICZ, ed. *Principles of Fluorescence Spectroscopy.* Boston, MA: Springer US, 2006, pp.331-351.

55. DASHTIEV, M., V. AZOV, V. FRANKEVICH, L. SCHARFENBERG and R. ZENOBI. Clear Evidence of Fluorescence Resonance Energy Transfer in Gas-Phase Ions. *Journal of the American Society for Mass Spectrometry*, 2005, **16**(9), pp.1481-1487.

56. STEVENS, B. The fluorescence quenching of anthracene, 9-phenylanthracene and 9: 10-diphenylanthracene in the vapour phase. *Transactions of the Faraday Society*, 1955, **51**, pp.610-619.

57. JEFFRIES, J.B. and D.R. CROSLEY. Collisional quenching and energy transfer in NS B 2Π. 1987, **86**(12), pp.6839-6846.

58. NIZAMOV, B. and P.J. DAGDIGIAN. Collisional Quenching and Vibrational Energy Transfer in the A 2Σ+ Electronic State of the CF Radical. *The Journal of Physical Chemistry A*, 2001, **105**(1), pp.29-33.

59. LLEWELLYN, E.J., B.H. LONG and B.H. SOLHEIM. The quenching of OH∗ in the atmosphere. *Planetary and Space Science*, 1978, **26**(6), pp.525-531.

60. BAILEY, A.E., D. HEARD, P.H. PAUL and M. PILLING. *Collisional quenching of OH (A 2Σ+, v' = 0) by N_2, O_2 and CO_2 between 204 and 294 K. Implications for atmospheric measurements of OH by laser-induced fluorescence.* 1997.

61. YAMASAKI, K., A. WATANABE, T. KAKUDA and I. TOKUE. Deactivation Rate Constants of OH(X2Πi, v = 1−4) by Collisions of NH_3. *The Journal of Physical Chemistry A*, 2000, **104**(40), pp.9081-9086.

62. DAILY, J.W. Saturation effects in laser induced fluorescence spectroscopy. *Applied Optics*, 1977, **16**(3), pp.568-571.

63.	RAVIKRISHNA, R., C.S. COOPER, N.M.J.C. LAURENDEAU and FLAME. Comparison of saturated and linear laser-induced fluorescence measurements of nitric oxide in counterflow diffusion flames. 1999, **117**(4), pp.810-820.

64.	FORSTER, R., M. FROST, D. FULLE, H. HAMANN, H. HIPPLER, A. SCHLEPEGRELL and J. TROE. High pressure range of the addition of HO to HO, NO, NO_2, and CO. I. Saturated laser induced fluorescence measurements at 298 K. *The Journal of Chemical Physics*, 1995, **103**(8), pp.2949-2958.

65.	BÄNSCH, C., J. KIECHERER, M. SZORI and M.J.T.J.O.P.C.A. OLZMANN. Reaction of dimethyl ether with hydroxyl radicals: kinetic isotope effect and prereactive complex formation. 2013, **117**(35), pp.8343-8351.

66.	KOHSE-HÖINGHAUS, K., W. PERC and T. JUST. Laser-Induced Saturated Fluorescence as a Method for the Determination of Radical Concentrations in Flames. 1983, **87**(11), pp.1052-1057.

67.	HARD, T.M., R.J. O'BRIEN, C.Y. CHAN and A.A. MEHRABZADEH. Tropospheric free radical determination by fluorescence assay with gas expansion. *Environmental Science & Technology*, 1984, **18**(10), pp.768-777.

68.	WINIBERG, F., S. SMITH, I. BEJAN, C. BRUMBY, T. INGHAM, T. MALKIN, S. ORR, D. HEARD and P. SEAKINS. Pressure-dependent calibration of the OH and HO_2 channels of a FAGE HOx instrument using the Highly Instrumented Reactor for Atmospheric Chemistry (HIRAC). *Atmospheric Measurement Techniques*, 2015, **8**(2), pp.523-540.

69.	SPEAK, T.H., M.A. BLITZ, D. STONE and P.W. SEAKINS. A New Instrument for Time Resolved Measurement of HO_2 Radicals. *Atmos. Meas. Tech. Discuss.*, 2019, **2019**, pp.1-30.

70.	KOVACS, T.A. and W.H. BRUNE. Total OH loss rate measurement. *Journal of Atmospheric Chemistry*, 2001, **39**(2), pp.105-122.

71.	SADANAGA, Y., A. YOSHINO, K. WATANABE, A. YOSHIOKA, Y. WAKAZONO, Y. KANAYA and Y. KAJII. Development of a measurement system of OH reactivity in the atmosphere by using a laser-induced pump and probe technique. 2004, **75**(8), pp.2648-2655.

72.	AMEDRO, D., K. MIYAZAKI, A. PARKER, C. SCHOERNAECKER and C. FITTSCHEN. Atmospheric and kinetic studies of OH and HO_2 by the FAGE technique. *Journal of Environmental Sciences-China*, 2012, **24**(1), pp.78-86.

73.	NEHR, S., B. BOHN, H. FUCHS, A. HOFZUMAHAUS and A. WAHNER. HO_2 formation from the OH + benzene reaction in the presence of O_2. *Physical Chemistry Chemical Physics*, 2011, **13**(22), pp.10699-10708.

74.	STONE, D., M. BLITZ, T. INGHAM, L. ONEL, D.J. MEDEIROS and P.W. SEAKINS. An instrument to measure fast gas phase radical kinetics at high temperatures and pressures. *Review of Scientific Instruments*, 2016, **87**(5), p.054102.

75.	STONE, D., L.K. WHALLEY, T. INGHAM, P.M. EDWARDS, D.R. CRYER, C.A. BRUMBY, P.W. SEAKINS and D.E. HEARD. Measurement of OH reactivity by laser flash photolysis coupled with laser-induced fluorescence spectroscopy. *Atmos. Meas. Tech.*, 2016, **9**(7), pp.2827-2844.

76.	MEDEIROS, D.J., M.A. BLITZ, L. JAMES, T.H. SPEAK and P.W. SEAKINS. Kinetics of the Reaction of OH with Isoprene over a Wide Range of Temperature and Pressure Including Direct Observation of Equilibrium with the OH Adducts. *The Journal of Physical Chemistry A*, 2018.

77.	ASSAF, E., L. LIU, C. SCHOEMAECKER and C. FITTSCHEN. Absorption spectrum and absorption cross sections of the $2\nu_1$ band of HO_2 between 20 and 760 Torr air in the range 6636 and 6639 cm^{-1}. *Journal of Quantitative Spectroscopy & Radiative Transfer*, 2018, **211**, pp.107-114.

78. ONEL, L., A. BRENNAN, M. GIANELLA, G. RONNIE, A.L. AGUILA, G. HANCOCK, L. WHALLEY, P.W. SEAKINS, G.A.D. RITCHIE and D.E. HEARD. An intercomparison of HO_2 measurements by fluorescence assay by gas expansion and cavity ring-down spectroscopy within HIRAC (Highly Instrumented Reactor for Atmospheric Chemistry). *Atmospheric Measurement Techniques*, 2017, **10**(12), pp.4877-4894.

79. CROWLEY, J.N., F.G. SIMON, J.P. BURROWS, G.K. MOORTGAT, M.E. JENKIN and R.A. COX. The HO_2 radical UV absorption-spectrum measured by molecular modulation, UV diode-array spectroscopy. *Journal of Photochemistry and Photobiology a-Chemistry*, 1991, **60**(1), pp.1-10.

80. TAATJES, C.A. and D.B. OH. Time-resolved wavelength modulation spectroscopy measurements of HO_2 kinetics. *Applied Optics*, 1997, **36**(24), pp.5817-5821.

81. JEMIALADE, A.A. and B.A. THRUSH. Reactions of HO_2 with NO and NO_2 studied by midinfrared laser magnetic-resonance. *Journal of the Chemical Society-Faraday Transactions*, 1990, **86**(20), pp.3355-3363.

82. THIEBAUD, J. and C. FITTSCHEN. Near infrared cw-CRDS coupled to laser photolysis: Spectroscopy and kinetics of the HO_2 radical. *Applied Physics B-Lasers and Optics*, 2006, **85**(2-3), pp.383-389.

83. GIANELLA, M., S. REUTER, A.L. AGUILA, G.A.D. RITCHIE and J.P.H. VAN HELDEN. Detection of HO_2 in an atmospheric pressure plasma jet using optical feedback cavity-enhanced absorption spectroscopy. *New Journal of Physics*, 2016, **18**.

84. BRUNE, W.H., P.S. STEVENS and J.H. MATHER. Measuring OH and HO_2 in the troposphere by laser-induced fluorescence at low-pressure. *Journal of the atmospheric sciences*, 1995, **52**(19), pp.3328-3336.

85. FUCHS, H., B. BOHN, A. HOFZUMAHAUS, F. HOLLAND, K.D. LU, S. NEHR, F. ROHRER and A. WAHNER. Detection of HO_2 by laser-induced fluorescence: calibration and interferences from RO_2 radicals. *Atmospheric Measurement Techniques*, 2011, **4**(6), pp.1209-1225.

86. EDWARDS, G.D., C.A. CANTRELL, S. STEPHENS, B. HILL, O. GOYEA, R.E. SHETTER, R.L. MAULDIN, E. KOSCIUCH, D.J. TANNER and F.L. EISELE. Chemical ionization mass spectrometer instrument for the measurement of tropospheric HO_2 and RO_2. *Analytical Chemistry*, 2003, **75**(20), pp.5317-5327.

87. HANKE, M., J. UECKER, T. REINER and F. ARNOLD. Atmospheric peroxy radicals: ROXMAS, a new mass-spectrometric methodology for speciated measurements of HO_2 and RO_2 and first results. *International Journal of Mass Spectrometry*, 2002, **213**(2-3), pp.91-99.

88. HIDY, G.M. Atmospheric Chemistry in a Box or a Bag. 2019, **10**(7), p.401.

89. LOCKHART, J.P.A., E.C. GROSS, T.J. SEARS and G.E. HALL. Kinetic study of the OH + ethylene reaction using frequency-modulated laser absorption spectroscopy. 2019, **51**(6), pp.412-421.

90. MARCUS, R.A. Unimolecular Dissociations and Free Radical Recombination Reactions. 1952, **20**(3), pp.359-364.

91. FROESE FISCHER, C. General Hartree-Fock program. *Computer Physics Communications*, 1987, **43**(3), pp.355-365.

92. ROOTHAAN, C.C.J. Self-Consistent Field Theory for Open Shells of Electronic Systems. *Reviews of Modern Physics*, 1960, **32**(2), pp.179-185.

93. HARTREE, D. The calculation of atomic structures. *Progress in Physics*, 1948, **11**, pp.113-143.

94. MØLLER, C. and M.S. PLESSET. Note on an Approximation Treatment for Many-Electron Systems. *Physical Review*, 1934, **46**(7), pp.618-622.

95. FRISCH, M.J., M. HEAD-GORDON and J.A. POPLE. A direct MP2 gradient method. *Chemical Physics Letters*, 1990, **166**(3), pp.275-280.

96. HEAD-GORDON, M., J.A. POPLE and M.J. FRISCH. MP2 energy evaluation by direct methods. *Chemical Physics Letters*, 1988, **153**(6), pp.503-506.

97. KRISHNAN, R. and J.A. POPLE. Approximate fourth-order perturbation theory of the electron correlation energy. *International Journal of Quantum Chemistry*, 1978, **14**(1), pp.91-100.

98. POPLE, J.A., J.S. BINKLEY and R. SEEGER. Theoretical models incorporating electron correlation. *International Journal of Quantum Chemistry*, 1976, **10**(S10), pp.1-19.

99. SİNANOĞLU, O. Many-Electron Theory of Atoms and Molecules. I. Shells, Electron Pairs vs Many-Electron Correlations. *Journal of Chemical Physics*, 1962, **36**(3), pp.706-717.

100. ČÍŽEK, J. On the Correlation Problem in Atomic and Molecular Systems. Calculation of Wavefunction Components in Ursell-Type Expansion Using Quantum-Field Theoretical Methods. *Journal of Chemical Physics*, 1966, **45**(11), pp.4256-4266.

101. III, G.D.P. and R.J. BARTLETT. A full coupled-cluster singles and doubles model: The inclusion of disconnected triples. *The Journal of Chemical Physics*, 1982, **76**(4), pp.1910-1918.

102. HOHENBERG, P. and W. KOHN. Inhomogeneous Electron Gas. *Physical Review*, 1964, **136**(3B), pp.B864-B871.

103. KOHN, W. and L.J. SHAM. Self-Consistent Equations Including Exchange and Correlation Effects. *Physical Review*, 1965, **140**(4A), pp.A1133-A1138.

104. POPLE, J.A., P.M.W. GILL and B.G. JOHNSON. Kohn—Sham density-functional theory within a finite basis set. *Chemical Physics Letters*, 1992, **199**(6), pp.557-560.

105. *Gaussian 09, Revision D.01* M. J. Frisch, G. W. Trucks, H. B. Schlegel, G. E. Scuseria, M. A. Robb, J. R. Cheeseman, G. Scalmani, V. Barone, G. A. Petersson, H. Nakatsuji, X. Li, M. Caricato, A. Marenich, J. Bloino, B. G. Janesko, R. Gomperts, B. Mennucci, H. P. Hratchian, J. V. Ortiz, A. F. Izmaylov, J. L. Sonnenberg, D. Williams-Young, F. Ding, F. Lipparini, F. Egidi, J. Goings, B. Peng, A. Petrone, T. Henderson, D. Ranasinghe, V. G. Zakrzewski, J. Gao, N. Rega, G. Zheng, W. Liang, M. Hada, M. Ehara, K. Toyota, R. Fukuda, J. Hasegawa, M. Ishida, T. Nakajima, Y. Honda, O. Kitao, H. Nakai, T. Vreven, K. Throssell, J. A. Montgomery, Jr., J. E. Peralta, F. Ogliaro, M. Bearpark, J. J. Heyd, E. Brothers, K. N. Kudin, V. N. Staroverov, T. Keith, R. Kobayashi, J. Normand, K. Raghavachari, A. Rendell, J. C. Burant, S. S. Iyengar, J. Tomasi, M. Cossi, J. M. Millam, M. Klene, C. Adamo, R. Cammi, J. W. Ochterski, R. L. Martin, K. Morokuma, O. Farkas, J. B. Foresman, and D. J. Fox, Gaussian, Inc., Wallingford CT, 2009

106. GRIMME, S. Density functional theory with London dispersion corrections. *Wiley Interdisciplinary Reviews: Computational Molecular Science*, 2011, **1**(2), pp.211-228.

107. LE CRÂNE, J.-P., M.-T. RAYEZ, J.-C. RAYEZ and E. VILLENAVE. A reinvestigation of the kinetics and the mechanism of the $CH_3C(O)O_2 + HO_2$ reaction using both experimental and theoretical approaches. *Physical Chemistry Chemical Physics*, 2006, **8**(18), pp.2163-2171.

108. LIU, C.X., Z.R. LI, C.W. ZHOU and X.Y. LI. Accurate Prediction of Thermodynamic Properties of Alkyl Peroxides by Combining Density Functional

Theory Calculation with Least-Square Calibration. *Journal of Computational Chemistry*, 2009, **30**(7), pp.1007-1015.

109.   MINENKOV, Y., A. SINGSTAD, G. OCCHIPINTI and V.R. JENSEN. The accuracy of DFT-optimized geometries of functional transition metal compounds: a validation study of catalysts for olefin metathesis and other reactions in the homogeneous phase. *Dalton Transactions*, 2012, **41**(18), pp.5526-5541.

110.   PAPAJAK, E. and D.G. TRUHLAR. Convergent Partially Augmented Basis Sets for Post-Hartree−Fock Calculations of Molecular Properties and Reaction Barrier Heights. *Journal of chemical theory and computation*, 2011, **7**(1), pp.10-18.

111.   KRISHNAN, R., J.S. BINKLEY, R. SEEGER and J.A. POPLE. Self-consistent molecular orbital methods. XX. A basis set for correlated wave functions. *Journal of Chemical Physics*, 1980, **72**(1), pp.650-654.

112.   MCLEAN, A.D. and G.S. CHANDLER. Contracted Gaussian basis sets for molecular calculations. I. Second row atoms, Z=11–18. *Journal of Chemical Physics*, 1980, **72**(10), pp.5639-5648.

113.   HALKIER, A., T. HELGAKER, P. JØRGENSEN, W. KLOPPER and J. OLSEN. Basis-set convergence of the energy in molecular Hartree–Fock calculations. *Chemical Physics Letters*, 1999, **302**(5), pp.437-446.

114.   PAPAJAK, E., J. ZHENG, X. XU, H.R. LEVERENTZ and D.G. TRUHLAR. Perspectives on basis sets beautiful: seasonal plantings of diffuse basis functions. *Journal of chemical theory and computation*, 2011, **7**(10), pp.3027-3034.

115.   TROE, J. Predictive possibilities of unimolecular rate theory. *The Journal of Physical Chemistry*, 1979, **83**(1), pp.114-126.

116.   TROE, J. Theory of thermal unimolecular reactions at low pressures. I. Solutions of the master equation. *The Journal of Chemical Physics*, 1977, **66**(11), pp.4745-4757.

117.   CRAMER, C.J. Essentials of Computational Chemistry: Theories and Models second edition. *In: Essentials of Computational Chemistry: Theories and Models second edition.* Wiley, 2004, pp.524-533.

118.   DAVID R., G., L. CHI-HSIU, M. CHRISTOPHER, P. MICHAEL J. and R. STRUAN H. MESMER: An Open-Source Master Equation Solver for Multi-Energy Well Reactions. *The Journal of Physical Chemistry A*, 2012, **116**(38), pp.9545-9560.

119.   MEDEIROS, D.D.J. *New Methods for Data Analysis of Complex Chemical Systems with Practical Applications for Atmospheric Studies.* Doctor of Philosophy thesis, University of Leeds, 2019.

2 Experimental Procedures

2.1 Principles of pulsed laser photolysis laser induced fluorescent measurements

Where direct kinetic measurements of gas phase reactions are required, pulsed laser photolysis (PLP) coupled to a time resolved detection method has been used to measure the rate coefficients of many processes important to atmospheric and combustion. (1-4) For the experiments carried out in this work, the principal detection method used was laser induced fluorescence (LIF). PLP-LIF will now be discussed and a detailed of description of the experimental setups that utilise the technique will be given.

2.1.1 LASERS

LASER (light amplification by stimulated emission of radiation) (5) is a system whereby optical amplification is achieved leading to a high-energy, coherent output. Although the initial definition applied only to visible light, with UVASER and IRASER being strictly intended for use in these other regions, these terms are either defunct or were never accepted, with wavelengths beyond visible being specified in the form UV-laser and IR-laser being favoured. The benefits of lasers as a light source over other sources comes from the high energy, directional, monochromatic, collimated light that is provided. Specific wavelengths allow for particular absorptions within a molecule or species to be targeted, and the high photon flux makes them suitable as photolysis sources.

Stimulated emission is a process for deactivation of an excited species where a photon induces loss of energy from the excited species by release of a photon with the same energy and the same phase, polarization and direction of travel as the inducing photon, Figure 2.1. (6, 7) The benefit of stimulated emission is that one seed photon can lead to many more photons of the same wavelength light by passing through an excited medium. By comparison, in spontaneous fluorescence the photon released can have a range of frequencies and can be released in any direction and phase.

If a reflective cavity is setup across this excited medium with non-reflective sides, any light that has a wavelength that matches the cavity length and matches a transition in the medium can be amplified. Any light that is spontaneously emitted in a plane outside the direction of the cavity will be lost and any light with a wavelength that does not match

a mode of the cavity will be lost through destructive interference; these two processes are shown in Figure 2.2. If one mirror is completely reflective and the other slightly transparent (output mirror) then a coherent beam of high energy light of defined wavelengths is emitted from the cavity. (8)
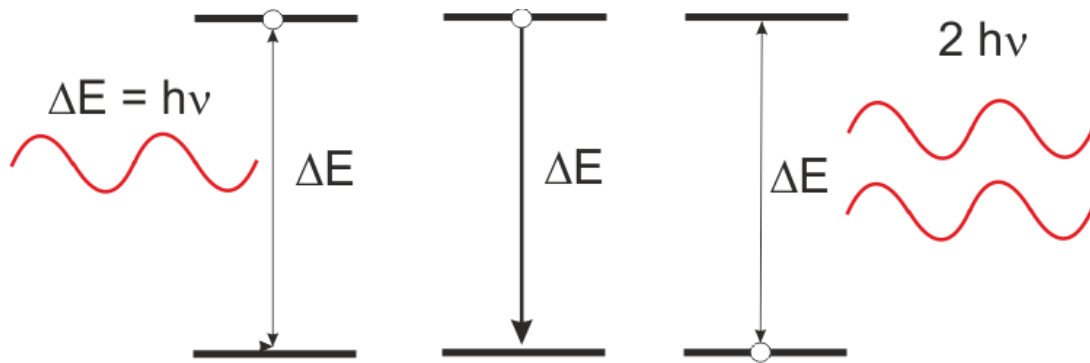
Figure 2.1. Stimulated emission is a quantum mechanical process that can occur where an incident photon meets an excited species. Where an energy gap in the excited species matches the energy of the incident photon the excited species can relax by emission of a photon with the same wavelength, direction of travel, polarization and phase.

Absorption and diffraction that occurs within the optical cavity are loss processes for light propagating in the optical cavity, the excited population in the cavity that allows stimulated emission is the gain. Where the gain is higher than the losses, amplification of the propagating light will occur. When stimulated emission occurs, an atom or molecule is returned to a lower state and the gain of the lasing medium is reduced. A balance between power output, pumping power and pulse length and laser efficiency is therefore formed.

Under most circumstances, however, stimulated emission is a minor process with respect to absorption, as the lower state (in general ground) population is generally larger than the upper state (excited). Where absorption dominates, the majority of photon molecular interactions in the gain medium will be loss to form excited molecules and amplification of the light will not be achieved. This presents the first issue in producing a laser system, for stimulated emission to dominate over absorption a population inversion (a more populated upper than lower state) must be achieved.
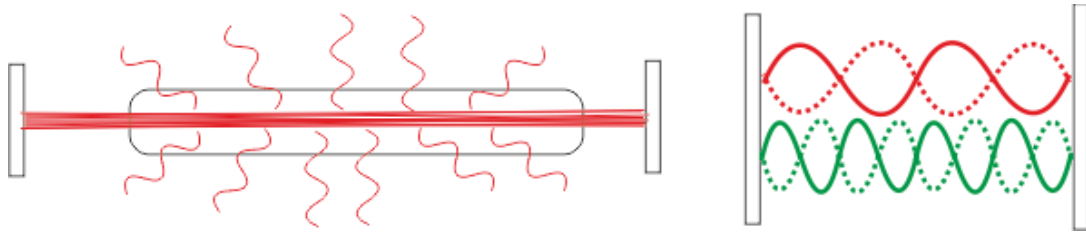
Figure 2.2. The left hand figure shows how if reflective surfaces with open sides are setup either side of the laser medium only light travelling on the axis of the mirrors will be propagated and amplified.The right hand figure shows that for a particular optical cavity length, only standing waves with specific wavelengths can propagate; wavelengths that do not match the cavity length will be lost through destructive interference. These two processes combined lead to the narrow wavelength specificity and highly directional light output from a laser.

Differing solutions to achieving population inversion lead to two main classes of lasers, namely multi-level lasers and exciplex lasers, the work carried out later utilised exciplex and Nd:YAG lasers. In the earliest solution to generating a population inversion, a ruby laser, this was achieved using the multi-level approach. The ruby laser is an example of a three level laser; the ruby laser lased at 694.3 nm and was pumped at 550 nm.(9) The principle of a three level laser, Figure 2.3, relies on a meta stable state being present below the pumping state, where sufficient pumping from the ground state followed by rapid conversion to the meta stable state can lead to population inversion.
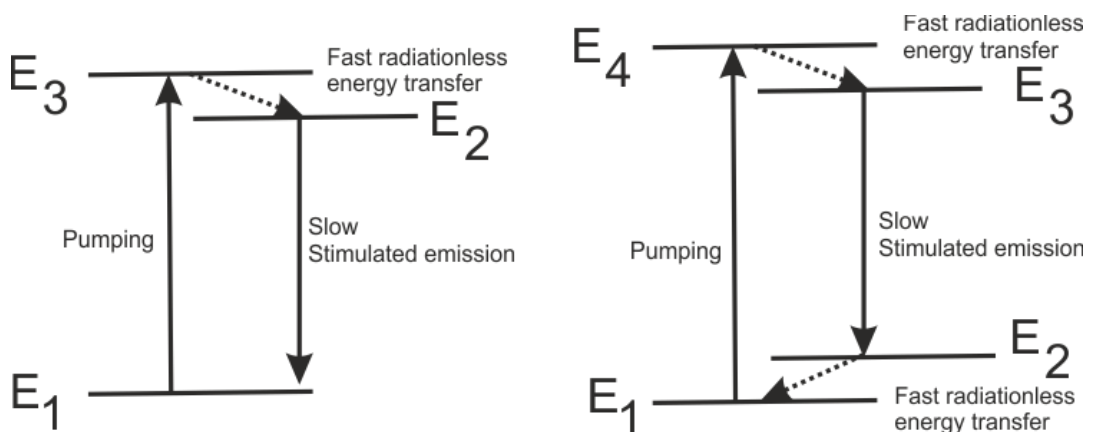
Figure 2.3. Energy level diagrams of 3 and 4 level lasers, solid arrows depict radiative transitions and dotted arrows 'fast' non-radiative processes. A three level system as depicted on the left was the principle of the first laser with pumping at 550 nm and lasing at 694.3 nm. A four level system as depicted on the right is the principle behind the Nd:YAG laser used extensively in this work, where pumping is at 750 or 810 nm and lasing occurs at 1064 nm.

Addition of a fourth level to the system can again allow for population inversion with much greater efficiency. In a 4 level laser, Figure 2.3, pumping from the ground state to a higher energy pumping state and in a manner similar to in a 3 level laser again this rapidly undergoes conversion to a meta stable state. In a 4 level laser, however, the metastable state undergoes fluorescence to a lower lasing level that is above the ground state in energy. By having a system where the lower lasing level is above the ground state in energy it is not necessary to achieve a population inversion with respect to the ground state, if transfer from the lower lasing level is fast, a population inversion can be achieved with high efficiency.

A 4 level laser is the principle behind Nd:YAG lasers operated at 1064 nm with pumping at 790-820 nm by a krypton flash lamp.(10) In the work carried out later Nd:YAG lasers were used both as photolysis sources and to pump dye lasers. HeNe lasers are a more complicated multi-level laser but can be considered a variant of a 4 level laser; here pumping is electrical discharge of helium and lasing occurs in neon following energy transfer from excited helium to excited states in neon.(11) Once excited neon undergoes laser action to a lower lasing level that is rapidly depopulated to lower energy levels to maintain the population inversion.
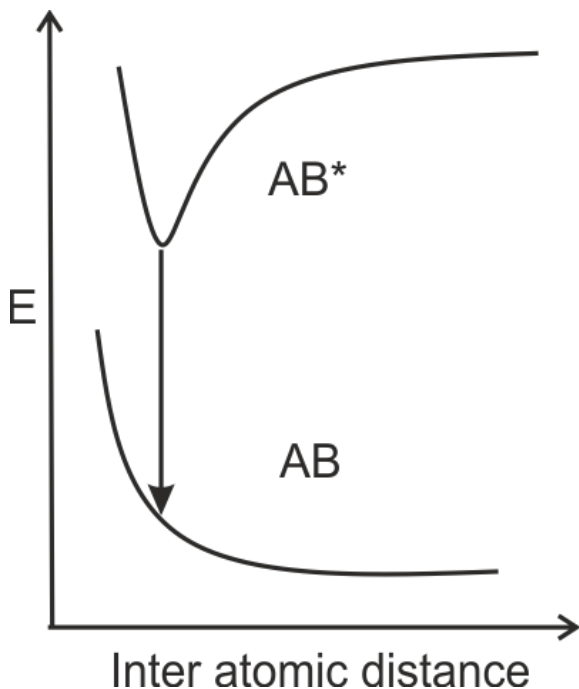
Figure 2.4. The principle of excimer (exciplex) lasersrelies on lasing action occurring between a bound excited state, formed from an electrical discharge, and a dissociative ground state.

A completely different solution to the problem of maintaining a population inversion is achieved in the case of exciplex (excimer) lasers, Figure 2.4, which utilise an unusual 2 level system. In excimer lasers, the upper excited level is a high energy but stable complex (for 248 nm KrF) and the lower ground state is unstable and dissociative. By having, a dissociative ground state there is no ability to build up a population of the lower level and as such, a population inversion is possible. Forming the high-energy excited dimers is achieved through an electrical discharge of the gas and by use of differing gas mixtures different wavelengths of light can be produced (XeF 351 nm, KrF 248 nm, ArF 193 nm, XeCl 308 nm). The first working excimer laser was a true excimer in that the excited bound molecule was an excited dimer of xenon, here the laser output was at 172 nm.(12) In the work carried out later the priciple photolysis source was an exciplex operating on KrF, with some experiments carried out using ArF.

2.1.2 Wavelength modification

Harmonic generation

The principal output of many lasers is often not of particular use for either photolysis of precursors, or the pumping of dye lasers, or use in photoionization. Where the primary output of a ruby laser lies in the visible region at 694 nm, UV light at 346.7 nm could be generated by passing the laser light through a quartz crystal at the correct angle. This occurred through the formation of the second harmonic of the ruby laser.(13) The principal output of a Nd:YAG laser is 1064 nm in the infra-red region; if 2 photons of energy can be coupled together the resultant photon has twice the energy and half the wavelength, this is referred to as the second harmonic, Figure 2.5. Coupling of photons together to generate subsequent photons with different energies can be achieved through the use of non-linear optics. For second harmonic generation non-linear polarization within the crystal produces a term with half the incident light wavelength and a term with no wavelength, this process is a form of sum frequency generation and results in the emission of one photon with twice the energy of the two input photons.(14)

Sum frequency generation can occur with differing wavelengths of light allowing the formation of a variety of different wavelengths, but in general the most common sum frequency generation used for Nd:YAG laser outputs are the 2nd 3rd and 4th harmonics (532 nm, 355 nm, 266 nm). Within the course of experimental work carried out in this work the 2nd harmonic (532 nm) was used to pump dye lasers to probe OH, and the 4th

harmonic (266 nm) was used as a higher wavelength photolysis source than 248 nm excimers. The 3rd harmonic of the Nd:YAG (355 nm) is commonly used in photo-ionisation mass-spectrometry (PIMS) where 355 nm is tripled to 118 nm for photo-ionisation.
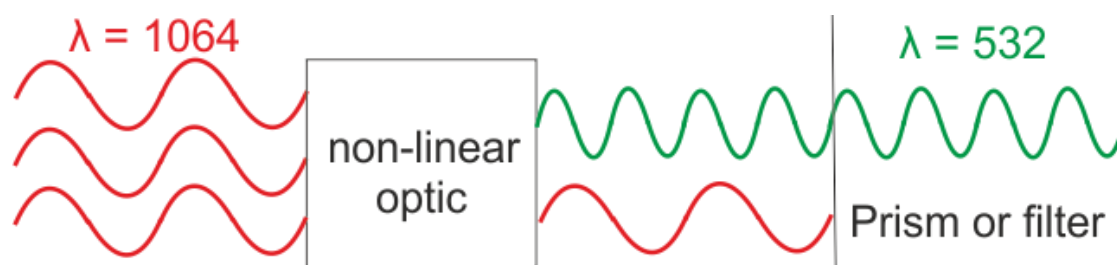
Figure 2.5. Within a non-linear optic, sum frequency generation produces a photon with half the wavelength by annihilation of two photons with the incident wavelength. Non-linear crystals have lower than complete conversion and as such some of the incident light will pass through unchanged. The output wavelengths from the non-linear crystal can be separated by a prism to selectively give only the lower wavelength upper harmonic light when required.

In the probe lasers systems (Nd:YAG pumped dye lasers) a second frequency doubling step was required post the dye laser wavelength shift to generate UV light at 308 nm or 282 nm for OH detection. There are many reasons that operating dye lasers in the visible range and doubling the light to the UV has been favoured, and a significant factor comes from the inherent advantages of using visible light. For shorter, UV, wavelengths higher threshold powers would be required due to the stronger spontaneous emissions and lower dye lifetimes, in addition even UV coated optics tend to have lower transparencies and greater losses than optics operated in the visible range.

By using the second harmonic and operating in the visible it is possible to access greater pulse energies from an Nd:YAG laser, and with lower threshold powers for lasing when using visible range laser dyes this leads to much higher efficiencies. In addition, BBO and KDP crystals are highly efficient at doubling visible light into the UV, and as such, these dye laser arrangements provide the required wavelengths for OH LIF detection with sufficient pulse energies (1-10 mJ).

Dye lasers

Dye lasers can be pumped by flash lamps or by backing pump lasers, where dye lasers were utilised in this work they were backed by the 532 nm doubled output of

Nd:YAG lasers. The input light is absorbed by large organic molecules and reemitted at a range of different wavelength.(15, 16) The dyes used in laser dyes tend to have large absorption and emission spectra, this allows for flexibility on the pump wavelength and with the use of frequency selection variable wavelength output.(17, 18) Frequency selection in the laser resonator can be achieved using birefringent tuners and or diffraction gratings.

Pumping of the dye cuvettes is performed perpendicular to the laser output, pump light excited the dyes to an excited singlet state that can undergo stimulated emission to produce the dye laser light. As the laser dyes are large organic molecules, the rate of forbidden transitions tends to be fast and as a result, the excited dye molecules rapidly undergo conversion to the triplet state, triplet state dye molecules do not produce the required stimulated emission. To combat this effect laser dyes are circulated through the dyes cells so as to minimise the triplet state excited molecule concentrations.

Mirror Dye cuvette Tuneable diffraction grating
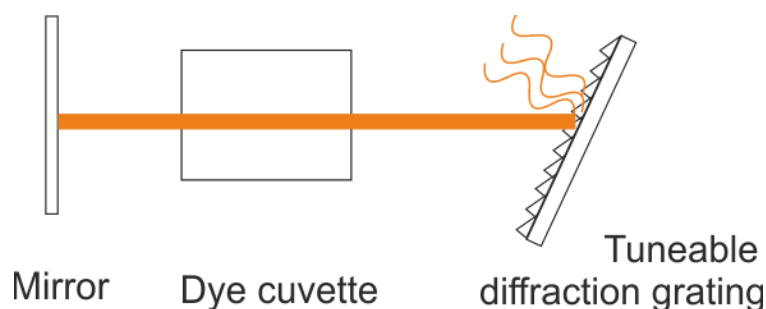
Figure 2.6. Using a mirror and a movable diffraction grating, individual wavelengths can be selectively propagated in a dye laserwith the other wavelengths emitted being lost. Diffraction gratings can allow for narrow linewidth output from dye lasers to be achieved over a broad spectral range, this makes dye lasers for the selectively probing of transitions required in LIF.

Diffraction gratings are reflective surfaces with parallel lines in the face, when light hits an angled face of a diffraction grating different wavelengths are dispersed out spatially. In the first highly wavelength selective dye lasers, a single grating provided the selectivity,(18) an example of this method is shown as Figure 2.6; the Spectron dye laser used in this work featured a single grating. More modern dye laser systems can feature double gratings, which provide greater wavelength control (factor of 2 to 3 on linewidth),(19) Figure 2.7. The Sirah dye lasers utilised in this work featured dual gratings. Greater wavelength selectivity has performance benefits for LIF where a precisely defined transition is probed; where broad probe light is used, fewer photons will be absorbed for

the same amount of scatter signal when compared with a tighter controlled wavelength probe beam, this is shown in Figure 2.8.
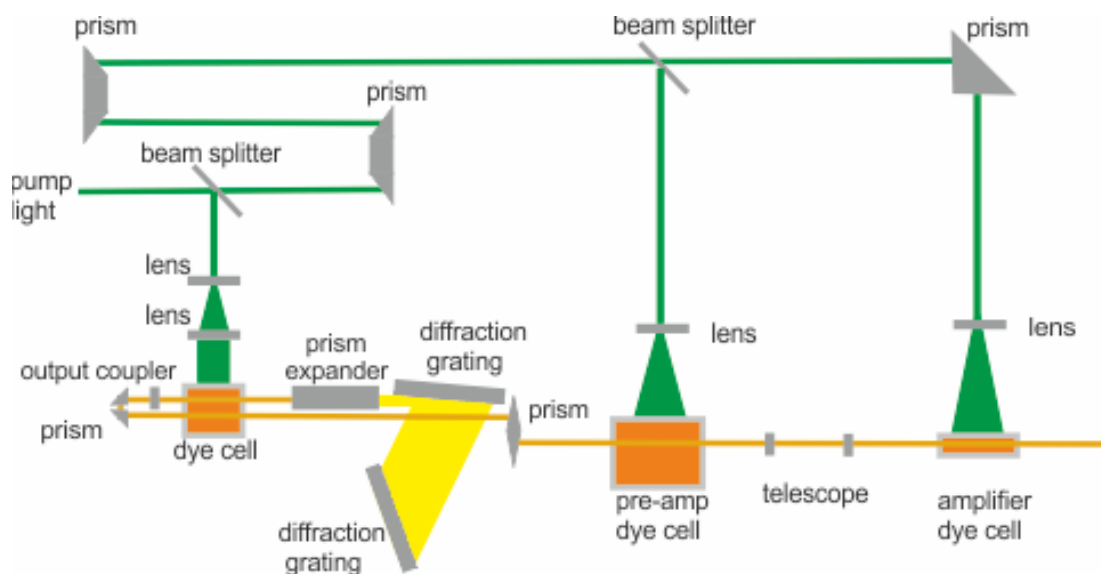
Figure 2.7 A twin-grated dye laser with three dye cells providing additional amplification of narrow line width light achieved from using two diffraction gratings. This schematic is of the Sirah dye lasers utilised for OH LIF experiments.

In the experiments where dye lasers were used as the probe lasers for OH LIF, the dyes chosen were Rhodamine 6G and DCM. DCM has a broad wavelength output peak at 590-670 nm allowing for 616 nm light to be selectively generated from the 532 nm pump light, after frequency doubling the 308 nm light for OH resonant LIF is formed. Rhodamine 6G has a strong absorption at 530 nm and a broad output at 550-590 nm with a peak output close to the 564 nm required for frequency doubling to 282 nm to probe OH off resonantly. The typical efficiency of the orange and yellow light output achieved from the Sirah dye lasers was 10-20 % with respect to the input green light.
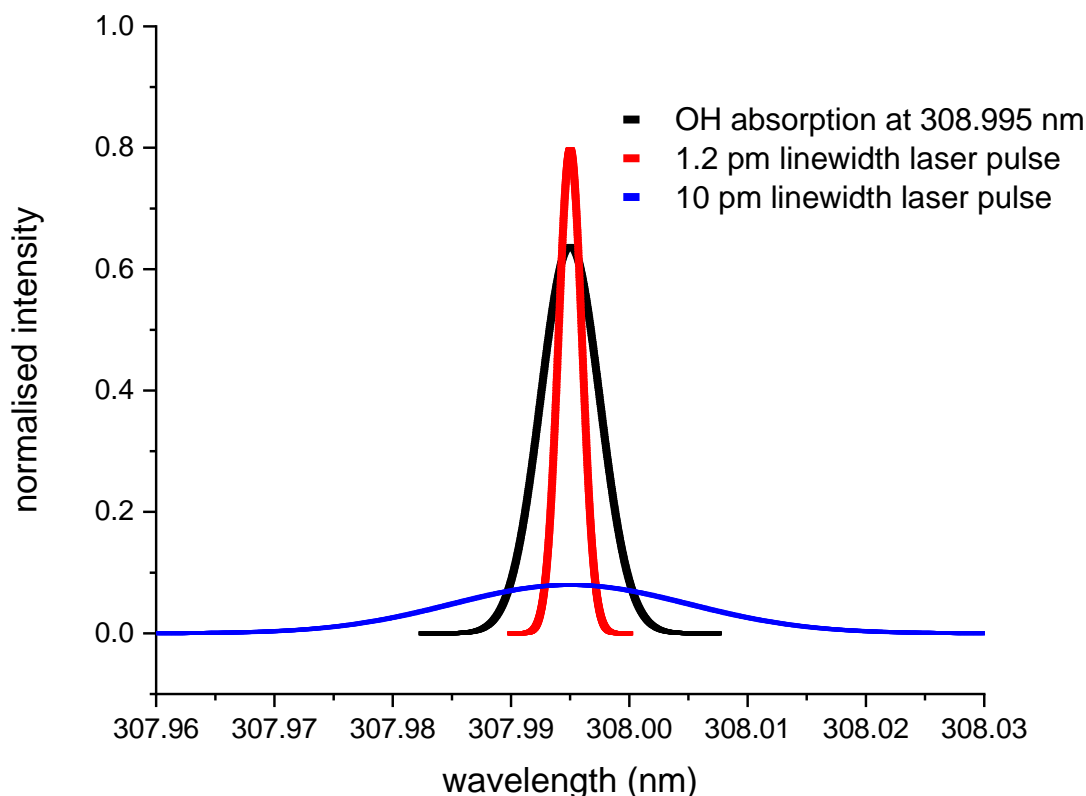
Figure 2.8 Two laser probe pulses at 308 nm with the same power but different wavelength resolutions (10 pm plotted as blue, and 1.2 pm plotted as red) are shown against the OH LIF line at 307.995 nm (peak width 2.5 pm plotted as black).

2.1.3 Pulsed Laser Photolysis (PLP)

Pulsed Laser Photolysis (PLP) or Laser Flash Photolysis (LFP) is a widely used experimental method for making direct kinetic measurements. Pulsed laser photolysis can be coupled to end-product analysis to give information on the different product channels and to measure the rate of formation. (20) As may be deduced from one name for this technique, laser flash photolysis, its origins pre date the existence of lasers for scientific measurements. In earlier experiments, photolysis was via a flash lamp. The technique involved the use of two photographic flash lamps; a millisecond high-powered flash and a lower energy flash lasting a few microseconds were fired at varied delays to each other controlled by a rotating wheel. The second (probe) flash was collected on a spectrographic plate to measure the changes of the transient species formed in the first flash.(21)

Flash photolysis experiments based on this principle allowed the measurement of radical kinetics on the microsecond and millisecond timescales. The advent of lasers with short controllable pulse lengths of high energy monochromatic light, allowed

measurement of kinetics on even a nano second timescales using electronic delay generators for timings.(22) The photolysis lasers used in this work, to initiate reactions, were Q-switched Nd:YAG lasers with the quadrupled output at 266 nm used , or excimer lasers at 248 (KrF) and 193 (ArF) nm.
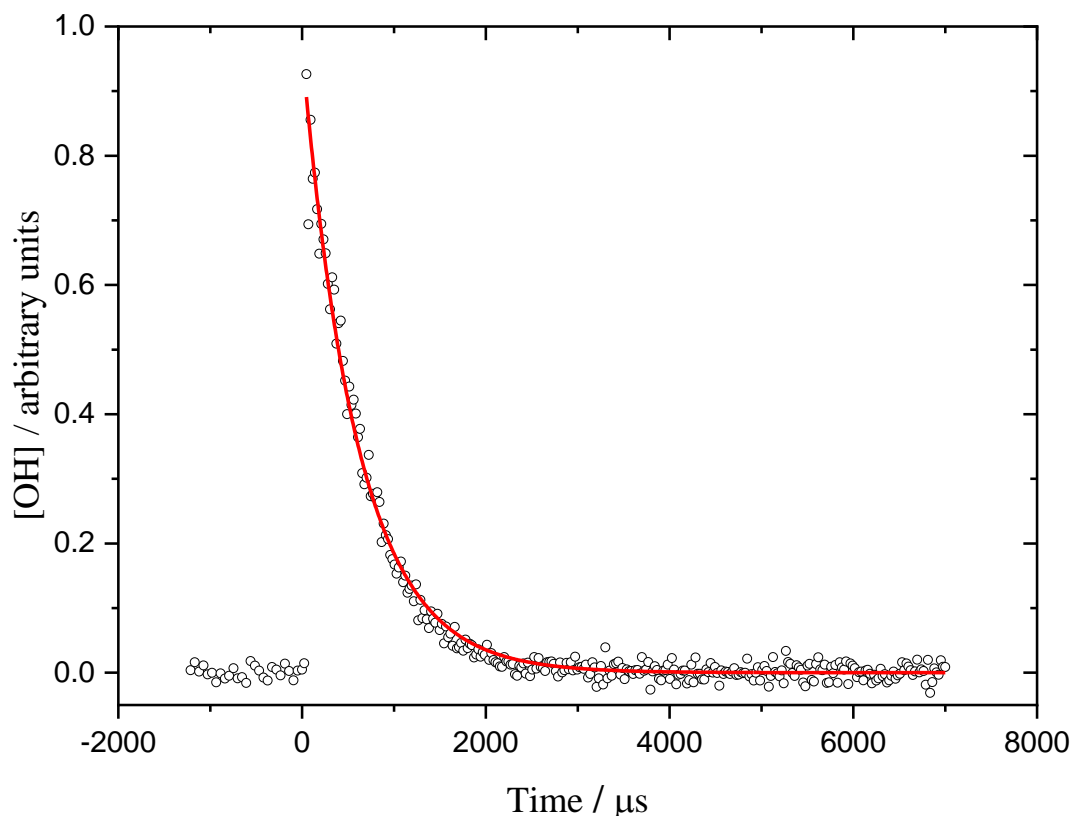
Figure 2.9. An example of a trace from a PLP LIF experiment, where the timing is the delay between the photolysis laser and the probe laser with time zero being when photolysis occurs. By scanning a range of delays, a full decay profile can be collected.

Excimer laser (Lamda Physik Compex 200) photolysis of a peroxide (H_2O_2, tBuOOH) was the primary source of radical formation used within this work; the advantage of this was that excimer lasers provide stable sources of high energy pulsed light at wavelengths suitable for breaking peroxide bonds (< 300 nm). Where longer wavelength light (>250 nm) was required to minimise photolysis of the compound being studied, 266 nm light from frequency quadrupled Nd:YAG lasers was used. Compared with the excimer lasers, the YAG lasers (Quantel Q-smart 850) had much smaller beam profiles (64 cm^2 for the Q-smart 850 versus 240 cm^2 for a Compex 200) and pulse widths (6 ns for the Q-smart 850 versus 25 ns for a Compex 200), although the beam profiles were not as even and laser power fluctuations were more noticeable.

For the work carried out that follows, the primary method of detection used after photolysis was laser induced fluorescence of OH radicals. This was carried out in a conventional slow flow reactor (<200 Torr) and in a high-pressure flow reactor where photolysis occurs that was sampled into a low-pressure detection cell where LIF was performed. Where the time delay between the photolysis laser and the probe laser are scanned in time, a trace of the form shown in Figure 2.9 can be built up. The products from these reactions were additionally studied by proton transfer reaction mass spectrometry (PTR-MS); however, this was not performed in a time resolved manner.

2.1.4 Timings and lasers

The use of LIF to probe PLP experiments relies on precisely controlling the delay time between when the lasers fire relative to each other and the time for which the detector signal is monitored. This is achieved using a digital delay generator (BNC DG535) to control the timings of the lasers and measuring the arrival of the probe light with a photodiode to fire an oscilloscope, which collects signal from the photodiode and photomultiplier tubes; a general schematic of this methodology is given as Figure 2.10. By measuring the arrival of the probe light, slight variations in timings from the delay generator had less of an effect on the observed OH LIF signal; in addition, measuring the probe signal with a photodiode allowed for correction of the OH LIF signal for variations in probe power.

When Nd:YAG (YAG) lasers were used they received two trigger pulses, the first to trigger the flash lamps and the second to trigger the Q-switch. Q-switching is the process that allows for the generation of short (<30 ns) pulses of high peak energy light. Without Q-switching, YAG lasers would either produce continuous output (CW), when diode pumped, or pulsed output with the same pulse width as the flash lamp pulse. It is possible to produce short pulses of light using modulation or gating of a CW laser although this produces a peak power output much lower than Q-switched lasers (Q-switching can increase peak power by orders of magnitude over cw output),(23) Figure 2.11. High power short energy pulses are highly beneficial for power dependent processes such as dye laser pumping or generating harmonics.(24) For example, second harmonic generation is quadratically dependant on the input power.(14)
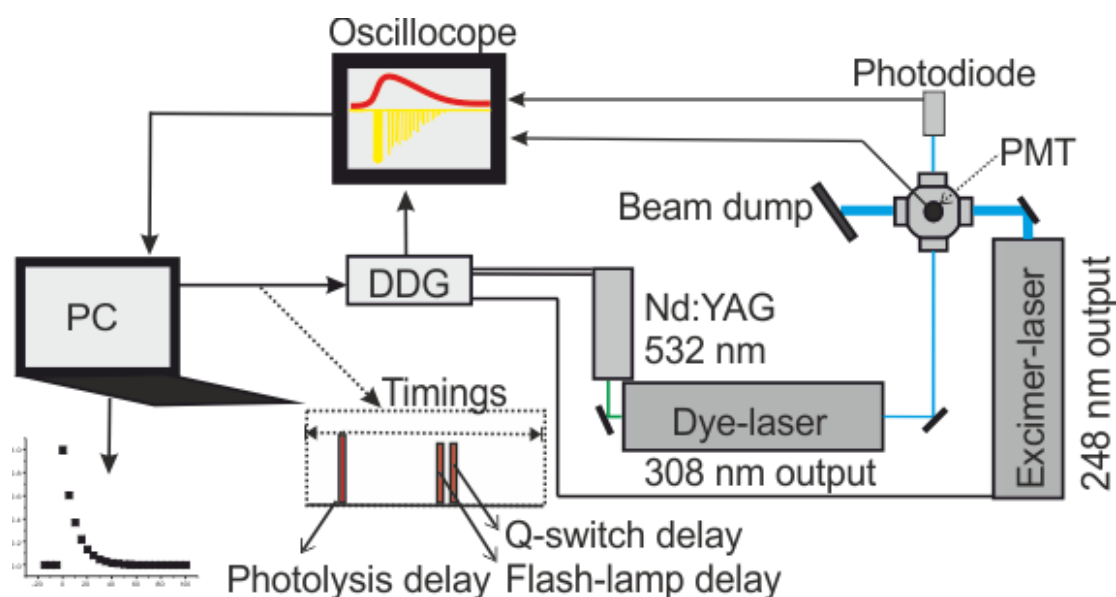
Figure 2.10. A general schematic for a pulsed laser photolysis laser induced fluorescent setup with OH detection. A computer provides timings to a digital delay generator (DDG) which controls the firing of the probe and photolysis lasers and receives the output of an oscilloscope. In this example, the Q-switch and probe flash lamp delays are fixed, and the photolysis laser delay is stepped in time to generate the full decay profile.

In actively Q-switched YAG lasers, a device prevents light from parsing the full laser cavity whilst the gain medium (Nd:YAG crystal) is pumped (flash lamp) causing an increase in energy in the gain medium. Once sufficient energy has been built up in the gain medium, the optic device that is preventing light from parsing the full cavity, is switched to allow this to occur, as light is allowed to travel through the cavity the crystal is rapidly depopulated through stimulated emission and the lasing action occurs (25), Figure 2.12. The device can be an electro optic device such as a Pockells or Kerr cell, or an acousto-optic modulator (Bragg cell).(26)

For Q-switching with an acousto-optic modulator an RF pulse is applied to diffract light and prevent it passing through the cell, a piezo-electric transducer attached to a crystal is used to generate the RF diffraction. When the switch is reversed, the diffractive losses are much lower and this allows for the rapid change in the losses required for active Q-switching.(27)
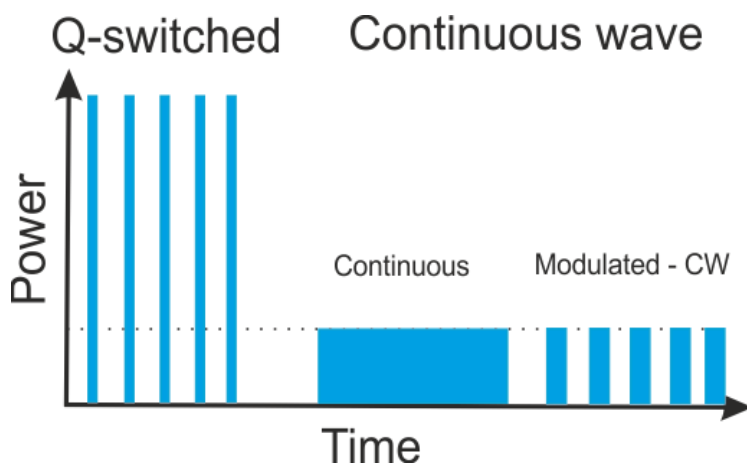
Figure 2.11. Q-switching allows for short high energy pulsed output (up to orders of magnitudes greater than cw) when compared to continuous wave (cw) or modulated continuous output.

Active Q-switching can allow the peak power of a pulsed laser to be varied, sub optimal Q-switch delay times that are too long or too short will result in lasing action occurring in a crystal where lower than peak energy gain is present. This flexibility allows the laser power of YAG lasers to be changed readily without any fundamental changes to the experimental setup. Being able to change the laser power of the probe laser can provide insight into the presence of any two-photon photolysis effects, where the laser power of the photolysis laser is changed the presence of photolysis of the reagent of study and of products can be assigned, and the radical concentration generated can be varied.
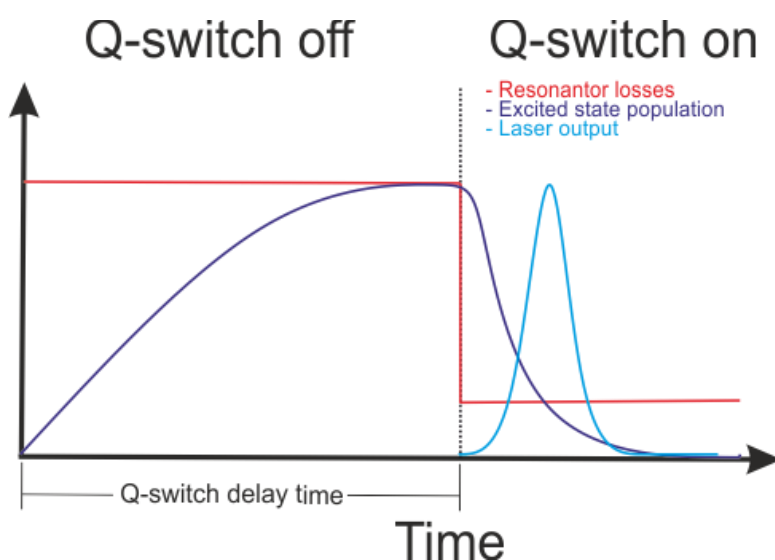
Figure 2.12. The time between the flash lamp being fired and the Q-switch being triggered is the Q-switch delay time. This delay allows for a build-up in the excited state population in the gain medium, when the Q-switch is then triggered this can be rapidly depopulated leading to high energy pulsed output.

2.2 Experimental setups for PLP-LIF
2.2.1 Low-pressure (conventional slow flow reaction cell)

The conventional slow flow reaction cell used to make kinetic measurements of OH loss was a stainless steel, six-way cross. The photolysis laser (248 nm, LPX 200) and probe laser (308 nm, Continuum precision-II pumped Sirah dye laser (DCM in methanol)) met perpendicularly in the centre of the reaction volume, and the photomultiplier tube (PMT – Perkin-Elmer C1943P) was situated above the reaction volume, perpendicular to the plane of the lasers. Between the reaction volume and the output window to the PMT, two parallel lenses focused light onto the detector and provided improved signal. An oscilloscope received the output from the PMT and from a photodiode, where the photodiode recorded the arrival of the probe pulse and the pulse energy, with the arrival of the photolysis pulse used to trigger the oscilloscope. The laser delays were controlled by a LabVIEW program that sent these to a digital delay generator (BNC-DG555), the LabVIEW program then received and averaged the output from the oscilloscope (Lecroy Waverunner LT-262).

The input gas flows to the reaction volume were delivered from a mixing manifold where calibrated mass flow controllers (MFCs) allowed for varied concentrations and flow rates to be produced. The pressure within the reactor was measured using a pressure gauge (MKS baratron – 1000 Torr) and temperature measurements of the flowing gas were made with type K thermocouples. The reactor pressure was maintained by a rotary pump (Edwards 18), where a valve between the reactor and the pump allowed the reactor pressure to be varied for the same total flow. Temperature control was provided by varying the voltage applied to a Watlow ceramic heater surrounding the reactor using a variac and allowed for experiments to be carried out over the temperature range 300 – 800 K. A detailed schematic of the low-pressure experimental bay is given as Figure 2.13.

For temperature assignment in the low-pressure cell a detailed parametrization of the effect of flow rate and total pressure on the difference between the thermocouple readout and the accurate temperature of the reaction volume exists. This parametrization was based on a large sample of measurements of the reaction of OH with methane, and OH with hydrogen that were carried out over a wide range of temperatures (400 – 800 K), and the parametrization was accurate at predicting the temperature of subsequent measurements ($\pm$ 5 K).
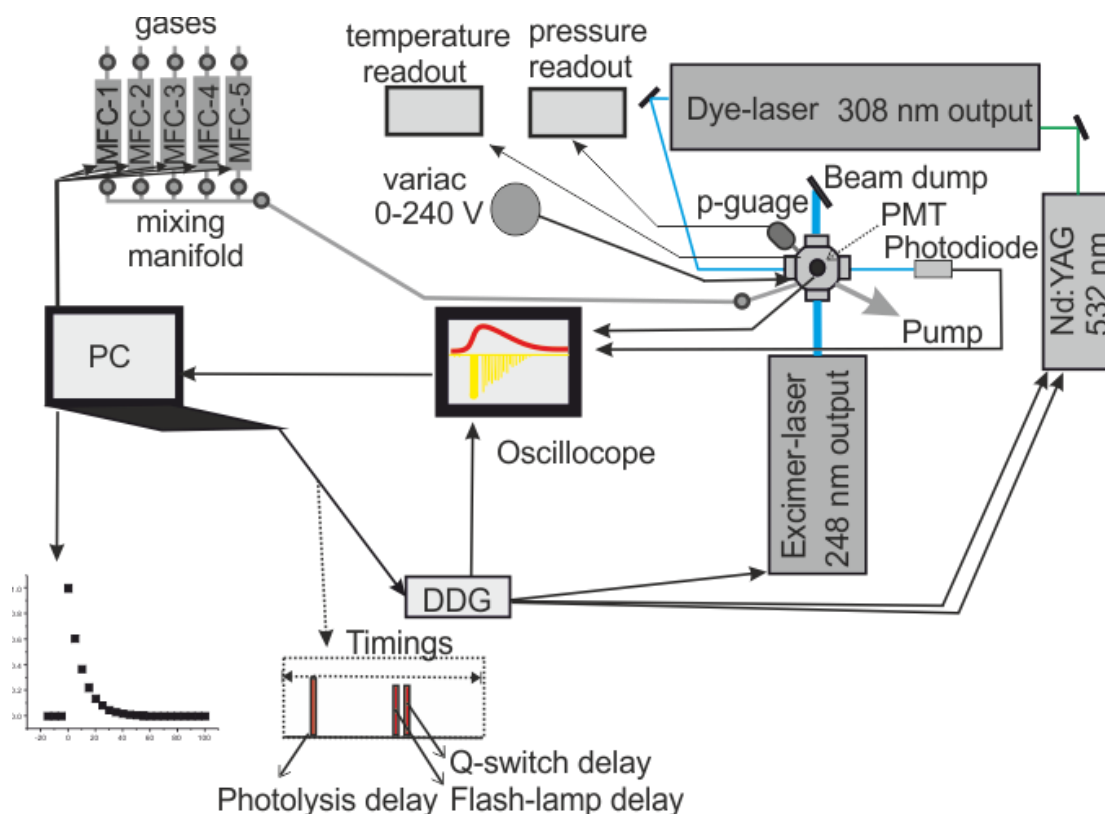
Figure 2.13. A schematic of the low-pressure PLP-LIF experimental setup used in this work.Gases were provided to the reaction cell from a mixing manifold through calibrated mass flow controllers, the pressure of the cell was maintained by a rotary pump and was measured by a baratron pressure gauge (1000 Torr). The temperature was set by varying the voltage applied to a ceramic heater using a variac, and was measured using type K thermocouples. A digital delay generator provided timings to the lasers, and LIF fluorescence was measured perpendicular to the plane of the lasers by a photomultiplier (Perkin-Elmer C1943P), and the probe power was measured on a photodiode.

The mixing manifold has two baratron pressure gauges (MKS, 1 Torr, 5000 Torr) that allow for precisely defined mixtures to be made up. For compounds that had low vapour pressures not conducive to making up known concentration mixtures and for the OH precursor, the reagents were added in a pressure regulated backing flow. Where compounds were added in a backing flow, the temperature was monitored and the flow through the bottles was kept below 500 SCCM allowing for close to the full vapour pressure to be sampled. This method will be referred to as the bubbler method, which is a misnomer as great care is taken to ensure that minimal disturbance of the liquid surface occurs so that only the equilibrium vapour pressure of the compound is sampled and not droplets.
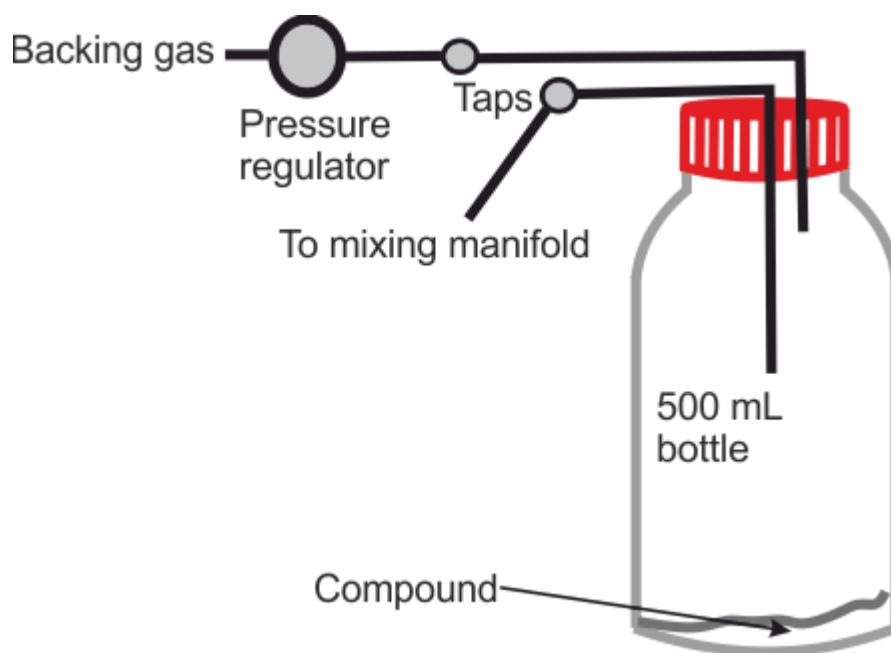
Figure 2.14. Depicts the method that will be referred to henceforth as the bubbler method. For compounds with low vapour pressure, or where high flows needed to be maintained for extended periods (OH precursors) the compounds were added to the reactors by sampling the vapour pressure with a pressure regulated backing flow of nitrogen.

The photomultiplier was operated in a non-gated mode and with the LIF detection being carried out on resonant the probe scatter and LIF signal overlapped. This overlap of LIF signal and probe scatter was not problematic for OH decay retrieval below 200 Torr in nitrogen. However, with increasing pressure and oxygen concentration quenching reduced the lifetime of the OH LIF signal and the overlap with the probe scatter became a limiting factor to the pressure and oxygen concentrations that could be explored (< 350 Torr). The experimental pressure range utilised in this work, with this setup was 5 – 120 Torr. This pressure difference was sufficient to ascertain if pressure dependences in the reaction kinetics were present, and higher pressure were probed using the high-pressure OH LIF system.

An example bimolecular plot (k_{obs} versus [RH]) generated, at 50 Torr and 298 K, in the low-pressure apparatus for the reaction of OH and dimethylformamide, DMF, is given as Figure 2.15, where the inset shows an example trace where four individual pulse probe events were averaged per time point and 220 time points were collected per decay. The resultant plot shows the excellent linearity that can be achieved when the bubbler method is used to deliver the compound of interest, and the inset shows the excellent precision with which OH decays could be recovered.
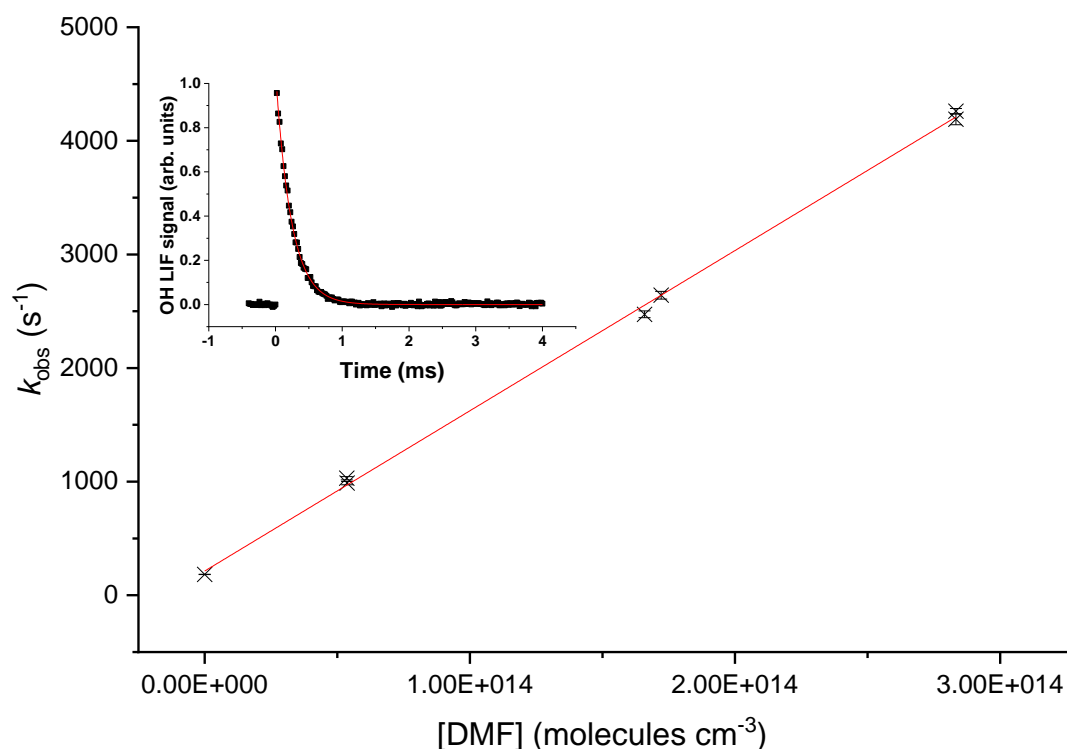
Figure 2.15. A bimolecular plot from the reaction of OH and dimethylformamide, carried out at 298 K and 50 Torr the slope of the plot gave $k_{bimolecular}$= (1.41 ± 0.04) × 10^{-11} cm^3 molecule^{-1} s^{-1}. The inset OH decay gave k_{obs} = (4260 ± 46) s^{-1} with 2.83 × 10^{14} molecule cm^{-3}, all errors given as 2 σ.

2.2.2 OH and HO₂ detection via LIF sampling from a high-pressure reactor

Reactions were carried out in a high pressure (0.5 – 5 bar) reaction cell which is a significant modification of an earlier system for OH detection described in *Stone et al.*(28) and schematics of which are shown in Figure 2.16 and Figure 2.17. The high-pressure reactor was a 0.5 m stainless steel tube with a 22 mm internal diameter. Gas flows were delivered to the high-pressure cell from a mixing manifold where calibrated mass flow controllers (MFC) allowed for accurate control of flow rates. Low vapour pressure compounds: OH precursors (H₂O₂), and substrates such as dimethyl formamide and butanol, were delivered to the mixing manifold from thermostatted bubblers in pressure regulated backing flows of nitrogen (N₂). High vapour pressure compounds of interest such as ethane and methane, and oxygen were delivered directly from cylinders into the mixing manifold through MFCs. The gas flowrate through the cell was kept under laminar conditions with typical Reynolds values (Re) of 480 (corresponding to a flow rate for an experiment of 10 SLM at 2 bar); in general, conditions were maintained between 400-800 Re (Re < 2400 = laminar flow), with some experiments carried out with higher flowrates

up to 1800 Re. Pressure gauges are present at the end of the mixing manifold before the high pressure reactor and on the output of the reactor, where simultaneous measurements the pressure gradients was typically under 200 Torr (1685 and 1524 Torr at 9.8 SLM).
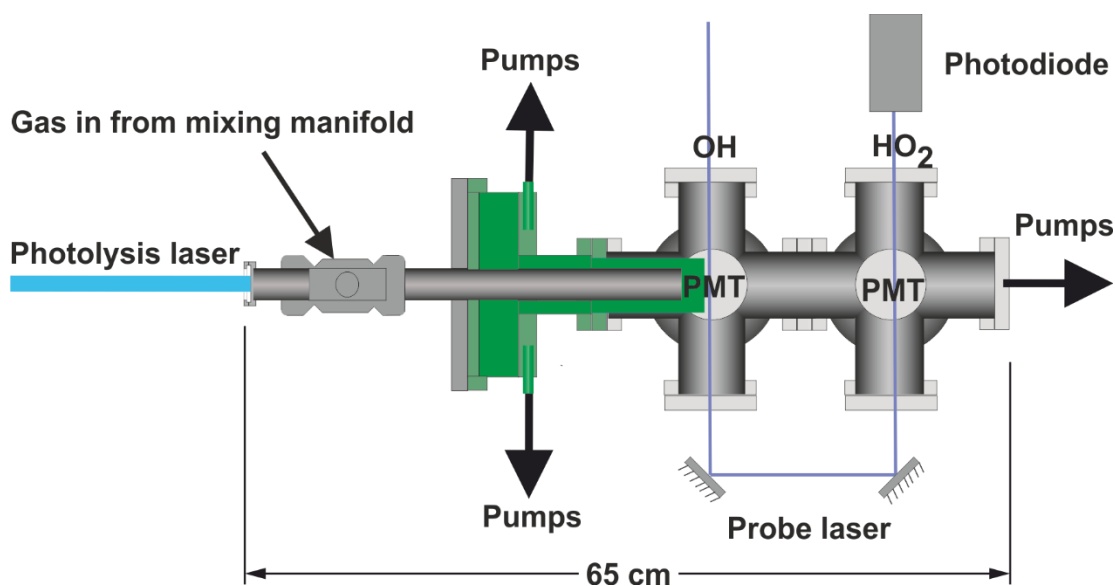
Figure 2.16 Schematic plan of the high-pressure apparatus for time resolved OH and HO_2 detection.

Temperature control of the reactor between room temperature and 800 K was achieved by altering the voltage applied to a coil heater (WATROD tubular heater, Watlow) over the last 30 cm of the stainless-steel tube. The heated region was fitted with a quartz liner (inner diameter 18 mm) to reduce wall-initiated chemistry. A temperature readout, from a type K thermocouple in the gas flow, close to the pinhole, was calibrated for given flow rates, pressures and voltage settings by measuring the highly temperature sensitive OH and methane rate coefficient, using the temperature dependence reported by Dunlop and Tully(2).

The use of a chemical thermometer was required as it is otherwise difficult to know the exact temperature at the pinhole and this will be described in greater detail later (Chapter 3). Even if location of the thermocouple was the sole error, introducing a thermocouple close to the reaction region would affect the gas flow in that region and cannot be used in routine operation. A translatable thermocouple has been passed along the axis of the high-pressure reactor over a variety of temperatures and showed that the temperature of the gas close to the pinhole strongly varies with axial location. In addition, radial profiles showed that in our system there was insufficient heating length to achieve uniform radial heating of the laminar gas. From the axial measurements it was observed

that slower flow rates (< 5 SLM) allowed for reduced axial temperature gradients. However, these measurements showed that the only manner to achieve an even thermal profile would be a static cell.

A permanently seated thermocouple, type K, was placed perpendicular to the flow close to the sampling region, measurements from this thermocouple were then compared with temperature assignments from the reaction of OH and methane using the temperature dependence assigned by Dunlop, J.R. and F.P. Tully (32). This was performed over a range of heater settings and flows to allow for temperature assignment. This method was also applied to a standard low-pressure cell where the flows can be reduced to slow enough flows that thermocouple measurements could accurately define the temperature to verify the method. Additionally, the well-determined OH and ethylene equilibrium was measured over a range of temperatures to provide an additional verification of the temperature assignment.

The method to assign a temperature from the reaction of OH and methane used the pseudo-first order rate coefficients ($k'_{OH,1st}$) measured at the first detection axis over a range of added methane flows. An estimate of the temperature was made from the thermocouple measurement. This estimated temperature was used, along with the pressure in the reactor, to calculate the added methane concentration. Comparing the predicted pseudo-first-order rate coefficient that this estimated concentration provided using the literature value of k_{OH+CH4} (32), to the measured rate coefficient, produced a difference for each point. The estimated temperature was then iteratively changed to minimize the difference between estimated and measured rate coefficients. For this minimum value, the difference between thermocouple measurement and actual temperature was tabulated against the voltage setting for the heater.

From measurements carried out at 1600 – 1700 Torr with 10 SLM, parameterizations were generated of the reaction the gas temperature as a function of both thermocouple measurement and the voltage applied to the heaters. A more detailed description of this method is described within instrument characterization (Chapter 3 section 3.4). The parameterizations used at the time this work was completed are given below. The paramterizations are improved and adjusted when any subsequent temperature measurements are performed. For the parameterization of the temperature from the thermocouple readout this is only applicable for experiments carried out with

the same location of the thermocouple; whenever the apparatus is dismantled new parameterizations are required.

Parameterization 1 (Temperature as a function of applied voltage):

$$\text{Temperature(K)} = ((-1.6954\times10^{-6})\times V^4) + ((3.9967\times10^{-4})\times V^3) - ((1.1703\times10^{-2})$$
$$\times V^2) + ((0.90968)\times V) + 25.002)$$

Parameterization 2 (Temperature as a function of thermocouple measurement):

$$\text{Temperature (K)} = 0.68 \times T1 + 99.8$$

The dependence of the temperature generated on the applied voltage was non-linear. The deviation of the temperature difference between the observed temperature on the thermocouple and the temperature measured from the bimolecular reaction of OH and CH_4 was well described as linear for the experimental range tested (400 and 850 K). Both parametrizations were used to estimate the temperature of the reactor for experiments where no OH and methane measurements were performed and has been shown to reliably predict the temperature of the reactor within 7 K when measurements of the temperature were subsequently made.

The photolysis of the OH precursor, H_2O_2, at 248 nm (Lambda Physik, Compex 200 operated using KrF) or 266 nm (frequency quadrupled Nd-YAG output, Quantel, Q-smart 850) initiated the chemistry. Where photolysis of water was used as the OH source, this was carried out at 193 nm, where the Compex 200 was operated on ArF.

$$H_2O_2 + h\nu \rightarrow 2OH \qquad \text{(R2.1)}$$

Hydrogen peroxide was used as the OH precursor for all experiments where HO_2 detection was performed, because it also acts as an internal calibrant to relate OH and HO_2, via reaction R2.2:

$$\textbf{OH} + H_2O_2 \rightarrow H_2O + \textbf{HO}_2 \qquad \text{(R2.2)}$$

However, in general, other OH precursors can be used. The OH precursor was maintained at low concentrations ($1 \times 10^{14} - 1 \times 10^{15}$ molecule cm^{-3}) to minimise errors associated with assigning pseudo-first-order kinetics for the loss of OH. Maintaining a low radical precursor concentration had the additional advantage of minimising attenuation of the photolysis beam, ensuring consistency in the initial radical concentrations generated along the length of the high-pressure cell. Initial OH

concentrations were in the range $2 \times 10^{11} - 5 \times 10^{13}$ molecule cm^{-3}; in general these concentrations are sufficiently low enough to reduce radical-radical reactions and this is discussed further in chapter 3.
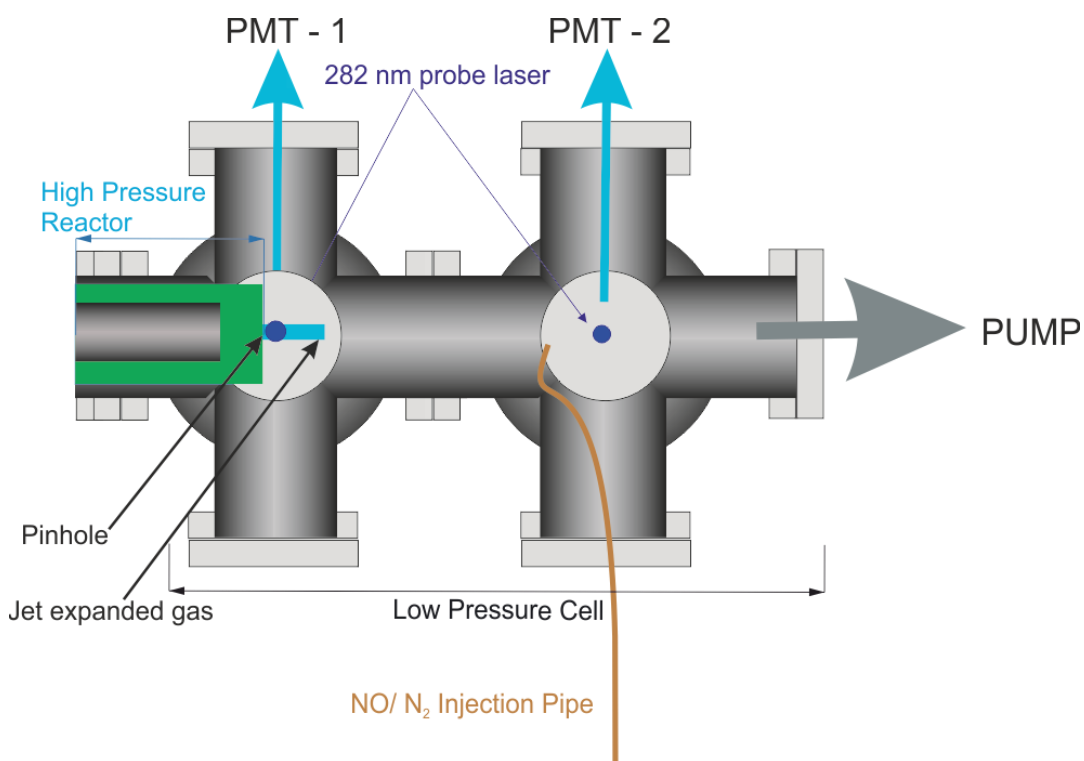
Figure 2.17 Detailed schematic elevation of the low-pressure detection region of the reactor.The green line represents the jet expanded gas; the jet breaks down after approximately 2 cm. NO was injected through a 1.5 mm id stainless steel tube after the breakdown of the jet.

A pinhole (diameter < 0.15 mm) at the end of the high-pressure reactor couples the reactor to the low-pressure (0.3 – 5 Torr) detection cell. Details on OH detection can be found in (28). The accuracy of the instrument for OH measurement has recently been verified by measurements of the rate coefficient of the reaction of OH with isoprene, (4) which are in excellent agreement with the literature. A more detailed schematic for the low-pressure detection cell is shown in Figure 2.17.

In the first low pressure detection cell, the OH was probed within the jet expanded gas, close to pinhole (<5 mm), perpendicular to the gas flow. The OH was detected by off-resonance laser induced fluorescence (LIF) at 308 nm following excitation with 282 nm light ($A^2\Sigma$ (v' = 1) $\leftarrow$ $X^2\Pi$(v'' = 0)). The 282 nm light was the frequency doubled output of a dye laser ((Rhodamine 6 G, Spectron) pumped at 532 nm by a Nd:YAG laser (Spectron), or (Rhodamine 6 G, Continuum) pumped by Nd-YAG

output (Quantel, Q-smart 850)). Measuring the off-resonance fluorescence allowed the use of a filter (308 ± 5 nm, Barr Associates) before the photomultiplier (Perkin-Elmer C1943P) to remove scattered light and improved the signal to noise ratio.
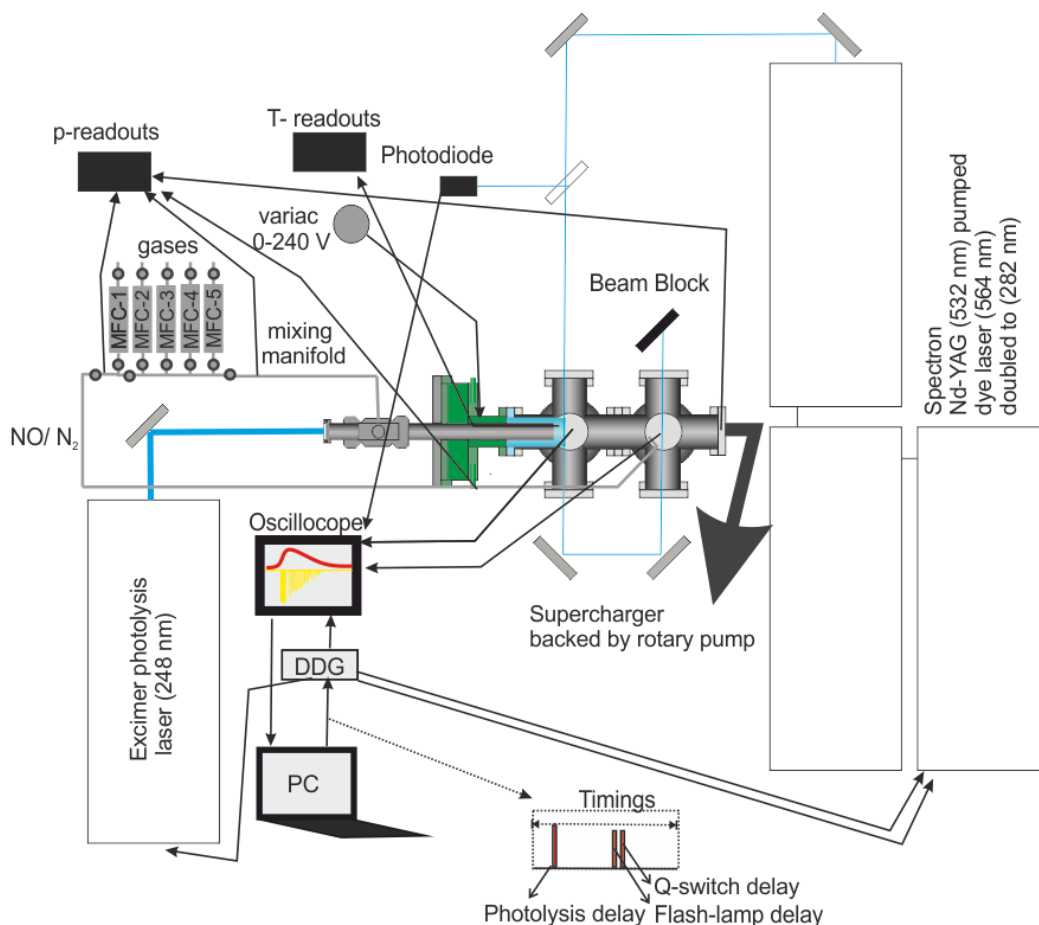
Figure 2.18 A schematic of the FAGE sampled high-pressure PLP-LIF setup where the laser alignment for the Spectron probe laser is shown. MFC-1 delivered flows of N2 and NO to the low-press LIF cell, with the remainder delivering the precursor, backing gas, oxygen and the reagent of study to the reactor via the mixing manifold.

A delay generator (BNC DG535) was used to vary the delay between the photolysis and probe lasers, facilitating generation of time profiles of the OH concentration. The traces were scanned through multiple times (5-20) and the signal at each time point was averaged, giving high precision OH loss traces, the schematic of this layout is given as Figure 2.18. An example OH trace from the first detection cell for reaction R5 is presented in Figure 2.19. As reactions were carried out under pseudo first order conditions ([OH] << [substrate]), the time dependence of the OH LIF signal, I_f, (proportional to the [OH]) was given by Equation 2.1:

$$I_{f,t} = I_{f,0}e^{-k_{OH}t} \qquad Equation \text{ } 2.1$$

where $k_{OH} = k_5[H_2O_2]$. In Figure 2.19 two traces are presented from the first, OH, detection axis, these two traces were taken in consecutive experiments with a constant $[H_2O_2]$ where the first trace ($k_{OH,1st} = (2351 \pm 22)$ s^{-1}) was taken where N_2 was flowed into the low pressure region, the second trace ($k_{OH,1st} = (2389 \pm 18)$ s^{-1}) was taken when this flow had been switched to NO to allow HO_2 detection in the second detection cell, errors are given as 2 σ. The similarity of the OH decay traces when either N_2 or NO was injected shows that there was no back streaming of NO in the low-pressure cell and hence no HO_2 conversion at the first detection axis.

Considering only the OH kinetic information collected in the first cell, the results have a high degree of precision and accuracy. This has been demonstrated in a recent publication on the reaction of OH and isoprene (C_5H_8) (4), and in the accuracy of the measurement of OH and n-butanol, both in the presence and absence of added O_2, that will be given later in chapter 4). The range over which this instrument can measure accurate and precise rate constants was assigned as 15 to 150,000 s^{-1}. Assignment of the upper limit was performed using the reactions of OH and ethylene and with photolysis of H_2O_2 at 248 nm as the source of OH. The reaction of OH and methane, and photolysis of water at 193 nm was used for validating removal rate coefficients smaller than was possible in the presence of hydrogen peroxide as an OH precursor (<500 s^{-1}). This is discussed in detail in the experimental developments chapter (Chapter 3).

HO_2 radicals were monitored by chemical transformation; titration of HO_2 to OH via reaction with NO (R3) in the low-pressure cell. Following the breakdown of the jet, after the Mach disk (>2 cm beyond the pinhole), a small flow (5 sccm) of NO or N_2 was introduced into the low-pressure cell via a 1.5 mm i.d. stainless steel pipe (for a typical 0.5 Torr pressure in the FAGE cell the NO concentration was 5.5×10^{13} molecule cm^{-3}). After passing through the first detection cell, the probe beam was redirected through the second low-pressure detection cell downstream of the NO pipe allowing for the measurement of the OH concentration by LIF in the same manner as in the first cell. The location of the mach disk was approximated from equation 2.2.

$$x_M = 0.67d\sqrt{p_o/p_b} \qquad Equation \text{ } 2.2$$
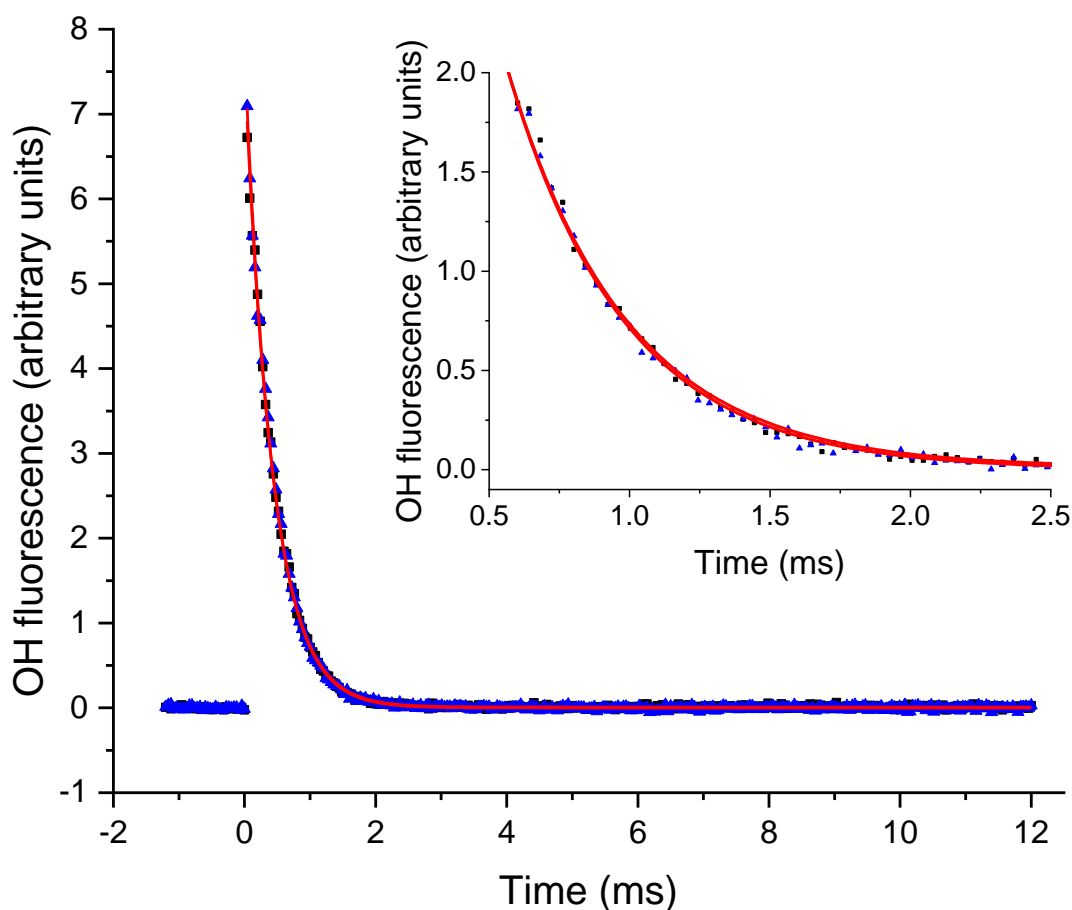
Figure 2.19 An example of the OH signal (blue triangles) collected at the first detection axis for the reaction of OH with H_2O_2 ($[H_2O_2] \approx 1.4 \times 10^{15}$ molecule cm^{-3}, with a flow of N_2 into the low-pressure cell, with black squares representing the subsequent trace taken with a flow of NO. The red lines represent the non-linear least squares fits to an exponential decay ($k_{OH,1st} = (2351 \pm 22)$ s^1 and $k_{OH,1st} = (2389 \pm 18)$ s^{-1}) 2 σ errors.

By switching between a flow of N_2 and NO, through the pipe, traces for OH loss and HO_2 formation could be obtained, examples are shown in Figure 2.20. Subtraction of the two OH traces in Figure 2.20, (upper, red trace is with NO injection and the signal corresponds to reactant OH and OH produced from the titration of HO_2 to OH, lower, blue trace with N_2 injection is reactant OH only) gave a resultant signal associated with HO_2 production in the high-pressure reactor, shown as the black trace in Figure 2.20. The signal from the first PMT allowed for correction of the signal heights at the second PMT for changes in the probe laser power or wavelength, any variations in laser power or wavelength affect the absolute signal retrieved from both PMTs; however, the relative signals retrieved from the PMTs remain consistent.
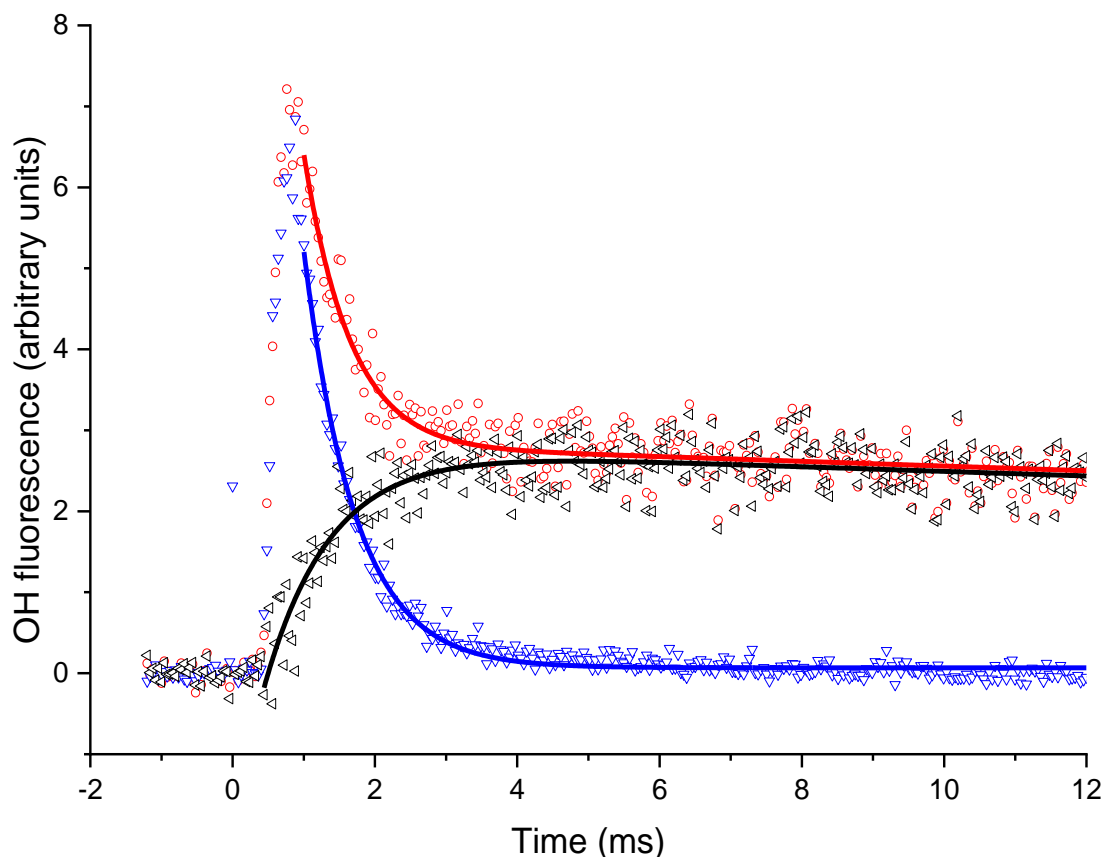
Figure 2.20   Examples of OH fluorescence traces collected at the second detection axis under the same conditions for Figure 3.The blue triangles are where N_2 has been injected through the pipe, i.e. no HO_2 to OH conversion. The OH signal profile differs from that in Figure 18, with $k_{OH,2nd}$ = (1390 ± 44) s^{-1} (2 σ errors). The red circles are the OH signal obtained with NO injection. The resultant OH trace associated with HO_2 formation in the high-pressure cell   obtained by subtracting the two OH traces, obtained with either NO or N_2 injection prior to the second detection axis, shown as black triangles, a biexponential growth and decay fit, black curve, gave a formation rate coefficient, $k_{HO2,2nd}$ = (1077 ± 152) s^{-1} (2 σ error).

As will be described in greater detail in the experimental developments section, the HO_2 formation traces and OH loss traces from the second cell generated kinetic parameters which differed from the accurate parameters collected at the first detection axis, $k_{OH,2nd}$ = (1390 ± 44) s^{-1} and $k_{HO2,2nd}$ = (1077 ± 152) s^{-1} where the accurate loss parameters from the first cell were $k_{OH,1st}$ = (2389 ± 18) s^{-1}, 2 σ errors. This difference was assigned as the result of transport effects.

Neither of the OH determinations in the two detection axes provide absolute measurements of radical concentrations. Each detection axis could be calibrated as for chamber measurements, but for our purposes, a calibration reaction linking photolytically produced OH and HO_2 removes many sources of error compared

to an absolute calibration. The reaction of OH with the radical precursor H_2O_2 which directly forms HO_2 with a 100 percent yield was used for calibration.

$$\textbf{OH} + H_2O_2 \rightarrow H_2O + \textbf{HO}_2 \qquad (R2.2)$$

For reactions carried out where a reagent was added in addition to the H_2O_2, the resulting ratios can be compared with those from the calibration reaction to allow assignment of an observed HO_2 yield. To assign the HO_2 yield from the test reaction required accounting for secondary HO_2 production in the high-pressure reactor, from $OH + H_2O_2$ and photolysis processes. From the known rate coefficients, it was possible to calculate the fraction of OH reacting with the H_2O_2 and hence the expected contribution to the HO_2 signal. Photolytic production of HO_2 was accounted for by measuring the observed HO_2 signal in the absence of any H_2O_2.

In a typical experiment, the reaction of OH and H_2O_2 would be carried out four times, twice in the absence of NO and twice with the addition of NO to calibrate the instrument. Exponential fits to the OH decay as monitored in the first cell determine the peak OH signal. The OH signals at the second detector recorded with only N_2 addition (reagent OH reaching the second detector) and subtracted from the signal with NO added (reagent OH and HO_2) to give the net HO_2 signal. This profile was fitted to, a biexponential growth and decay function, to extract the peak HO_2 signal for that set of conditions. Combinations of traces were then used to obtain an averaged value (and uncertainty) of the signal on the first PMT (OH) to the net HO_2 signal at the second PMT for this calibration reaction where OH reactant and HO_2 product have a 1:1 relationship. The same process was then performed in the presence of the compound of study. The removal pseudo-first-order rate coefficient with H_2O_2 and the reagent of study ($k'_{OH,1st} = k_{OH+H2O2}[H_2O_2] + k_{OH+TEST}[TEST]$) was compared to the removal pseudo-first-order rate coefficient with only H_2O_2 ($k'_{OH,1st} = k_{OH+H2O2}[H_2O_2]$) to assign what fraction of the OH reacted with the H_2O_2 precursor and hence the resulting contribution to the observed HO_2. Comparison of the remaining peak ratio to the ratio from the H_2O_2 and OH calibration experiment provided the experimentally derived HO_2 yield for reaction of OH and the reagent of study.

Branching ratios to direct HO_2 formation could be assigned with an accuracy of ~10 %, the limitations to this were signal to noise effects, where improved signal to noise could be achieved by increasing the precursor concentration and photolysis energy.

However, this was limited by the need to ensure pseudo-first-order conditions were maintained and to minimize radical-radical processes. Ensuring the dominant reaction was between OH and the reagent of study, whilst still being able to accurately measure the initial OH conditions, provided a limit to the maximum removal rates achievable ($k_{OH,1st}$ < 30,000 s^{-1}).

2.2.3 Summary of the PLP-LIF experimental apparatuses

For the conventional slow-flow low-pressure PLP-LIF cell the signal to noise generated was excellent, allowing for high precision decays to be collected. This method has previously been robustly shown to provide accurate results where the concentration of reagent added is well known. Where bubblers were used linear bimolecular plots can be generated for low volatility compounds.

For the FAGE sampled high pressure reactor, use of H_2O_2 as an OH precursor has been shown to provide a reliable method of internally characterizing our system for HO_2 yield detection. Interferences that could arise from using this precursor for HO_2 detection have been accounted for, and the presence of water that the H_2O_2 precursor introduces has no effect on the sensitivity of the LIF method, unlike IR absorption methods.

By performing reactions under low NOx and low radical densities (<1×10^{13} molecule cm^{-3}), HO_2 yields formed on fast timescales (> 300 s^{-1}) can be assigned to direct HO_2 channels or reactions of alkyl (R) radicals with oxygen. Whilst some time-resolution is lost at the HO_2 detector, sufficient time-resolution is retained in order to separate varying sources of HO_2.

The FAGE sampling method allows for accurate and precise OH kinetics to be recovered where OH LIF measurements are performed in the 'jetting' and accurate rate coefficients can be recovered from 10 – 150 000 s^{-1}. Where OH detection is made at a distance beyond the breakup of the 'jet' the kinetics recovered can be corrected up to removal rates of 1500 s^{-1}.

For both the high- and low-pressure systems, thermocouple measurements were corrected for the temperature at which the reaction occurred through parametrizations based on the measurement of the temperature sensitive reactions, OH with methane and OH with hydrogen.

2.3 Experimental use of PTR-TOF-MS
2.3.1 Principles of PTR-TOF-MS

Time of flight mass spectrometry (TOF-MS) takes a full spectrum in each TOF cycle, and where the resolution is sufficient it is even possible for isobaric species to be resolved. The advantage a TOF-MS provides over a quadrupole mass spectrometer is that it allows for the changes in multiple peak areas to be observed quasi simultaneously. The cost of time of flight over quadrupole mass spectrometers is a reduction in absolute sensitivity. When the TOF is performing mass analysis, no additional ions can be detected whereas in a quadrupole MS there is no dead time during which ions are not detected. Where absolute sensitivity is not considered problematic; TOF mass spectrometers provide a highly versatile detection method.

The principle of TOF-MS is that the time taken between being sampled and being detected is proportional to the mass to charge ratio. By introducing a reflectron, ions that have travelled through a free field region are slowed then returned into the free field region where they are detected. Two advantages of using a reflectron are that the kinetic energy distribution within the direction of travel can be corrected for species with the same m/z ratio, and that a higher TOF path-length can be incorporated in a flight tube of the same length.

To take maximum advantage of TOF-MS when measuring mixtures of compounds, minimising fragmentation during ionization is important. In electron ionization and electro spray ionization mass spectrometry compounds fragment greatly and the fragmentation pattern can be used to identify the chemical responsible. However, when analysing a mixture rather than individual compounds, fragmentation can make identification of the compounds present in the mixture complex. Two important soft ionization methods are chemical ionization and photo ionization. In this work the principle ionization method was chemical ionization mass spectrometry, where the reaction utilised was protonation of VOCs by hydronium ions (H_3O^+) and hydronium ion clusters.

$$R + H_3O^+ \overset{k_{19}}{\leftrightarrow} RH^+ + H_2O \qquad\qquad (R2.3)$$

Where a species has a proton affinity far above that of water (690 kJ mol^{-1}) then the equilibrium between the protonated and deprotonated form will be far to the right

and collisions will in general result in protonation. For compounds where this is true, the proton transfer reaction rate coefficient (k_{19}) will be close to the collision limit. The ion molecule collision limit is dependent on the dipole moment of the molecule but is in general in the low 10^{-9} cm^3 s^{-1}.

One advantage of using this ionisation method is that the generally used backing gases: nitrogen, oxygen, helium, argon, have proton affinities far below that of water. In addition: chlorine (Cl_2), ozone (O_3), and hydrogen peroxide (H_2O_2), have proton affinities below that of water meaning they will not be ionised. The inability of the technique to detect the species that are generally present in vastly higher concentrations (backing gases) and high concentrations (radical precursors and ozone) means that measurements can usually be made without any requirement for pre-concentrating or separation.

Where the proton affinity of the compound and water are similar (e.g. formaldehyde 718 kJ mol^{-1}) then the position of the equilibrium will depend on the relative concentrations of the species and of water. This can lead to a humidity dependence of the protonation and as such, this can mean that detection of certain compounds (e.g. formaldehyde) can be limited under most reactor conditions.

For most reactor conditions and when sampling high relative humidities, an additional complication to protonation can occur through the presence of water clusters. Water can cluster to hydronium (H_3O^+) ions to form protonated water dimer, trimer and tetramers. Where these clusters are present some protonation of VOCs will occur via reaction with these clusters and the rate of protonation from the clusters (k_{37} reaction with protonated water dimer, and k_{55} transfer from protonated water trimer) tend to be slower. For compounds where their proton affinity is between that of water (690 kJmol^{-1}) and water dimer (808 kJ mol^{-1}) the influence of water cluster will further complicate the protonation of the VOC as these collisions will be deprotonating as opposed to protonating reactions.

$$R + (H_2O)_n H_3O^+ \xleftrightarrow{k_{37}, k_{55}} RH^+ + (H_2O)_{n+1} \qquad \text{(R2.4)}$$
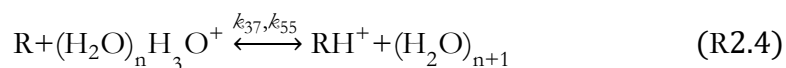
Further reactions can occur through the transfer of hydronium (H_3O^+) as opposed to protons (H^+) occurring leading to ionised masses 18 mass units (amu) higher than the protonated VOC. Formation of water clustered to protonated VOCs can also

occur where water molecules cluster to protonated species as opposed to from the transfer of protonated water clusters.
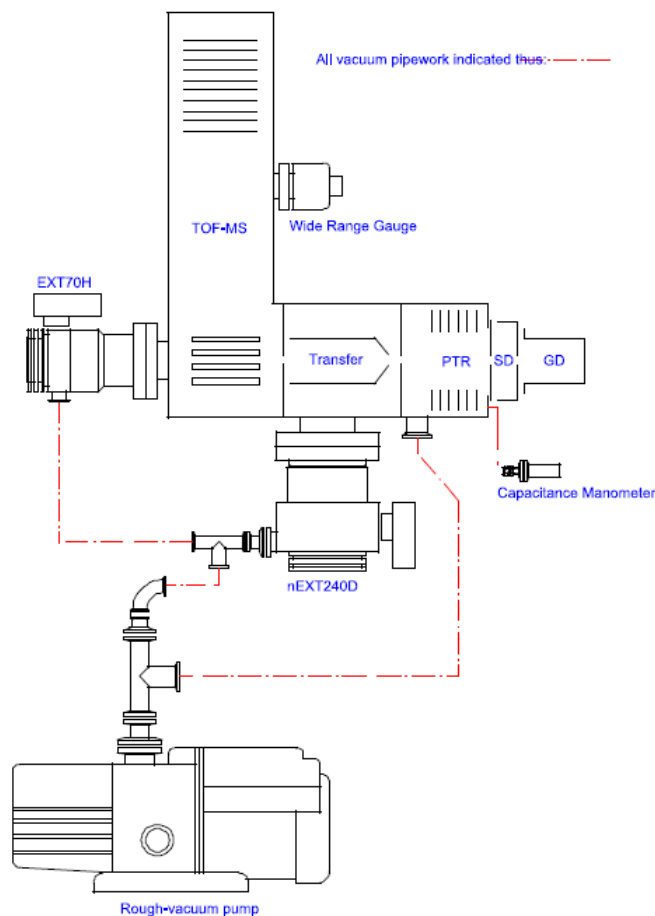
Figure 2.21 A schematic of the KORE mk I PTR-TOF-MS, the different sections are labelled in blue, and the external pipework for gas flows are depicted by the dashed red lines. Figure taken from the KORE hardware reference guide. (29)

In the KORE mk I PTR-TOF-MS which is shown as Figure 2.21, the hydronium ions are formed in a discharge of water vapour within a hollow cathode source (glow discharge –GD region). Following the glow discharge, the ion beam passes through a source drift (SD) region that allows for collisions between water molecules and any unwanted ions formed in the discharge (O^+, H^+, H_2^+, OH^+, N^+, N_2^+) before entry into the discharge. These collisions allow for charge transfer and proton transfer to occur and ensure that the output ions to the PTR reactor is almost exclusively H_3O^+ ($\approx$99.5 %).(29) The source drift and the PTR reactor are shown in Figure 2.22.
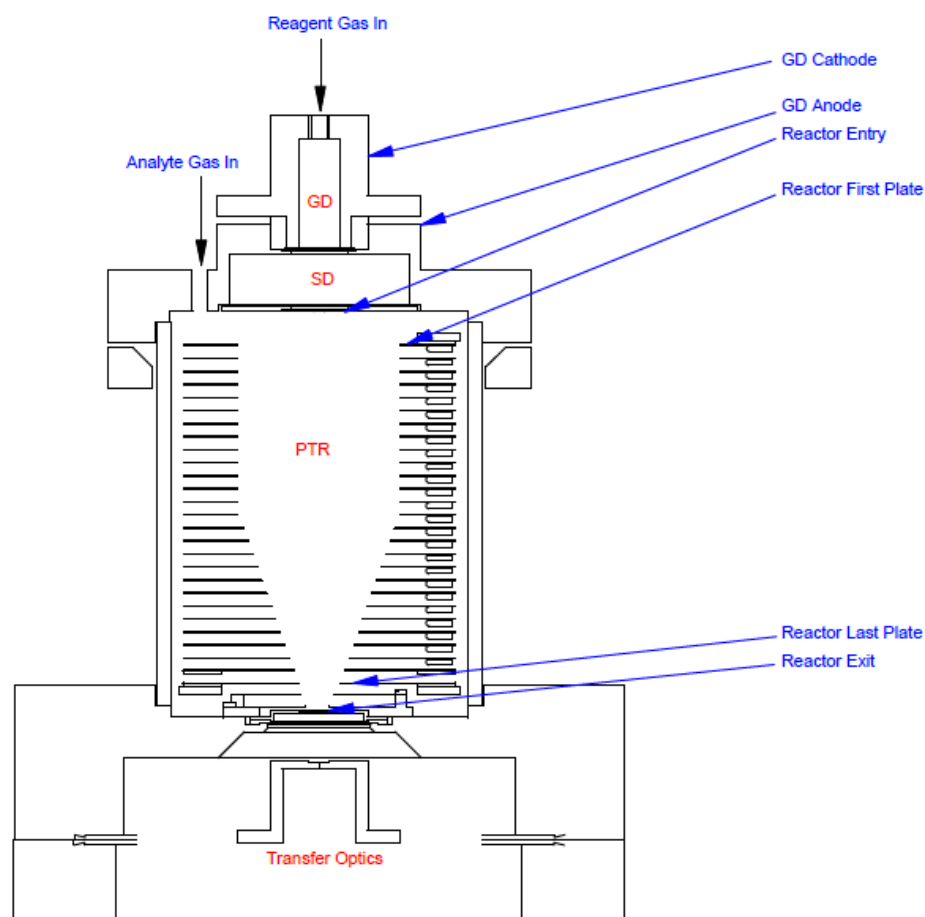
Figure 2.22 A schematic of the section of the KORE PTR-TOF-MS that is housed within an oven, the sections are labelled in red. Figure taken from the KORE hardware reference guide. (29)

From the source drift, the flow from the discharge continues through a voltage gradient into the PTR reactor which is maintained at a low pressure (0.5 - 4.0 mbar) via a rotary pump attached to the PTR exit. The voltage gradient is maintained between the SD exit and the PTR entry and reduces the back diffusion of analyte from the PTR reactor into the SD. A potential difference between the reactor entrance and reactor exit directs the ion flow along the reactor. The analyte is added parallel to the glow discharge and at low pressures diffusion into the flow from the discharge region is fast allowing for reactions between hydronium ions and VOCs from the analyte to occur.
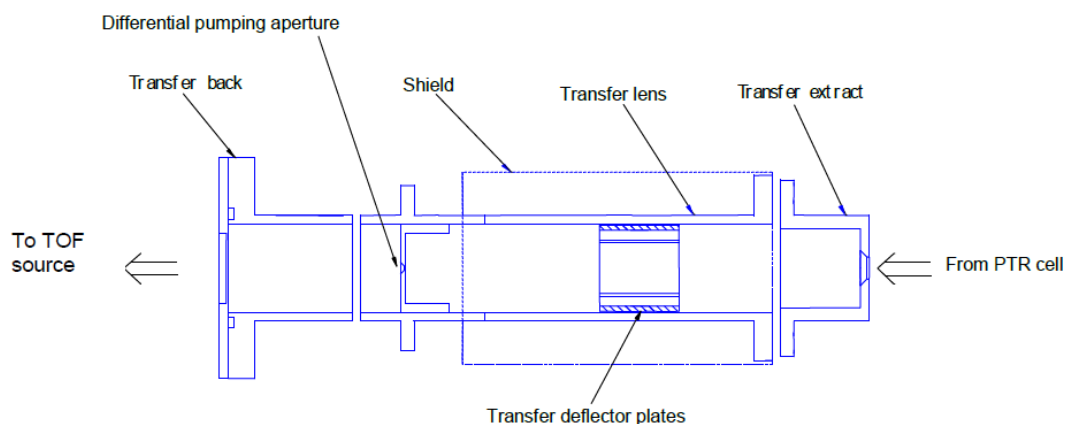
Figure 2.23 The transfer optics take the output of the PTR reactor and produce a stream of ions directed at the TOF source.The PTR is sampled though a slit and the output of the transfer region passes through a differential pumping aperture allowing for an intermediary pressure to be maintained between the high pressures in the PTR reactor and the high vacuum maintained in the TOF. Figure taken from the KORE hardware reference guide. (29)

The output of the PTR reactor is sampled by the transfer optics, shown in Figure 2.23. which provide the link between the PTR reactor and the TOF source. The transfer optics contain a differential pumping aperture and sample the PTR reactor through a 1 mm aperture, this allows for changes in pressure between the high pressures in the PTR reactor (0.5 – 4 mbar) and the high vacuum of the TOF ($1 - 10 \times 10^{-7}$ mbar) to be achieved via the intermediary pressure region. In addition, the lenses contained within the transfer region direct a divergent output from the PTR reactor into the TOF source, whilst actively selecting charged ions over neutrals.

When the ions arrive at the TOF source, they are travelling orthogonal to the direction of travel in the TOF, Figure 2.24. The TOF source provides a pulsed output of ions to the TOF from the continuous ions stream from the transfer region, and changes the direction of travel of those ions. The TOF source comprises a back plate and a pulsed extractor plate, with two further charged plates (intermediate electrode (Inter), FFR) that provide impetus to the ion beam as it is accelerated into the TOF.

Two pairs of electrodes (deflectors) in the X and Y direction then achieve corrections to the direction of travel for the ions as they leave the source. These are required to counteract the velocities that ions have when they arrive at the source. The deflectors have a fixed voltage (FFR) and variable voltage plate (X def / Y Def); the variable voltage plates were optimized to produce the largest signal on the detector.

78
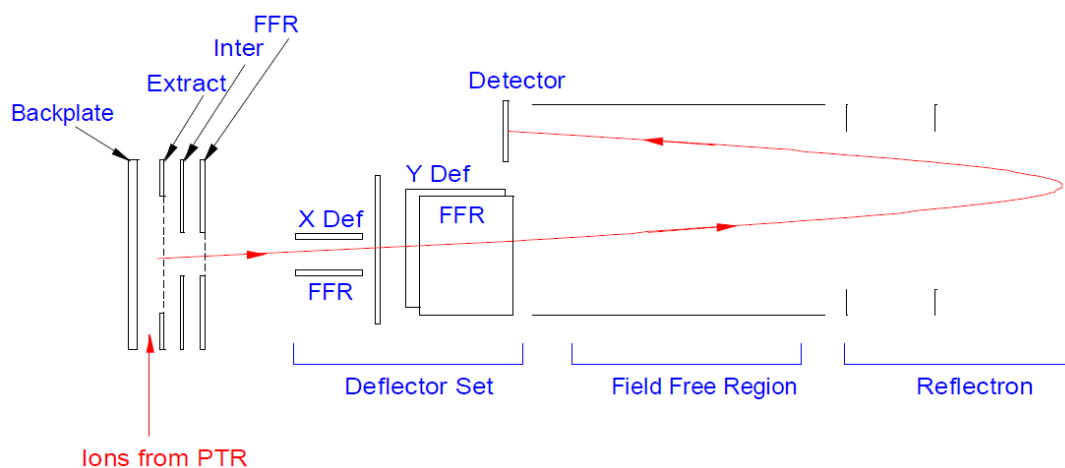
Figure 2.24 A depiction of how an orthogonal TOF coupled to a reflectron can be used to sample the continuous output of the PTR reactor.The ion flows are shown in red, where X and Y are used X refers to direction in line with the detector and Y refers to movement in the plane orthogonal to the detector. Figure taken from the KORE hardware reference guide. (29)

After being directed by the deflectors ions pass into the field free region (FFR), where the ions beam is not interacted with externally. Flight through the field free region is where the mass distribution in travel times occurs. Ions pass through the FFR twice being slowed and returned through the FFR by the reflectron before they strike a dual micro-channel plate detector (MCP). MCP detectors are ideal for measuring arrival times with high time resolution; however, they can suffer from overload effects whereby if two ions arrive close enough in time only one may be counted. It takes 4-8 ns for an individual ion to be counted so if two ions arrive within this window only one signal count is outputted.

$$mass = \left(\frac{t - t_0}{Cb}\right)^2 \qquad Equation\ 2.3$$

Arrival times at the MCP detector can be converted into mass using Equation 2.3, t_0 and Cb are calculated from the arrival times of known peaks in the time spectra and can be automatically generated using the KORE software's calibration routine. A full TOF cycle takes 40 microseconds with the average peak width covering 70-90 ns; in general, multiple TOF cycles are recorded and the signals at each point are summed over multi second timescale to produce higher sensitivity mass spectra.

When multiple spectra are taken as a series, the evolution of particular mass windows can be defined and this can allow the instrument to be used for kinetic

measurements. In general, when used to measure the time evolution of a mass peak this was performed with sampling frequencies between 10 and 60 s, higher time resolution was possible, but this produces lower sensitivity due to a reduction in counts above the background, and smaller changes in counts with fewer TOF cycles.

2.3.2 Generating absolute concentrations from PTR-TOF-MS

For direct kinetic measurements or for the calculation of product yields, and any other situation where absolute concentrations are required, then it is preferable that the signal from the PTR-TOF-MS is calibrated. Where calibration is not possible, but the proton transfer reaction rate coefficients are known, it is possible to use these to accurately define the concentrations measured. One point that should be noted is that, where concentration has been used, here it is actually more accurate to describe mixing ratios. The responses measured by the PTR-TOF-MS are independent of the pressure of the gas being sampled provided the same PTR reactor pressure is maintained and as such concentrations are not measured, mixing ratios are measured.

Where direct calibrations of peak masses are used, a plot of peak response against mixing ratio can allow for the assignment of responses where the mixing ratio is unknown. In general, this response is linear above the limit of quantification until the detection of that mass peak begins to become overloaded. Where a parent mass peak becomes overloaded it is possible to use the presence of isotope peaks to assign the mixing ratio experienced. Where the H_3O^+ concentration is severely depleted the response of isotope peak against mixing ratio may become non-linear and as such under these conditions it would not be possible to accurately define concentrations purely by extrapolation of a linear calibration plot.

It should additionally be noted that because of the sensitivity of both the fraction of a VOC protonated and the fragmentation of the VOC to the 'collision energy', water concentration and reactor pressure, calibrations are only accurate for specific sets of reactor conditions, and are only accurate for some VOCs for a given relative humidity of the sampled gas.

Where calibrations are not possible it is possible to calculate the fraction of a given compound that will be protonated from the concentration of water monomer, dimer and trimer and their individual protonation rate constants. When the fraction protonated is

coupled with mass transfer curves for the TOF and the branching ratio for the individual fragments formed following protonation, it is possible to assign concentrations in the absence of a calibration. Although the accuracy can be improved by linking this to calibration experiments.

2.3.3 Setting reactor conditions

Setting the reactor conditions required optimizing them for a given experiment, for experiments sampling from chambers in general this required maximising the overall signal response. This was because in typical chamber studies, the reagent of study or reagents of study and the products tend to be in similar concentrations and as such unless many compounds fragment to similar masses, raw signal response is more important than reducing fragmentation.

The standard conditions used for most chamber experiments were: a PTR reactor pressure of 2.0 mbar, a potential difference of 400 V, with a PTR reactor temperature of 100 °C. These conditions led to a typical collision energy of 100 Td, this was coupled to a water flow that was low enough to only produce a minor water trimer peak (<500 counts in 18 seconds). Collision energy is measured in Townsends (Td) which is a measure of the reduced electric field (E/N) across the PTR reactor; in SI units a Td is equal to 1×10^{-21} V m^2.

For experiments carried out under pseudo first order conditions fragmentation minimization and reducing the background of product peaks became more important than raw signal intensity. For these situations reactor conditions were often set to much lower collision energies and much higher flow rates of water than for typical chamber experiments. Greater detail on these requirements is covered in the experimental developments chapter (3.2.1).

Where conditions were modified from those typically used for chamber experiments the method used was generally the same. Two peaks of interest would be selected, one representing a positive peak to be maximised and one a negative peak caused by a side reaction that was to be minimised, the entry voltage would then be adjusted to find an optimal setting with respect to the two peaks and the results would be noted, and an example spectrum would be taken, the water flow would then be adjusted up and the process of adjusting voltages would be performed again. Giving a range of optimal water

flow and entry voltages, this would then be repeated for different reactor pressures, from the spectra collected over all these conditions the best conditions could be assigned. For a given reaction e.g. OH and n-butanol the optimum reactor conditions could depend on which product was being studied and it was possible for several sets of conditions being used to study the same reaction where each condition provided different information.

2.3.4 Summary of PTR-TOF-MS

PTR-TOF-MS provides a soft ionisation method that is sensitivity to a wide variety of VOCs, in particular oxygenated VOCs. The technique can measure the time evolution of multiple species on the multi second timescale; this allows the technique to be used in atmospheric measurements and kinetic experiments. Where PTR-TOF-MS is used for relative rate studies then no calibration is required, for direct kinetic, and atmospheric measurements the peak responses can be calibrated or assigned in theory from the protonation kinetics.

2.4 References

1. MEDEIROS, D.J., M.A. BLITZ and P.W. SEAKINS. Exploring the features on the OH + SO$_2$ potential energy surface using theory and testing its accuracy by comparison to experimental data. *Physical Chemistry Chemical Physics*, 2018, **20**(13), pp.8984-8990.

2. DUNLOP, J.R. and F.P. TULLY. A kinetic study of hydroxyl radical reactions with methane and perdeuterated methane. *The Journal of Physical Chemistry*, 1993, **97**(43), pp.11148-11150.

3. BLITZ, M.A., R.J. SALTER, D.E. HEARD and P.W. SEAKINS. An Experimental and Master Equation Study of the Kinetics of OH/OD + SO$_2$: The Limiting High-Pressure Rate Coefficients. *The Journal of Physical Chemistry A*, 2017, **121**(17), pp.3184-3191.

4. MEDEIROS, D.J., M.A. BLITZ, L. JAMES, T.H. SPEAK and P.W. SEAKINS. Kinetics of the Reaction of OH with Isoprene over a Wide Range of Temperature and Pressure Including Direct Observation of Equilibrium with the OH Adducts. *The Journal of Physical Chemistry A*, 2018.

5. GOULD, R.G. The LASER, light amplification by stimulated emission of radiation. *In: The Ann Arbor conference on optical pumping, the University of Michigan*, 1959, p.128.

6. EINSTEIN, A. Strahlungs-emission und-absorption nach der Quantentheorie. *Verhandlungen der Deutschen Physikalischen Gesellschaft.*, 1916, **18**, pp.318-323.

7. EINSTEIN, A. Zur quantentheorie der strahlung. *Physikalische Zeitschrift*, 1917, **18**, pp.121-128.

8. SIEGMAN, A.E. Laser beams and resonators: the 1960s. *IEEE Journal of Selected Topics in Quantum Electronics*, 2000, **6**(6), pp.1380-1388.

9. MAIMAN, T.H. Stimulated Optical Radiation in Ruby. *Nature*, 1960, **187**(4736), pp.493-494.

10. GEUSIC, J.E., H.M. MARCOS and L.G.V. UITERT. LASER OSCILLATIONS IN Nd-DOPED YTTRIUM ALUMINUM, YTTRIUM GALLIUM AND GADOLINIUM GARNETS. 1964, **4**(10), pp.182-184.

11. BENNETT, W.R. Gaseous Optical Masers. *Applied Optics*, 1962, **1**(S1), pp.24-61.

12. BASOV, N., V. DANILYCHEV, Y.M. POPOV and D. KHODKEVICH. Laser Operating in the Vacuum Region of the Spectrum by Excitation of Liquid Xenon with an Electron Beam. *Soviet Journal of Experimental Theoretical Physics Letters*, 1970, **12**, p.329.

13. SAVAGE, A. and R.C. MILLER. Measurements of Second Harmonic Generation of the Ruby Laser Line in Piezoelectric Crystals. *Applied Optics*, 1962, **1**(5), pp.661-664.

14. BOYD, R., W *Nonlinear Optics*. 3rd ed. Oxford, UK: Academic Press, 2008.

15. SOROKIN, P.P. and J.R. LANKARD. Stimulated Emission Observed from an Organic Dye, Chloro-aluminum Phthalocyanine. *IBM Journal of Research and Development*, 1966, **10**(2), pp.162-163.

16. SCHÄFER, F.P., W. SCHMIDT and J. VOLZE. ORGANIC DYE SOLUTION LASER. *Applied Physics Letters*, 1966, **9**(8), pp.306-309.

17. SOFFER, B.H. and B.B. MCFARLAND. CONTINUOUSLY TUNABLE, NARROW-BAND ORGANIC DYE LASERS. *Applied Physics Letters*, 1967, **10**(10), pp.266-267.

18. SHANK, C.V. Physics of dye lasers. *Reviews of Modern Physics*, 1975, **47**(3), pp.649-657.

19. PHYSICS, S. Precision scan - Amplified pulsed dye lasers. *sirah data sheet*, 2010, pp.1-4.

20. TKACHENKO, N.V. Chapter 7 - Flash–photolysis. *In:* N.V. TKACHENKO, ed. *Optical Spectroscopy*. Amsterdam: Elsevier Science, 2006, pp.129-149.

21. PORTER, G. Flash Photolysis and Spectroscopy. A New Method for the Study of Free Radical Reactions. *Proceedings of the Royal Society of London. Series A, Mathematical and Physical Sciences*, 1950, **200**(1061), pp.284-300.

22. PORTER, G. and M.R. TOPP. Nanosecond flash photolysis. *Proceedings of the Royal Society of London. A. M athematical Physical Sciences*, 1970, **315**(1521), pp.163-184.

23. MCCLUNG, F.J. and R.W. HELLWARTH. Giant Optical Pulsations from Ruby. 1962, **33**(3), pp.828-829.

24. LI, A.D. and W.C. LIU. 4 - Optical properties of ferroelectric nanocrystal/polymer composites. *In:* S.C. TJONG and Y.W. MAI, eds. *Physical Properties and Applications of Polymer Nanocomposites*. Woodhead Publishing, 2010, pp.108-158.

25. TARASOV, L.V. *Laser physics and applications.* Moscow: Mir Publishers, 1986.

26. KOECHNER, W. and M. BASS. *Solid-State Lasers: A Graduate Text.* Springer, New York, NY: Springer 2006.

27. LEKAVICH, J. Basics of acousto-optic devices. *Lasers and Applications*, 1986, pp.59-64.

28. STONE, D., M. BLITZ, T. INGHAM, L. ONEL, D.J. MEDEIROS and P.W. SEAKINS. An instrument to measure fast gas phase radical kinetics at high temperatures and pressures. *Review of Scientific Instruments*, 2016, **87**(5), p.054102.

29. KORE. *Hardware Reference Unipolar Vertical PTR-TOF Mass Spectrometer.* Unpublished, 2015.

3 Experimental developments

3.0 Outline of chapter 3

The OH/HO$_2$ apparatus was characterized by measuring yields from the reactions of OH with H$_2$O$_2$ (1:1 link between OH and HO$_2$), with C$_2$H$_4$/O$_2$ (where secondary chemistry can generate HO$_2$), with C$_2$H$_6$/O$_2$ (where there should be zero HO$_2$ yield) and with CH$_3$OH/O$_2$ (where there is a well-defined HO$_2$ yield which depends on the amount of oxygen present). Transport effects on the observed HO$_2$ and OH kinetics were analyzed for the effect transport has on the accuracy of the assignment of rate coefficients. Where OH is detected on the first detection axis, it has been shown that it is possible to accurately measure OH pseudo-first-order loss processes up to ~150,000 s^{-1}. From the second detection axis, transport significantly impacted the observed kinetic parameters, and therefore, first order rate coefficients for HO$_2$ formation could only be assigned accurately for values of less than 1000 s^{-1}. Never the less, this limited degree of temporal resolution can help to distinguish between primary and secondary HO$_2$ production.

Issues arise measuring the temperature of gases in a flowing system, and this was amplified when the reaction being studied was sampled through a pinhole. The temperature dependence of the well characterized reaction of OH and methane was used to assign the temperature of the reaction zone over a range of conditions which could be parameterized as: Temperature (K)= $((-1.6954 \times 10^{-6}) \times V^4) + ((3.9967 \times 10^{-4}) \times V^3) - ((1.1703 \times 10^{-2}) \times V\wedge2) + ((0.90968) \times V) + 25.002)$, where V was the voltage applied from the variac.

The importance of minimizing non-proton transfer ionization (ionization by H$_2$O$^+$, OH+, O+, O++) by the use of more linear flow regimes in TOF-PTR-MS reactors has been demonstrated. The importance of minimizing such ionization has been shown to be of key importance when there are high reagent to product-species ratios. For some experiments (i.e. experiments on small carbonyls carried out in EUPHORE), the approach for minimizing analyte fragmentation led to insufficient sensitivity, and in these cases reactor conditions with lower water flows and higher collision energies were used.

3.1 Introduction

The final experimental setups described in Chapter 2 were the result of several iterations; developments towards reaching the final designs and operational modes will be

described in this chapter. The process that was developed for the assignment of temperatures will be outlined, and PTR-MS reactor conditions and the placement of NO injection for the titration of HO_2 to OH will be detailed.

3.1.1 Modification of the KORE TOF-PTR-MS to sample high concentrations and low pressures.

Conventional use of a TOF-PTR-MS has focused on conditions that maximize raw signal, which is key for detection of VOCs from ambient air where concentrations are typically in the pptv – ppbv range. When used to sample chambers, where, in general concentrations are higher (ppbv - ppmv) the limit of detection (LOD) can become less important. When sampling from experiments running in a manner used to make direct kinetic measurements, the concentrations are higher still. Under these conditions detecting the raw signal becomes trivial; signal to noise and fragmentation become the limiting factors. When sampling from low-pressures (< 400 mbar), there was insufficient backing pressure to maintain adequate PTR reactor pressures. As such, the original instrument was postproduction modified in Leeds with the assistance of KORE, in order to sample from pressures as low as 40 mbar.

3.1.2 The importance of understanding temperature in a flowing system.

The layout of the high-pressure apparatus provides challenges for the accurate measurement of the temperature at which the reaction occurs; for reactions occurring on a millisecond timescale, the relevant reaction distance from the sampling pinhole is approximately 0.05 - 0.5 mm. Compared with a conventional slow flow laser flash photolysis/laser induced fluorescence (LFP-LIF, PLP-LIF) apparatus, where the reaction volume is the overlap of the perpendicular photolysis and probe laser beams, it is difficult to accurately position the thermocouple, and additionally, any thermocouple located close to the sampling pinhole may affect the flow into the low pressure system.

Alongside the difficulties associated with accurately siting a thermocouple (unlike in a quasi-static cell), there are additional errors – kinetic, conduction and radiative – which derive from measuring the temperature of a flowing gas with a thermocouple. Additional experiments were therefore performed to determine the temperature, based on the well characterized and temperature sensitive reaction of OH and methane.

When the original high-pressure setup was commissioned, as described in Stone et. al., (8) work was performed to assess the axial temperature gradient present in the high-

pressure system. This was performed both with and without the use of a preheater, before the final coil heated section. In this work, errors in temperature due to axial temperature gradients were assessed as being minor and as such, the use of a thermocouples sited perpendicular in the flow was sufficient to assign the temperature at which the measured reaction occurred.

For most bimolecular reactions, even where there is an observable temperature dependence, the bimolecular removal rates tend to differ by less than an order of magnitude over the range 300 – 700 K. For processes such as these, a small error in the temperature (< 5 %) tends to produce an even smaller error in the observed rate coefficient well within the normal experimental error bounds; experimental errors in bimolecular removal rates are typically 5 - 10 %.

When intramolecular processes occur after the initial OH reaction, these processes have much higher activation energies and hence a greater sensitivity to temperature. For a typical decomposition reactions of an alkyl (R) or alkyl peroxy (RO$_2$) radical, or for systems where OH can be returned from an adduct well for example OH and ethylene or OH and isoprene, the rate at which OH is returned can vary significantly with the temperature between 300 and 700 K. For many of the systems of interest there is little or no observed OH returned at over 2 bar and at 300 K. As the temperature of the reaction is increased the return rate also increases; as these processes often require passing over a barrier to OH reformation they can often display an Arrhenius type dependence. (9)

Where the dependence of a rate coefficient is exponential with respect to changes in temperature, a small error in assigned temperature can lead to a much greater error in the expected OH return rate. A major intention of the use of the high-pressure system is to study reactions of importance for low temperature combustion, and understanding these reactions involves defining the temperature dependence of OH recycling and OH chain branching processes. It is of crucial importance, therefore, that the temperature at which OH recycling is observed can be defined with a high degree of accuracy. Where the errors that come from assigning temperature from a distantly sited thermocouple become significant, alternative methods, including chemical thermometers, become important.

3.1.3 Development of the high-pressure reactor for detecting OH and HO_2

The project involved the development of an instrument to simultaneously detect OH and HO_2 radicals. The study of OH and HO_2 is of importance to the modelling of both atmospheric and combustion chemistry, as has been described in the introductory chapter (Chapter 1 section 1). (1, 2) Many atmospheric and combustion reactions in the presence of oxygen lead to the generation of peroxy-radicals (RO_2). For certain RO_2 there is a potential to generate OH and HO_2 on a fast timescale, and for others OH and HO_2 will be produced on a slow timescale. Therefore, for some species, RO_2 radicals can provide an interference for the observed HO_2 yields, especially when the HO_2 yield is assigned by chemical transformation. Three well known reactions were chosen to characterize the instrument, OH and ethane (R3.1), OH and ethylene (R3.2), and OH and methanol (R3.3):

$$OH + C_2H_6 \rightarrow H_2O + C_2H_5 \tag{R3.1}$$

$$OH + C_2H_4 \rightarrow HOC_2H_4 \tag{R3.2}$$

$$OH + CH_3OH \rightarrow H_2O + CH_2OH, CH_2OH + O_2 \rightarrow HO_2 + HCHO \text{ (fast)} \tag{R3.3a, R3.4}$$

$$OH + CH_3OH \rightarrow H_2O + CH_3O, CH_3O + O_2 \rightarrow HO_2 + HCHO \text{ (slow)} \tag{R3.3b, R3.5}$$
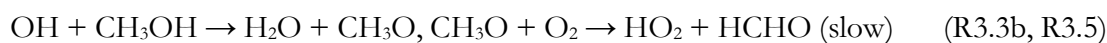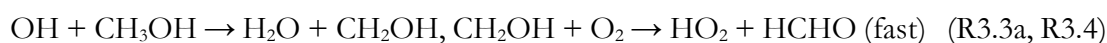
OH and ethane (R3.1) gives an assessment of any false HO_2 yields generated from RO_2 and NO from prototypical alkyl based RO_2 species that will be formed from many atmospherically relevant reactions. Ethylene and OH (R3.2) forms a hydroxy alkyl peroxy radical – the typical RO_2 species known to create interferences in FAGE HO_2 detection systems (3-5). Understanding, and thereby minimizing, the HO_2 yield from this reaction allowed for limits to the selectivity of the instrument to be determined. The kinetics and branching ratio for the reaction of OH with methanol is a well understood; (6, 7) the two isomeric radical products react with oxygen on differing timescales to generate HO_2. Complete conversion of both isomers should yield to 100 % HO_2.

Transport effects after the breakup of the sampling jet mean that rate coefficients measured in the second cell $k_{X,2nd,}$ (X = OH or HO_2, differ from each other (transport effects scale with mass) and from those made in the first detection axis ($k_{OH,1st}$). Pseudo-first-order rate coefficients from the two detection axes are compared to ascertain whether measurements in the second detection axes can be used to make quantitative kinetic measurements.

3.2 Instrument Development

3.2.1 Developing PTR reactor conditions, and sampling methods
3.2.1.1 Sampling from the high-pressure system

When setting up the KORE PTR-MS to sample from the time resolved kinetic experimental bays, initial work was performed sampling from the high-pressure apparatus. Sampling from this experiment was selected as the above atmospheric pressure of the output was not significantly different from sampling from the atmospheric pressure for which the instrument was initially designed.

Early work was performed at the manufacturer's advised sampling conditions; these had PTR reactor conditions of 100 °C and 0.5 mbar, with the minimal flow of water added that allowed for a sustainable discharge to occur. The PTR voltages were then modified to vary the 'collision energy' (CE). When run under these conditions, excellent responses were produced for the peaks of interest; however, even for relatively simple systems it was clear the fragmentation could be significant.

To evaluate the ability of this system to assign product yields, the reaction of OH and methanol in the presence of oxygen was initially chosen (R3.3-3.5). Under these conditions, only the minor reaction of OH with the OH precursor would not lead to the formation of formaldehyde. The photolysis energy and hydrogen peroxide concentration were known and hence the experimental OH concentration could be calculated from Equation 3.1.

$$[OH] = \left(2 * \left(\frac{k_{obs}}{1.7E-12}\right) * \left(\frac{Energy * 2.48E-5}{h*c}\right) * 8.6E-20\right) cm^{-3} \quad Equation\ 3.1$$

Combining the OH concentration with a calibration plot (response against formaldehyde concentration), the potential accuracy of using the PTR-TOF-MS for assigning product yields could be assessed. For the experimental validation of PTR-MS product measurements in practice, a second reaction of OH and ethanol, with a calibration plot of acetaldehyde, was used. The selection of OH and ethanol was due to the greater ease of producing known concentrations of acetaldehyde for a calibration plot compared with formaldehyde although the fraction of reaction leading to acetaldehyde is slightly <1.

The PTR-MS system was designed with the measurement of trace species as its primary objective where the absolute signal is the most important factor governing the

limit of detection (LOD) and the limit of quantification (LOQ). LOD and LOQ are the key characteristics by which analytical instruments are compared. Measuring from the kinetic reactors utilized here, however, the reagent of study (RH) is usually maintained under pseudo first order conditions with respect to the OH concentration. This means that the concentration of products formed can often be a 100th to a 10000th of the concentration of the added reagent of study. When a product mass coincides with a fragmentation or feature in the mass spectrum due to the presence of the reagent of study, the proportional change in the peak area could be so small as to leave the instrument blind to this.
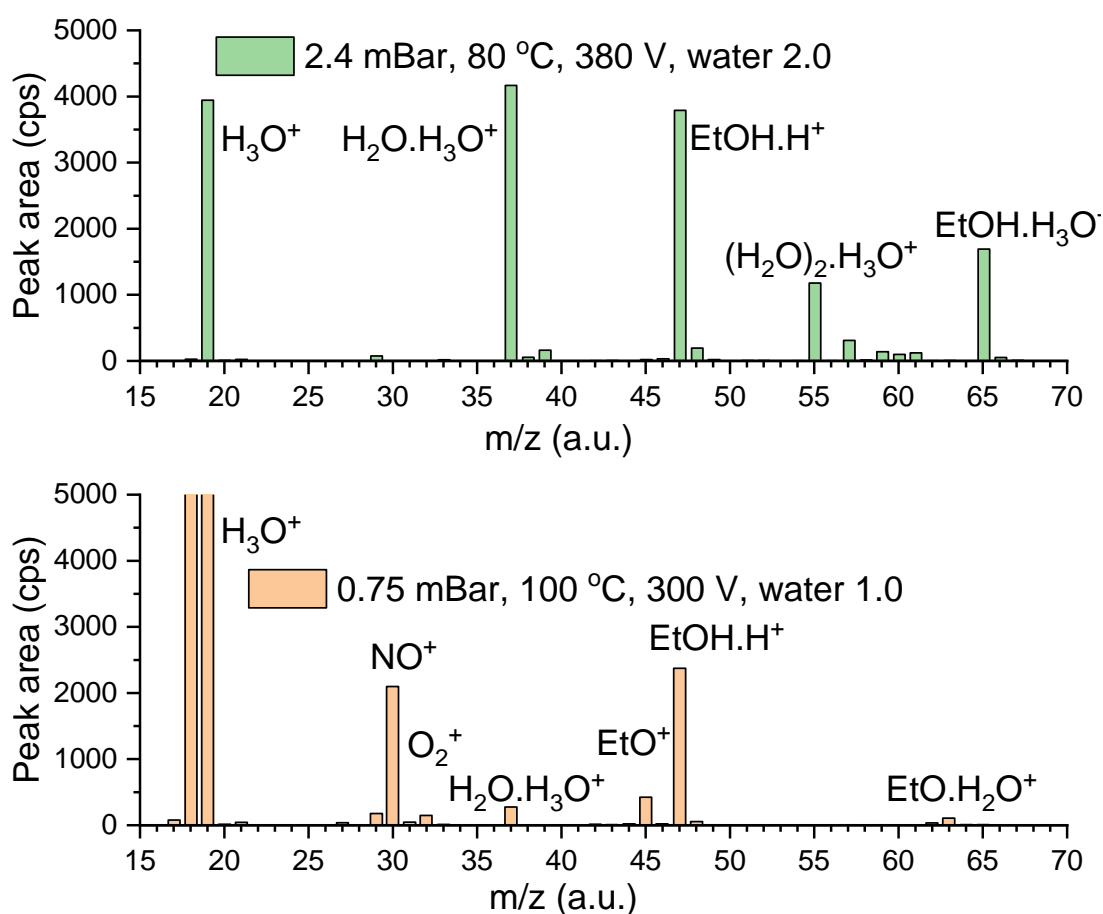
Figure 3.1 Shows PTR-TOF-MS spectra obtained from sampling the high-pressure system, where the ethanol concentration was 2.5×10^{14} molecule cm^{-3} at 2 bar with 10 SLM of nitrogen. The upper spectrum, green, was obtained at higher PTR pressures and water flows and shows minimized fragmentation at *m/z* 45 than the lower trace. The lower trace, orange, was obtained at 0.75 mbar and a lower flow of water shows significant formation of *m/z* 45 assigned to back streaming of sample gas into the discharge region.

For the reaction of OH and ethanol producing acetaldehyde, the parent ethanol peak is m/z 47 ($CH_3CH_2OHH^+$) and the parent mass of the product acetaldehyde peak is m/z 45 (CH_3CHOH^+). When only ethanol was added in a backing gas of nitrogen, a significant peak at m/z 45 was present on the spectrum. The m/z 45 peak was present without an OH precursor and without photolysis occurring. Minimization of this peak was possible by varying the collision energy, but it was still over 5 % of the parent ethanol peak, even with the lowest collision energies for which a discharge could be maintained at 0.5 mbar. An example spectrum showing a significant fragmentation peak is present is shown in Figure 3.1, where the spectra was taken at 0.75 mbar. In Figure 3.1 the notation describing how much water was added to the PTR reactor defined a flow of 1 as the point at which sufficient water was added to maintain a constant discharge.

Although improvements on the initial setup were made to reduce fragmentation, the observed fragmentation peak was still far greater than the expected product peak would be. In the 0.75 mbar spectrum, the m/z peak at 45 from the discharge ionization was 19 % of the height of the m/z 47 peak from the proton transfer ionization of ethanol. A background signal of 19 % when product formation would be expected to be under 1 % meant the background would make product quantification difficult.

The cause of the observed fragment ion needed to be established. The formation of an ion at m/z -1 was not caused by the well-established fragmentation, found in long chain alcohols (propanols, butanols etc), at m/z -17. [10, 11] In alcohols, the fragmentation at m/z -17 occurs through the loss of water following protonation,[12] and a different mechanism was required to produce a fragment at m/z -1.

It was not apparent how forming m/z -1 was caused by fragmentation of excited protonated ethanol. Additionally, charge transfer chemistry was invalidated as being the source of the observed fragmentation, because this would not lead to the formation of a mass, one unit down from ethanol, even if charge transfer between ethanol and H_3O^+ occurs.

The conclusion arrived at was that this observed peak was created in the discharge itself. The fragment was either being produced from ethanol directly, or else, formed close to the discharge by ionization from species other than H_3O^+, through the loss of a hydride ion. In a hollow cathode discharge of water, H_2O^+, OH+, O+, O++ are formed.[13]

These species rapidly react with water present in the flow, and their presence rapidly decreases with distance travelled.

Whether ionization to m/z 45 was assigned to direct ionization in the discharge, or by reaction with species other than H3O+ formed in the discharge, this peak was thought to provide evidence of analyte back-streaming into the discharge region. Back-streaming is a product of diffusion against the general direction of flow in the PTR reactor. Diffusion is greatly affected by pressure and so operating the instrument with a higher reactor pressure would reduce back-streaming. In addition, higher flow rates of water through the discharge would increase the linearity of the flow conditions in this region.

When operating at 3.0 mbar and significantly higher flows of water, the m/z 45 peak observed was less than 0.2 % of the parent ethanol peak, which was assigned by comparison to the O^{18} isotope peak of ethanol (m/z 49). From this observation, it was apparent that back streaming had been minimized. Operating under these conditions led to changes in the ratio of the water cluster peaks, with significant water dimer and trimer peaks and a small water tetramer peak present. Where significant water clustering was present, the protonation reactions could no longer be assumed to be have occurred solely with monomer H_3O^+.

Protonation of VOCs by water dimer is significant in PTRs run in this manner. In general these rate coefficients are less well known than those for monomer water protonation reactions. Where the specific rate coefficients were not available, the only method to accurately assign concentrations is through direct calibration. For some species, including formaldehyde (≈ 712.9 kJ mol^{-1}),[14] the proton affinity is below that of water dimer (≈ 808 kJ mol^{-1})[15] where this is true water will deprotonate rather than protonate the species of study, reducing the overall sensitivity.

Where PTRs are operated at high reactor pressures, dimerization of VOCs and complexation of water to protonated VOCs can be observed in significant amounts. Complexation and dimerization can lead to the formation of a wide variety of different clusters. The presence of many cluster peaks can generate complicated and difficult to interpret mass spectra, where in addition to the protonated parent mass peak (m/z X+1), m/z X+19, 2X+1, X+37 are also observed. If the cluster peaks fall on masses in the spectrum where product formation would not be expected, then even complex mass

spectra can allow for product assignment. Where cluster peaks fall on expected product masses this is not necessarily possible.

Where the difference in proton affinities of water monomer (≈ 690 kJ mol^{-1})(15) and the reagent of study are similar, the position of the equilibrium allowing for protonation is dependent on the water concentration. Formaldehyde is such a case, (proton affinity = 712.9 kJ mol^{-1});(14) an increase in water flow from the KORE initial conditions made the PTR method unsuitable for formaldehyde observation, because the equilibrium was shifted away from protonated formaldehyde. As discussed earlier, the presence of water dimer will also reduce the ability to form protonated formaldehyde. For our experiments, this meant that measuring formaldehyde formation from methanol reactions would not be possible; either formaldehyde was not protonatable, or else fragmentation of methanol close to the discharge blocked the formaldehyde peak.(16, 17)

For many other compounds, variation of the PTR pressures, voltages, and water flows, could be optimized to get maximum product formation and minimal parent compound fragmentation. These conditions varied, depending on the compound of interest and the products that were to be monitored. As such, lists of optimized parameters were kept for individual reactions.

A general method for optimizing conditions was developed; this involved monitoring the C^{13} peak of the parent ion, and an important product peak, whilst the collision energy was optimized. The reactor pressure and water flows would then be varied, where at each new pressure and water flow the collision energy would again be optimized. Once the product peak to parent mass ratio was minimized for each set of conditions, the relative ability to observe product formation was then tested. By comparing the spectra generated from these, an optimal set of conditions for a reaction could be assigned.

With respect to observation of acetaldehyde formation from the reaction of OH and ethanol, the best conditions determined were: a PTR pressure of 2.4 mbar, an oven temperature of 80 °C, with an entry voltage of 380 V, giving a 'collision energy' of 82 Td. An example spectrum taken under these conditions is given in Figure 3.1, where the flow of water was twice that required to maintain a discharge in the spectrum obtained at 0.75

mbar, with which it is compared. In this case, by comparison to the O^{18} peak, less than 0.2 % of the ethanol was ionized in the discharge region.

In the high-pressure system, it became clear that the axial temperature gradient, discussed in the temperature section later, would lead to a product spectrum encompassing a wide range of temperatures. A long pre-heater section that had been part of the earlier design (Figure 3.3), described in Stone *et al.* (4) had by now become defunct as it did not remove the temperature errors, but did increase the amount of precursor and reagent pyrolysis. This long section (60 cm) versus the short-heated region (20 cm), meant that room temperature experiments would dominate the observed products.
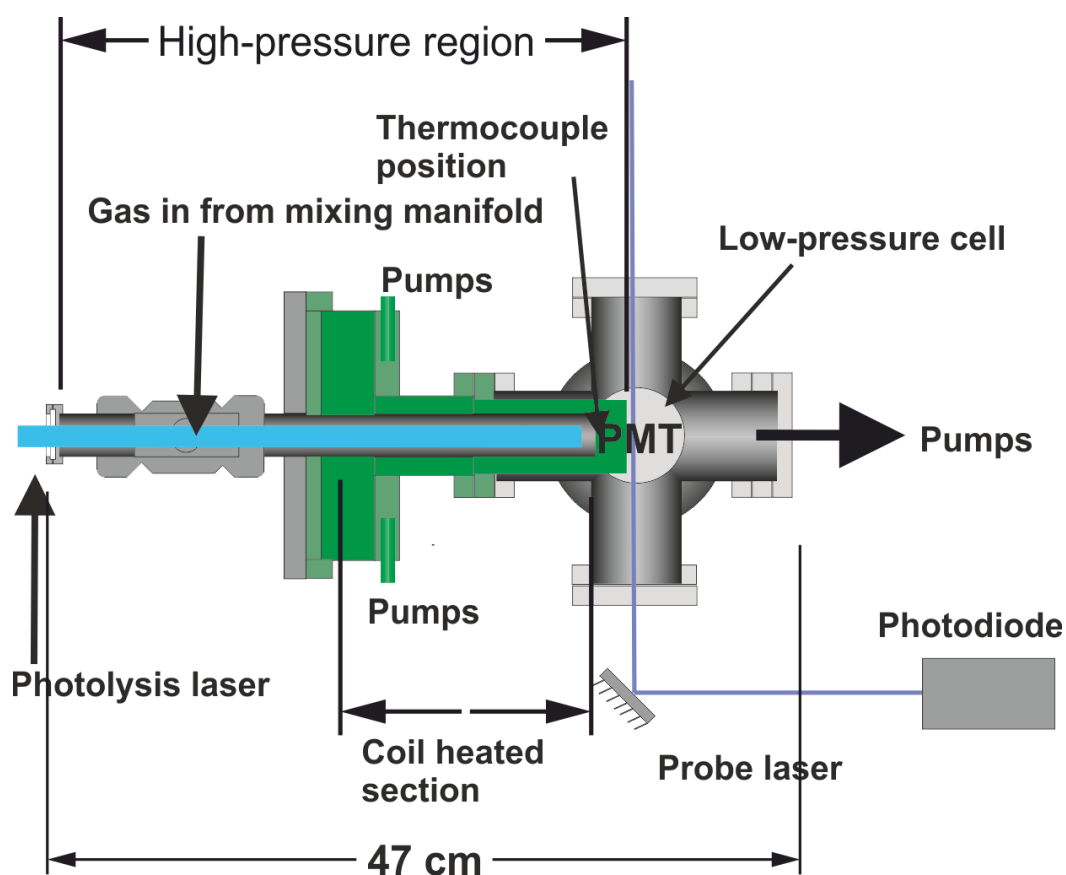
Figure 3.2 A schematic of the high-pressure system, once the pre heater had been removed. Removing the pre-heater allowed for a greater proportion of the PTR-MS sampled gas to have been photolysed whilst at an elevated temperature, when compared with the old system, Figure 3.3. The residence time in the shortened reactor is 1.4 seconds.

The now defunct pre-heating section was therefore removed; this led to a system, Figure 3.2 , which features a short section of coil heated stainless steel tubing lined with

glass, pinhole sampled by the FAGE OH cell, with the bulk of the gas flow then being sampled by the TOF-PTR-MS. Although this cannot completely remove the range of temperatures that are present in the product spectra, it vastly reduced the weighting towards room temperature products.

Reducing the weighting of lower temperature gas allowed for some assignment of changes to product spectra by temperature. The temperature at which a spectrum was collected, when given in the text, means the temperature at which the OH measurements were made not the specific temperature at which the observed masses were produced. Where new peaks appeared or old peaks reduced in size with temperature, qualitative assessments could be made of changes in product branching ratio with temperature.

3.2.1.2 Sampling from low-pressures and performing chamber studies

When sampling from conventional 'slow-flow quasi static' low-pressure cells by the PTR-MS, the ability to provide sufficient backing pressure to generate PTR pressures over 1.0 mbar required high pressures in the reaction cells (>250 mbar). Significant quenching of the OH LIF signal occurred when the reaction cells were operated at the pressures (> 400 mbar) required to generate the PTR reactor pressures (> 2.0 mbar) that prevent back-streaming.

To alleviate this issue, the sampling system in the PTR was redesigned and rebuilt, where direction and new components were provided by KORE. Installation of this modified system required replacement of the internal sampling system with wider bore parts. The previous sample valve was replaced with a manual valve that allowed for a wider range of valve positions than had been possible with the old system.

Once the new sampling system had been installed, PTR reactor pressures as high as 3.0 mbar were possible when sampling from <150 mbar. This allowed for simultaneous OH kinetics measurements and PTR-MS sampling to be carried out. Where simultaneous OH kinetics and PTR spectra were taken, any changes in observed masses with temperature could be used to deduce the presence of new reaction routes beginning to occur. For the reaction of OH and dimethyl formamide, Chapter 5, the appearance of a yield of imine product coincided with OH recycling beginning to occur, and verified that this was likely from the aldehydic abstraction site.

Beyond the scope of merely observing product formation, the PTR-MS sampling allowed verification of the presence of heterogeneous processes. This provided important

insight into complicated systems where OH kinetics differs greatly from those expected for OH and the reagent of study. Heterogeneous processes were observed both in the presence and absence of an OH precursor for many compounds. For amines, PTR-MS sampling provided additional observation of homogeneous gas phase acid base chemistry.

For some reactions carried out in the HIRAC chamber, similar PTR conditions were applied to those used for the high-pressure system. When the instrument was used at EUPHORE, the lower VOC concentrations meant that fragmentation minimization was no longer the primary focus; LOD and LOQ became the limiting factors in the same manner required for atmospheric measurements. Where this was the case, a setup of CE 400 V, PTR pressure 2.0 mbar at 100 °C and with moderate H_2O flow (where there was almost no observable water trimer present) was used. These conditions improved signal responses; however, they did lead to increases in the fragmentation of parent masses, and the observation of some back streaming of analyte into the source. For many reactions carried out in HIRAC, similar conditions to those utilized in EUPHORE were sufficient to assign the chemistry present.

3.2.2 Understanding temperature in a flowing reactor

The high-pressure system, as described in Stone *et al.*(8) (shown in Figure 3.3), was used to measure a variety of reactions, which included the reaction of OH and dimethyl ether (DME). At elevated temperatures in the presence of oxygen, OH and DME is known to recycle OH, and at higher temperatures, this reaction can undergo chain branching.(18, 19) When experiments were carried out in both the high-pressure setup and in a conventional low-pressure slow flow reactors, the observed OH return rates at the same temperatures were shown to differ.

Using master equation (ME) calculations to fit the returned OH return rates in both the high- and low-pressure systems, the same barrier height for OH recycling could not fit both data sets. The data from the high-pressure system required a higher barrier than the data collected from the low-pressure experiments. The only satisfactory explanation that could bring agreement between the bays was a reduction in the temperatures assigned to the traces from the high-pressure setup.
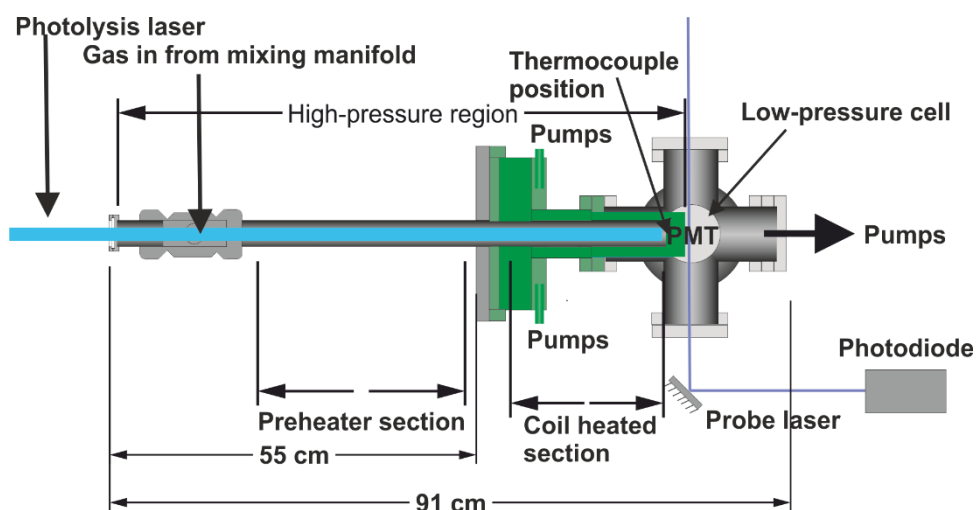
Figure 3.3 A schematic of the initial high-pressure system as described in Stone et al.(8) later modifications to this system involved the removal of the preheated section and addition of a second low-pressure cell for HO_2 detection. Typical residence time at 5 litres per minute in the reactor was 3 seconds of which 0.66 of a second was in the coil heated section.

In an attempt to rectify this, the original 'coil' heated high-pressure reactor was replaced with a reactor where the final heated section was no longer a stainless-steel tube surrounded by a coil heater, but was a block containing cartridge heaters. This cartridge heated block did not seem to improve the difference between observed OH return values from the high-pressure and low-pressure experiments. A copper spacer was then attached to the end of the high-pressure reactor to provide thermal contact to the pinhole section. This seemed to reduce the difference between high-pressure bay experiments and low-pressure bay experiments. Yet there was still disagreement, and as such, further work to examine the temperature gradients in the reactor was carried out.

Visualizing the temperature issues themselves was therefore undertaken, at first by removing the outside of the high-pressure reactor to reveal the cartridge heated section inside. From images of this, it was apparent that there was a significant variation in the temperature of the block, as can be seen in Figure 3.4. In part, this arose from the structure of the cartridge heaters, where they do not provide an even heat along their whole length. In cartridge heaters, the ends of the heater remain cold with respect to the central region. When these heaters were then placed in a block they did not lead to even heating of the block they were in contact with, and were positioned such that the end portion of the block was in contact with the cold tip of the heaters.
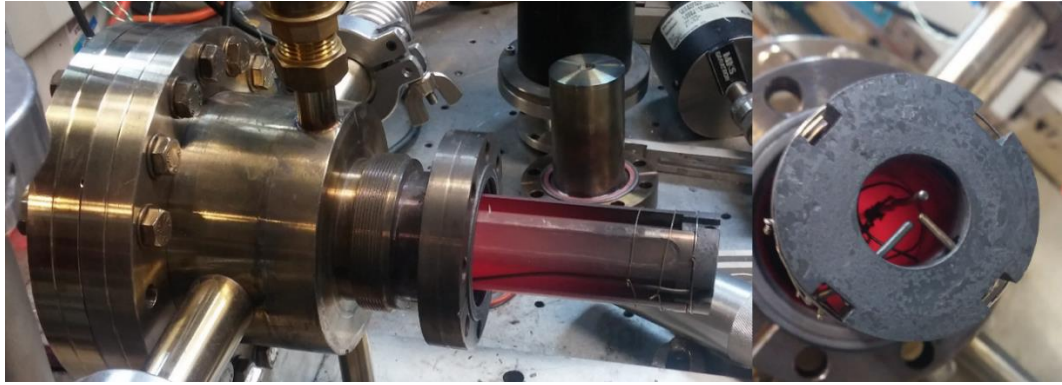
Figure 3.4 The temperature gradient across the cartridge heated block is visible in the right hand image where 100 V was applied to the heaters; in the left hand image the position of permanently placed thermocouples and the movable axial thermocouple can be seen.

The visually observed gradients across the cartridge-heated block led to the reintroduction of the earlier coil heated design. The coil heater suffered from the same issue—that the end of the heater is not actively heated. However, because of the nature of how the heater is used, this section could be bent away from the face of the pinhole and so did not significantly affect the observed heating of the gas flow. In addition, by arranging the coil heater to have a non-even spread in the distance between the coils, the heating could be concentrated towards the rear portion of the coil heater. Using the coil heater, good thermal contact with the pinhole body could also be established, especially when compared with the cartridge-heated design that required a spacer to allow for this.

Neither the cartridge heated block nor the coil heated pipe design could bring the assigned temperature between experiments performed in the low and high-pressure systems into good agreement. To map out temperature gradients, a translatable thermocouple was inserted into the reactor. This translatable thermocouple could be used to measure axial temperature gradients when the reactor was complete, and radial temperature gradients when the reactor was open. This was performed for both the cartridge-heated block and for the coil heated design.

The radial temperature gradients were measured under both laminar (Re < 1800) and turbulent (Re > 2900) flow conditions (Re – Reynolds number, a dimensionless quantity that is used to describe and predict flow dynamics). Under turbulent flows, it was not possible to heat the central gas adequately, even with the use of the preheater (Temperature < 300 °C). Under laminar conditions, there was a large temperature gradient

between the central gas and the flow, closer to the walls, but this was reduced by slowing the overall flow rate.

When axial temperature gradients were measured, the thermocouple was moved from measuring the face of the pinhole section against the gas flow along the reactor. The temperature profile of the gas with respect to distance along the reactor could then be mapped out. In general, for a given flow setting the gas began cold (room temperature) and slowly heated towards a peak value then began to plateau and fall, before rapidly dropping closer to the pinhole face, one example of such a profile is shown in Figure 3.5.
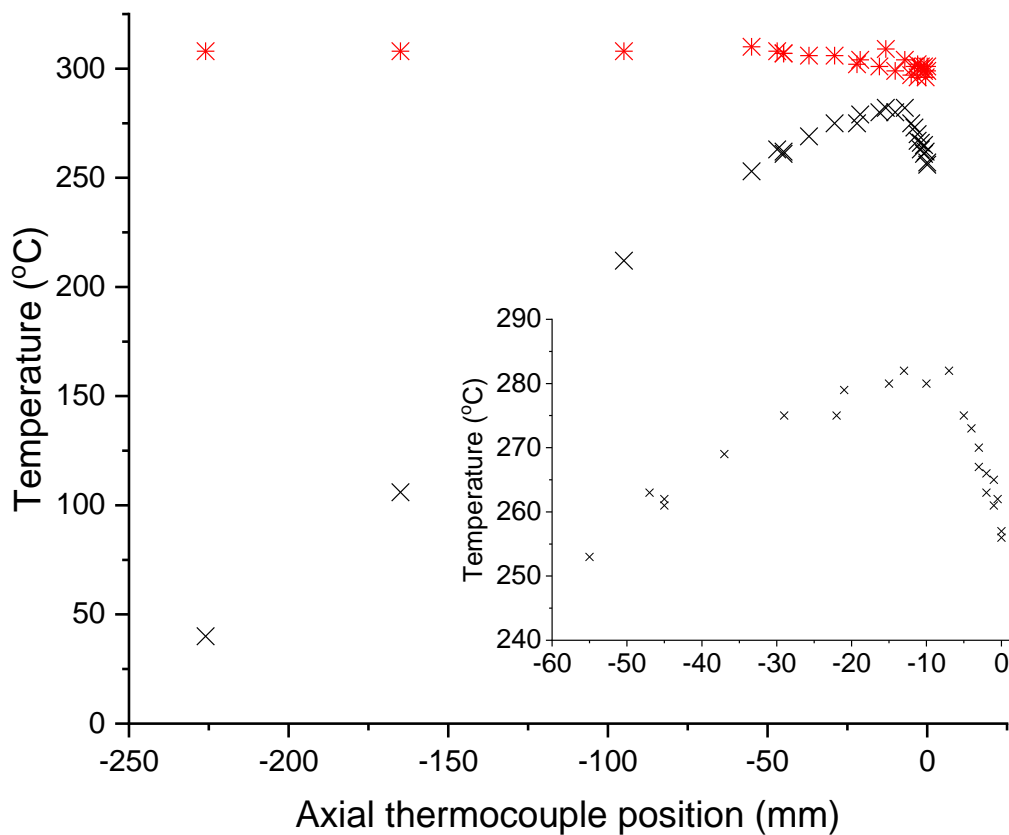
Figure 3.5. An example axial thermocouple profile measured at a variac setting of 108 V, with a flow of 6.24 SLM nitrogen at 1.4 bar. Axial thermocouple measurements are shown as black crosses; the permanently seated thermocouple are given as red. The permanently seated thermocouple gave a temperature reading of 303 °C when the axial thermocouple gave a pinhole temperature of 256 °C. The inset shows the temperature experienced over the final centimetres before contact with the pinhole.

The slower the net flow rate, the lower the apparent fall at the end of the reactor became, and as such, it became apparent that experiments carried out with slower flow rates would provide smaller temperature gradients. When the cartridge heated block and coil heated reactor were compared, the difference between peak temperature observed

and temperature at the pinhole was significantly smaller for the coil-heated model. These observations are consistent with better thermal contact between the heater and the pinhole section, and of an improved heating regime where the heating was concentrated towards the end of the reactor.

Minimizing the difference between the peak temperature experienced, and the temperature at which the kinetics is measured, ensures cleaner chemistry. High temperatures increase pyrolysis of both reactants and precursors, and can lead to the formation of products that interfere with the observed OH kinetics. For the cartridge-heated block, the hottest walls were at a distance from the pinhole (50 – 75 mm), whereas in the coil-heated model, the hottest walls are closer to the pinhole (5- 15 mm) due to the uneven coiling of the heater. Shifting the hottest region closer to the pinhole reduced heterogeneous chemistry.

When the axial temperature measurements were made, the position of the translatable thermocouple influenced the temperature recorded on the thermocouple fixed in place perpendicular to the flow. That the translatable thermocouple influenced the flow of the gas meant that these measurements were not accurate for the true gas temperatures in the absence of the axial thermocouple. The axial measurements did though; give valuable insight into how flow conditions and heater placement effects varied the difference between the observed temperature and the target temperature.

As thermocouple measurements could not be used to measure the temperature of the gas where the reaction was occurring, chemical methods to define the temperature were adopted. The primary chemical thermometer measurements were of the reaction of OH and methane (CH_4). The reaction of OH with methane varies greatly over the experimental temperature ranges primarily utilized in the high-pressure bay (300 – 800 K, $5.6 \times 10^{-15} – 7.9 \times 10^{-13}$ cm^3 $molecul^{-1}$ s^{-1}). By measuring the OH kinetics the temperature variation between the central gas and the thermocouple measurement could be defined.

The advantage of using a chemical thermometer to assess the temperature of a set of flow conditions is that it does not influence the flow conditions in the way a mechanical thermometer does. In addition, it is only a measure of the temperature at which the reaction occurred and is not influenced by external factors, where mechanical measurements would be influenced by radiative heating and conduction effects. For the reaction of OH and CH_4 in the temperature regime 300 – 800 K, the energy released from

the reaction and any subsequent RO_2 chemistry should not significantly increase the temperature of the flow.

An example bimolecular plot, Figure 3.6, for the reaction OH and CH_4 was produced under the same flow conditions, and at the same variac setting as the previous example thermocouple profile, Figure 3.5, (6.24 SLM (6240 cm^3 min^{-1} atm^{-1}) at 1.4 bar). Using the published OH and methane temperature dependence from Dunlop and Tully (20) and the measured rate coefficient k_{OH+CH4} = (1.258 ± 0.01) × 10^{-13} cm^3 $molecule^{-1}$ s^{-1}, the temperature was assigned as 522 ± 2 K. The difference between the observed temperature of the thermocouple measurement (256 ± 3 °C, 529 K) and the OH and CH_4 value (249 ± 2 °C, 522 ± 2 K) can be assigned to the modified flow conditions present when the translatable thermocouple was being used.
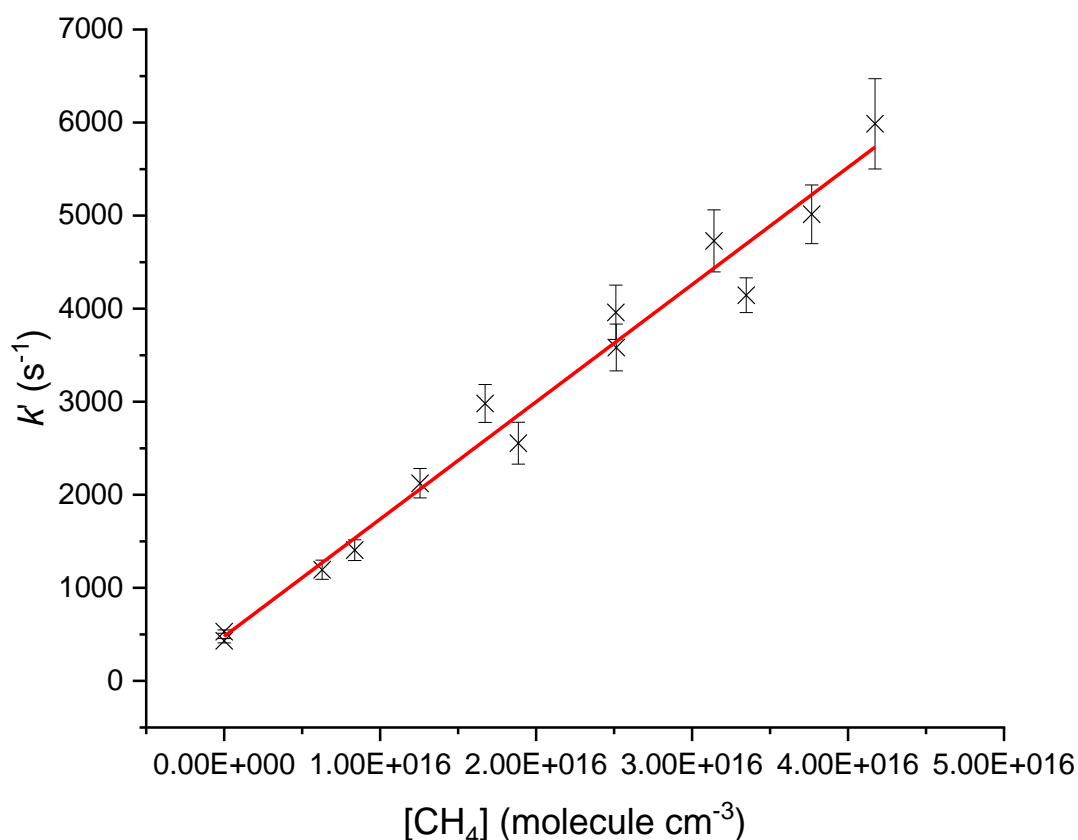
Figure 3.6 A bimolecular plot of OH and methane measured collected at an elevated temperature defined as 249 ± 2 °C from the kinetic measurement itself (2σ error), using k_{OH+CH4} = (1.258 0.01) × 10^{-13} cm^3 $molecule^{-1}$ s^{-1}, and the measurements of Dunlop and Tully.(20) The flow conditions were 6.240 SLM of nitrogen at 1.4 bar with a thermocouple measurement of 295 °C, comparable to those in Figure 3.5.

The assignment of the difference to the presence of the axial thermocouple was supported by differences in the observed temperature measured at the permanently

situated thermocouple in the two experiments (295 versus 303 ℃). Observation of changes in the temperature of the gas flow further demonstrated that axial thermocouple measurements could not be used to define the temperature. Axial temperature measurements did provide insight into the relative merits of differing flow conditions, where slower overall flows had a small difference between peak gas temperature and the temperature of the gas adjacent to the pinhole (< 1mm).

Using the knowledge gathered from the earlier thermocouple measurements, the flow settings for parametrization were chosen. It was known that slower flows produced more even axial gradients, but slow flows, especially at elevated temperatures, led to increased pyrolysis of both the compounds of interest and the OH precursors. From experiments carried out with OH and CH_4 with H_2O_2 as an OH precursor, a pressure adjusted flow rate of 5 SLM was chosen as the optimal flow rate. Use of the pre-heater was attempted and this did not significantly reduce the difference between the measured temperature on a thermocouple versus the temperature assigned from OH and CH_4. The pre-heater allowed a higher overall temperature to be reached, but this came at the cost of significantly increased reagent and precursor pyrolysis. The use of pre-heating gas in the high-pressure reactor was therefore not considered to be beneficial and became defunct in the operation of the apparatus.

A series of experiments were carried out with the same flow conditions (5 SLM at 2 bar) with OH and CH_4, with varying variac voltages. The measured OH and CH_4 temperature was then parametrized as a function of thermocouple readout and of the variac voltage. Both of these methods were in general, effective at predicting the temperature of new flow conditions within 10 K; however, subsequent OH and CH_4 measurements were taken for each new set of flow conditions and the results were added to the parametrization.

Parameterization 1 (Temperature from voltage):
$$Temperature(K) = ((-1.6954 \times 10^{-6}) \times V^4) + ((3.9967 \times 10^{-4}) \times V^3) - ((1.1703 \times 10^{-2}) \times V^2) + ((0.90968) \times V) + 25.002)$$

Parameterization 2 (Temperature from central thermocouple):
$$Temperature\ (K) = 0.68 \times T1 + 99.8$$

This became the established method for assigning temperatures to reactions carried out in the high-pressure system, and has been described in detail in the experimental section (section 2.2.2). When this method was tested in the conventional slow flow low-pressure cells, temperature variations were observed between the

thermocouple readout, and that assigned from OH and methane. In the low-pressure system, the individual temperature deviations were greatly dependent on both the bath gas and the total flow rate through the reactor. Subsequently, detailed parametrizations of flow conditions for these cells were performed and proved highly accurate at defining the expected temperatures, given flow rates and thermocouple measurements (< 10 K error).

3.2.3 The importance of the site for NO delivery on the selectivity of HO$_2$ detection

For the initial design to allow for HO$_2$ detection, by titration with NO, it was assumed that delivering NO at the earliest opportunity would encourage the most effective titration of HO$_2$ to OH. Where the early titration of HO$_2$ occurs the OH formed can be detected within the jetting gas and provide accurate HO$_2$ kinetics. The understanding that there is a reduction in the viability of kinetic measurements with distance, was based on the initial development of the FAGE sampled high pressure reactor by Stone et al. (8) In that work, it was shown that OH kinetic traces were significantly affected by sampling at distances much greater than 15 mm from the pinhole aperture.
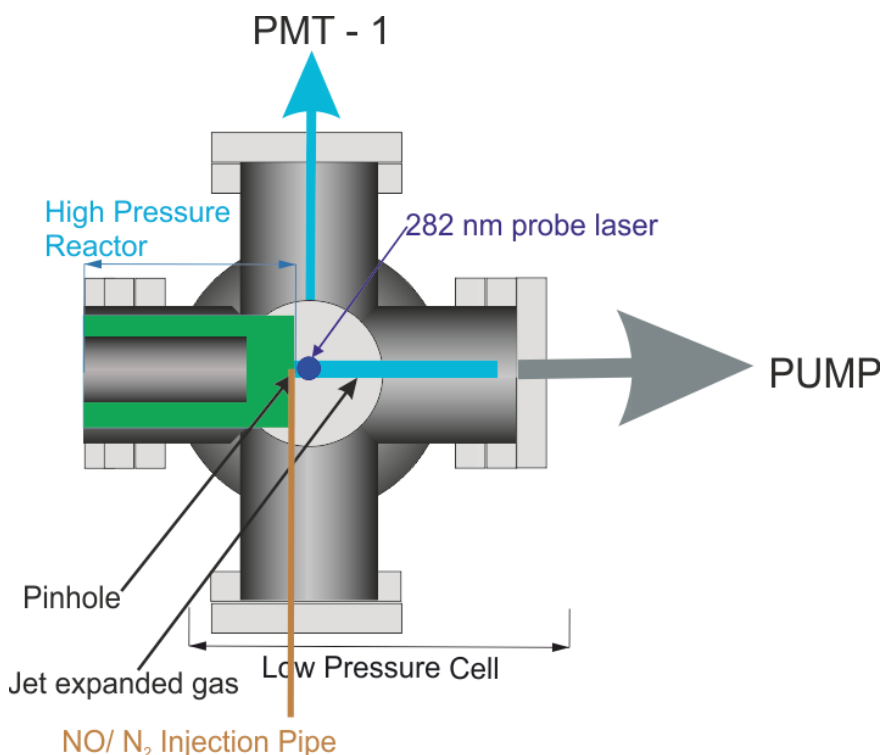
Figure 3.7 Initial layout of low-pressure cell for HO$_2$ sampling where HO$_2$ titration was attempted by the addition of a pipe for injecting NO to the setup presented in Stone *et al.*(8).

To facilitate early addition of NO the original pinhole, which featured a flat face with a single hole through which the gas was sampled, was replaced. The replacement pinhole featured a perpendicular trough across the face that led to the lip of the central sampling hole. A pipe for delivery of NO (stainless steel 1.5 mm id) was aligned in this trough so that NO would be delivered as early as possible to the 'jetting gas', and this design is shown in Figure 3.7.
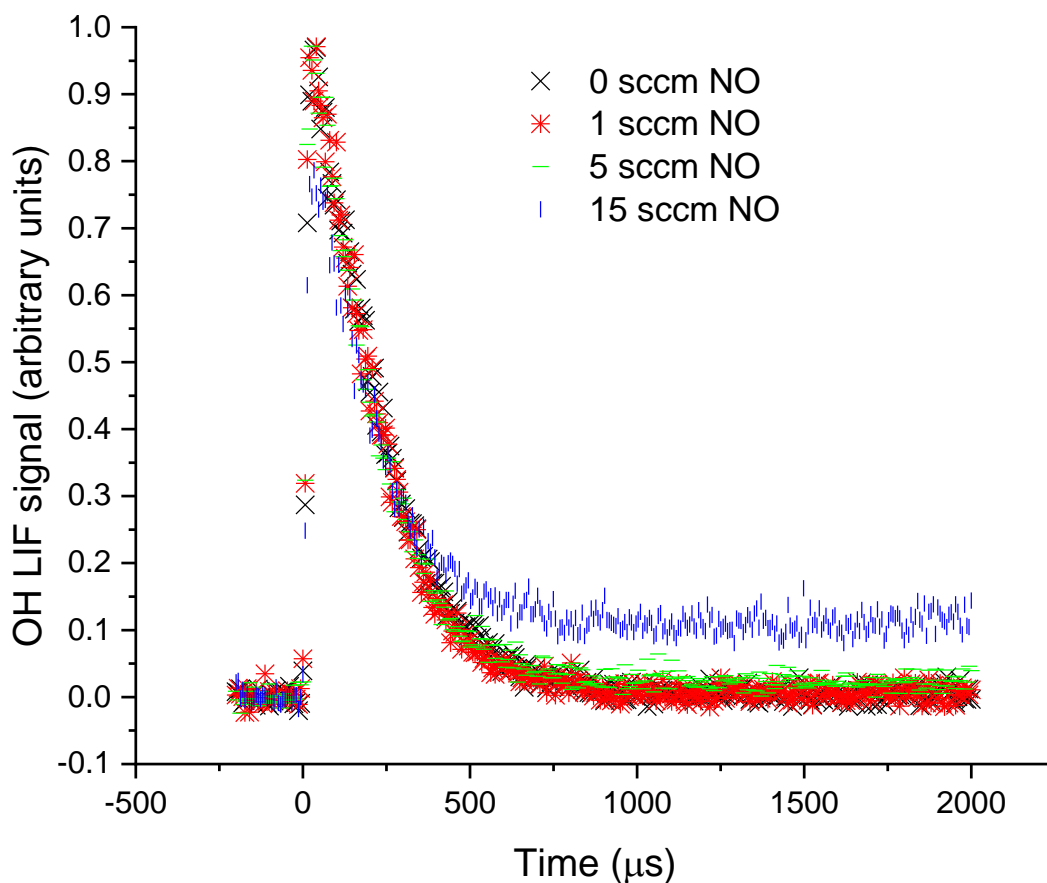
Figure 3.8 OH and H_2O_2 performed in the initial FAGE cell setup for HO_2 detection with photolysis of H_2O_2 at 248 nm, over varying NO $0 - 5 \times 10^{14}$ molecule cm^{-3} (0 − 15 sccm).

Initial work, carried out with this system, produced promising results for the calibration reaction of OH and hydrogen peroxide; it appeared that HO_2 could be titrated to OH with yields of OH from HO_2 greater than 30 % of the initial OH peak. An example of such a trace from this initial setup is given as Figure 3.8; sampling by the 282 nm probe laser occurred less than 5 mm (typically 1-2 mm) from the face of the pinhole. If HO_2 was being titrated to OH by reaction with NO only in the jetting gas, this titration was happening very efficiently indeed.

The ability of the instrument to selectively detect HO_2 was tested by the introduction of a species known to be a problematic interference; hydroxyethyleneperoxy formed from the reaction of OH and ethylene in the presence of oxygen. It was predicted that this interference would be low, unlike in FAGE detection of HO_2 performed in atmospheric measurements and in chamber studies, where this interference is significant. (3, 5, 21) The reason for the expectation of this interference being minimal, was based on the kinetics. For an interference to the assigned HO_2 signal to occur, NO initiates a decomposition of the interfering RO_2, and leads to the formation of a species that must then react with oxygen to form HO_2, which must then subsequently react with NO to form OH. The reactions are shown in further details as reactions 3.6 and 3.7 for ethylperoxy, and reactions 3.4, 3.8 and 3.9 for hydroxyethyleneperoxy; the speed of R3.4, even in low oxygen ($<1 \times 10^{15}$ molecule cm^{-3}) conditions, allows for prompt HO_2 formation.

$CH_3CH_2O_2 + NO \rightarrow CH_3CH_2O + NO_2$ (R3.6)   ($k_{3.6, 298 K} = 8.70 \times 10^{-12}$ cm^3 molecule^{-1} s^{-1}) (22)

$CH_3CH_2O + O_2 \rightarrow CH_3CHO + HO_2$ (R3.7)   ($k_{3.7, 298 K} = 9.48 \times 10^{-15}$ cm^3 molecule^{-1} s^{-1}) (22)

$HOCH_2CH_2O_2 + NO \rightarrow HOCH_2CH_2O + NO_2$ (R3.8)   ($k_{3.8, 298 K} = 9.00 \times 10^{-12}$ cm^3 molecule^{-1} s^{-1}) (22)

$HOCH_2CH_2O \rightarrow CH_2O + HOCH_2$ (R3.9)   ($k_{3.9, 298 K} = 1.3 \times 10^5$ s^{-1}) (23)

$CH_2OH + O_2 \rightarrow CH_2O + HO_2$ (R3.4)   ($k_{3.4, 298 K} = 9.60 \times 10^{-12}$ cm^3 molecule^{-1} s^{-1}) (22)
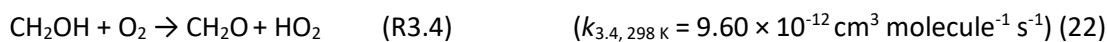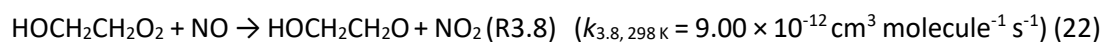
The speed of the 'jetting gas', once it had passed through the pinhole, was 125 m s^{-1} and therefore, the time taken from initial contact with NO, to sampling by LIF, was 25-35 microseconds. With an oxygen concentration in the jet of $<1 \times 10^{15}$ molecule cm^{-3}, and a room temperature $CH_2OH + O_2$ rate coefficient of 9.6×10^{-12} cm^3 molecule^{-1} s^{-1} it would take over 100 microseconds for one lifetime of this reaction. The reaction has a positive temperature dependence and so its lifetime could be expected to be even longer in the cooled jet. Before CH_2OH is formed, the initial $OOCH_2CH_2OH$ radical reacts with NO (with a rate coefficient of 9×10^{-12} cm^3 s^{-1}, and an NO concentration of 5×10^{14} cm^{-3}); the lifetime of this reaction in the 'jet' would be over 200 microseconds.

When this experiment was performed, the observed false HO_2 yield from the reaction of OH and ethylene was equivalent to that observed for OH and hydrogen peroxide. This observation of high levels of RO_2 titration to OH, raised the possibility that the NO reaction to reform OH was not occurring in the jet. The timescale available for RO_2 titration to occur in the 'jet' (35 microseconds) was far shorter than the hundreds

of microseconds required for even minimal titration of hydroxyethyleneperoxy to HO_2 to occur. In addition, where the reaction of ethane and OH in high oxygen was carried out a high apparent HO_2 yield from ethylperoxy, radicals was also observed.

It was considered that this could be caused by NO reactions occurring in the turbulent gas that preceded the formation of the jet expansion, and that this interference could be masking the NO reactions in the 'jetting' gas. To minimize the potential for this occurring, the site of the NO addition was changed. The NO addition pipe was then centered 10 mm (position 2 in Figure 3.9) from the face of the pinhole directly under the 'jetting' gas. Thereby, it was hoped the majority of reaction of HO_2 with NO to form OH would then occur in the 'jet' itself.
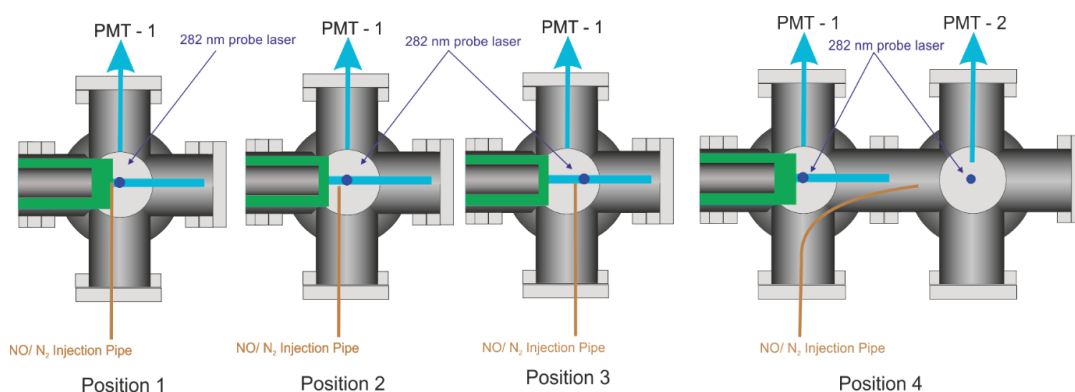
Figure 3.9 The four different positions of the pipe for NO addition.Positions 1-3 were all performed in the first OH LIF detection cell, while position 4 required the addition of a second detection cell and separate imaging to detect OH beyond the breakdown of the jet.

The reaction of OH with H_2O_2, ethylene, and ethane were again carried out. These experiments provided an apparent yield of OH from the titration of hydroxyethyleneperoxy in agreement with that observed from the titration of HO_2, and again produced a high yield from ethylperoxy. The pipe was then moved further from the pinhole (position 3 in Figure 3.9), with sampling of OH at the furthest edge of the sampling region and the high false yield was still present for ethylperoxy and hydroxyethylperoxy.

To explain these observations, it became apparent that the LIF signal detected must be influenced by a degree of interaction between the non-jetting gas and the jetting gas. In the turbulent outflow around the central cone of the jet expansion, there will be stagnant and back flowing gas. In this flow regime, the eddy currents of gas had enough time for efficient titration of hydroxyethyleneperoxy to OH. The OH was either being

sampled by the LIF detection following titration within the eddy current gas, or was diffusing into the 'jet'.
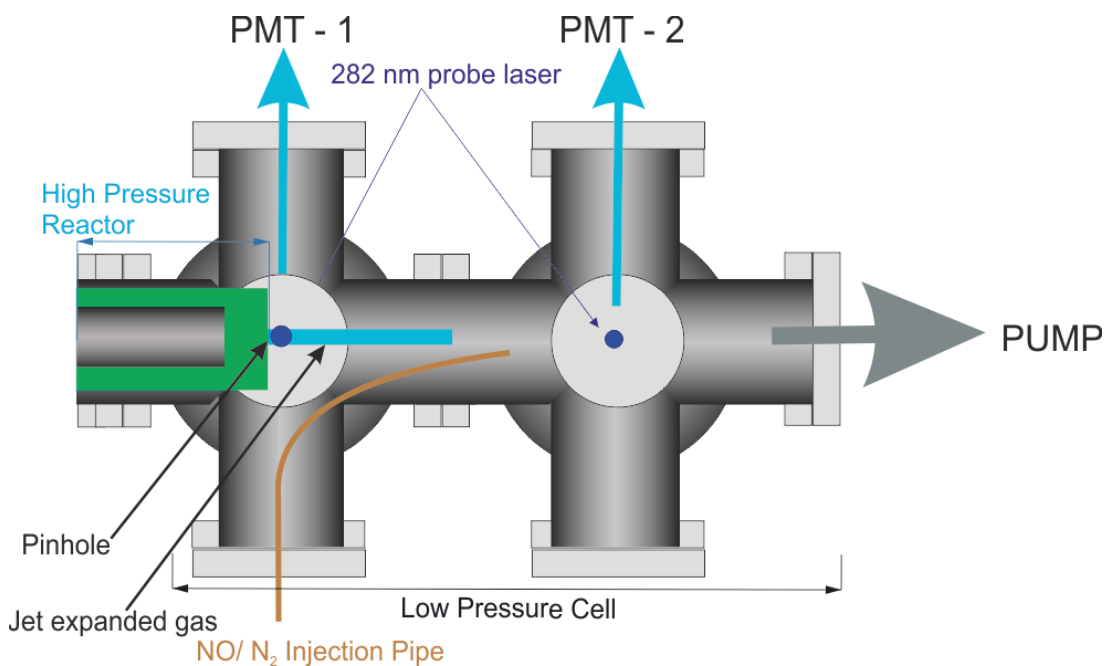
Figure 3.10 A schematic of the adapted FAGE cell that allows for simultaneous OH kinetic measurement on the first OH detection axis, PMT-1, and HO_2 yield detection after titration of HO_2 to OH following the breakdown of the 'jet' on a second detection axis, PMT-2.

To allow for effective titration of HO_2, and to ensure that any added NO added did not produce significant interaction with the gas being sampled in the jetting region, the NO injection pipe was situated well beyond the breakdown of the 'jet', 15 cm from the face of the pinhole. This required alteration of the low-pressure OH detection cell, so that there were two OH detection regions instead of the initial one, and is shown in Figure 3.10.

Performing the NO titration reaction in this manner would not allow for the same accuracy and time resolution for OH and HO_2 measurement that would hypothetically have been available in the jetting gas. As the 'jet' breaks down there is some degree of scrambling of the gas (non linear flow regime) that leads to a broadening in the arrival times of molecules to the sampling laser. Additionally, a mass transport effect became apparent where OH and HO_2 had differing arrival times; this difference is displayed in Figure 3.11.
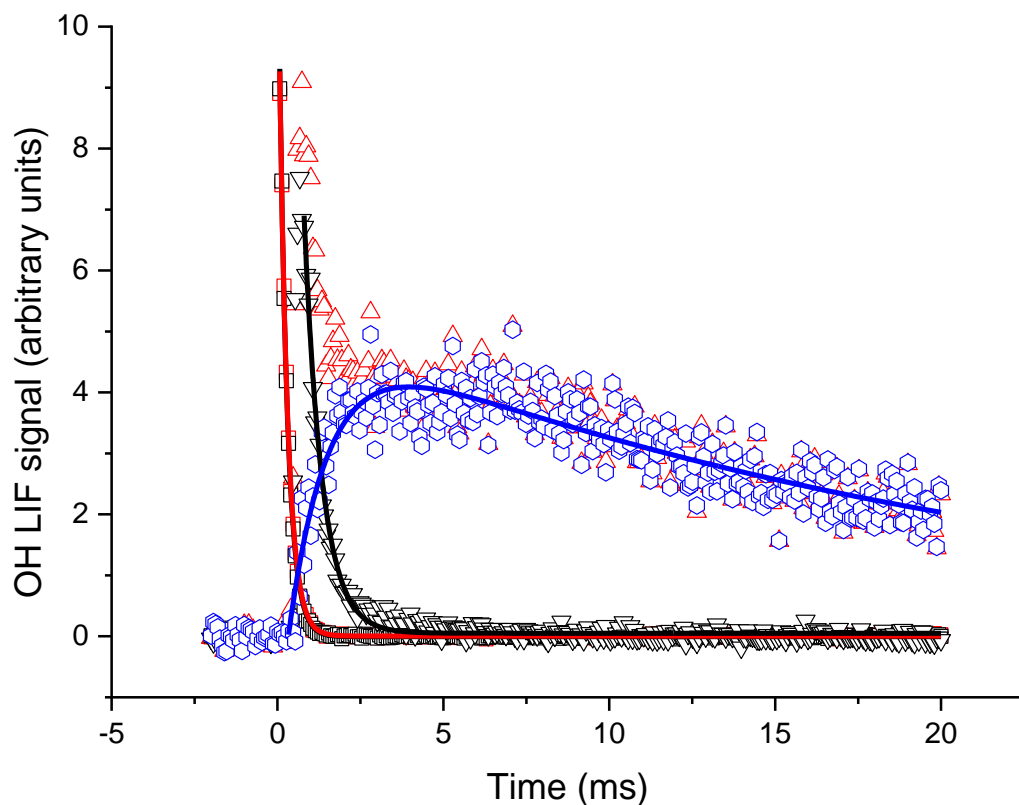
Figure 3.11 Traces detected on the first and second detectors for consecutive experiments. Black and red squares are OH signal detected on the 1st detection axis, they follow first order decays with k_{obs} = 3954 ± 24 s^{-1} and 4059 ± 22 s^{-1}. For the second detection axis, black triangles, the loss of OH in the trace is non-exponential, with k_{obs} = 1842 ± 34 s^{-1}. OH has a slower arrival time at 0.3-0.7 ms in the second cell to the first cell which had an arrival time of 0.03 ms. For the OH and HO$_2$ trace, red triangles, and the subsequent HO$_2$ trace, blue circles, the time delay between OH and HO$_2$ arrival to the detection region is shown as a shoulder in the OH and HO$_2$ trace. When the HO$_2$ trace was fitted with a growth a decay curve, the HO$_2$ formation rate was $k_{HO2-form}$ = 841 ± 62 s^{-1}, with an HO$_2$ loss of $k_{HO2-loss}$ = 47 ± 2 s^{-1}.

In the 'jet', all molecules travelled at the speed of the backing gas, but outside the jet, molecules instead moved with an average velocity that depended on their mass and temperature. This mass transport effect leads to a broadening of the arrival times of individual molecules, and this produces the observed difference between the average arrival of OH and HO$_2$ at the second detection axis.

Notably, arrival at the second detection axis (15 cm) took significantly longer than arrival at the 1st detection axis (> 500 microseconds versus 35 microseconds). This delay between initiation of the reaction in the flash and arrival at the detection axis had a significant impact on the speed limit of the detectable kinetics, Figure 3.11. Additional to the speed limit being reduced compared to the 1st detection axis, a large reduction in OH

concentration and therefore OH LIF signal occurred at much lower removal rates than for the 1st detection axis.

Because of the problems discussed above, OH kinetics are assigned only from the 1st detection axis. Kinetic parameters recovered from HO$_2$ profiles from the 2nd detection axis were corrected using a parametrization of the difference in observed kinetics on the 1st detector to the observed kinetics on the 2nd detector. The process of correction is described in section 3.3.2 and is illustrated in Figure 3.14 & Figure 3.15. Although assignment of kinetics was not fully quantifiable, due to the low removal rates (<100 s^{-1}) of HO$_2$ typical in the experiments carried out, HO$_2$ yields were.

3.3 Instrument Validation

3.3.1 Instrument characterization for HO$_2$ yield detection

The selectivity in measuring HO$_2$ concentrations plays an important role in the viability of a detection method for monitoring reactions important for atmospheric chemistry. At high pressures, the reaction of NO with many atmospherically relevant RO$_2$ species in the presence of oxygen induces HO$_2$ formation. This effect was minimized by performing the titration in the low-pressure cell with the NO + HO$_2$ reaction under 'starved NO' conditions. This premise was validated by measuring the OH + ethane and OH + ethylene HO$_2$ yields under high oxygen conditions. In our system, the typical oxygen concentrations in the high-pressure reactor were varied, at between 1×10^{16} and 1×10^{19} molecule cm^{-3}, which led to concentrations in the low-pressure cell of 3×10^{12} to 3×10^{15} molecule cm^{-3}.

Sensitivity in measuring OH yields can allow for the assignment of different product or reaction channels for a given VOC. By measuring the reaction of OH and methanol and varying the added oxygen concentration, it was possible to assign the hydroxy and methyl abstraction channels. This meant that methanol and OH at low and high oxygen was chosen as an ideal test case for assessing the sensitivity of the instrument for the assignment of HO$_2$ yields.

3.3.1.1 Interference by RO_2 species

The reaction of OH + ethane (R3.1) under high oxygen conditions permits the rapid formation of the ethylperoxy radical, which is an RO_2 radical that has a typical slow, NO propagated, route to HO_2 formation (R3.6 – R3.7).

$CH_3CH_2O_2 + NO \rightarrow CH_3CH_2O + NO_2$ (R3.6) ($k_{3.6, 298 K} = 8.70 \times 10^{-12}$ cm^3 molecule^{-1} s^{-1}) (22)

$CH_3CH_2O + O_2 \rightarrow CH_3CHO + HO_2$ (R3.7) ($k_{3.7, 298 K} = 9.48 \times 10^{-15}$ cm^3 molecule^{-1} s^{-1}) (22)
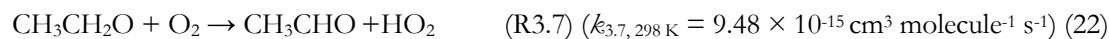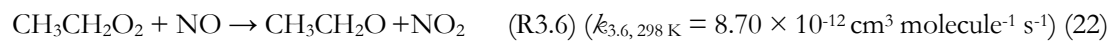
Under a variety of NO flows, the apparent HO_2 yield for the OH + C_2H_6 system was 3 ± 6 %, which indicates that for most reactions carried out in our system, chemical transformation by reaction with NO was sensitive to HO_2 rather than RO_2 species, where the RO_2 radical was the product of O_2 addition to a simple alkyl radical.

The reaction of ethylene and OH (R3.2) in the presence of oxygen forms the hydroxyethylperoxy radical ($HOCH_2CH_2O_2$), and reaction of the $HOCH_2CH_2O_2$ with NO in the presence of O_2 provides a route for the prompt regeneration of OH. For this reaction in the revised configuration for NO addition, an apparent HO_2 yield of 100 ± 15 % was initially observed; however, by varying the concentration of NO added to the low pressure cell (in our experiment between 5×10^{13} and 5×10^{14} molecule cm^{-3}), the formation rate of OH was reduced minimizing the apparent yield observed (< 70 %),(for an NO concentration of 5×10^{13} molecule cm^{-3}), with the observed rate of OH regeneration (<300 s^{-1}).

$HOCH_2CH_2O_2 + NO \rightarrow HOCH_2CH_2O + NO_2$ (R3.8)($k_{3.8, 298 K} = 9.00 \times 10^{-12}$ cm^3 molecule^{-1} s^{-1}) (22)

$HOCH_2CH_2O \rightarrow CH_2O + HOCH_2$ (R3.9) ($k_{3.9, 298 K} = 1.3 \times 10^5$ s^{-1}) (23)

$CH_2OH + O_2 \rightarrow CH_2O + HO_2$ (R3.4) ($k_{9, 298 K} = 9.60 \times 10^{-12}$ cm^3 molecule^{-1} s^{-1}) (22)
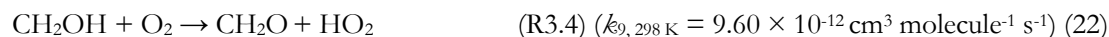
Therefore, for test reagents that generate radicals similar to hydroxyethylperoxy, our instrument will detect both HO_2 and RO_2, with some selectivity for HO_2. But for reactions that generate radicals similar to ethyl or methyl peroxy, this instrument will selectively detect HO_2.

3.3.1.2 Assigning accurate yields, OH + methanol

Measuring the reaction of OH and methanol with sufficient oxygen (R3) has a well-established 100 % HO_2 yield. Through comparison of the yields measured from the reaction of OH with H_2O_2 and OH and methanol, the use of H_2O_2 as a standard was validated. Where the reaction of OH and methanol was carried out under lower oxygen,

only the α branching fraction led to HO_2 generation, and thus the sensitivity of the instrument could be assessed.

The branching ratio for the α abstraction to yield CH_2OH (R3a) reported by the IUPAC evaluation, and based on the experimental data of McCaulley $et\ al.$ (24), is α = (85 ± 8) % at room temperature with the methoxy yield as the remainder (15 ± 8) %. Reaction 3 was studied at room temperature with the reaction being initiated by the photolysis of H_2O_2 at 248 nm. In the presence of low concentrations of oxygen (< 1 × 10^{16} molecule cm^{-3}), the α abstraction still leads to prompt formation of HO_2 via R4, but R5, $CH_3O + O_2$, occurs on a much longer timescale and was not observed under these conditions. The observed HO_2 yield, (87 ± 10) %, with the error given as 2 σ, (first row of Table 3-1) is the fraction of reaction R3 forming CH_2OH and is consistent with the IUPAC evaluation.

$OH + CH_3OH \rightarrow H_2O + CH_2OH$ | $CH_2OH + O_2 \rightarrow HO_2 + HCHO$ (fast)   (R3a, R4)

$OH + CH_3OH \rightarrow H_2O + CH_3O$ | $CH_3O + O_2 \rightarrow HO_2 + HCHO$ (slow)   (R3b, R5)
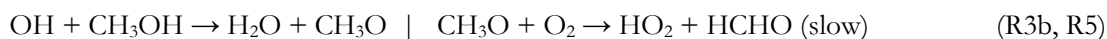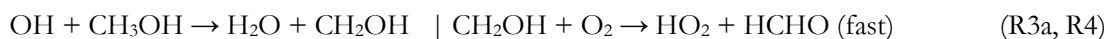
Table 3-1 HO_2 yields from the reaction of OH with CH_3OH with varying $[O_2]$ carried out 295 K. Errors given as 2 σ.

$[O_2]$/ molecule cm^{-3}	HO$_2$ Yield (%)				Average HO$_2$ Yield (%)
	Expt 1	Expt 2	Expt 3	Expt 4	
<1 × 10^{16}	90	89	79	88	(87 ± 10)
2 × 10^{18}	93	94	100	99	(97 ± 6)
6× 10^{18}	103	97	101	97	(99 ± 4)
	98	102	98	98	

When higher concentrations of oxygen were used (2-6 ×10^{18} molecule cm^{-3}), the timescale for HO_2 production from reaction R5 decreases, and now both abstraction channels led to HO_2 detection in our apparatus. The resulting observed HO_2 yield (second row of Table 1) was consistent with 100 % conversion of OH to HO_2. The measurement of a 100 % yield for OH and methanol using the reaction of OH with H_2O_2 as an internal standard verified that this method of internal calibration was indeed valid.

In addition, the reproduction of the expected HO_2 yields from the literature branching ratios for the reaction of OH with methanol under varying $[O_2]$, demonstrated that the instrument could be used to accurately measure HO_2 yields with high precision.

3.3.2 Assessment of transport effects on observed kinetics

Due to the differing conditions in the two detection regions, the kinetics observed at the first detection axis, where OH LIF was performed in the jet-expanded gas, and in the second detection region, where LIF is performed 15 cm downstream from the pinhole after the breakdown of the jetting gas, will be treated separately. For validating the accuracy of the OH kinetics in the first cell, the reactions of OH and methane (CH_4) (20), and OH and ethylene (C_2H_4) (25, 26) were studied. The high accuracy and precision of this setup for measuring OH removal kinetics has been demonstrated in the work of Medeiros *et al.*, where the instrument was used to study the reaction of OH and isoprene (C_5H_8) and reproduced the literature bimolecular rate coefficient within 1 %(27).

$$OH + CH_4 \rightarrow H_2O + CH_3 \qquad\qquad\qquad (R3.10)$$

$$OH + C_2H_4 \rightarrow HOC_2H_4 \qquad\qquad\qquad (R3.2)$$

$$OH + C_5H_8 \rightarrow HOC_5H_8 \qquad\qquad\qquad (R3.11)$$

When these reactions (R3.2, R3.10, R3.11) were carried out at room temperature the expected bimolecular rate coefficients could be reproducibly and accurately measured for observed rate coefficients less than 150,000 s^{-1}.

Studies on the reaction of OH and ethylene at room temperature and 2.2 bar, shown in Figure 3.12, gave a value of $k_{3.2} = (8.33 \pm 0.16) \times 10^{-12}$ cm^3 molecule^{-1} s^{-1} (2σ errors) which matched well with literature high pressure limits for OH and ethylene; where a direct pulsed laser photolysis laser induced fluorescence study by Tully (26) gave $k_{3.2} = (8.47 \pm 0.24) \times 10^{-12}$ cm^3 molecule^{-1} s^{-1}, and a relative rate study by Atkinson and Aschmann (25) found $k_{3.2} = (8.11 \pm 0.37) \times 10^{-12}$ cm^3 molecule^{-1} s^{-1}, and a direct study using frequency modulated absorption spectroscopy and computational calculations by Lockhart *et al.*(28) gave a range for $k_{3.2} =(8.54 - 9.0) \times 10^{-12}$ cm^3 molecule^{-1} s^{-1} slightly higher than the experimental value in this work. However, for pseudo-first order rate coefficients above ~150000 s^{-1}, there was no longer a linear dependence of the rate coefficient with reagent concentration; transport effects are becoming significant even for OH detection in the jetting region.
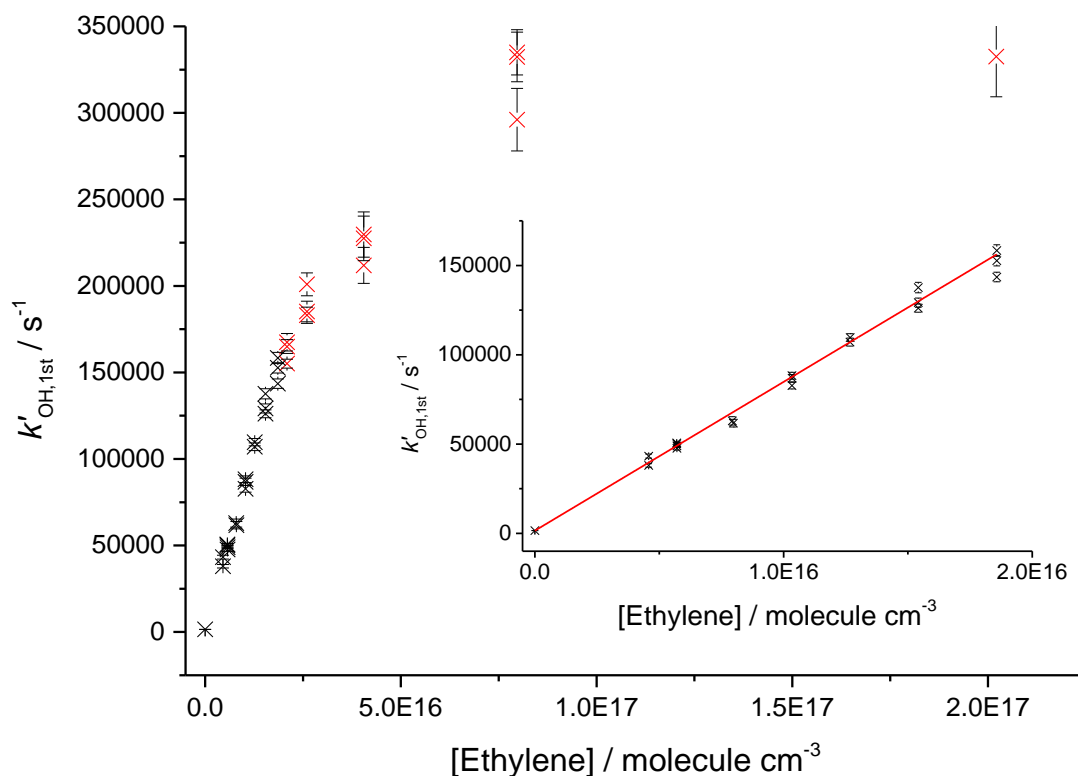
Figure 3.12 Bimolecular plot of the pseudo-first-order rate coefficient at the first detector, $k'_{OH,1st}$, vs the ethylene concentration. The figure demonstrates a linear relationship below ~150,000 s^{-1} (see inset for detail in linear region) but with increasing curvature, due to transport effects at higher values of $k'_{OH,1st}$. Black point's symbolize where the experimental rate coefficient was linear with the concentration of ethylene, red points showed a greater than 5 % difference from linearity.

As the added concentration of ethylene was linearly increased, the removal rate for the OH also increased linearly. Above 10,000 s^{-1}, the timescale of transport and reaction began to overlap. As the removal rate was increased further, above 30,000 s^{-1}, the peak OH concentrations in the high-pressure section could no longer be reliably assigned from the OH detected in the low-pressure cell. However, up to 160,000 s^{-1} the kinetics of OH loss and transport were still sufficiently separated in time to allow an accurate rate coefficient to be assigned. Above 160,000 s^{-1} the timescale for transport and removal were no longer well separated and the observed removal rate differed from the true removal rate in the high-pressure region. An example trace is shown in Figure 3.13, where above 300,000 s^{-1} no observed increases in removal rate had occurred with increasing ethylene concentration, which led to a 50 % difference between the actual and observed rate for OH loss. For the systems we studied, reaction of OH and precursor was kept below 2500 s^{-1} and thus the range of rate coefficients that could be accurately measured in the first cell was more than sufficient.
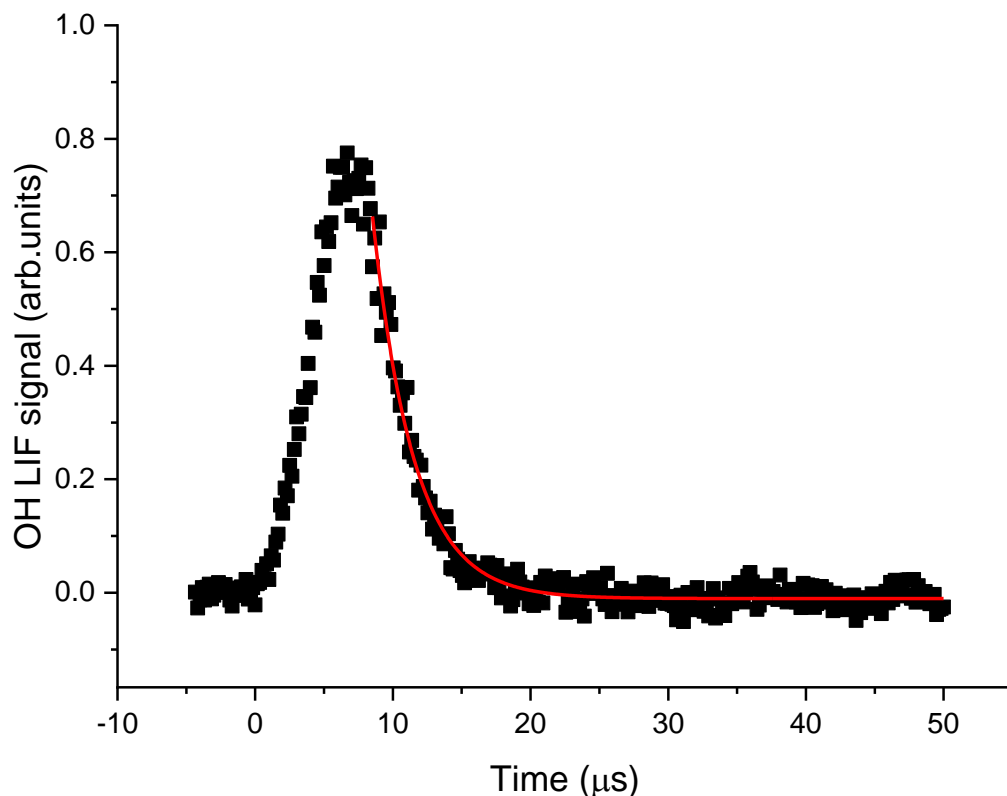
Figure 3.13 The transport and loss processes in this decay have become conflated, a simple exponential fit to the loss portion of the trace gives an observed loss rate of 300,000 s^{-1} which is lower than that expected from OH and ethylene (680,000 s^{-1}, 8.5 × 10^{-12} cm^3 molecule^{-1} s^{-1}, [C$_2$H$_4$]= 8 × 10^{16} molecule cm^{-3}).

The OH traces detected in the second cell deviated from those observed from the first cell, as can be seen in Figure 3.11. There is understandably an increased time delay from time zero (the photolysis laser pulse) to arrival of OH radicals at the second detection axis, due to the increased distance travelled after sampling (> 150 mm versus < 5 mm). Additionally, the arrival of OH to the second axis is spread out further in time due to transport issues relating to both non-linear flow conditions at the breakdown of the jet, and the arrival of the OH being affected by its velocity distribution (29-31). Figure 3.14 shows a plot of the observed OH rate coefficients from the first detection axis ($k_{OH,1st}$) against observed rate coefficients from the second detection axis ($k_{OH,2nd}$). For values of k_{OH} below 2500 s^{-1} it was possible to accurately assign an expected OH removal rate for reactions observed in the second cell ($k_{OH,2nd}$), given the observed OH kinetics at the first detection axis ($k_{OH,1st}$). This process allowed for comparison of the kinetics for OH removal and HO$_2$ production.

114
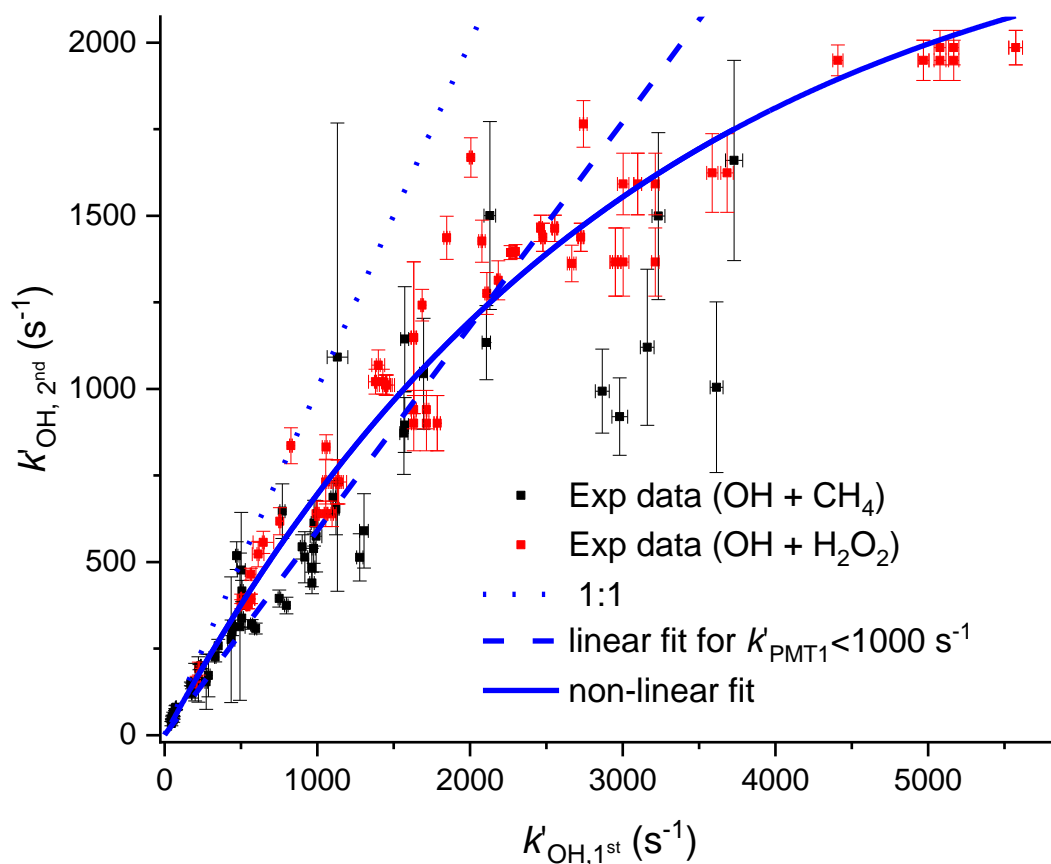
Figure 3.14 Relationship between the observed rate coefficient observed in the first cell ($k_{OH,1st}$) and the observed OH removal rate in the second cell ($k_{OH,2nd}$). The difference is non-linear but a simple fit to this could be used to assign removal rates to traces observed in the second cell below 2,500 s^{-1}. The solid blue line is a non-linear fit of the form, $y = A * (1 - e^{-b*x})$, where A was a limit value above which no increase in measured rate coefficient would be observed.

As mentioned above, the observed kinetics in the second cell are significantly affected by the velocity distribution of the species being detected. There is therefore a deviation between the observed kinetics expected from the measurement of the OH radical loss, and the kinetics for HO_2 formation due to the differing masses of OH and HO_2. The slower transport of HO_2 with respect to OH is apparent in the earlier example trace, Figure 3.11, where it leads to a shoulder in the OH and HO_2 trace. Figure 3.15 shows the pseudo-first order rate coefficients for OH removal ($k'_{OH,2nd}$) and HO_2 production ($k'_{HO2,2nd}$) determined at the second detection axis, plotted against the OH removal at the first detection axis.
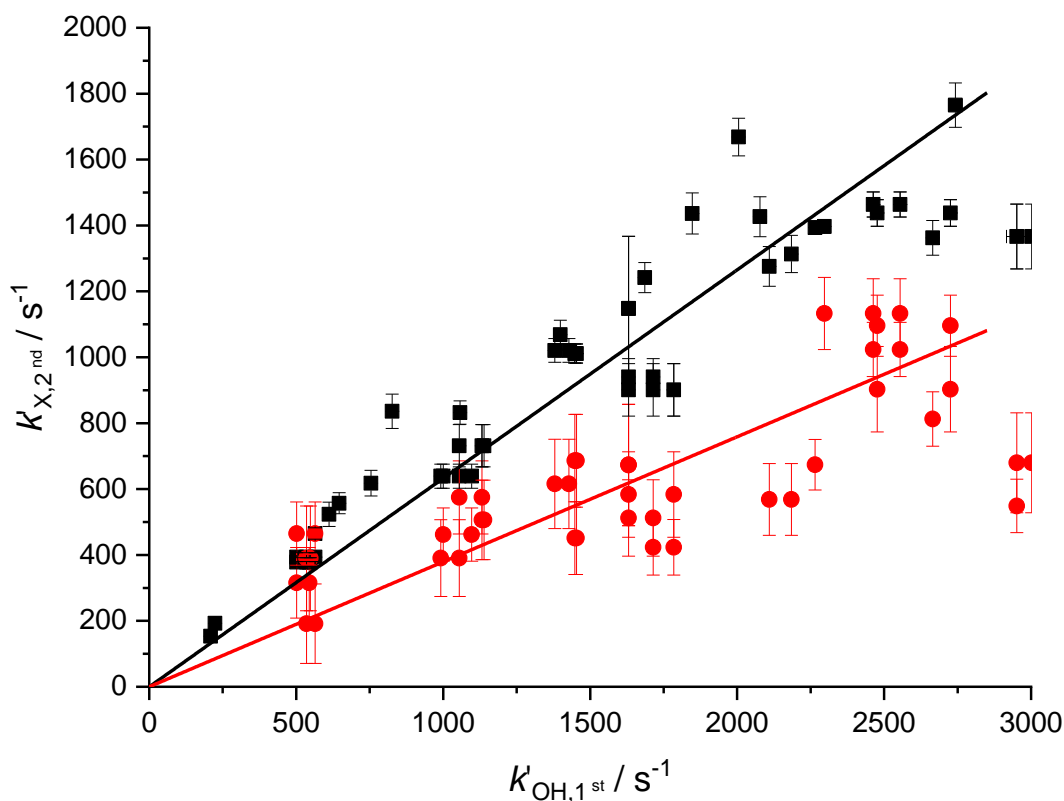
Figure 3.15 Relationship between the pseudo-first-order rate coefficient for OH loss observed in the first cell ($k'_{OH,1st}$) and the observed rate coefficients in the second cell ($k'_{X,2nd}$ where X = OH or HO_2) a non-linear fit can be used to assign removal rates and HO_2 formation rates to traces observed in the second cell below 2,500 s^{-1}. The red and black fits to the data had a ratio of gradients of 0.60 ± 0.14, concordant with deviation due to mass transport effects.

The two fits to the data shown in Figure 3.15 had a ratio of gradients concordant with the root of the masses for HO_2 and OH, 0.60 ± 0.14 versus the expected relationship of 0.73. As with Figure 3.14, it is possible to establish a calibration graph that relates the kinetics of HO_2 production at the second detection axis with the primary kinetics taking place in the high pressure reactor. This means that the timescale over which the HO_2 yield was observed could be assigned and therefore it is possible to attribute HO_2 yields to fast processes, intramolecular RO_2 decompositions or R + O_2 reactions, or to slower radical-radical reactions.

3.3.3 Assessing temperature gradients

The axial temperature measurements carried out earlier, an example is shown as Figure 3.5, showed that there is a steep temperature gradient close to the face of the pinhole in

116

the high-pressure reactor. With respect to traces, detected distance from the face of the pinhole is time in the measured decay. As such, a deviation in temperature with distance could potentially produce a temperature gradient with time in the traces obtained.
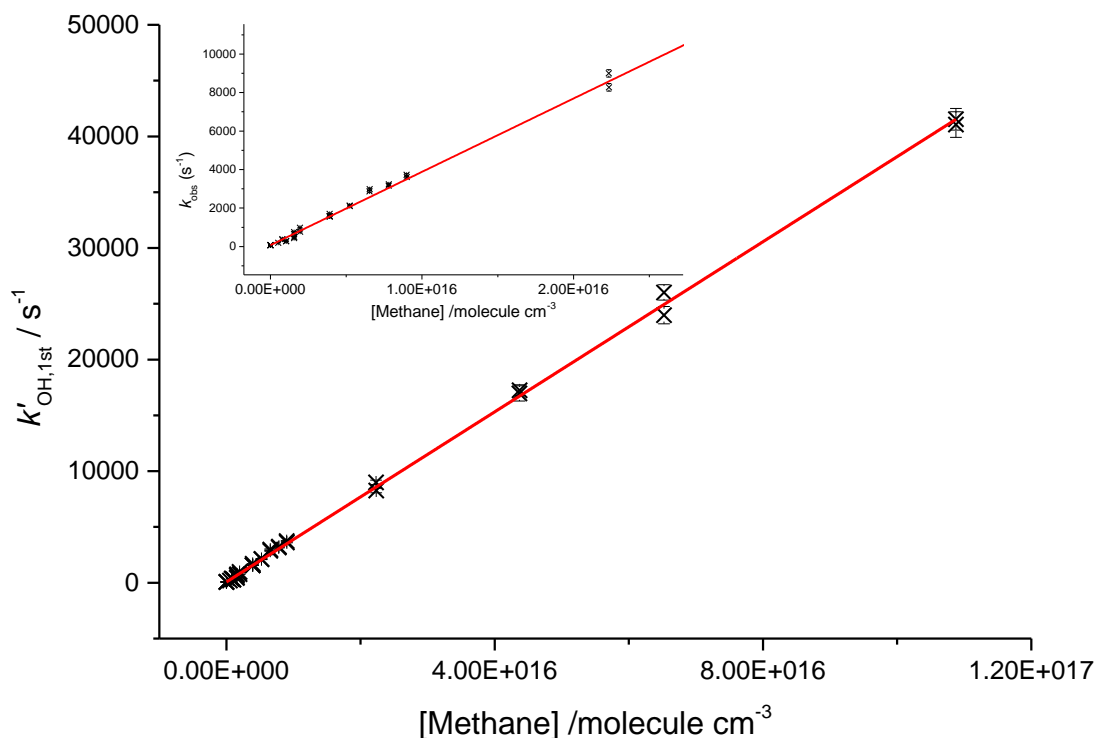
Figure 3.16 A bimolecular plot for the reaction of OH and methane at 680 K, 2.3 bar using 193 nm photolysis of water as an OH precursor. Here the inset shows that even at removal rates < 1000 s^{-1} the plot is still linear, indicating that within the measured experimental timescales there is little deviation in temperature.

To assess the axial temperature gradients in the gas sampled through the pinhole over the timescales of reactions measured, OH and methane rate coefficients were measured using photolysis of water at 193 nm as a source of OH. Using water photolysis allowed for low removal rates of OH by precursor and assignment of OH and methane over a range of pseudo-first-order rate coefficients ($k'_{OH,1st}$) $100 - 40000$ s^{-1} as shown in Figure 3.16. This was performed at two temperatures (505, 680 K), and the slope of observed OH removal rate coefficients against concentration of methane appeared linear over the full range for both temperatures, thus verifying that over the distances sampled within experimental timeframes there is a minimal temperature gradient.

3.3.4 Influence of radical radical chemistry.

In general, work performed in the high-pressure apparatus was carried out with concentrations of OH in the low $\times 10^{12}$ cm^{-3}. The rate of typical radical radical reactions are therefore in general much slower than the reaction between radicals and the reagents being studied. In the absence of a compound of interest however removal of OH by reaction with the precursor was generally $500 - 3000$ s^{-1}; with an IUPAC recommended literature rate constant for OH and HO$_2$ of 1.1×10^{-10} cm^3 s^{-1} (1) radical radical chemistry may become important as $[OH]_0$ increases above the low $\times 10^{12}$ cm^{-3}.

When the system was modelled, it became apparent an effect from radical radical losses should have been observed on HO$_2$ yields. This effect would have been exacerbated where experiments were carried out at 10Hz, through the build-up of substantial concentrations of HO$_2$ pre flash. From a simple model of the system the apparent HO$_2$ yield in the presence of a large excess of methanol and with an OH concentration under 1×10^{13} cm^{-3} could be expected to be greater than 200 %, Figure 3.17.
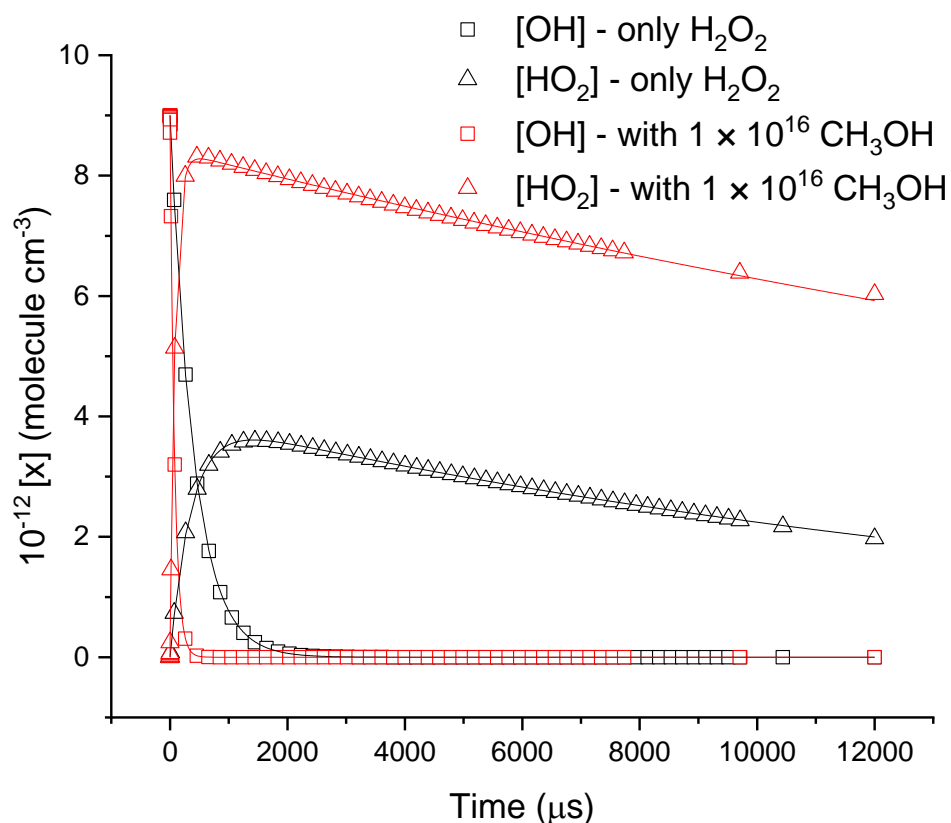
Figure 3.17 A simulation of the expected HO$_2$ yields for reaction of 9×10^{12} OH with 1×10^{15} H$_2$O$_2$ with 6×10^{18} O$_2$, in the presence and absence of 1×10^{16} methanol. Where the removal of OH by reaction with the HO$_2$, OH were included, and accounting for the loss of HO$_2$ via reaction with HO$_2$, OH, CH$_3$O and diffusion.

Taking several values of the pump laser power (1, 16, 55 mJ cm^{-2}) additional HO$_2$ yield experiments with methanol were performed. Reactions were carried out with 6×10^{18} cm^{-3} oxygen to ensure fast titration of CH$_3$O to HO$_2$ and to prevent any CH$_3$O+HO$_2$ chemistry occurring. From the OH removal kinetics a hydrogen peroxide concentration of $\approx 1.1 \times 10^{15}$ cm^{-3} was assigned, where the pump laser power was 16 mJ cm^{-2} per pulse the estimated OH concentration was $\approx 3 \times 10^{12}$ cm^{-3} and the HO$_2$ decay profile matched the expected removal via HO$_2$ HO$_2$ this would produce. At a much lower pump energy of 1 mJ cm^{-2} per pulse the OH concentration was estimated to be $\approx 1.2 \times 10^{11}$ cm^{-3}. The HO$_2$ yields collected from these two experiments were (99 $\pm$ 2) % at 3×10^{12} cm^{-3} OH and (99 $\pm$ 7) % at 1.2×10^{11} cm^{-3} OH. An example comparison at 3×10^{12} cm^{-3} OH is shown as Figure 3.18. In addition at 1.2×10^{11} and 3×10^{12} cm^{-3} [OH] no repetition rate dependence on the observed HO$_2$ yield was observed, and as such any build-up of HO$_2$ before the flash when experiments were carried out at 10 Hz with respect to experiments carried out at 1Hz does not influence the observed HO$_2$ yields.
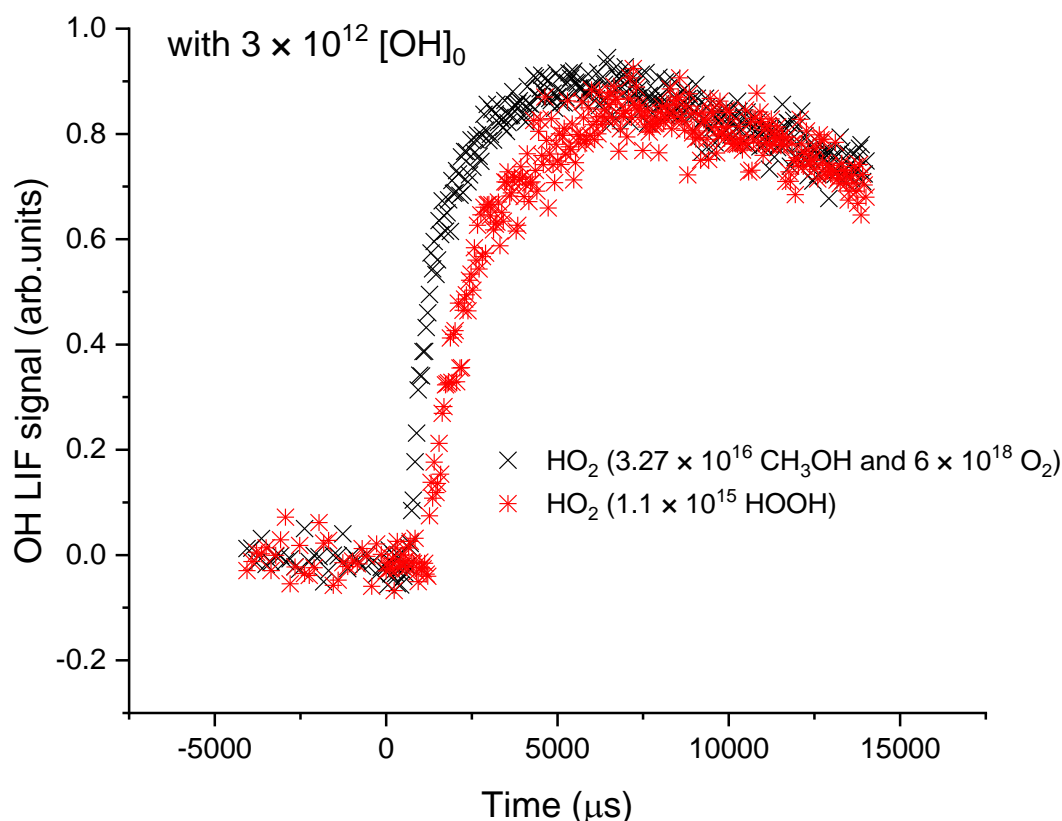
Figure 3.18 A comparison of an HO$_2$ trace with no methanol and 3.27×10^{16} methanol, both traces were taken with 6×10^{18} O$_2$ and 3×10^{12} OH. The assigned HO$_2$ yield was ≈ 100 %.

An additional yield was also measured for OH with 2.7×10^{15} cm^{-3} H$_2$O$_2$ and 55 mJ cm^{-2} of photolysis energy, with an OH concentration of 2.6×10^{13} cm^{-3} (Figure 3.19). At this much greater OH concentration the HO$_2$ yield assigned was (98 ± 3) % and this is close to the upper limit of the [OH] achievable in this system.

Fits to the tails of the HO$_2$ traces in the presence of methanol were not statistically faster than for those taken with the same radical concentrations in the absence of methanol and this is observable in Figure 3.18 and Figure 3.19, in the similarity of the shape of the tails. This confirmed that CH$_3$O was indeed efficiently titrated and was not responsible for erroneously low HO$_2$ yields from methanol being assigned.
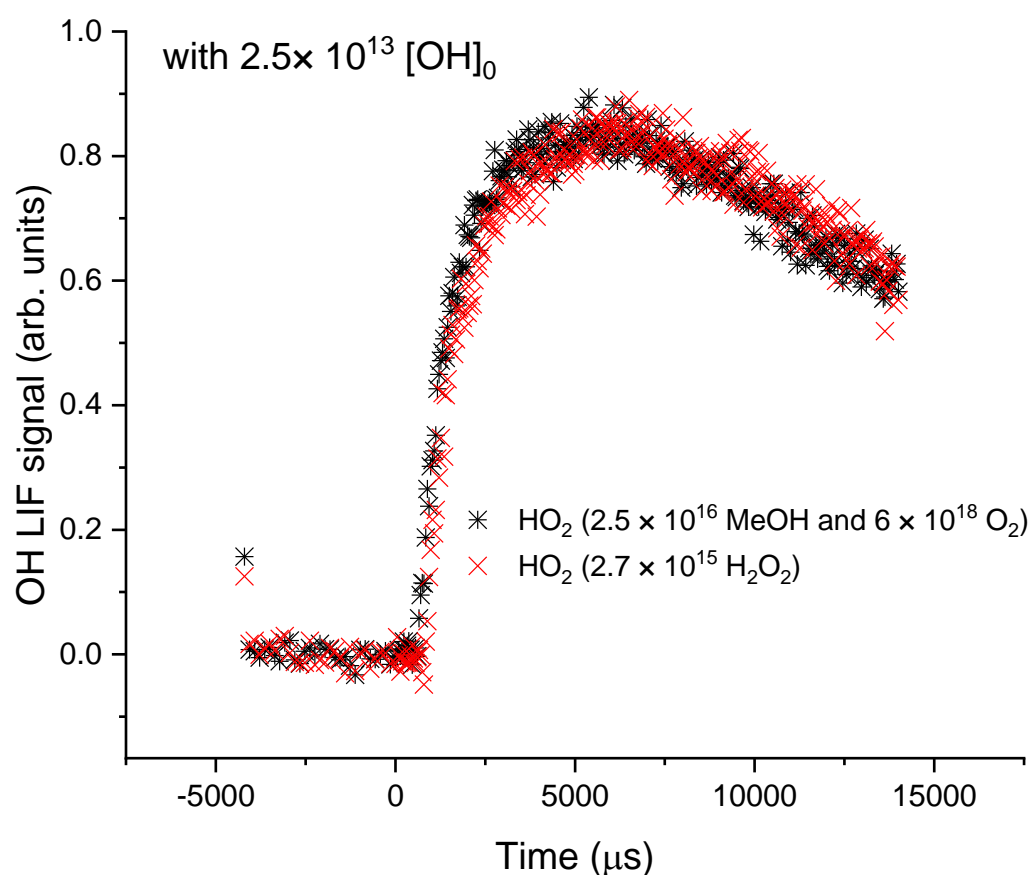
Figure 3.19 HO$_2$ yields from experiments carried out with 2.7×10^{15} H$_2$O$_2$ in 6×10^{18} oxygen with a [OH] $\approx 2.5 \times 10^{12}$ in the presence and absence of 2.5×10^{16} MeOH. The HO$_2$ yield was assigned as $\approx$100 %.

Doubling of the methanol concentration did not change the observed decay of HO$_2$ in the tails nor the peak HO$_2$ concentration assigned. The lack of a dependence on methanol concentration showed that under our conditions, less than 1×10^{17} cm^{-3} CH$_3$OH, no significant complexation of HO$_2$ to CH$_3$OH occurred.

In addition to differences in HO_2 yields from the model, where OH concentrations were varied between 1×10^{11} and 5×10^{13} cm^{-3}, changes in the OH removal kinetics (k_{obs}) could approach 50 %. The high-pressure system can precisely measure OH removal kinetics within a precision sufficient to assign the expected difference in removal rates if OH reaction with HO_2 is a significant loss process for the setup.

Figure 3.20 Varying the laser power between 0.75 and 16 mJ cm^{-2} per pulse with 6 × 10^{14} cm^{-3} H_2O_2, the typical experimental conditions used in the high-pressure system. Any difference in OH kinetics due to OH and HO_2 was within experimental error. The photolysis energy was varied by the introduction of meshes with 0, 1, 2, 3 meshes providing the four different initial OH concentrations plotted above.

Therefore, experiments were carried out varying the pump laser power from 0.75 to 16 mJ cm^{-2} per pulse at 6×10^{14} cm^{-3} H_2O_2 (0.07-1.7E12 cm^{-3} OH), and this produced no observed OH removal kinetic dependence on pump energy, Figure 3.20. Experiments were then performed at pump energies of 1 and 16 mJ cm^{-2} per pulse with 1×10^{15} cm^{-3} H_2O_2 the change in the average values for the rate of OH +H_2O_2 returned were (1920 ± 50) s^{-1} at 3×10^{12} cm^{-3} OH and (1900 ± 170) s^{-1} at 1.8×10^{11} cm^{-3}, two example experiments from these are shown as Figure 3.21.

Figure 3.21 OH removal kinetics measured with the same [H_2O_2] and varied OH concentration, at 1.8×10^{11} OH k_{obs}=(1883 ± 90) s^{-1} and 3.2×10^{12} OH with k_{obs}= (1884 ± 17) s^{-1} .

Experiments were then carried out varying the probe energy between 1 mJ and 60 mJ with 2.7×10^{15} cm^{-3} H_2O_2, where this was carried out a small dependence was observed for k_{obs} on radical concentration with a dependence of 1.4×10^{11} molecule cm^{-3} s^{-1} on the OH concentration, Figure 3.23. The observed removal rate variance with changes in OH concentration between 5×10^{11} and 3×10^{13} cm^{-3} (Figure 3.22) cannot be described well if the rate coefficient for OH and HO_2 is greater than 1×10^{-11} cm^{-3}. The increase in observed rate coefficient with laser power was in good agreement with a simple model of the effect expected from the reaction of OH with OH. Therefore it is expected to be responsible for only a small error in any assigned HO_2 yields where OH concentrations are kept below 1×10^{13} cm^{-3} and OH and H_2O_2 is maintained above 1500 s^{-1}.
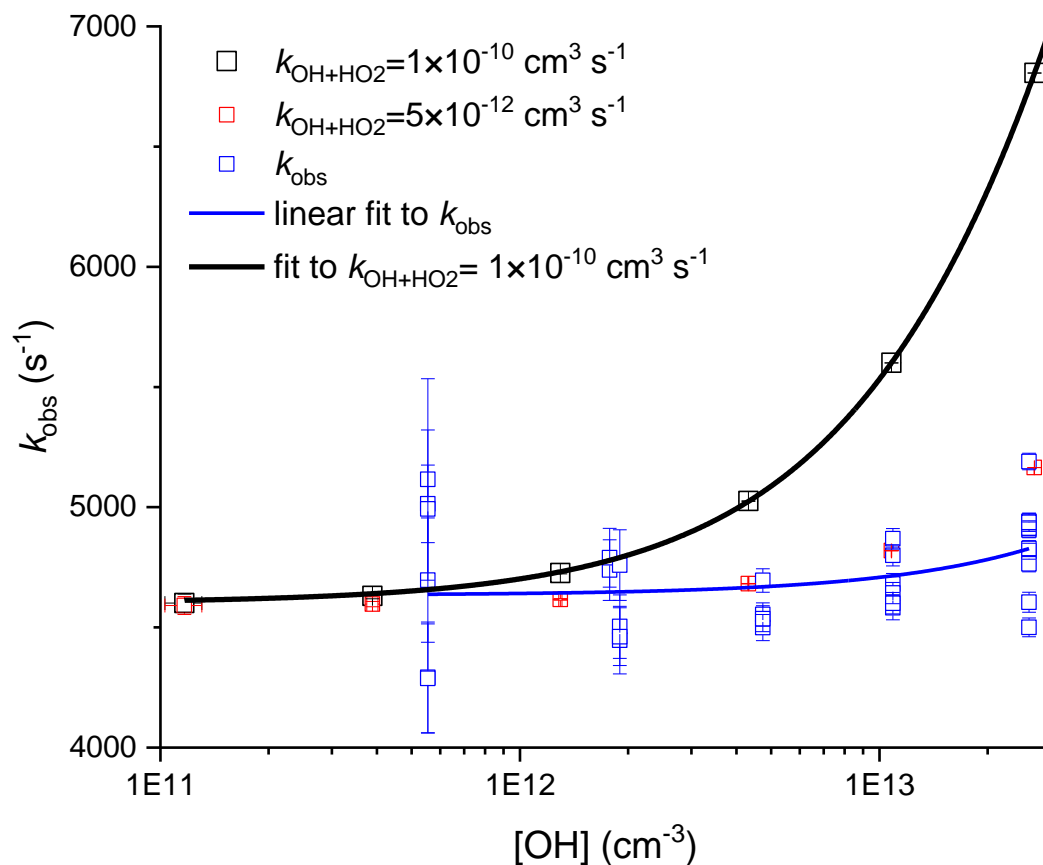
Figure 3.22 Expected and observed OH removal rates with 2.7×10^{15} cm^{-3} H$_2$O$_2$ and 1-60 mJ cm^{-2} photolysis energy at 248 nm and 10Hz The introduction of 0, 1, 2, 3, 4 meshes to reduce the photolysis light produced the five different initial OH concentrations plotted above.

The assignment of a lower observed reaction rate of OH and HO$_2$ to complexation of HO$_2$ to water would require far above the expected equilibrium ratio of complexed HO$_2$, and additionally no observed yield changes were present when the water concentration in the flow was changed by a factor of 3.

Additional experiments were then carried out in a conventional slow-flow low-pressure cell to measure the reaction of OH and H$_2$O$_2$ at two photolysis energies (1 mJ cm^{-2} and 117 mJ cm^{-2}), shown as Figure 3.23. As with the high-pressure system if the reaction of OH with HO$_2$ was the IUPAC literature value of 1.1×10^{-11} cm^3 s^{-1} then a large deviation in the observed removal kinetics of 40 % have occurred where the OH concentration was varied from 2.4×10^{11} to 2.7×10^{13} cm^{-3} in the presence of 1.3×10^{15} cm^{-3} H$_2$O$_2$ at 400 mbar in Argon.
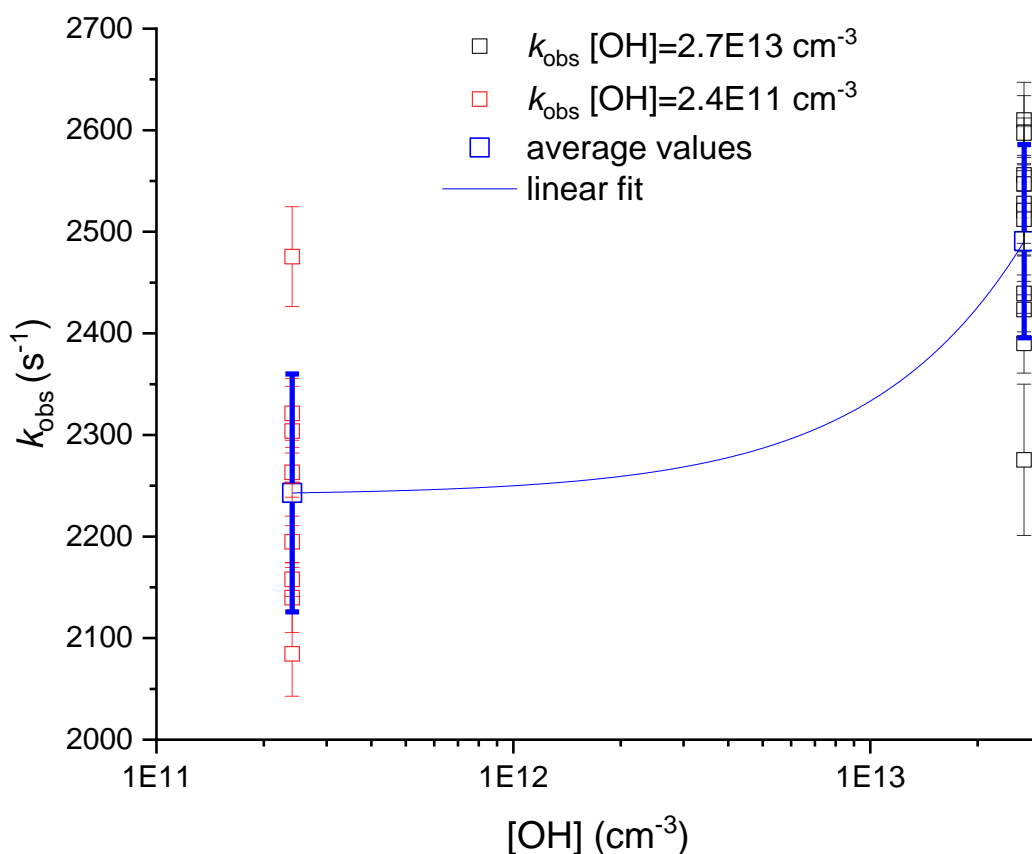
Figure 3.23 The observed OH removal rates at 2.4×10^{11} and 2.7×10^{13} cm^{-3} OH in 400 mbar of Argon with 1.3×10^{15} cm^{-3} H$_2$O$_2$. A linear fit to the data gave (9.3 ± 1.6) ×10^{-12} cm^3 s^{-1} with an average increase in observed rate of (11 ± 7) %.

As can be seen in the plot where the series of experiments was carried out there was only a small increase in observed removal rate, far lower than the expected 40 % increase. Because the concentration of H$_2$O$_2$ varied slightly over the course of the measurements only reactions taken consecutively should be compared explicitly, and when this was carried out the increase in reaction rate due to a 100 fold increase in OH concentration was (11 ± 7) %. This behavior was evaluated using the same model as used earlier but with the pressure dependent reactions adjusted to 400 mbar. Where a value for OH + OH was set to 8 × 10^{-12} cm^3 s^{-1} in line with that expected from the combination of the recombination reaction from Wagner *et al.* (2) and the IUPAC (1) recommended bimolecular rate coefficient, then any observed difference in removal rates can be explained as observation of OH + OH, leaving a maximum value for OH + HO$_2$ as <5 × 10^{-12} cm^3 s^{-1}. When the OH + OH rate used was 4 × 10^{-12} cm^3 s^{-1} in line with both IUPAC recommended values (1) then a maximum value for OH and HO$_2$ of (1 ± 1) × 10^{-11} cm^3 s^{-1} could be assigned.

Where the higher OH + OH removal value from Wagner *et al.* (2) was used, the high-pressure experiments and the low-pressure experiments were in perfect agreement that the OH + HO$_2$ removal observed was less than 5×10^{-12} cm^3 s^{-1}. When the lower OH + OH value from IUPAC was used, the slightly higher OH HO$_2$ rate obtained (($1 \pm 1) \times 10^{-11}$ cm^3 s^{-1}) in the low-pressure experiments would provide an improved fit to the observed chemistry in the high-pressure experiments than the literature value of 1×10^{-10} cm^3 s^{-1}.

That the reaction of OH + HO$_2$ has no effect on the reaction of OH with H$_2$O$_2$ where the OH was formed from the photolysis of H$_2$O$_2$, is supported by a previous paper on the reaction of OH with H$_2$O$_2$.(3) In Wine et al. the removal kinetics were not perturbed by the addition of O$_3$ to increase the initial HO$_2$ concentrations and OH concentrations with respect to the H$_2$O$_2$ concentration. In this work radical concentrations were in the range $(1-9) \times 10^{12}$ cm^{-3} for OH and where O$_3$ was added this increased the [OH] by up to a factor of 9.

This work verified that for the high-pressure system when the photolysis energy was kept below 30 mJ cm^{-2}, radical-radical reactions did not influence the observed OH removal kinetics nor the HO$_2$ yields. However, where higher photolysis energies were used OH + OH loss both perturbed the observed OH removal rate with H$_2$O$_2$, and introduced a small deviation in the assigned HO$_2$ yields that can now be accounted for within the analysis.

3.3.5 Ethanol and OH evaluating PTR-MS product analysis and HO$_2$ yields.

Running the PTR under the modified conditions (3.0 mbar PTR reactor and high H$_2$O flows), a calibration plot of the acetaldehyde concentration delivered through the high-pressure system, against observed counts was established, Figure 3.24. Both the parent mass (m/z 45) and the respective C13 peak (m/z 46) were plotted; both were linear within the range of added acetaldehyde ($3.5 \times 10^{12} - 1.75 \times 10^{13}$ molecule cm^{-3}) indicating there were no overload effects over this range of concentrations. Both the acetaldehyde calibration and the OH and ethanol experiments were carried out with PTR conditions of 79°C, 2.4 mbar, and with an entry voltage of 380 V, which gave a 'collision energy' of 82 Td.
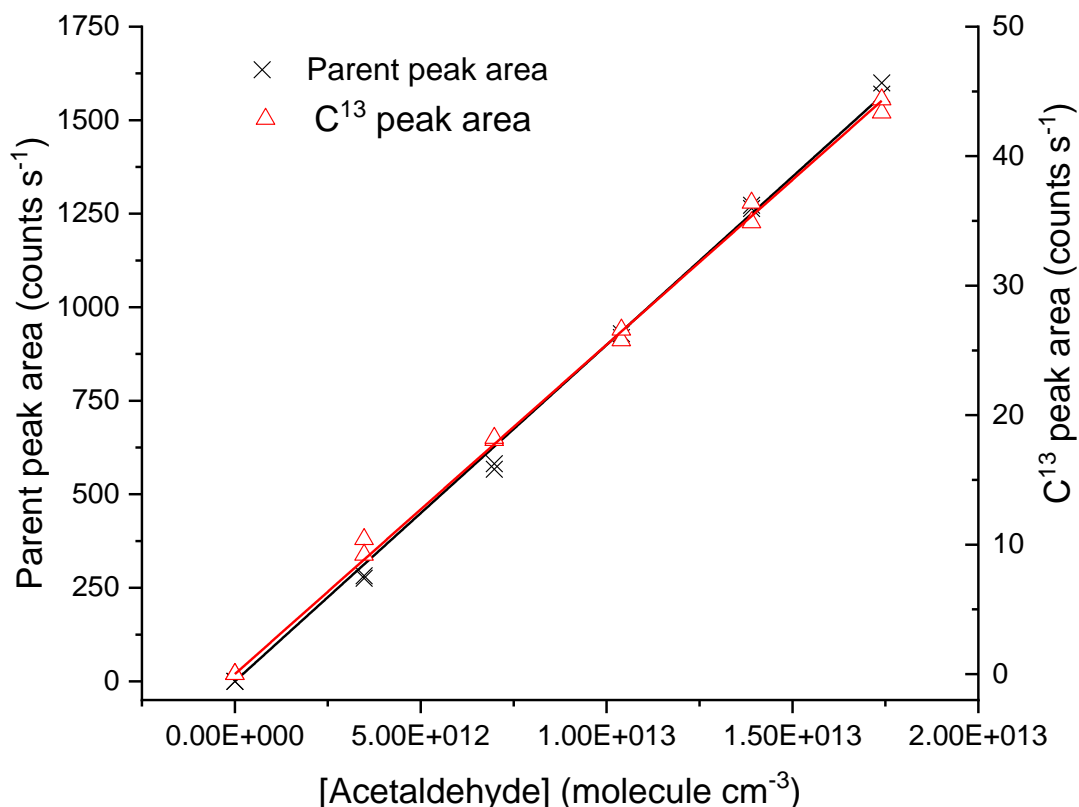
Figure 3.24 The observed change in PTR-MS peak areas observed over a range of added acetaldehyde, where both the parent mass (m/z 45) and the C^{13} peak (m/z 46) showed a linear relationship with added acetaldehyde indicating there was no overload affects within this range.

Photolysis experiments were performed using both tertiary butyl hydroperoxide (tBuOOH) and hydrogen peroxide (H_2O_2) as OH precursors. The experiments were carried out with a high oxygen concentration (5.3×10^{17} molecule cm^{-3}) to ensure that radicals formed from the abstractions were intercepted. The high-added oxygen introduced did provide the potential that the minor abstraction could be completely converted to glycoaldehyde (m/z 61); however, this was not calibrated as the low volatility of glycoaldehyde made producing a known standard complex.

The repetition rate of the photolysis laser was varied and the effect on the observed acetaldehyde counts was measured, and are plotted in Figure 3.25. For the range of repetition rates tested (0.2 – 5 Hz) there was a linear relationship between product formation and repetition rate. For the reactor setup used during these experiment, the time for transport through the photolysis region was 3 seconds, and as such, above 0.33 Hz multiple photolysis events would have occurred for the gas being sampled. For experiments carried out at 0.4 Hz and above, the response in formation of acetaldehyde

remained linear with repetition rate, which meant that although multiple photolysis events occurred, these did not significantly influence the observed chemistry.
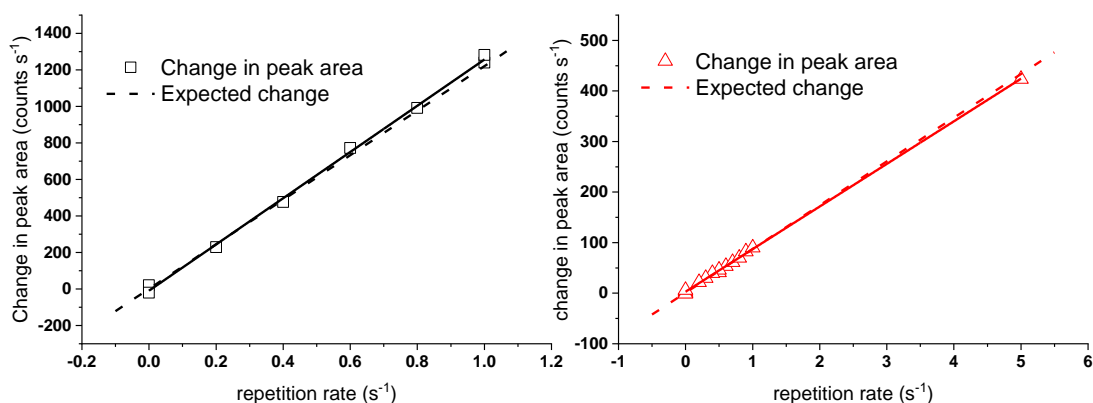
Figure 3.25 PTRMS observation of acetaldehyde formation versus repletion rate. The LHS plot, black, shows an experiment carried out with tBuOOH as an OH precursor plotting acetaldehyde formation from the reaction of OH and ethanol (1.0 × 10^{15} molecule cm^{-3}) in the presence of oxygen (5.3 × 10^{17} molecule cm^{-3}). The plot on the RHS, red, shows the reaction of OH and ethanol (2.5 × 10^{14} molecule cm^{-3}) in the presence of oxygen (5.3 × 10^{17} molecule cm^{-3}) over a range of repetition rates (0.2 – 5 Hz) with hydrogen peroxide as an OH precursor. Dashed lines represent the expected response from the expected OH concentration generated.

For reactions where the ability to assign product formation required that only a single photolysis event had occurred, the maximum repetition rate was 0.3 Hz. Once the preheated region was removed, the maximum repetition rate was increased to 1 Hz.

The expected yields of acetaldehyde from OH and ethanol using both H_2O_2 and tBuOOH as OH precursors were calculated in the following manner. First the k_{obs} from the removal rate in the absence of ethanol was measured, for H_2O_2 this was 950 ± 24 s^{-1}. With $k_{OH+H2O2} = 1.7 \times 10^{-12}$ cm^3 molecule^{-1} s^{-1} (33), this gave [H_2O_2] = $5.6 \pm 0.6 \times 10^{14}$ molecule cm^{-3}. The laser power was measured, and at 248 nm this corresponded to 2.43 × 10^{16} photons cm^{-3}. At 248 nm H_2O_2 has an absorption cross-section of 9.25×10^{-20} cm^2 molecule^{-1} (34) giving 0.0022 % photolysis. The photolysis of hydrogen peroxide has an OH quantum yield of 2. The OH concentration $(2.52 \pm 0.16) \times 10^{12}$ molecule cm^{-3} was then derived by combining the photolysis yield with the hydrogen peroxide concentration. The alpha abstraction that leads to acetaldehyde formation is 0.92,(35) and therefore the expected concentration of acetaldehyde was $(2.31 \pm 0.16) \times 10^{12}$ molecule cm^{-3}. The same calculation was then performed for tBuOOH.

When the expected acetaldehyde concentration was combined with the gradient from the calibration graph, Figure 3.24, an expected relationship between counts and

repetition rate was generated. This expected relationships is plotted as the dashed lines in Figure 3.25, where they compare well with the linear fits to the observed product formation.

The gradients of the linear fits, to counts against repetition rate, combined with a throughput time of 2.98 seconds gave single photolysis event yields. For tBuOOH, the yield of acetaldehyde per photolysis was $(3.43 \pm 0.10) \times 10^{13}$ molecule cm^{-3} which compared excellently with the expected yield of $(3.38 \pm 0.14) \times 10^{13}$ molecule cm^{-3}. The acetaldehyde yield from the reaction carried out with hydrogen peroxide was $(2.28 \pm 0.06) \times 10^{12}$ molecule cm^{-3} which again compared excellently with the expected yield of $(2.31 \pm 0.16) \times 10^{12}$ molecule cm^{-3}.

Instead of comparing the observed and expected yields, the branching ratios for OH and ethanol were experimentally assigned from the observed yields. Using the results above, the α branching fraction was assigned as 91 ± 6 % from the experiment carried out with H_2O_2 as the OH precursor, and 93 ± 3 % from the experiment carried out with tBuOOH as the OH precursor, where the errors are given as 2 sigma. Using the average of the two experiments, gave an alpha abstraction branching ratio of 0.92 ± 0.04 which is in excellent agreement with the previous experimental value published by Carr et. al. of 0.92 ± 0.08 (35), which was derived from a detailed kinetic study using isotopic substitution.

Adding HO_2 yields for the reaction of OH and ethanol can provide similar insight into the OH and ethanol branching ratios. As stated previously, the branching ratios for the reaction of OH with ethanol are $\alpha = 92 \pm 8$ % at room temperature with the β yield as 100-α %.(35) In the presence of sufficient oxygen ($>5 \times 10^{17}$ molecule cm^{-3}) the α-abstraction leads to prompt formation of HO_2, with the β-abstraction leading to the formation of an RO_2 radical. Therefore, the expected HO_2 yield is the alpha branching fraction, but the experimentally observed yield can include interference from hydroxyethyleneperoxy radicals.
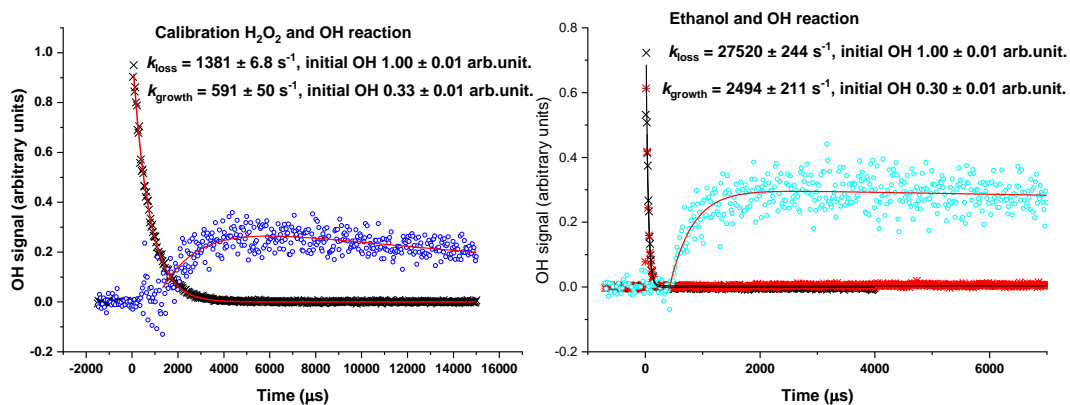
Figure 3.26 The OH traces and resultant OH from HO_2 traces associated with HO_2 yield assignment for an OH and ethanol measurement at (2.55 bar, 9.2×10^{15} molecule cm^{-3} ethanol, 5×10^{18} molecule cm^{-3} oxygen, 8×10^{14} molecule cm^{-3} H_2O_2). Processing these traces gave an OH + H_2O_2 contribution of 2 %, when this was accounted for an HO_2 yield from OH and ethanol of 91 % was assigned.

Experimentally, the average HO_2 yield assigned to the traces was 91 ± 12 %; an example experiment included in this average is shown as Figure 3.26. The excellent agreement between the expected and measured values validated the accuracy of this method for assigning HO_2 yields, even in the presence of radicals that have a known potential for interferences. Using the reaction of OH and ethanol, the ability to couple accurate end-product analysis, from both TOF-PTR-MS measurements and HO_2 yield detection, to the high-pressure system for collecting OH removal kinetics has thus been clearly demonstrated.

3.4 Summary

The importance of understanding the temperature of a flowing system has been discussed, and the use of chemical thermometers paired with thermocouple measurements has been validated for OH and methane. The temperature dependence of this reaction allows for the precise assignment of elevated temperatures, without the requirement to mechanically probe the gas in the reaction region. In addition, for the flow conditions assessed via the reaction of OH and methane, there was no observed temperature gradient for experimental timescales ranging between 100 microseconds and 95 milliseconds.

The effect that back streaming of sample gas into the corona discharge as a source of both mass peaks and fragmentation in PTR-MS measurements has been highlighted. The use of higher reactor pressures, and higher flow rates of water through the discharge

region, has been demonstrated to reduce fragmentation. Although, this was paired with a reduction in the ability to ionize particular compounds, including formaldehyde.

For the measurement of HO_2 yields, the ability to selectively detect HO_2 over RO_2 has been shown by the reaction of OH with ethane, where ethylperoxy titration was a minor interference (<5 %). The ability to mitigate the interference from species such as hydroxyethylperoxy. The timescale of OH regeneration from the RO_2 was slowed compared with that regenerated from HO_2 by performing the experiments under a 'starved NO' environment.

The validity of using the reaction of OH with H_2O_2 as the 100 % HO_2 yield standard was clearly demonstrated by comparison with the test reaction OH and methanol in high oxygen. In addition, for the reaction of OH and methanol under varied oxygen, the time resolution of the HO_2 detection was sufficient to differentiate the two routes to HO_2 formation. Where the alpha abstraction product CH_2OH and the beta abstraction product CH_3O have well separated reaction rates with oxygen, the differing HO_2 yields from low and high oxygen experiments showed the high precision with which HO_2 yields could be defined. For reactions carried out with a photolysis laser power under 50 mJ cm^{-2}, radical-radical reactions negligibly influence any observed OH removal kinetics and had no influence on the assignment of HO_2 yields.

For the reaction of OH with ethanol in the presence of oxygen, the simultaneous measurement of OH kinetics with the detection of an HO_2 yield provided the alpha branching fraction. Where the HO_2 yield 91 $\pm$ 12 % is in agreement with product formation observed by PTR-TOF-MS, 92 $\pm$ 4 %. Comparison of these with the literature ratio from Carr et al. 92 $\pm$ 8 % validated the ability of this instrument to provide branching ratios from both PTR product studies, and HO_2 yields.

3.5 References

1. MONKS, P.S. Gas-phase radical chemistry in the troposphere. *Chemical Society Reviews*, 2005, **34**(5), pp.376-395.
2. STONE, D., L.K. WHALLEY and D.E. HEARD. Tropospheric OH and HO$_2$ radicals: field measurements and model comparisons. *Chemical Society Reviews*, 2012, **41**(19), pp.6348-6404.
3. FUCHS, H., B. BOHN, A. HOFZUMAHAUS, F. HOLLAND, K.D. LU, S. NEHR, F. ROHRER and A. WAHNER. Detection of HO$_2$ by laser-induced fluorescence: calibration and interferences from RO$_2$ radicals. *Atmospheric Measurement Techniques*, 2011, **4**(6), pp.1209-1225.
4. HARD, T.M., R.J. O'BRIEN, C.Y. CHAN and A.A. MEHRABZADEH. Tropospheric Free-radical determination by FAGE. *Environmental Science & Technology*, 1984, **18**(10), pp.768-777.
5. WHALLEY, L.K., M.A. BLITZ, M. DESSERVETTAZ, P.W. SEAKINS and D.E. HEARD. Reporting the sensitivity of laser-induced fluorescence instruments used for HO$_2$ detection to an interference from RO$_2$ radicals and introducing a novel approach that enables HO$_2$ and certain RO$_2$ types to be selectively measured. *Atmospheric Measurement Techniques*, 2013, **6**(12), pp.3425-3440.
6. ATKINSON, R., D. BAULCH, R. COX, J. CROWLEY, R. HAMPSON JR, J. KERR, M. ROSSI and J. TROE. Summary of evaluated kinetic and photochemical data for atmospheric chemistry. *Not in System*, 2001, pp.1-56.
7. JIMÉNEZ, E., M.K. GILLES and A.R. RAVISHANKARA. Kinetics of the reactions of the hydroxyl radical with CH$_3$OH and C$_2$H$_5$OH between 235 and 360 K. *Journal of Photochemistry and Photobiology A: Chemistry*, 2003, **157**(2), pp.237-245.
8. STONE, D., M. BLITZ, T. INGHAM, L. ONEL, D.J. MEDEIROS and P.W. SEAKINS. An instrument to measure fast gas phase radical kinetics at high temperatures and pressures. *Review of Scientific Instruments*, 2016, **87**(5), p.054102.
9. SMITH, I.W.M. The temperature-dependence of elementary reaction rates: beyond Arrhenius. *Chemical Society Reviews*, 2008, **37**(4), pp.812-826.
10. HOUSE, E. Refinement of ptr-ms methodology and application to the measurement of (o)VOCs from cattle slurry. 2009.
11. BRILLI, F., B. GIOLI, P. CICCIOLI, D. ZONA, F. LORETO, I.A. JANSSENS and R. CEULEMANS. Proton Transfer Reaction Time-of-Flight Mass Spectrometric (PTR-TOF-MS) determination of volatile organic compounds (VOCs) emitted from a biomass fire developed under stable nocturnal conditions. *Atmospheric Environment*, 2014, **97**, pp.54-67.
12. LINDINGER, W., A. HANSEL and A. JORDAN. On-line monitoring of volatile organic compounds at pptv levels by means of proton-transfer-reaction mass spectrometry (PTR-MS) medical applications, food control and environmental research. *International Journal of Mass Spectrometry and Ion Processes*, 1998, **173**(3), pp.191-241.
13. YUJIE WANG, C.S., JIANQUAN LI, HAIHE JIANG, YANNAN CHU. Proton Transfer Reaction Mass Spectrometry (PTR-MS). *In*: M.S. LEE, ed. *Mass spectrometry handbook*. John Wiley & Sons, 2012, pp.605-630.
14. CZAKÓ, G., B. NAGY, G. TASI, Á. SOMOGYI, J. ŠIMUNEK, J. NOGA, B.J. BRAAMS, J.M. BOWMAN and A.G. CSÁSZÁR. Proton affinity and enthalpy of formation of formaldehyde. *International Journal of Quantum Chemistry*, 2009, **109**(11), pp.2393-2409.

15. GOEBBERT, D.J. and P.G. WENTHOLD. Water Dimer Proton Affinity from the Kinetic Method: Dissociation Energy of the Water Dimer. *European Journal of Mass Spectrometry*, 2004, **10**(6), pp.837-845.

16. WRIGHT, R. *Calibration Methodology for PTR-MS*. thesis, 2017.

17. SCHRIPP, T., C. FAUCK and T. SALTHAMMER. Interferences in the determination of formaldehyde via PTR-MS: What do we learn from m/z 31? *International Journal of Mass Spectrometry*, 2010, **289**(2–3), pp.170-172.

18. ESKOLA, A.J., S.A. CARR, R.J. SHANNON, B. WANG, M.A. BLITZ, M.J. PILLING, P.W. SEAKINS and S.H. ROBERTSON. Analysis of the Kinetics and Yields of OH Radical Production from the $CH_3OCH_2 + O_2$ Reaction in the Temperature Range 195–650 K: An Experimental and Computational study. *The Journal of Physical Chemistry A*, 2014, **118**(34), pp.6773-6788.

19. ZÁDOR, J., C.A. TAATJES and R.X. FERNANDES. Kinetics of elementary reactions in low-temperature autoignition chemistry. *Progress in Energy and Combustion Science*, 2011, **37**(4), pp.371-421.

20. DUNLOP, J.R. and F.P. TULLY. A kinetic study of hydroxyl radical reactions with methane and perdeuterated methane. *The Journal of Physical Chemistry*, 1993, **97**(43), pp.11148-11150.

21. HARD, T., L. GEORGE and R. O'BRIEN. FAGE Determination of Tropospheric HO and HO_2. *Journal of the atmospheric sciences*, 1995, **52**(19), pp.3354-3372.

22. ATKINSON, R., D.L. BAULCH, R.A. COX, J.N. CROWLEY, R.F. HAMPSON, R.G. HYNES, M.E. JENKIN, M.J. ROSSI and J. TROE. Evaluated kinetic and photochemical data for atmospheric chemistry: Volume II - gas phase reactions of organic species. *Atmospheric Chemistry and Physics*, 2006, **6**, pp.3625-4055.

23. ORLANDO, J.J., G.S. TYNDALL, M. BILDE, C. FERRONATO, T.J. WALLINGTON, L. VEREECKEN and J. PEETERS. Laboratory and Theoretical Study of the Oxy Radicals in the OH- and Cl-Initiated Oxidation of Ethene. *The Journal of Physical Chemistry A*, 1998, **102**(42), pp.8116-8123.

24. MCCAULLEY, J.A., N. KELLY, M.F. GOLDE and F. KAUFMAN. Kinetic studies of the reactions of F and OH with CH_3OH. *Journal of Physical Chemistry*, 1989, **93**(3), pp.1014-1018.

25. ATKINSON, R., S.M. ASCHMANN, A.M. WINER and J.N. PITTS. Rate constants for the reaction of OH radicals with a series of alkanes and alkenes at 299 +/- 2 K. *International Journal of Chemical Kinetics*, 1982, **14**(5), pp.507-516.

26. TULLY, F.P. Laser photolysis laser-induced fluorescence study of the reaction of hydroxyl radical with ethylene. *Chemical Physics Letters*, 1983, **96**(2), pp.148-153.

27. MEDEIROS, D.J., M.A. BLITZ, L. JAMES, T.H. SPEAK and P.W. SEAKINS. Kinetics of the Reaction of OH with Isoprene over a Wide Range of Temperature and Pressure Including Direct Observation of Equilibrium with the OH Adducts. *Journal of Physical Chemistry A*, 2018, **122**(37), pp.7239-7255.

28. LOCKHART, J.P.A., E.C. GROSS, T.J. SEARS and G.E. HALL. Kinetic study of the OH + ethylene reaction using frequency-modulated laser absorption spectroscopy. 2019, **51**(6), pp.412-421.

29. MOORE, S.B. and R.W. CARR. Molecular velocity distribution effects in kinetic studies by time-resolved mass-spectrometry. *International Journal of Mass Spectrometry and Ion Processes*, 1977, **24**(2), pp.161-171.

30. TAATJES, C.A. How does the molecular velocity distribution affect kinetics measurements by time-resolved mass spectrometry? *International Journal of Chemical Kinetics*, 2007, **39**(10), pp.565-570.

31.   BAEZA-ROMERO, M.T., M.A. BLITZ, A. GODDARD and P.W. SEAKINS. Time-of-flight mass spectrometry for time-resolved measurements: Some developments and applications. *International Journal of Chemical Kinetics*, 2012, **44**(8), pp.532-545.

32.   DUNLOP, J.R. and F.P. TULLY. A kinetic study of OH radical reactions with methane and perdeuterated methane. *Journal of Physical Chemistry*, 1993, **97**(43), pp.11148-11150.

33.   ATKINSON, R., BAULCH, D. L., COX, R. A., CROWLEY, J. N., HAMPSON, R. F., HYNES, R. G., JENKIN, M. E., ROSSI, M. J., AND TROE, J. Evaluated kinetic and photochemical data for atmospheric chemistry: Volume I - gas phase reactions of Ox, HOx, NOx and SOx species. *Atmospheric Chemistry and Physics*, 2004, **4**, pp.1461-1738.

34.   BURKHOLDER, J., S. SANDER, J. ABBATT, J. BARKER, R. HUIE, C. KOLB, M. KURYLO, V. ORKIN, D. WILMOUTH and P. WINE. *Chemical kinetics and photochemical data for use in atmospheric studies: evaluation number 18*. Pasadena, CA: Jet Propulsion Laboratory, National Aeronautics and Space Administration, 2015.

35.   CARR, S.A., M.A. BLITZ and P.W. SEAKINS. Site-Specific Rate Coefficients for Reaction of OH with Ethanol from 298 to 900 K. *The Journal of Physical Chemistry A*, 2011, **115**(15), pp.3335-3345.

4 Application of the system for OH and HO$_2$ measurement to butanol oxidation

4.0 Summary of chapter 4

OH and HO$_2$ radicals are closely coupled in the atmospheric oxidation and combustion of volatile organic compounds (VOCs). Simultaneous measurement of HO$_2$ yields and OH kinetics can provide the ability to assign site-specific rate coefficients that are important for understanding the oxidation mechanisms of VOCs. By coupling a FAGE LIF detection system, described in detail in chapters 2 and 3, for OH and HO$_2$ with a high-pressure laser flash photolysis system, it is possible to both collect high precision pseudo first order OH decays and to determine HO$_2$ yields via time resolved measurements. This time resolution allows discrimination between primary HO$_2$ from the target reaction and secondary production from side reactions.

As an application of the new OH and HO$_2$ instrument, the reaction of OH with n-butanol has been studied at 293 and 616 K. The bimolecular rate coefficient for OH and butanol at 293 K, $(9.2 \pm 0.4) \times 10^{-12}$ cm^3 molecule^{-1} s^{-1}, is in good agreement with recent literature, verifying that this instrument can measure accurate OH kinetics, in addition to measuring HO$_2$ yields. At 616 K the regeneration of OH in the absence of O$_2$, from the decomposition of the β-hydroxy radical, was observed, which allowed the determination of the fraction of OH reacting at the β site (0.24 ± 0.04). Direct observation of the HO$_2$ product in the presence of oxygen has allowed the assignment of the α-branching fractions (0.57 ± 0.06) at 293 K and (0.54 ± 0.04) at 616 K); branching ratios are key to modelling the ignition delay times of this potential 'drop-in' biofuel.

4.1 Introduction

4.1.1 OH and HO$_2$ detection by LIF from a high pressure reactor

In Scheme 4.1, the reaction of alkoxy radicals with molecular oxygen is a major route to HO$_2$ formation; however, this is not the only significant HO$_2$ formation process; for example, in the atmospheric oxidation of n-butanol, HO$_2$ can be formed via two different mechanisms. Abstraction by OH at the α position leads to a radical which reacts with oxygen to directly produce HO$_2$ and n-butanal (R4.1a, R4.2) whereas abstraction at other sites leads to alkylperoxy radical (C$_4$H$_9$O$_2$) formation with varying fractions of the RO$_2$ forming alkoxy radicals, and subsequently HO$_2$ (1) on a longer timescale.

$$OH + CH_3CH_2CH_2CH_2OH \rightarrow CH_3CH_2CH_2CHOH + H_2O \qquad (R4.1a)$$

$$CH_3CH_2CH_2CHOH + O_2 \rightarrow HO_2 + CH_3CH_2CH_2CHO \qquad (R4.2)$$
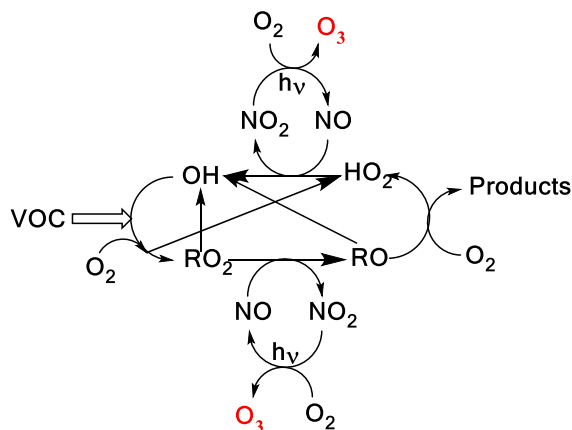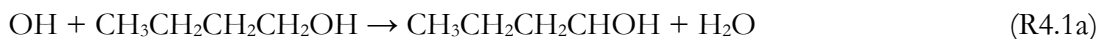
Scheme 4.1 A simplified tropospheric HOx cycle showing the importance of these short-lived radical species both to the chemical removal of VOCs and the formation of ozone.

The fraction of alkoxy radicals formed depends on the mechanism of RO_2 removal (reaction with NO or self or cross-reactions) and the yield of HO_2 from the alkoxy radical depends on the competition between decomposition, isomerization and reaction with O_2, which in turn will depend on the structure of the alkoxy radical, temperature, pressure and concentration of oxygen (2). Therefore, in order to determine the HO_2 yield from the OH initiated oxidation of compounds such as n-butanol, it is important to have a selective, sensitive and time resolved method of HO_2 detection.

HO_2 detection by LIF can be potentially sensitive to interferences from certain RO_2 species which may also be converted to OH on short timescales. As has been discussed earlier in chapter 3, interferences can be minimized by short conversion times between NO injection and OH monitoring, utilizing low pressures, high flow rates of the sample gas, and low NO concentrations to separate OH generation from HO_2 and RO_2, reduced conversion of HO_2 reduces the sensitivity of this technique and as such in practice a compromise between selectivity and sensitivity is used (3-5).

This work describes the study of OH initiated n-Butanol oxidation, carried out in the FAGE based instrument for OH and HO_2 detection described in Chapters 2 and 3, which is itself a development on an earlier FAGE based instrument for time-resolved OH detection (6). In this improved system, laser flash photolysis in a high pressure (up to 5 bar), temperature controllable (300 – 800 K) reactor generated radicals which were then

135

sampled through a pinhole forming a jet within the low pressure detection region. OH radicals were monitored by LIF close to the pinhole. The jet breaks down after ~20 mm and NO was injected after this point to convert some HO_2 into OH, which was then detected by a second monitoring system.
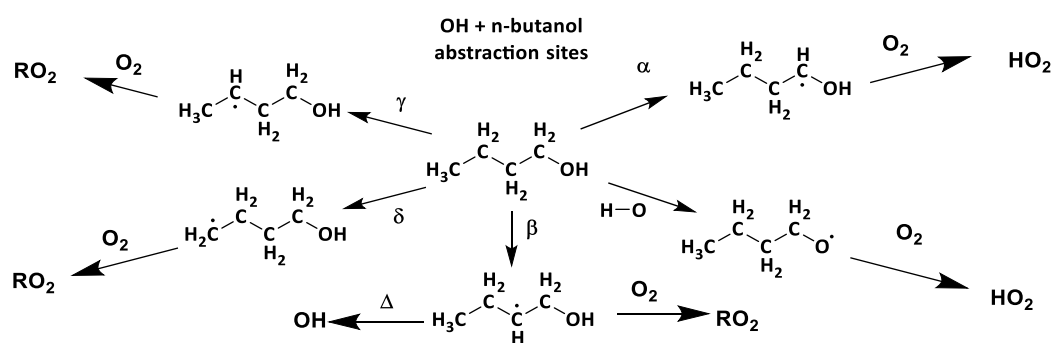
Scheme 4.2 The potential sites for OH abstractions in the oxidation of n-butanol. Of particular importance to low temperature combustion is the ratio of α to β branching fractions where α attack leads to chain inhibition and beta to chain propagation.

The branching ratios for the sites of OH attack on n-butanol, as presented in Scheme 4.2, are of significance to the modelling of the ignition delay times for n-butanol (7). Abstractions at the α and OH positions are chain terminating reactions at low temperatures due to the formation of the relatively inert HO_2 radical, and abstraction at the β site leads to chain propagation, through OH recycling. The new high pressure instrument permitted determination of the attack at the α and β sites; attack at the α site leads to prompt HO_2 formation in the presence of O_2; at elevated temperatures biexponential fits to non-single exponential OH loss traces in the absence of O_2 (due to decomposition of the β hydroxy radical to OH and iso-butene) allowed for attack at the β site to be measured.

From the work carried out on OH and methanol and OH and ethane described in chapter 3, it is believed that for simple RO_2 radicals this instrument can selectively titrate HO_2 to OH. However, for OH and ethylene the assigned HO_2 yield was caused by the titration of hydroxyetheylene peroxy. Studying the reaction of OH and butanol provides a potential interference where abstraction from the beta position can lead to the formation of an allylic hydroxy peroxy radical, at higher temperature the R radical decomposes to recycle OH and so cannot lead to HO_2 formation. By measuring the HO_2 yield as a function of temperature, assignment of the influence of the RO_2 species on the observed HO_2 yields can be assessed.

4.2 Experimental results

4.2.1 Room temperature OH kinetics

At room temperature under pseudo-first-order conditions ($[OH] < 3 \times 10^{12}$ molecule cm^{-3}, [n-butanol] $> 1.5 \times 10^{14}$ molecule cm^{-3}), the OH loss traces recovered from the first detection axis from the jet expanded gas corresponded closely to single exponential decays. These decays relate to the overall loss process for the reaction of OH with n-butanol:

$$OH + n\text{-}C_4H_9OH \rightarrow H_2O + \text{isomers of } C_4H_9O \tag{R4.1}$$
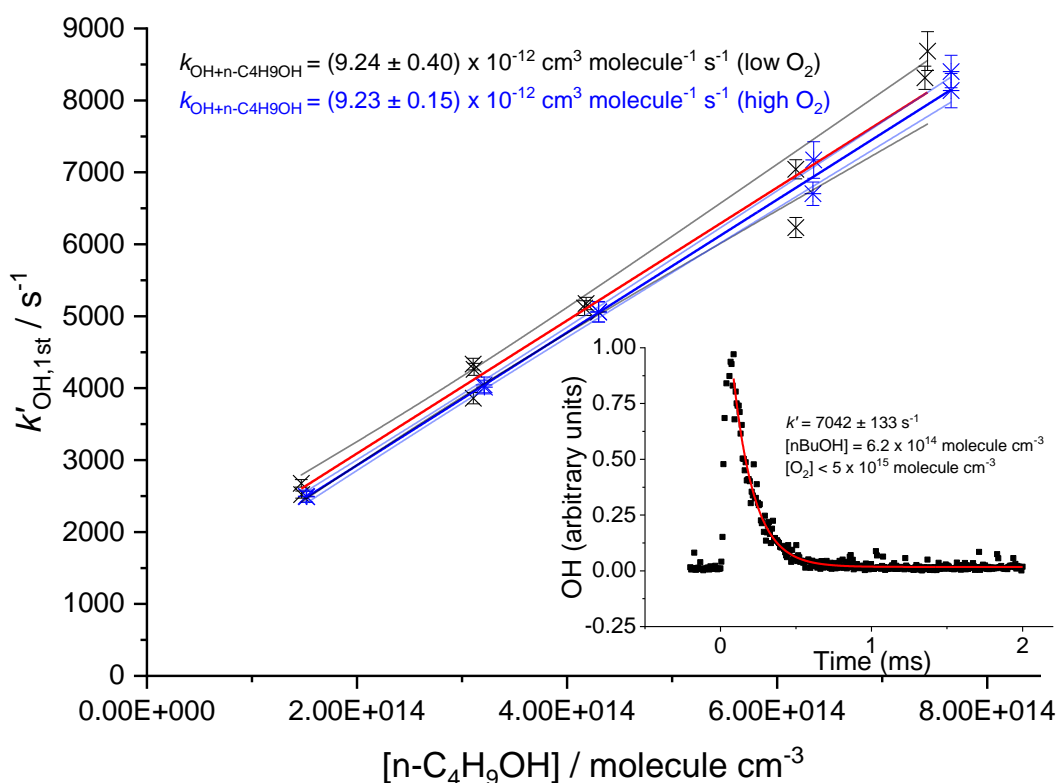
Figure 4.1   Plots $k'_{OH,1st}$ against the concentration of butanol, at two oxygen concentrations, $< 5 \times 10^{15}$ molecule cm^{-3} and 1.2×10^{19} molecule cm^{-3}. Bimolecular rate coefficients were taken from the slopes as $(9.24 \pm 0.40) \times 10^{-12}$ cm^3 molecule^{-1} s^{-1} under low oxygen conditions (black symbols with 95 % confidence limits), and $(9.23 \pm 0.15) \times 10^{-12}$ cm^3 molecule^{-1} s^{-1} under high oxygen conditions (blue symbols with 95 % confidence limits). The inset shows a typical OH temporal profile at the first detection axis.

The resulting rate coefficients were plotted against the concentration of butanol, in the presence of both low and high oxygen, as shown in Figure 4.1 (low oxygen $< 5 \times 10^{15}$ molecule cm^{-3}, high oxygen 1.2×10^{19} molecule cm^{-3}), where $k_{obs} = k_{bi} \times$ [butanol],

giving a resultant bimolecular removal rate of $k_{bi} = (9.24 \pm 0.40) \times 10^{-12}$ cm^3 molecule^{-1} s^{-1} under low oxygen conditions, and $k_{bi} = (9.23 \pm 0.15) \times 10^{-12}$ cm^3 molecule^{-1} s^{-1} under high oxygen conditions. The good agreement between the measured rate coefficients with varying [O$_2$] verifies that, as expected under our experimental conditions at room temperature, the R radical formed from the β abstraction does not undergo fragmentation to OH and but-1-ene. The resultant combined data gives an overall 293 K bimolecular rate coefficient for OH and n-butanol of $k_{bi} = (9.2 \pm 0.5) \times 10^{-12}$ cm^3 molecule^{-1} s^{-1}, which is in excellent agreement with the recent work of McGillen *et al.* (1) of $k_{bi,296} = (9.68 \pm 0.75) \times 10^{-12}$ cm^3 molecule^{-1} s^{-1}.

4.2.2 Room temperature HO$_2$ results

Experiments were carried out in high oxygen conditions ($3 \times 10^{17} - 1.2 \times 10^{18}$ molecule cm^{-3}), at 296 -303 K, and high pressures (1800 - 2000 Torr) of N$_2$ bath gas using photolysis of hydrogen peroxide at two different wavelengths (248 nm and 266 nm), and the resulting HO$_2$ yields are shown in Table 4-1. The resulting HO$_2$ yield was determined to be (58 ± 7) % at 266 nm, and (55 ± 12) % at 248 nm. As there is no significant variation in the yield with laser wavelength or power, the data in Table 4-1 can be treated as 12 independent estimates of the yield, giving an averaged HO$_2$ yield of 57% with a standard error (95%) of 6%. Therefore, under the experimental conditions (pressure >1800 Torr, [O$_2$] > 3×10^{17} molecule cm^{-3}), the HO$_2$ yield, which originates from OH attack at the α abstraction site, was (57 ± 6) %, with a minor contribution from abstraction from the hydroxyl group. The yield assigned is in good agreement with McGillen *et al.* (1) 57%, and Cavalli *et al.* (8) 52 ± 7 %.

Table 4-1 HO$_2$ yields from experiments carried out at room temperature (293 – 298 K) with reaction initiated by photolysis of H$_2$O$_2$ at 248 nm and 266 nm.

Laser wavelength/nm	HO$_2$ Yield (%)							Average Yield (%)
	Expt 1	Expt 2	Expt 3	Expt 4	Expt 5	Expt 6	Expt 7	
266	61 ± 7	54 ± 4	46 ± 5	56 ± 7	54 ± 7	67 ± 10	66 ± 6	58 ± 7
248	63 ± 2	68 ± 2	48 ± 5	52 ± 5	49 ± 5			55 ± 12

Experiments were carried out with photolysis at 266 nm and at a variety of laser energies (range) at 248 nm, the yields remained consistent with photolysis wavelength and power. Varying the laser power did alter the profiles of the HO$_2$ traces recovered; the growth rates remained unaffected but the tails changed; decreasing laser power slowed

the removal rate of HO_2 (from greater than 100 s^{-1} to under 10 s^{-1}) showing that radical-radical processes are the main source of HO_2 loss from the system. If radical-radical reactions were an important source of any observed HO_2 yield changing laser power would have altered the HO_2 yield and additionally the HO_2 growth kinetics.

4.2.3 Higher temperature – HO_2 yield and OH recycling
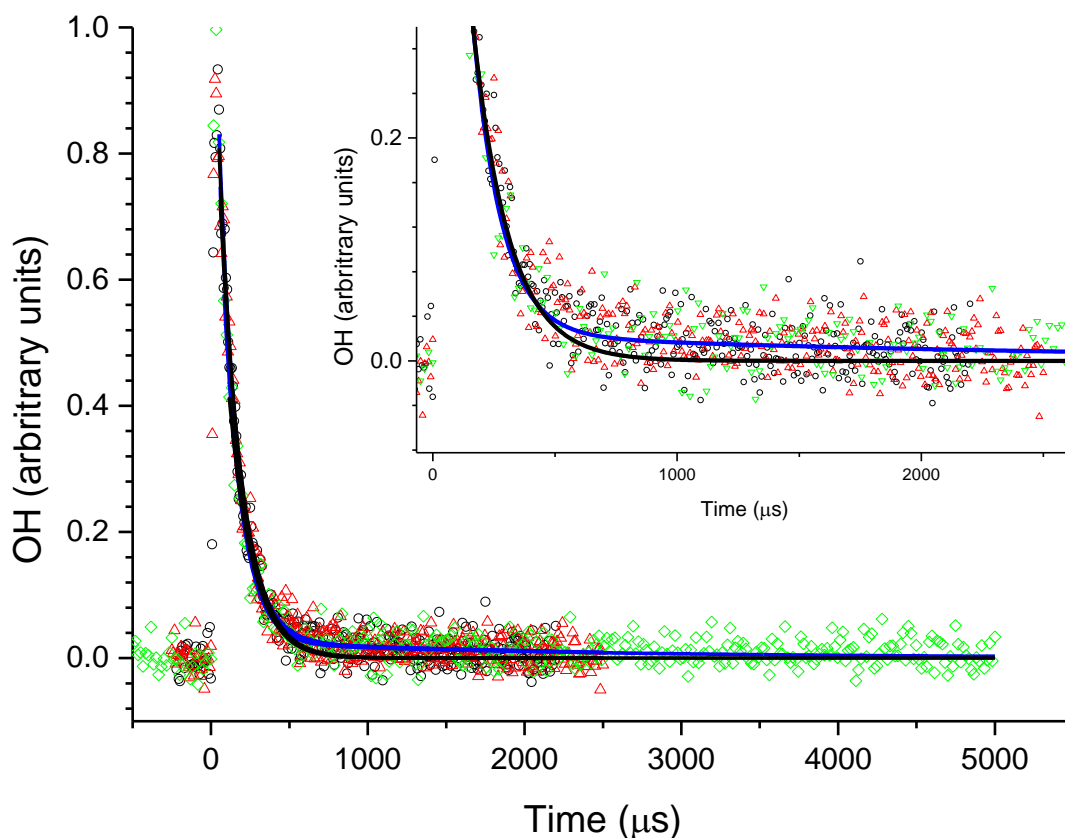
Figure 4.2 An example of the OH signal collected at the first detection axis for the reaction of OH with n-butanol ([nBuOH] ≈ 1.4×10^{15} molecule cm^{-3}, at 616 K. The inset displays a magnified view of the 2.5 ms of the decay. The black line represents the least squares fits to an exponential decay ($k'_{17,1st}$ = (6780 ± 380) s^{-1}), with the blue line representing a bi-exponential fit ($k_{17,biexp,1st}$ = (8190 ± 180) s^{-1})).

The R radical formed from abstraction at the β site ($CH_3CH_2CHCH_2OH$) can regenerate OH and form iso-butene, Scheme 4.2, in the absence of added oxygen. This process was not observed at ambient temperatures (293-305 K) but at elevated temperatures, 616 K – 660 K, the OH loss observed at the first detection axis was no longer well described by a single exponential loss process, Figure 4.2. The non-exponential decays formed were due to OH being returned following decomposition of

the β R radical. Biexponential fits to the recycling traces gave the fraction of OH returned, the β branching fraction as $(23 \pm 4)\%$, Table 4-2.

Table 4-2 OH recycling and HO₂ yields from experiments carried out under elevated temperatures (> 600 K) all experiments were carried out with photolysis at 248 nm.

Temperature (K)	Fraction of OH returned (%)	Observed HO₂ Yield (%)
616	24.2 ± 4.1	54 ± 4
622	24.4 ± 4.9	
636	25.7 ± 5.6	
657	18.1 ± 4.0	

The HO₂ yield measured at an elevated temperature (616 K), where OH recycling was also observed, was 54 ± 4 % (Table 4-2) which is within error of the value (57 ± 6 %) measured at room temperature (293 K), although it is not possible to partition the HO₂ yield between α and OH abstraction. Over the temperature range tested the branching ratio for OH attack at the α position is therefore also likely to remain unchanged. With the sum of the α and β sites contributing $(78 \pm 4)\%$, at 616 K, the remainder being the δ and γ sites. These results are in excellent agreement of the product study of Cavalli *et al.* (8) which found $(52 \pm 7)\%$ α from the butanal product yield and (23 ± 4) % β from the propanal yield using FTIR detection and the site specific analysis by McGillen *et al.* (1) (57 % α and 26% β). The product study of Hurley *et al.* (9) found 44 ± 4 % α and 19 ± 2 % β values which are lower than our experimental values but are within the combined error ranges. However, it should be noted that the β branching fraction of 23 ± 4 % measured in this study was obtained at elevated temperatures, 616 – 660 K.

4.3 Summary

It has been demonstrated earlier that this instrument can reliably assign HO₂ yields and simultaneously measure OH kinetics (Chapter 3), here it has been shown that this can be carried out even under conditions that include high temperatures and high oxygen concentrations, which could be challenging for other detection systems. Such conditions are important for exploring key combustion chemistry reactions, and for converting slow

atmospherically relevant processes to the microsecond timescales required to minimize secondary or heterogeneous chemistry.

For the reaction, illustrated in this chapter of OH with butanol in the presence of oxygen, the simultaneous measurement of OH kinetics and HO_2 yields can provide important site-specific information, which is important to the modelling of its application as a fuel. In other systems, the onset of HO_2 formation could allow for the assignment of new channels becoming important within complex mechanism, potentially allowing for verifying the onset of OOQOOH chemistry within OH regeneration processes.

4.4 References

1. MCGILLEN, M.R., M. BAASANDORJ and J.B. BURKHOLDER. Gas-Phase Rate Coefficients for the OH + n-, i-, s-, and t-Butanol Reactions Measured Between 220 and 380 K: Non-Arrhenius Behavior and Site-Specific Reactivity. *The Journal of Physical Chemistry A*, 2013, **117**(22), pp.4636-4656.

2. ORLANDO, J.J., G.S. TYNDALL and T.J. WALLINGTON. The atmospheric chemistry of alkoxy radicals. *Chemical Reviews*, 2003, **103**(12), pp.4657-4689.

3. FUCHS, H., B. BOHN, A. HOFZUMAHAUS, F. HOLLAND, K.D. LU, S. NEHR, F. ROHRER and A. WAHNER. Detection of HO_2 by laser-induced fluorescence: calibration and interferences from RO_2 radicals. *Atmospheric Measurement Techniques*, 2011, **4**(6), pp.1209-1225.

4. HARD, T.M., R.J. O'BRIEN, C.Y. CHAN and A.A. MEHRABZADEH. Tropospheric Free-radical determination by FAGE. *Environmental Science & Technology*, 1984, **18**(10), pp.768-777.

5. WHALLEY, L.K., M.A. BLITZ, M. DESSERVETTAZ, P.W. SEAKINS and D.E. HEARD. Reporting the sensitivity of laser-induced fluorescence instruments used for HO_2 detection to an interference from RO_2 radicals and introducing a novel approach that enables HO_2 and certain RO_2 types to be selectively measured. *Atmospheric Measurement Techniques*, 2013, **6**(12), pp.3425-3440.

6. STONE, D., M. BLITZ, T. INGHAM, L. ONEL, D.J. MEDEIROS and P.W. SEAKINS. An instrument to measure fast gas phase radical kinetics at high temperatures and pressures. *Review of Scientific Instruments*, 2016, **87**(5), p.054102.

7. AGBRO, E., A.S. TOMLIN, M. LAWES, S. PARK and S.M. SARATHY. The influence of n-butanol blending on the ignition delay times of gasoline and its surrogates at high pressures. *Fuel*, 2017, **187**, pp.211-219.

8. CAVALLI, F., H. GEIGER, I. BARNES and K.H. BECKER. FTIR kinetic, product, and modeling study of the OH-initiated oxidation of 1-butanol in air. *Environmental Science & Technology*, 2002, **36**(6), pp.1263-1270.

9. HURLEY, M.D., T.J. WALLINGTON, L. LAURSEN, M.S. JAVADI, O.J. NIELSEN, T. YAMANAKA and M. KAWASAKI. Atmospheric Chemistry of n-Butanol: Kinetics, Mechanisms, and Products of Cl Atom and OH Radical Initiated Oxidation in the Presence and Absence of NOx. *The Journal of Physical Chemistry A*, 2009, **113**(25), pp.7011-7020.

5 An experimental and computational study of the OH initiated oxidation of DMF

5.0 Summary of chapter 5

This work provides a summary of an extensive body of work studying the reaction of OH and dimethyl formamide (DMF). Direct OH kinetic measurements over an extensive temperature range (300 – 650 K), and pressure range (9 – 1800 Torr) for DMF gave $k_{OH+DMF}=1.317\times10^{-11}(\frac{T}{298})^{-0.5}e^{37.16/RT}$ cm^3 molecule^{-1} s^{-1}, with an ambient temperature value of $k_{298\,K}= (1.30 \pm 0.12) \times 10^{-11}$ cm^3 molecule^{-1} s^{-1}. For DMF, OH kinetic measurements were coupled to product studies via sampling with a TOF-PTR-MS, and indirect HO$_2$ detection via titration to OH. The experimental work on OH and DMF was supported by *ab initio* calculations and master equation work that allowed for evaluation of the routes to OH regeneration that were observed at temperatures over 450 K. From fitting these *ab initio* calculations to the experimental data for DMF the RO$_2$ to QOOH isomerisation barrier was assigned as (107.8 ± 1.3) kJ mol^{-1} and the QOOH decomposition to OH barrier as (90.3 ± 26.0) kJ mol^{-1}, with respect to the zero point energies of the well.

5.1 Introduction

The study of hydroxyl radical (OH) reactivity with amides, in particular N,N'-dimethylformamide (DMF), the structure of DMF is shown in Scheme 5.1, is of atmospheric importance. Notably, amides are often important high-volume industrial chemicals (>220,000 tonnes of DMF is produced per year world wide (1)); they are also products of the oxidation of more reduced nitrogen compounds (including amines used for carbon capture and storage), (2-8) and amides are often released from the degradation of organic matter. (9) Amides have not been the subject of the same number of studies as alcohols or aldehydes. (10) Additionally, there is evidence that the OH initiated oxidation of amides can lead to the formation of toxic and carcinogenic products, which include isocyanates, nitramines and nitrosomines. (3-8, 10-19)

Previous studies on the OH initiated oxidation of DMF have been performed at room temperature. The kinetics of the reaction of OH and DMF have been measured by relative rate methods, with several different reference compounds by Solignac *et al.* as (1.4

± 0.3) × 10^{-11} cm^3 molecule^{-1} s^{-1} (18), and by direct measurements as (0.80 ±0 .26) x 10^{-11} cm^{3}molecule^{-1}s^{-1} , by Bunkan *et al. (20)* The work by Bunkan *et al.* was performed over the temperature range 260 – 295 K. This work focuses on extending the temperature range from room temperature up to 600 K.

Scheme 5.1: The initial alkyl (R) radicals formed from the OH abstraction from dimethylformamide (DMF). Branching fractions are taken from Bunkan et al. (22)
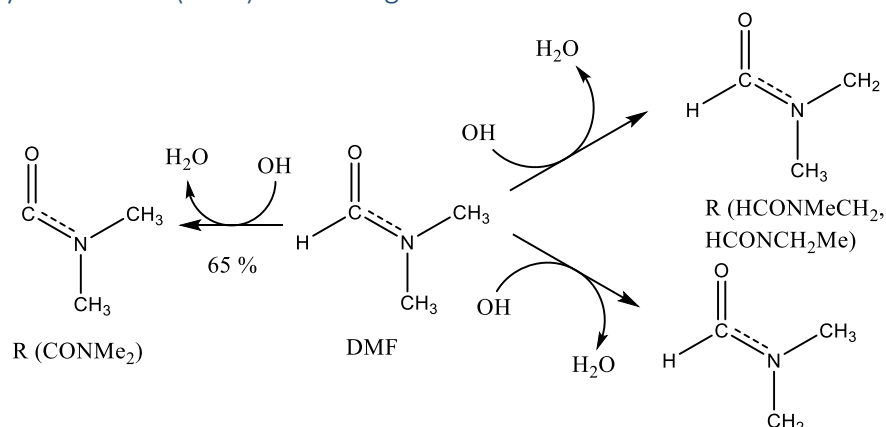
Product studies by Bunkan *et al.* showed high branching ratios for the aldehydic abstraction (65 %), (20) as shown in Scheme 5.1. Under ambient conditions, abstraction at the aldehydic position leads to the formation of an N centred radical. N centred radicals react slowly with oxygen (13, 21) and as such reactions with NO and NO$_2$ become more important, and these lead to the formation of nitramines and nitrosamines. (17, 22) Nitramines and nitrosamines are highly toxic and carcinogenic compounds (13, 23). That OH initiated amide oxidation appears to have a high potential for the formation of nitramines and nitrosamines in high NOx environments,(20) Scheme 5.2, is important. Formamides can be formed as a secondary products from amines released by carbon capture and storage (CCS) plants, (8, 24-28) which are typically high NOx environments. The majority product formed from abstraction from the methyl groups under ambient conditions has been shown to be N-formyl-N-Methyl-Formamide. (10, 20)
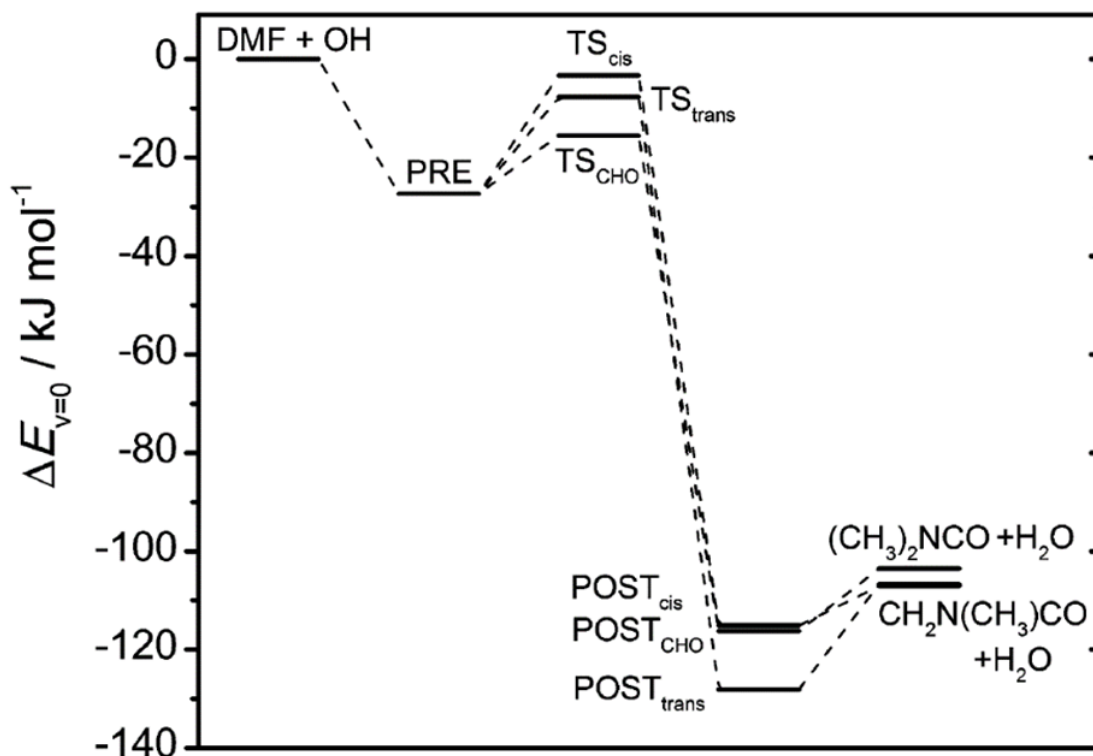
Figure 5.1: PES showing the energetics of the different abstraction reactions for DMF + OH with a low barrier for the aldehydic abstraction and the equivalency of the energies of the two isomers of the methyl abstractions alkyl radical. Taken from Bunkan *et al.* (22).

Scheme 5.2: The aldehydic abstraction channel under atmospheric conditions from Bunkan *et al.* (22).
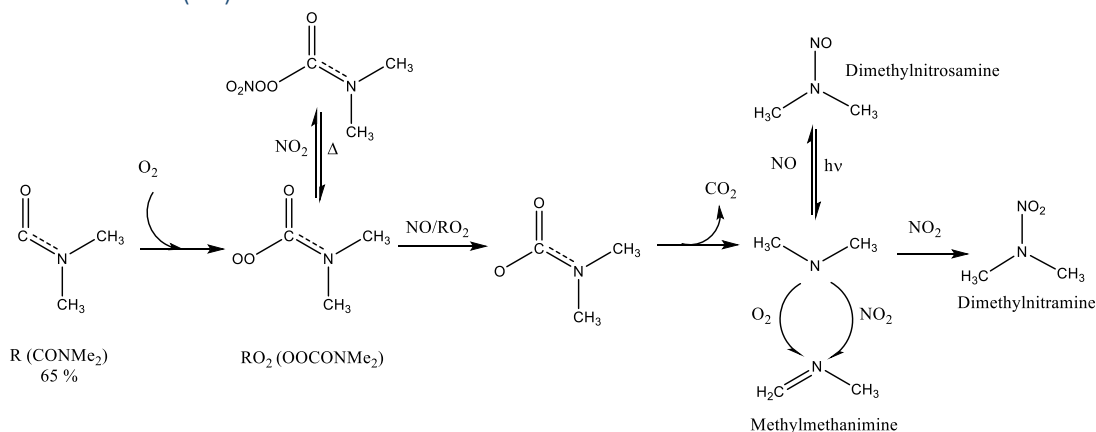
This work also explores how the oxidation pathways change with temperature, this could be of importance if the disposal of degraded amine wash solutions is to be via incineration and for the chemistry of biomass combustion plumes.

Computational work published by Bunkan *et al.* (20) provided a potential energy surface (PES) for the abstraction reaction, Figure 5.1, and for the subsequent oxygen

addition surfaces, Figure 5.2, at the CCSD(T*)-F12a/aug-ccpVTZ//MP2/aug-ccpVTZ level. The work by these authors, focussed on atmospheric conditions; a significant barrier to the isomerisation of the RO_2 to the QOOH radical and a large barrier to R fragmentation under atmospherically relevant temperatures meant further reactions were not of significant impact to their work.
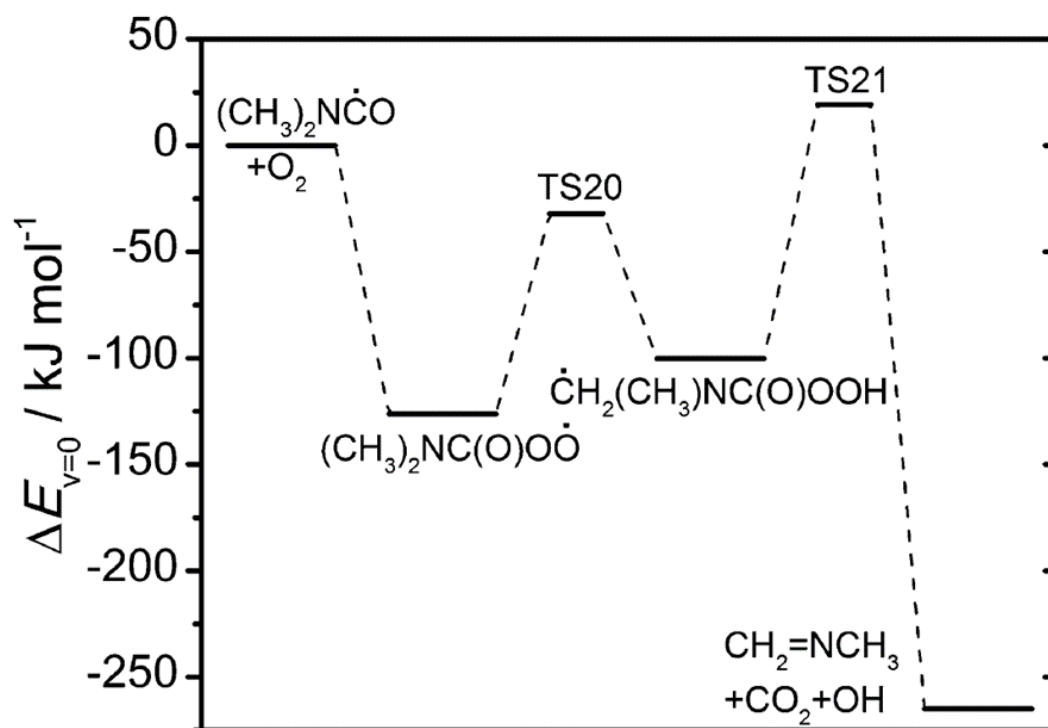
Figure 5.2: PES for the R+O_2 surface following abstraction at the aldehydic site. Taken from Bunkan *et al.* (22)

This work explores a higher temperature regime than Bunkan *et al.* and, as such, the computational work has focussed on studying key steps within low temperature combustion systems. Particular objectives include studying the R (amidyl) radical decomposition reaction and the ability of the system to recycle OH, where OH regeneration from the RO_2 (amidylperoxy), QOOH (hydroperoxyamidyl) and OOQOOH (hydroperoxyamidylperoxy) radicals is considered (shown as Scheme 5.3), over a variety of oxygen conditions, and over the temperature range (300 – 650 K).

The ability to reform OH from RO_2 and QOOH radicals and the ability to intercept QOOH radicals with O_2 to form OOQOOH are of great significance to combustion modelling. (29-36) The stability of the QOOH radical formed from the amide relative to the RO_2, and the significant barrier to QOOH decomposition from Bunkan *et al.* (Figure 5.2), (20) would allow for the QOOH radical well to be populated and as such

146

for QOOH to be efficiently intercepted by oxygen even at elevated temperatures (> 500 K).
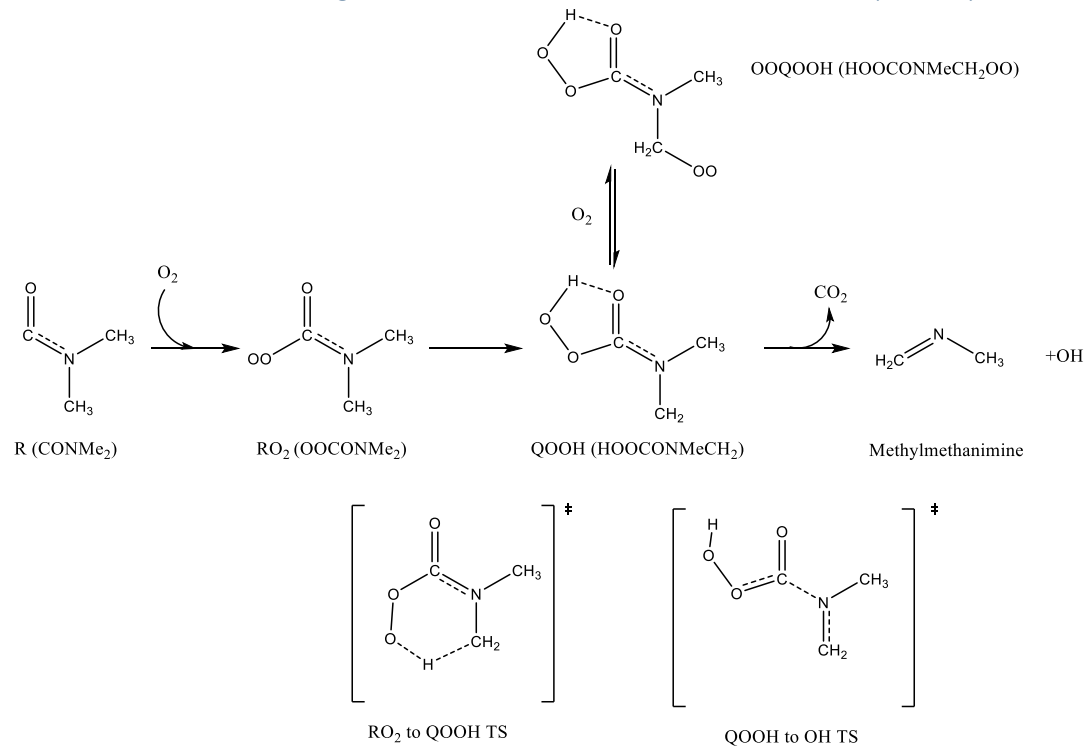
It followed that, by varying the oxygen conditions and observing how this affected the OH return rate coefficient and the HO_2 yields, would allow for parameters to be assigned for interception of both the R and QOOH radicals by oxygen. Direct observation and assignment of the kinetics of the QOOH radical formation and of the QOOH + O_2 reaction is an important area of study (30, 37) that so far has been limited to systems where the QOOH radical is not formed from the interception of an alkyl radical by oxygen, (38) or to systems where the QOOH radical is stable towards reaction with O_2, (39) or rapidly decomposes before reaction with O_2 where rate of QOOH decomposition is fast with respect to QOOH + O_2. (40, 41)

5.2 Experimental results

Data were predominantly collected in the high-pressure reactor system for OH and HO_2 detection that was coupled to a PTR-TOF-MS for end-product analysis, additional OH measurements were performed in a conventional low-pressure quasi-static cell. Delivered concentrations of dimethyl formamide were calculated from the Antoine equation, $\log(P/bar) = A - [B/(T/K + C)]$, using $A = 3.93068$, $B = 1337.716$, $C = -82.648$ which were experimentally measured over the range $303 - 363$ K and were taken

from Gopal *et al.* (42) The temperature of the bubbler was monitored with a thermometer and the backing pressure to the bubbler was monitored using a line regulator. If a better temperature dependence of the vapour pressure for DMF becomes available, the bimolecular rate coefficients given in this work should be summarily adjusted to account for this.

5.2.1 Room temperature OH and DMF rate coefficients and HO$_2$ yields

Bimolecular plots were generated over a range of pressure, an example room temperature plot, collected at high-pressures (1500 Torr) is shown in Figure 5.3, the high-pressure work was carried out as described in the experimental (chapter 2). A summary of the high-pressure data gives k_{OH+DMF} = (1.30 $\pm$ 0.15) x 10^{-11} cm^{3}molecule^{-1}s^{-1} at 295 $\pm$ 3 K, where error in k is given as 2 σ.

Although it is unlikely that there is any pressure dependence if direct OH abstractions dominate as is described by Bunkan *et al.,* Figure 5.1 (20), if the abstraction reaction occurs via addition to the carbonyl preceding an abstraction as suggested by Solignac *et al.*(18) this process could exhibit pressure dependence. In addition, for systems where OH recycling occurs, the amount of recycling observed at ambient temperatures can be pressure dependant.

Prompt OH recycling can occur because there are insufficient collisions to thermalize the RO$_2$ radicals formed into the RO$_2$ well, before the internal isomerization reactions occur to form QOOH radicals, and where the collisional stabilization of the QOOH radical is slow with respect to decomposition. To assess if this well-skipping OH recycling was present at room temperature, and if there was any evidence of OH addition, measurements were performed at 9 Torr and 52 Torr, in a conventional low-pressure cell, as described in chapter 2.
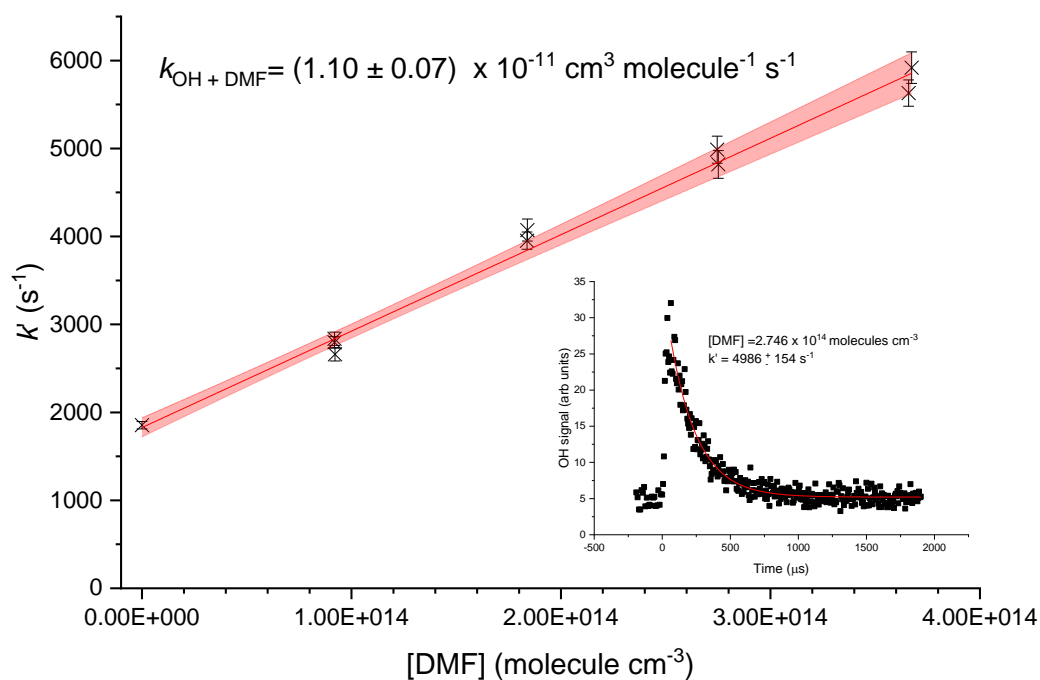
Figure 5.3: An example bimolecular plot taken at 297 K and 1830 Torr. The inset trace is an example showing the high precision with which the OH removal rates could be assigned, even when the OH fluorescence signal was sub optimal. The resultant bimolecular rate coefficient contained only the statistical error of the fits, and was assigned as $(1.10 \pm 0.07) \times 10^{-11}$ cm^{3}molecules^{-1}s^{-1}, errors given as 2 σ.

There was no evidence of any non-exponential kinetics being observed in the traces collected at either 9 or 52 Torr. The bimolecular plots gave $k_{OH+DMF} = (1.65 \pm 0.32) \times 10^{-11}$ cm^{3}molecules^{-1}s^{-1} at 9 Torr, and $k_{OH+DMF} = (1.44 \pm 0.04) \times 10^{-11}$ cm^{3}molecules^{-1}s^{-1} at 52 Torr, where errors were given as 2 σ. These were within the experimental error of the high-pressure values, and as such, it was assigned that there was no experimental evidence for any OH recycling under ambient conditions. These values were outside the experimental precision; however, due to the delivery issues with DMF they were within the accuracy of the high-pressure value. If any chemically activated route to prompt OH regeneration was present, this would lead to a lower observed bimolecular removal rate at lower pressures and this was not observed.

The ability to simultaneously collect OH kinetics and HO$_2$ yields was utilised during some of the experiments carried out at room temperature. Any HO$_2$ formed must be formed on a fast timescale, as described in chapter 3, and as such must come from a direct R + O$_2$ or RO$_2$ decomposition reaction, under our experimental conditions. It was noted that there was an apparently substantial HO$_2$ yield of 35 ± 7 % at room temperature, when photolysis was carried out at 248 nm. It was not immediately apparent where a prompt

149

source for this HO$_2$ yield could be found, from either the aldehydic, Scheme 5.2, or the methyl abstraction channels, shown as Scheme 5.4.
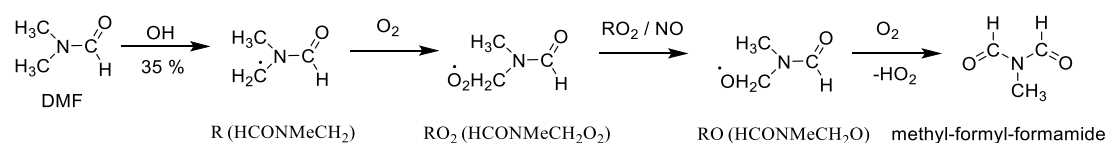
Scheme 5.4 The methyl abstraction reaction scheme adapted from Bunkan et al. (20). The route to HO$_2$ formation requires RO$_2$-RO$_2$ chemistry for HO$_2$ radicals to be generated.
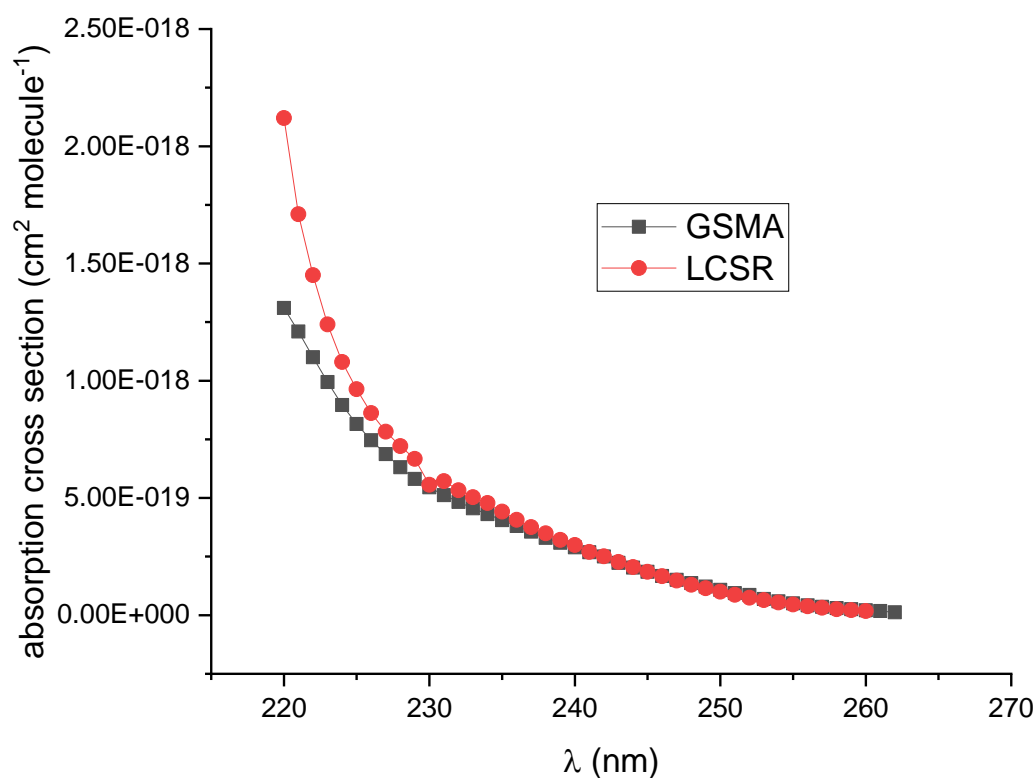
Figure 5.4 The UV absorption cross-section of N,N'-DMF, measured by Chakir *et al.*,(43) and plotted from the room temperature values given from the Mainz spectral atlas. (44) Red circles were measured at LCSR in Orléans, and grey squares at GSMA in Reims.

A potential route to HO$_2$ formation was identified as being via photolysis of DMF itself, as DMF has a large UV absorption cross-section at 248 nm (2×10^{-19} cm^2 molecule^{-1}). (43) With photolysis of DMF cleaving either an H atom or HCO, both of which would lead to prompt HO$_2$ formation, under our experimental conditions ($> 1 \times 10^{16}$ molecule cm^{-3} O$_2$). Experiments were therefore carried out with photolysis at 266 nm, here the apparent HO$_2$ yield was greatly reduced to less than 5 ± 8 %. Additional

experiments were also carried out with photolysis at 248 nm in the absence of an OH precursor; these experiments showed significant HO_2 signal in the absence of any OH signal.

The experiments carried out at 266 nm showed that HO_2 detection could be used as an effective way to monitor how significant photolysis of DMF itself was as a source of radicals to any subsequently observed chemistry. Additionally, this shows that 266 nm photolysis often allows for 'cleaner' experiments than photolysis at 248 nm or 193 nm, where photolysis of reagents can be significant.

5.2.2 Room temperature PTR-MS for DMF

TOF-PTR-MS spectra were taken at room temperature, with photolysis at 248 nm and at 1 Hz. When the reaction was performed in a NOx free system, the only significant product formation observed was at m/z 60 and 88. When NO_2 was then introduced (2.5×10^{16} molecule cm^{-3}) a peak at m/z 91 was also observed. These were assigned as N-formyl-n-methyl-formamide at 88 (87+1), the major product from the methyl abstraction sites, Scheme 5.4. A product at m/z 60 (59+1; $CH_3NCHOH\ H^+$, $CH_3NHCHO\ H^+$) was observed, and was in competition with m/z 88 under lower oxygen regimes and was assigned as a product from the fragmentation of the alkoxy radical, $CH_3N(CHO)CH_2OO$. Dimethylnitramine m/z 91 (90+1) formed via titration of the nitrogen centred radical, formed from the aldehydic channel, with NO_2 and was the only PTR-MS observable product, under atmospheric conditions under our experimental timescales, from the aldehydic abstraction reaction, Scheme 5.2. The same product at m/z 91 could also potentially be formed from the direct photolysis of DMF at 248 nm.
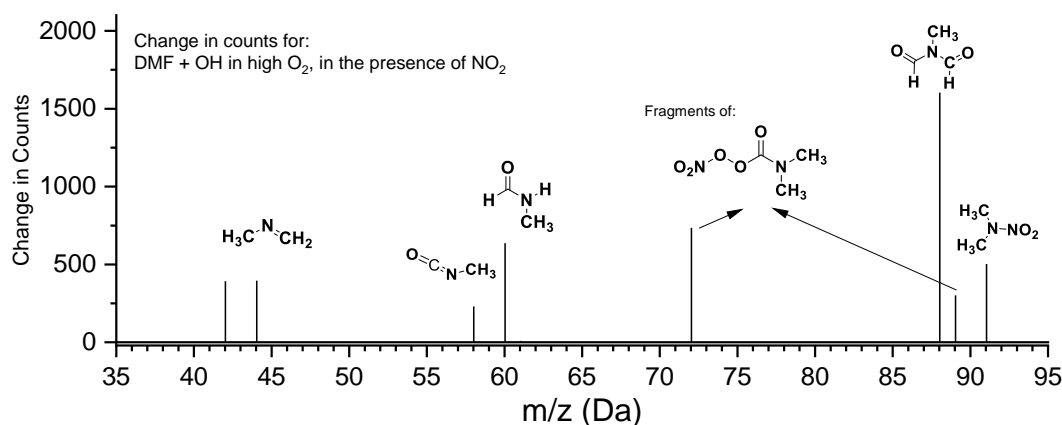
Figure 5.5 The observed change in peak area observed from the reaction of DMF with OH at room temperature (293 K) in high oxygen (7.6×10^{17} molecule cm^{-3}) in the presence of NO_2 (2.5×10^{16} molecule cm^{-3}), where reaction was initiated by photolysis of H_2O_2 at 248 nm.

5.2.3 Elevated temperature OH and HO$_2$ for DMF

Over the range of temperatures studied (293 – 615 K) there was evidence for a negative temperature dependence for the OH + DMF reaction (shown in Figure 5.6) with k_{OH+DMF} at 611 K potentially as low as $(0.50 \pm 0.04) \times 10^{-11}$ cm^{3}molecule^{-1}s^{-1}. However, designation of this temperature dependence is impacted by several sources of experimental error, loss of reagents and inaccuracies in assignments of the temperature are significant above 550 K. At elevated temperatures (> 500 K) there was evidence from the PTR-MS spectra for loss of diemthylformamide via pyrolysis and reaction with the OH precursors. At 500 - 650 K, the DMF peak at m/z 74 was dependent on the oxygen concentration and peroxide flow, and could be reduced to 20 % of the room temperature value for the same input flow conditions). As the PTR-TOF-MS is a mixing ratio detector, when the flows delivered are the same, the same peak areas should be observed on the PTR-MS, above 550 K, the peak areas observed for DMF and its ^{13}C peak were lower than at room temperature, and this reduction in peak area was dependant on the percentage of oxygen in the flow. A modified Arrhenius fit ($k=A(\frac{T}{298})^{n}e^{-Ea/RT}$) to the data in Figure 5.6 gave ($k=1.317\times10^{-11}(\frac{T}{298})^{-0.5}e^{37.16(J\,mol^{-1})/RT}$) giving $k_{298\,K}=(1.30 \pm 0.12) \times 10^{-11}$ cm^3 molecule^{-1} s^{-1}.
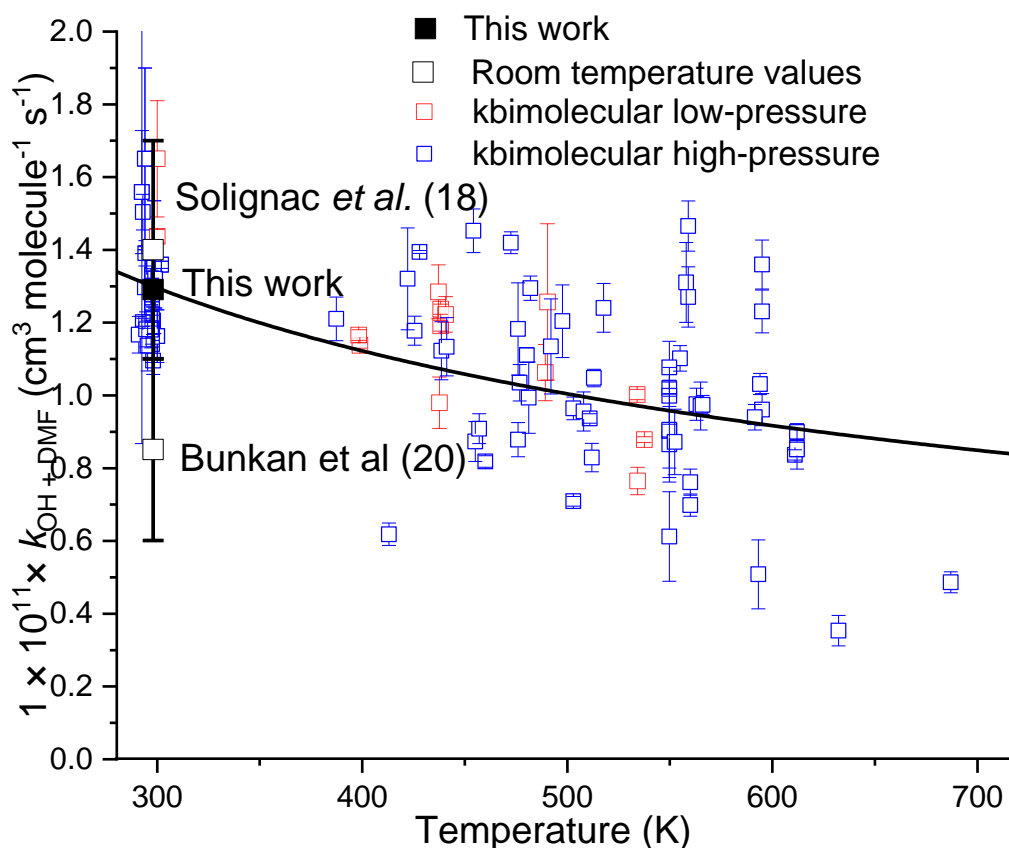
Figure 5.6: The temperature dependence of OH and dimethylformamide. Above 450 K where, recycling is observed k_{OH+DMF} was assigned from biexponential fits; above 550 K pyrolysis can be significant. The average room temperature high pressure value, given as a black square, is compared with the values of Solignac *et al.* (18) and Bunkan *et al..* (20), these values are shown as open black squares, individual experiments carried out at low pressures (< 100 Torr) are given as open red squares, and those taken at the high pressure (> 1300 Torr) as open blue squares.

Interestingly, in the presence of oxygen at temperatures above 450 K, experimental OH traces ceased to conform well to single exponential kinetics, shown clearly in Figure 5.7. These traces had a fast initial loss of OH followed by a much slower loss regime. Experiments were performed with photolysis at 248 nm and 266 nm, with additional experiments performed in the absence of an OH precursor. These experiments showed no OH formation in the absence of a precursor, and verified that the observed OH recycling was not a product of direct photolysis of DMF, and was from an OH initiated chemistry.
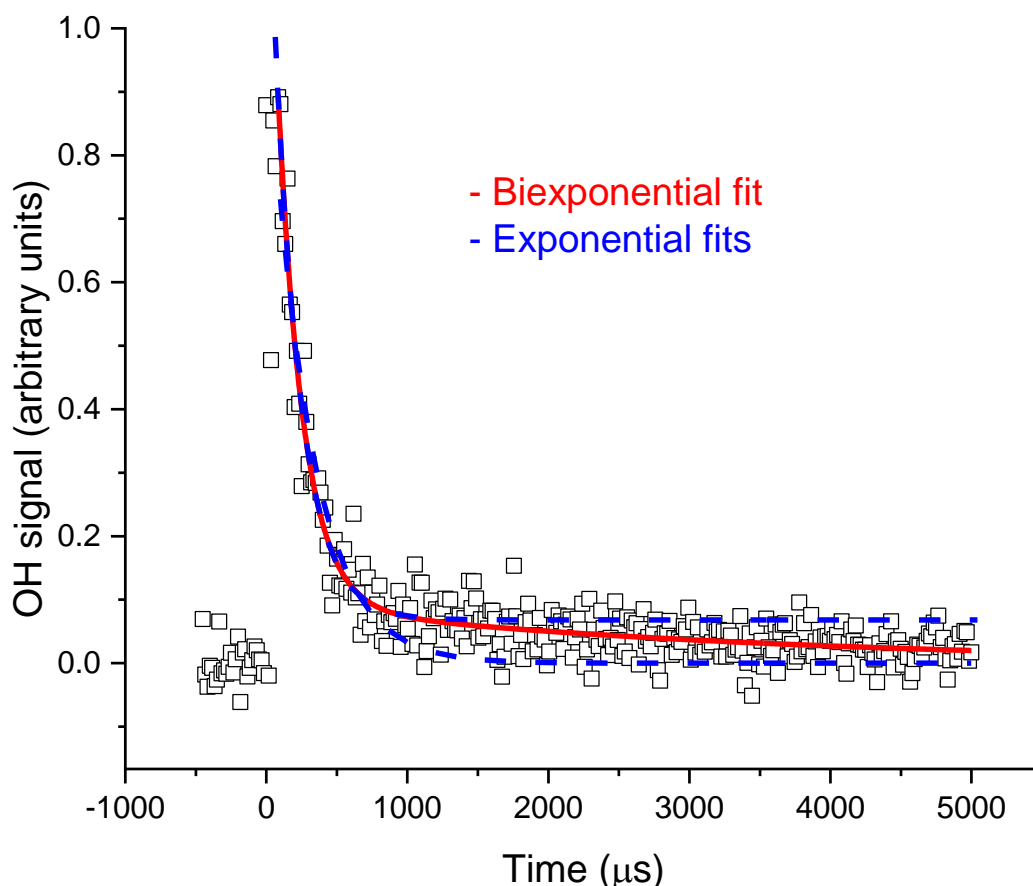
Figure 5.7: An example multi-exponential OH decay trace, taken at 550 K in the presence of O_2, and compares exponential fits to a biexponential fit, using the model shown in Scheme 5.5. With k_a= (4236 ± 235) s^{-1}, at [DMF] = 3.45 × 10^{14} molecule cm^{-3}, with k_B= (414 ± 45) s^{-1} in the presence of 1.4 × 10^{18} molecule cm^{-3} of oxygen.

Scheme 5.5: The model utilised for the simple biexponential fit, shown diagrammatically, this considered the OH radical kinetics giving k_a, k_b, and k_2. The dotted line accounts for all loss process that followed the initial abstraction which did not lead to OH reformation.
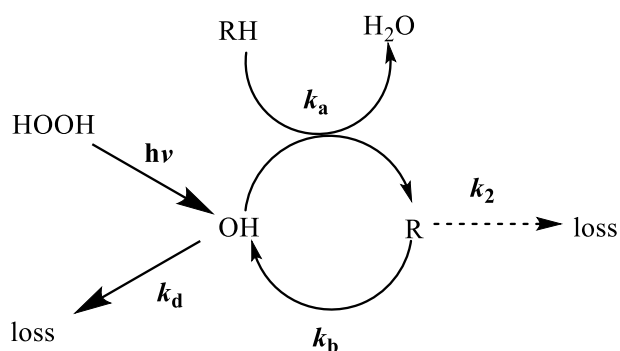
The non-single exponential decay was a consequence of OH being regenerated, initial fits of these traces used a simplified biexponential decay model, shown in Scheme 5.5, that

assumes the amidyl radical either reacts to reform OH or on to form other products. The model returns parameters k_a, k_b, k_2, if the baseline and loss rates are fixed, from a given trace.
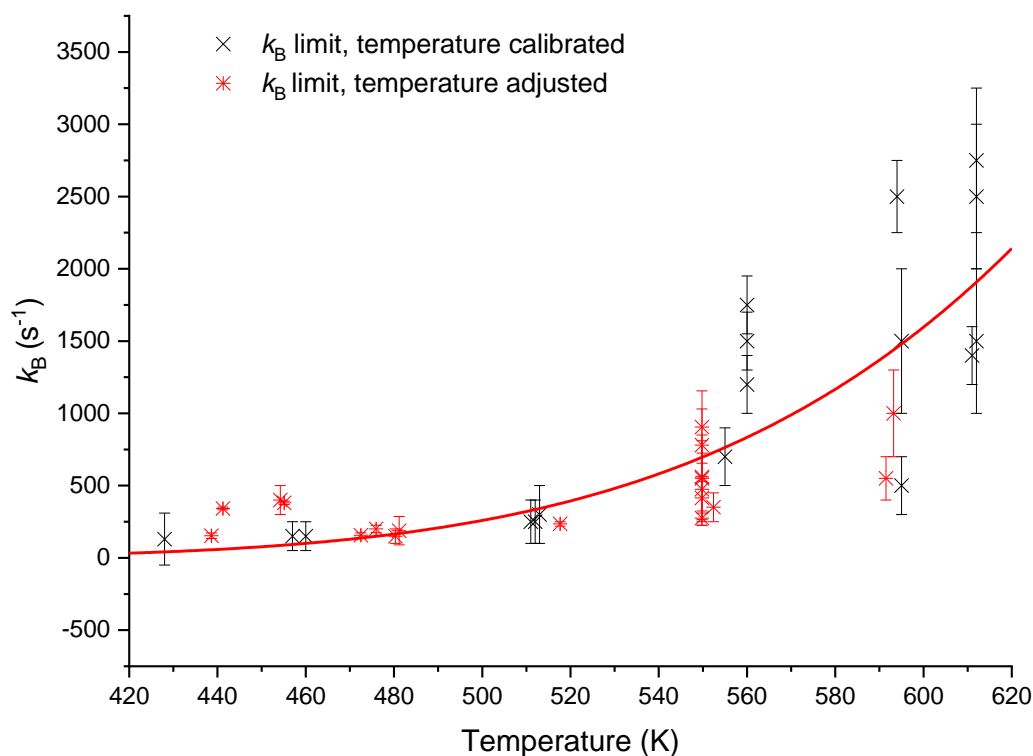
Figure 5.8: The temperature dependence of the return rate coefficient for OH, k_b. The values in red use an adjusted temperature to account for thermocouple errors by a parameterization, the black points were performed at a temperature where OH + CH_4 had been measured under the same flow conditions. The red curve is an exponential fit, with $k_{b,298K}=(0 \pm 15)$ s^{-1}. As R + O_2 was in competition with R decomposition the high oxygen limit for the return parameter was plotted, k_B limit.

The return rate coefficient, k_b, was measured over a range of temperatures (450 – 650 K) and showed a strong temperature dependence, Figure 5.8. This temperature dependence could be assumed to be related to the barrier to RO_2 QOOH isomerisation, or to the barrier to OH reformation from the QOOH or OOQOOH radicals.

The return rate parameter, k_b, was also collected over a variety of added oxygen concentrations (1×10^{17} - 3×10^{18} molecule cm^{-3}) and in the absence of added O_2 (< 2 $\times 10^{16}$ molecule cm^{-3}). Plotting return rate versus oxygen concentration at a given temperature, an example of which is shown in Figure 5.9, reveals two regions: a return rate limited region at higher oxygen concentrations where the rate of recycling is

independent of oxygen concentration, and an oxygen limited region where the rate of OH recycling is dependent on the amount of oxygen added to the system.
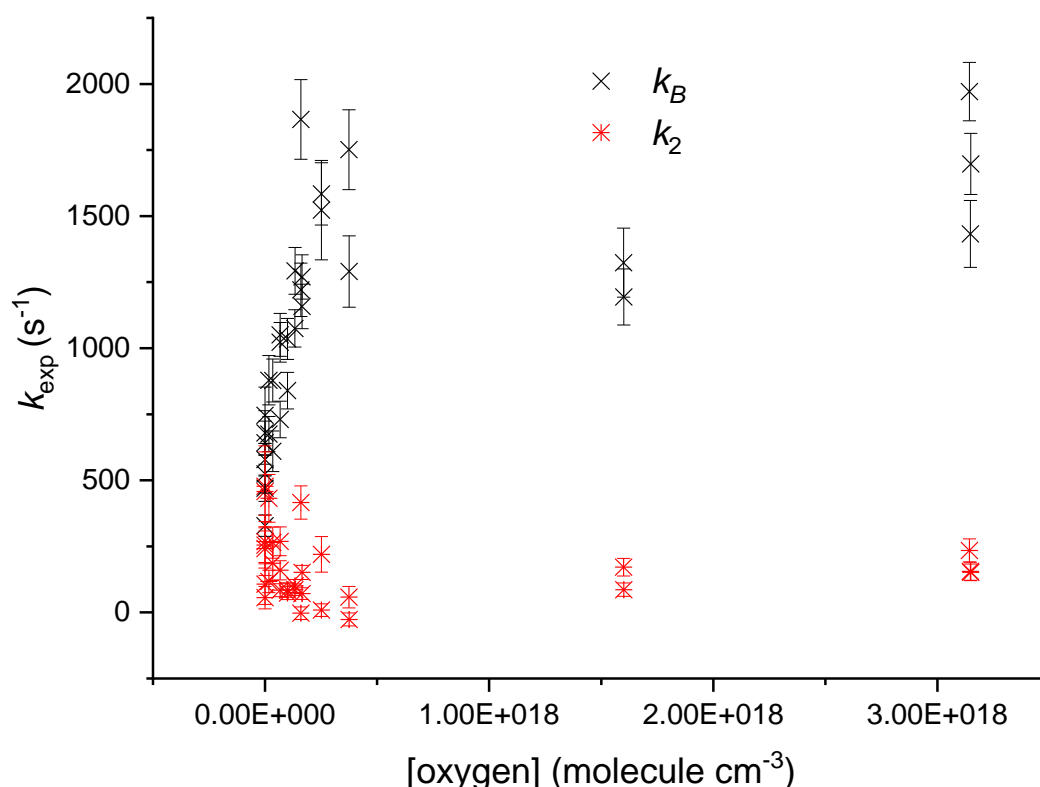
Figure 5.9: Plots the oxygen dependence of the return rate coefficient, k_b plotted as black crosses, at 550 K, and 1500 Torr. The relationship between k_2, plotted as red crosses, to k_b at low oxygen is due to the competition between fragmentation and interception by oxygen.

The cause of this oxygen dependence was assigned as amidyl radical decomposition being in competition with the $R+O_2$ reaction. As the R radical decomposition is very temperature sensitive, so is the oxygen dependence of the return rate coefficient. To allow for improved data analysis required a more complicated method of fitting the data, where the $R+O_2$ reaction was no longer assumed to be instantaneous but instead both the decomposition rate and the $R+O_2$ reaction rate were fitted; for clarity this model is shown in Scheme 5.6. R radical decomposition was assigned from computational work carried out using MESMER, (master equation solver for multi-energy well reactions) to carry out master equation calculations, on a high level *ab initio* surface (CCSD(T)/CBS(dz,tz,qz,5z)//mp2/6-311++g(3df,3pd)), to give calculated rate coefficients for each experimental condition.

By using the fit with parameterised R+O$_2$ and R decomposition, Scheme 5.6, the alkyl + O$_2$ reaction rate and the dependence of OH recycling on the oxygen concentration could be assigned. An example global analysis of the experimental data taken over a variety of oxygen concentrations as shown in Figure 5.9 is presented in Figure 5.10. This fit allowed the assignment of both the R + O$_2$ reaction and the high oxygen limit OH return rate values. This model also allowed us to separate well skipping OH from that regenerated from the RO$_2$ reactions, and showed well skipping to be a minor channel (< 10 %) even at elevated temperatures and low pressures (< 10 torr, 450 K).
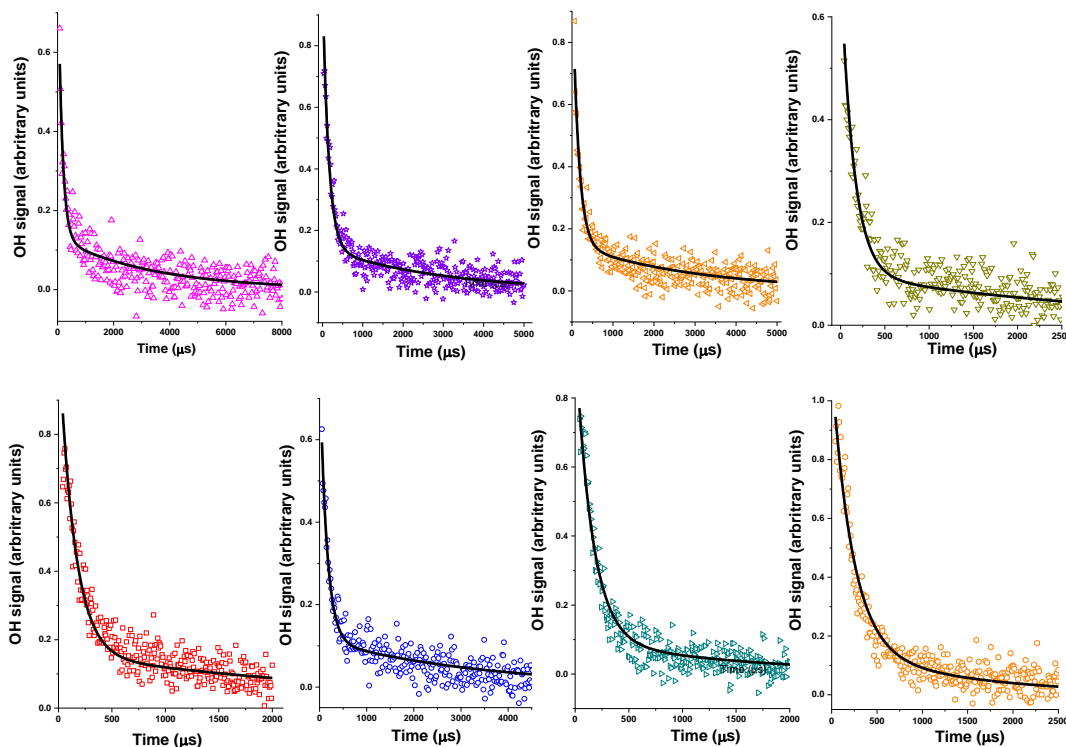
Figure 5.10: Eight example traces from 31 taken with a range of added $[O_2]$ (< 2 ×10^{16} – 3.2 ×10^{18} molecules cm^{-3}), and [DMF] (5 × 10^{14} – 1.0 ×10^{15} molecules cm^{-3}) at 559 ± 5 K and 1600 Torr were fitted globally fixing only k_d ((1470) s^{-1}) and k_L ((4325) s^{-1}). This global fit using Scheme 5.6 returned values of k_{1bim} = (1.465 ± 0.069) × 10^{-11} cm^3 molecule^{-1} s^{-1}, k_{2O} = (6.22 ± 0.27) × 10^{-13} cm^3 molecule^{-1} s^{-1}, k_{rO} < (1.0 ± 10) × 10^{-18} cm^3 molecule^{-1} s^{-1}, with k_3 = (1215 ± 22) s^{-1}and k_4 = (36.7 ± 7.9) s^{-1}.

At lower temperatures (<550 K) the small rate for OH recycling led to the R + O_2 rate coefficient being ill defined, this was in part due to the high concentrations of oxygen added in the high-pressure system in even the 'oxygen free' reactions (< 2 ×10^{16} molecule cm^{-3}). Above 550 K, the rate coefficients for recycling and for R decomposition were significantly large enough to allow for the R + O_2 rate coefficient to be reasonably well defined. These R + O_2 rate coefficients were later used as initial inputs in master equation calculations (an initial input of 4 × 10^{-12} cm^3 molecule^{-1} s^{-1}, with upper and lower bounds of (0.5,10) × 10^{-12} cm^3 molecule^{-1} s^{-1}).
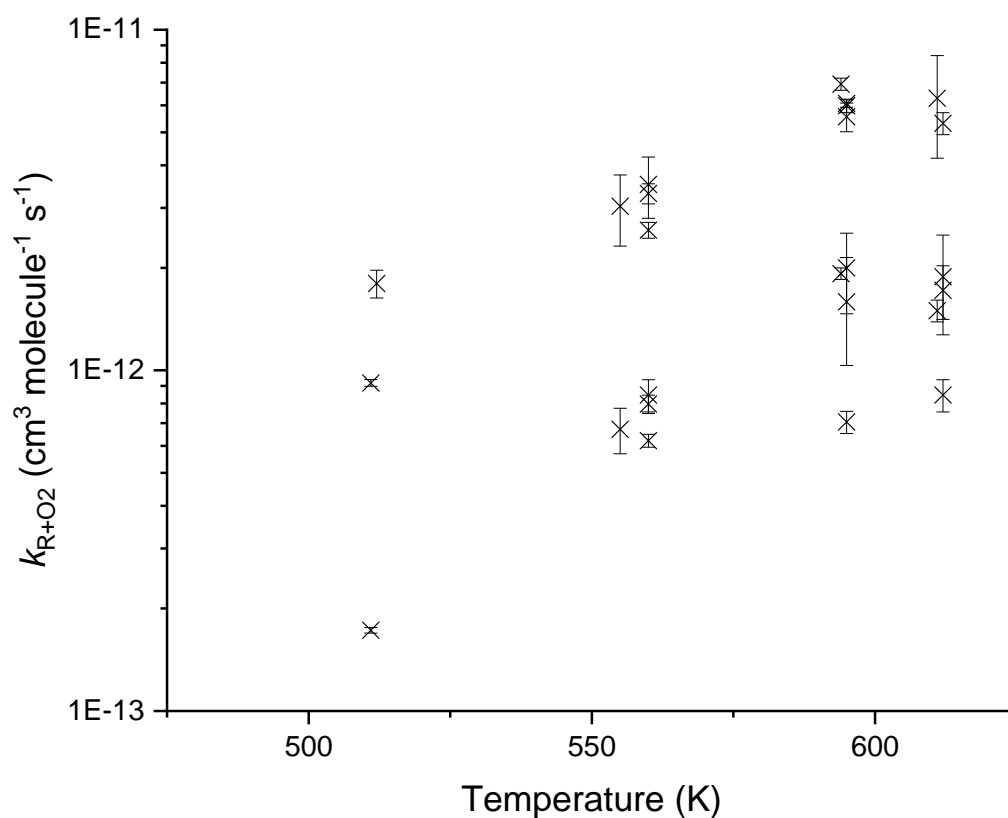
Figure 5.11: Shows the range of R+O₂ rate coefficients calculated, the lower the return rate coefficient the less well defined the value for R+O₂ returned, and above a limit value of added oxygen it was not possible to assign R + O₂. R decomposition, k_L, was taken from calculations performed on the PES shown in Figure 18.

In addition to evaluating the R + O₂ reaction rates, shown in Figure 5.11, the return rate coefficients obtained, from these global analysis fits, were independent of the oxygen environments under which the experiments were taken. The resultant return rate parameters, k_3, were plotted as a function of temperature in Figure 5.12, in addition to the high oxygen limit values of k_b, where Scheme 5.5 was used, collected under both low (< 100 Torr) and high pressure conditions (>1300 Torr). These experimental return rate coefficients were used in conjunction with MESMER, in order to evaluate the PES where R+O₂ leads to OH, and is described in more detail in section 5.32.
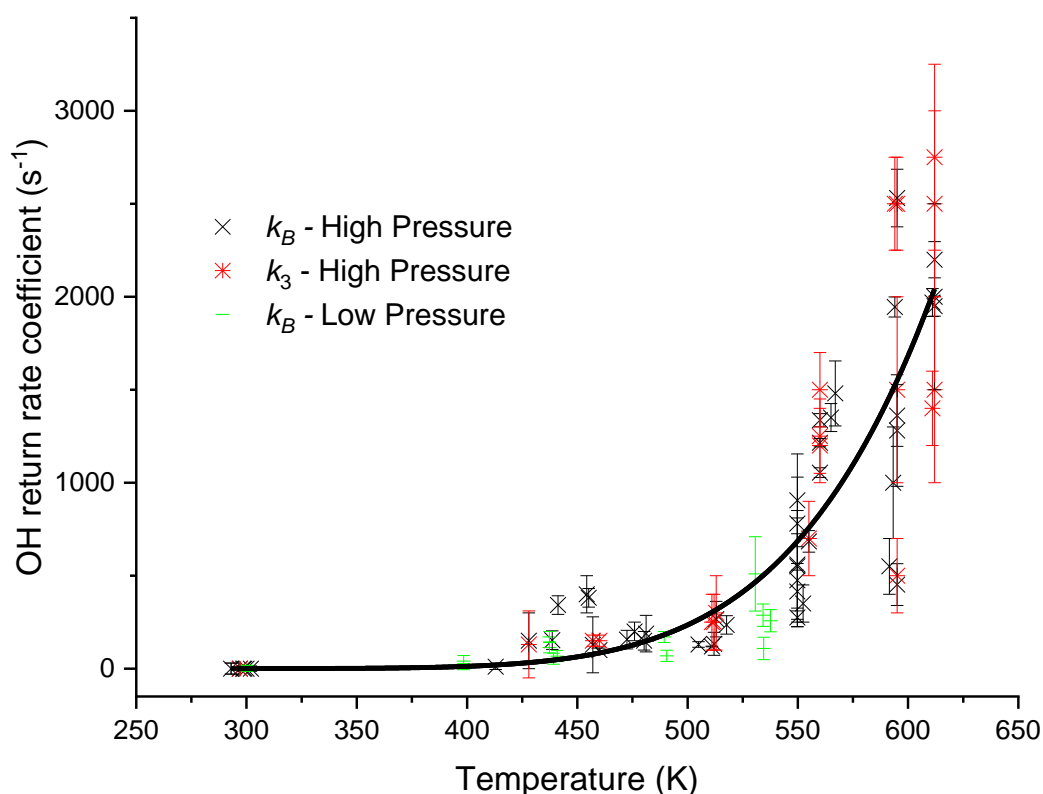
Figure 5.12: The temperature dependence of the return rate coefficient that was used as an input to MESMER master equation calculations, where a simple exponential fit to the data gave a barrier height of 74 ± 4 kJ mol^{-1}.

In a simplified form, the MESMER analysis entailed fitting the computationally derived eigenvalue for OH reformation to the experimentally determined OH reformation rates over a range of pressure and temperatures. The eigenvalues generated from MESMER analysis of the potential energy surfaces (Figures 5.14, 5.15, 5.16) showed that the rate coefficient for coming out of the RO$_2$ well was of a similar magnitude to the OH regeneration eigenvalue. This means that this process was likely the rate-limiting step in the OH recycling process, and as such, MESMER analysis of the kinetics alone was not able to simply define the QOOH decomposition barrier height beyond it being beneath the RO$_2$ – QOOH isomerization barrier. In addition, it meant that this system is not sensitive to the selectivity between QOOH decomposition and QOOH interception by oxygen in our experimental setup.

QOOH to OH fragmentation provides only stable products and no ability to form HO$_2$, when compared with OOQOH decomposition that for DMF would produce OH and HO$_2$. The HO$_2$ yield would provide information on the significance of QOOH interception. Further experimental work on this may allow for the evaluation of the

QOOH + O_2 rate coefficient. However, within our system where photolysis is performed at either 266 nm or 248 nm HO_2, yields are not clean with photolysis providing a large source of HO_2, with apparent HO_2 yields of > 240 ± 15 % at 248 nm and 40 ± 10 % at 266 nm at 500 K. Photolysis of an OH precursor at longer wavelengths (for example 280 nm from a dye-laser) may allow for HO_2 yields to be measured at temperatures where OH recycling can occur.

When this work was carried out the DMF absorption spectrum had not been measured over an extensive temperature range, there being only two observed published works on the gas phase absorption cross-section. (43, 45) The work of Chakir *et al.* observed no significant temperature dependence to the cross section, but this was measured over the range 306-333 nm.(43) The observed higher degree of photolysis at 500 K versus 300 K is in line with what may be expected, given that photolysis is occurring in the wings of the UV absorption spectrum of DMF. In general UV absorption peaks broaden with temperature, it is reasonable to assign that the absorption cross-section at 266 nm would increase with temperature. That at both RT and 500 K the observed HO_2 yield depends on the wavelength at which the compound is photolysed supports the hypothesis that the HO_2 formed is from photolysis and not OH reactions.

5.2.4 Elevated temperature PTR-MS for DMF

As the temperature was increased the yield of m/z 91 decreased, m/z 44 (43+1) (route to these are in Scheme 5.2), and 58(57+1), 76(57+19) peaks become more pronounced, structures for these masses are shown earlier in Figure 5.5. This behaviour was, as one would expect with the N-NO₂ bond being labile and as such at higher temperatures, this compound was not likely to be stable. Additionally, as the temperature of the reaction system was elevated, new reaction channels were opened up, where there is sufficient energy for the RO₂ to QOOH reaction to be rapid on experimental timeframes, and formation of the imine and methylisocyanate becomes possible. In addition to RO₂ isomerization, it is reasonable to expect the rate of reaction for NMe₂ with oxygen to increase with temperature again leading to imine formation, Scheme 5.2.

It was additionally possible to monitor the reduction in the DMF parent mass peak as temperatures were increased from room temperature. This reduction was due to pyrolysis within the reactor, catalysed by the high temperature walls. This effect was exacerbated in the presence of the OH precursor (H_2O_2) which also undergoes pyrolysis

at elevated temperatures. Loss of the reagent due to this effect was significant, and could be as great as 80 % at 600 K from the PTR-MS peaks. This is however, likely to be an overestimation as it is an averaged value of all the gas flow that passes through the heated region and pyrolysis is likely to be higher where walls can catalyse the process, which was in addition to the axial temperature gradient across the reactor. Under laminar flow conditions, the axial mixing is slow and as such, it is not possible to use the total reduction in the PTR-MS peaks alone to define the thermal loss of DMF where the OH measurements were taken.

5.3 Ab Initio computational Work on DMF + OH

OH regeneration in the reaction of OH and dimethyl formamide (DMF) was observed; to understand the origin of this observation master equation calculations needed to be undertaken. These were performed with the master equation solver for multi energy well reactions (MESMER) (46) which required structures and energies from *ab initio* calculations. The published work for the potential energy surface (PES) of DMF by Bunkan et al. (20) showed no simple route for OH regeneration. As such, additional work to further evaluate this PES was carried out.

5.3.1 Ab Initio calculations – DMF + OH abstraction and R decomposition

Initial a*b initio* calculations on the PES were carried out in Gaussian 09 (47) using the density functional theory (DFT) method M06-2X (48) with a fully augmented aug-cc-pVTZ (aug cc-pVTZ abbreviated to ATZ) basis set (49) for optimization of structures and frequency calculations. This yielded a very similar surface to that published (20) with only minor differences due to different rotational minima for the stationary points.

Single point energies for the $CONMe_2 \rightarrow CO + NMe_2$ reaction were calculated with three higher level CCSD(T) calculations with aug-cc-pVDZ, aug-cc-pVTZ and aug-cc-pVQZ basis sets (50) and these were then extrapolated to the basis set limit. Extrapolation to the CBS limit was carried out using separate exponential extrapolation of the Hartree Fock and correlation energies, (51) and using a mixed Gaussian extrapolation of the CCSD(T) values as described by Peterson *et al.* (52) These calculations were computationally expensive, and as such, it was decided to compare the results of

these calculations to the results of a minimally-augmented (jun-cc-pVXZ) series extrapolation.

For the correlation consistent minimally-augmented basis set, jun-cc-pVXZ, the complete basis set (CBS) was again evaluated through the extrapolation of double, triple and quadruple zeta basis sets. (53) The results had a remarkably similar accuracy to the fully augmented CCSD(T)/CBS extrapolation results, Table 5-1. This result meant that minimal augmented CBS extrapolations were selected to be used as the method of choice for subsequent single point energy calculations on larger species on the R + O$_2$ surface.

Table 5-1   Compares the energies of the R fragmentation reaction following abstraction at the aldehydic position, all single point energies are from CCSD(T) energy calculations on M06-2X/aug-cc-pVTZ structures with zero-point corrections from the M06-2X calculations. CCSD(T) calculations were performed in Gaussian 09, where the F12 approximation was made the calculation as performed in MOLPRO 2010.

Basis set	CONMe2 kJ mol^{-1}	(CO-NMe2) TS kJ mol^{-1}	CO + NMe$_2$ kJ mol^{-1}
aug-cc-pVDZ	0	78.6	39.9
jun-cc-pVDZ	0	77.7	29.3
aug-cc-pVTZ	0	91.1	54.4
jun-cc-pVTZ	0	90.8	50.9
aug-cc-pVQZ	0	94.1	56.9
jun-cc-pVQZ	0	94.2	55.8
aug-cc-pVXZ(CBS)	0	95.6	58.0
jun-cc-pVXZ(CBS)	0	96.0	58.3
CCSD(F12)/aug-cc-pVTZ	0	96.4	60.3

The OH reaction with DMF can occur, via a pre reaction complex (PRC), over three competing abstraction barriers (where TS1 is the aldehydic H, and TS2, TS3 are methyl abstractions) as shown in Figure 5.13. The barrier to abstraction from the aldehydic position is significantly lower than that from the methyl positions. The difference in methyl abstraction energies can be assigned to hydrogen bonding between the OH radical and the carbonyl oxygen stabilising the lower energy transition state. High-level computational surfaces (CCSD(T)/CBS//MP2/6-311++g(3df,3pd)) were calculated for the methyl surfaces, section 5.3.3. Once the initial abstractions were accounted for, the methyl abstraction surfaces did not produce significant improvements

to the MESMER analysis, but did provide enhanced cost and as such they were neglected when fitting experimental and simulated OH regeneration eigenvalues.
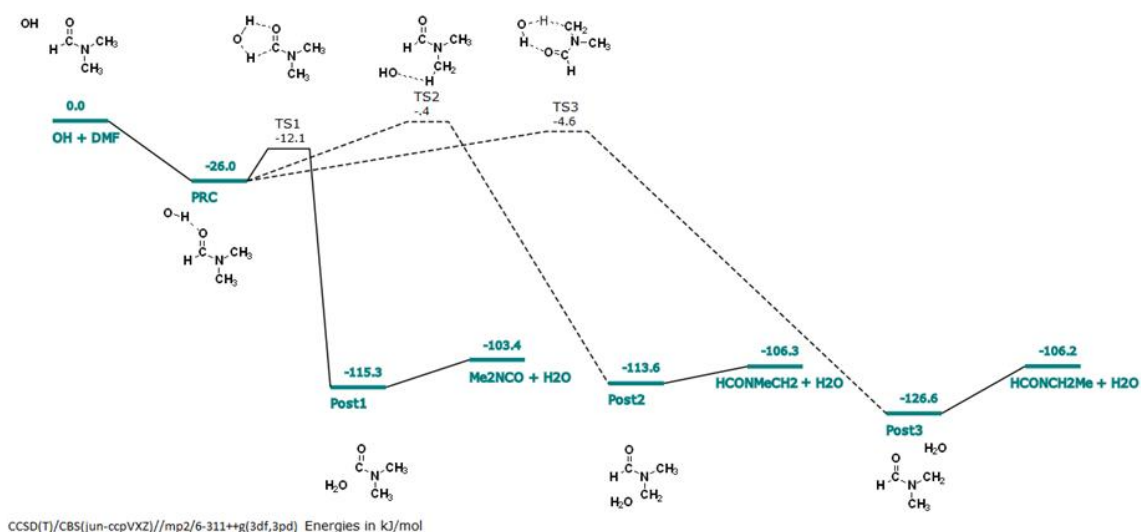
Figure 5.13: shows the abstraction channels available for the reaction of OH and DMF (Dimethyl formamide). Structures were optimized and frequencies were calculated at the mp2/6-311++g(3df,3pd) level, and single point energies were calculated at the CCSD(T) complete basis set level (CBS), where the CBS limit was assigned from the extrapolation (52) of the partially augmented correlation consistent jun-cc-pVXZ levels (dz,tz,qz). (54) Tunneling was accounted for using a one dimensional Eckart model.

5.3.2 Ab Initio calculations – $CONC(CH_3)_2 + O_2$

Initial work was carried out to produce a M06-2X/aug-cc-pVTZ PES, with CCSD(T)/CBS(jun-cc-pVXZ) single point energy calculations, this did not provide a simple route to the observed OH recycling, as the surface was in good agreement with the work of Bunkan *et al.* (20), with a high barrier to QOOH decomposition. The height of the apparent barrier to OH recycling, from the alkyl hydroperoxy radical (QOOH), was identified as being higher than might be expected for the breaking of an O-O peroxy bond (>180 kJ mol^{-1}). Relaxed scans of this bond were therefore performed, geometric optimizations of the apparent stationary points on these scans were carried with several DFT functionals ((use of GD3 empirical dispersions noted as /GD3) M06-2X, mPW3PBE,SOGGA11X, M11, M11/GD3, PBE1PBE, PBE1PBE/GD3, PW91PBE, PBEh1PBE, wB97XD TPSSTPSS, TPSSTPSS/GD3), with the augmented 6-311++g(3df,3pd) basis set, these yielded comparably similar structures for the O-O bond breaking transition states.

164
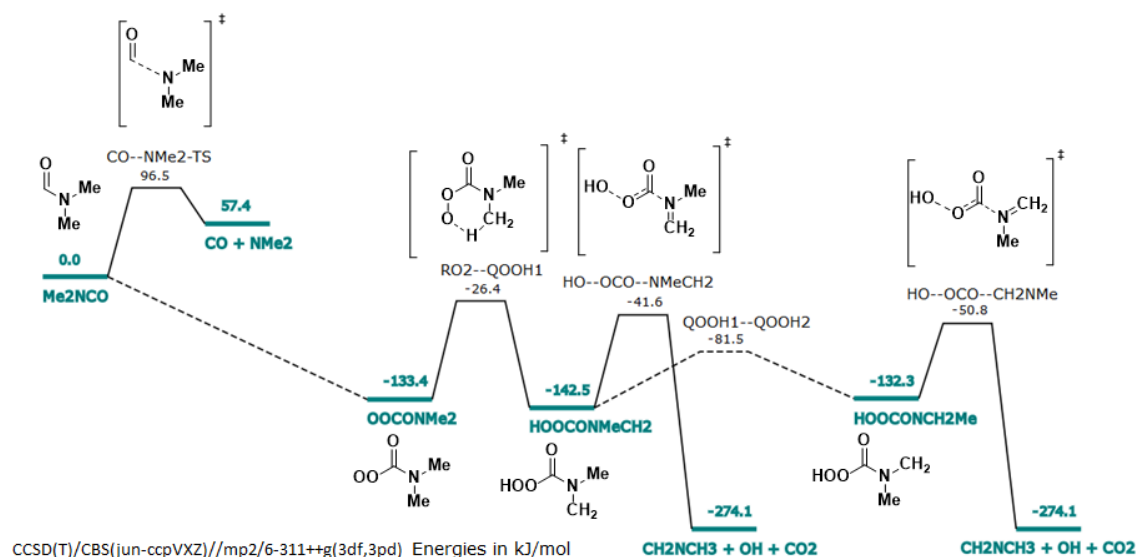
Figure 5.14: shows the R + O_2 surface for the R radical formed from the abstraction of the aldehydic site of DMF. This surface includes the decomposition of the R radical that can become significant at high temperatures. Structures were optimized and frequencies were calculated at the mp2/6-311++g(3df,3pd) level, and single point energies were calculated at the CCSD(T) complete basis set level (CBS), where the CBS limit was assigned from the extrapolation (52) of the partially augmented correlation consistent jun-cc-pVXZ levels (dz,tz,qz). (54)

Of particular importance to this work, when the same relaxed scan of the O-O bond in the QOOH radical was performed with the second order Moller-Plesset (MP2) (55) functional, a much lower energy pathway to O-O bond cleavage became apparent. It was notable that during this bond breaking process the radical twisted out of the planar arrangement seen for the rotational minima of the QOOH radicals, which was not observed for the higher energy QO-OH transition state. When the CCSD(T)/CBS(jun-cc-pVXZ) single point energy for the lower energy QO-OH transition state was calculated it was significantly lower than the RO_2-QOOH isomerization energy. A full surface was therefore calculated, Figure 5.14, with structural optimizations and frequencies calculated at the mp2/6-311++g(3df,3pd) level and with CCSD(T)/CBS single point energy calculated. When this surface was modelled in MESMER it did indeed provide a fast route to OH recycling in line with the required experimental timescale.

The new transition state was additionally optimized, with the previously used DFT functionals to validate that this structure was indeed a valid transition state to OH regeneration. When CCSD(T)/CBS extrapolations were performed on the DFT and MP2

geometries the resultant energies were in agreement, -70.3 and -50.8 kJ mol^{-1} with respect to R+O$_2$ shown in Table 5-2, that there was indeed a low barrier to QOOH fragmentation to regenerate OH, however the energies themselves differed significantly.

Table 5-2 Compares the dependence of the zeropoint corrected energies of CCSD(T)/CBS extrapolations on the method used to optimize some initial geometries on the R + O$_2$ surfaces (Figures 5.14 and 5.15). M06-2X/aug-cc-pVTZ is noted as M06-2X, MP2/6-311++g(3df,3pd) is noted as MP2.

S.P.	Struc. Method.	Freq. Method.	CCSD(T) E / H	zpe / H	E, kJ mol^{-1}
RO$_2$	M06-2X	M06-2X	-397.8207557	0.0994340	-134.3
	M06-2X	MP2	-397.8207557	0.0993063	-134.5
	MP2	MP2	-397.8207557	0.0988466	-133.4
	MP2	M06-2X	-397.8207557	0.0991593	-134.1
RO$_2$ - QOOH	M06-2X	M06-2X	-397.7750851	0.0933919	-30.2
	M06-2X	MP2	-397.7750851	0.0939875	-28.5
	MP2	MP2	-397.7746972	0.0927868	-26.4
	MP2	M06-2X	-397.7746972	0.0937773	-28.9
QOOH-1	M06-2X	M06-2X	-397.8220255	0.0975620	-143.3
	M06-2X	MP2	-397.8220255	0.0973143	-142.0
	MP2	MP2	-397.8223694	0.0972383	-142.5
	MP2	M06-2X	-397.8223694	0.0972527	-143.9
QOOH1 - QOOH2	M06-2X	M06-2X	-397.7999421	0.0974505	-84.8
	M06-2X	MP2	-397.7999421	0.0960643	-88.3
	MP2	MP2	-397.7995542	0.0976312	-81.5
	MP2	M06-2X	-397.7995542	0.0974736	-81.9
QO--OH-2	M06-2X	M06-2X	-397.7945520	0.0960020	-73.0
	M06-2X	MP2	-397.7945520	0.0979232	-69.3
	MP2	MP2	-397.7884438	0.0982242	-50.8
	MP2	M06-2X	-397.7884438	0.0955768	-57.7

The difference in single point energies showed that the choice of method used to generate the initial surface can significantly influence the resultant single point energies calculated, and can produce larger errors than the experimental errors. The observed differences here are significantly greater than might be expected for the CCSD(T)/CBS energies which are often believed to have 'chemical accuracy', defined as <4 kJ mol^{-1}. (56)

This method dependence was shown to be minimal for minima on the surface, within 1.5 kJ mol^{-1}, and more significant for transition states, in general within 5 kJ mol^{-1}. The greatest method dependence being for the decompositions of the QOOH radicals to OH, which comparing MP2 to M06 differed by more than 20 kJ mol^{-1}, this can be explained as an effect of the spin contamination of these transition states, due to the simultaneous formation and breaking of multiple bonds.

After comparing the M06-2X transition states to the MP2 transition states, the MP2 surface was chosen to be used in the subsequent master equation calculations. This choice was made because the difference had been assigned to spin contamination, and Gaussian 09 (47) automatically uses spin projection which can help to alleviate spin contamination issues. Additionally, it should be noted that although DFT functionals in general do allow for dramatically reduced calculation costs to produce superior answers with respect to MP2, by their very nature it is impossible to completely prevent spin contamination for DFT functionals. If a DFT functional did exist that could completely remove spin contamination, then it would be in fact an exact functional!

However, to ensure that this decision did not influence the final obtained results, a full CCSD(T)/CBS//M06-2X with M06-2X/ATZ frequencies, R + O$_2$ surface was calculated, Figure 5.15. For the M06-2X/ATZ QO-OH transition state structure, the CCSD(T) single point energy calculations and additional MP2 frequency calculations, the initial SCF (self consistent field) convergences failed. It required the use of an extended version of quadratic convergence (SCF=XQC) to allow the calculations to run to completion. Although this will not have fully accounted for the issues arising from spin contamination, the greatly improved wavefunction this option produced reduced the effect. Once the full surface had been obtained, additional master equation calculations were performed on it, in the same manner as for the MP2 surface.
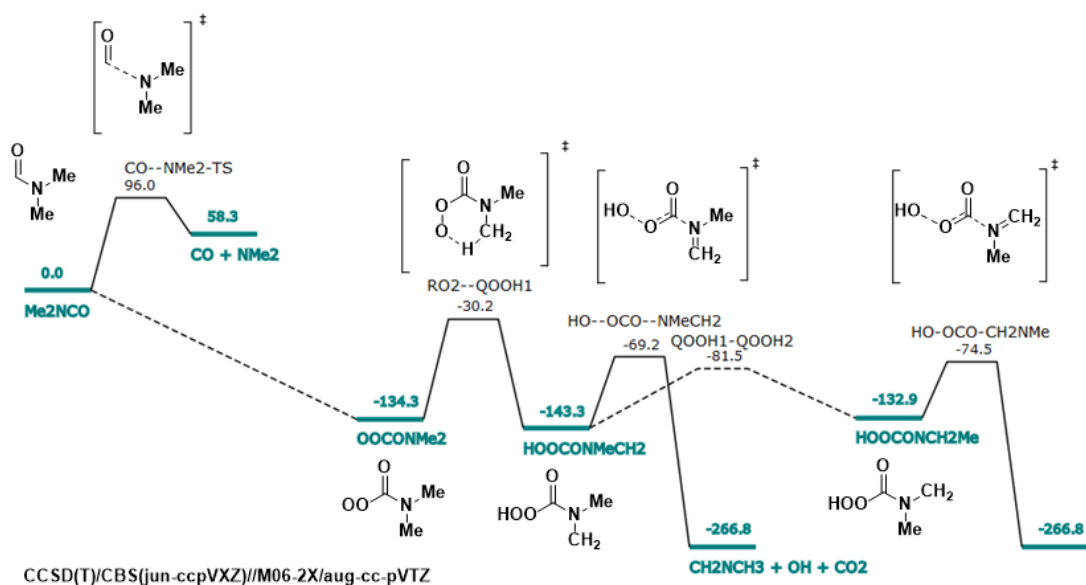
Figure 5.15 Shows the M06-2X/ATZ R + O_2 surface with single point energies calculated at the CCSD(T) complete basis set level (CBS) in the same manner previously described. (48, 52, 53)

To calculate the QOOH + O_2 surface, only calculations at the M06-2X/ATZ level were used. This decision was taken because of the significantly reduced computational costs, which allowed for the calculations to be performed. MP2 calculations and CCSD(T) calculations were too computationally expensive on the computer clusters available to this work. The results of the M06-2X/ATZ calculations are given as Figure 5.16.
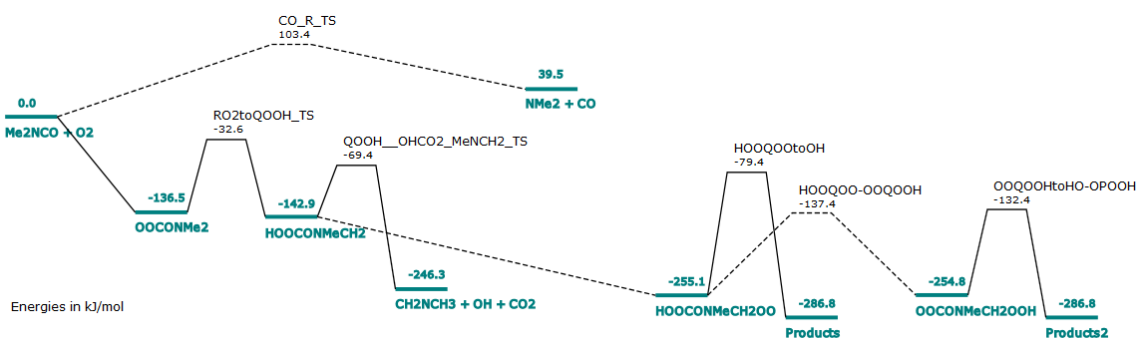
Figure 5.16 Provides a simplified R + O_2 and subsequent QOOH + O_2 PES computed at M06-2X/aug-cc-pvTZ (48).

The relative heights of the QOOH to OH and RO_2 to QOOH barriers meant that once the QOOH radical was formed, OH regeneration via QOOH fragmentation, would be fast and as such sufficient oxygen was required in subsequent simulations to permit oxygen to intercept QOOH, and for OOQOOH formation.

5.3.3 Ab Initio calculations – HCONC(CH$_3$)CH$_2$ + O$_2$ and HCONC(CH$_2$) CH$_3$ + O$_2$

Potential energy surfaces for the reactions of the radicals formed from the methyl abstractions and oxygen were calculated at both the M06-2X/ATZ level and MP2/6-311++g(3df,3pd) level with single point energies on the MP2 surface additionally calculated at the CCSD(T)/CBS level. These calculations were performed in the manner described earlier in section 5.3.1. and the resultant CCSD(T)/CBS//mp2/6-311++g(3df,3pd) surfaces are given as Figure 5.17 and Figure 5.18.

Energies in kJ/mol
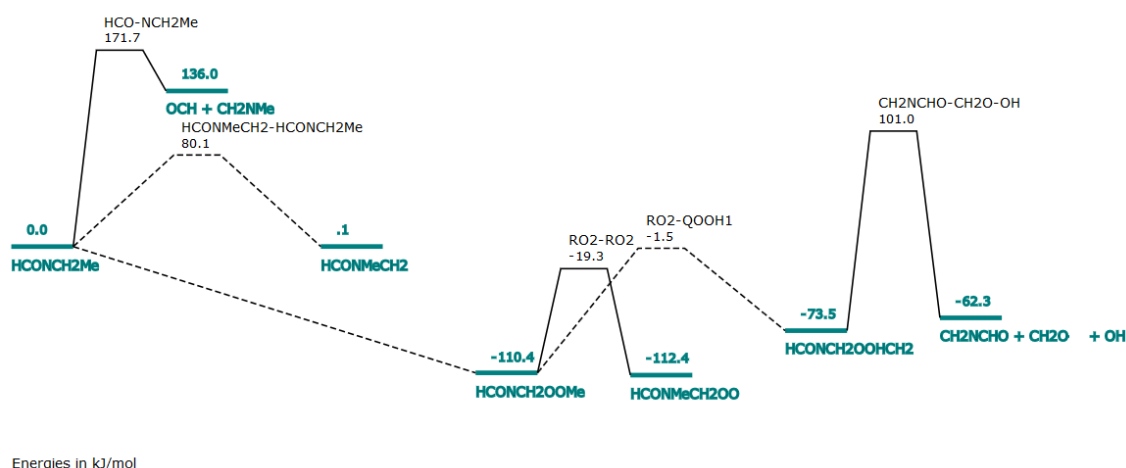
Figure 5.17 PES for the HCONCH$_2$Me and O$_2$ reaction with CCSD(T)/CBS extrapolation for single point energies, with structures and frequencies at the MP2/6-311++g(3df,3pd) level, as used in section 4.3.1. This surface does not show any prompt route to OH regeneration, however there are barriers to rotation of the R and RO$_2$ radicals present in Figure 20 of 80 and -19.3 kJ mol^{-1}, compared to the energy of R+O$_2$.

In Figure 5.17, the PES for the lowest energy methyl abstraction, it is clearly apparent that any OH reformation that comes from this surface must come via the RO$_2$ rotamer. The planarity of the initial RO$_2$ structure prevents the radical from internally abstracting from the aldehydic site. Internal abstraction from the other methyl group provides a route to the formation of a QOOH radical, however the barrier to the QOOH radical formed from this decomposing to OH is too significant to be important. The RO$_2$ rotamer that allows for QOOH decomposition is the same as the RO$_2$ formed from interception of the R radical from the higher energy methyl abstraction, Figure 5.18. The barrier to R radical rotation of 80.1 kJ mol^{-1} means that in low oxygen or high temperature environments, it will equilibrate between the rotamers, and as such this may provide a route to the R radical formed from the higher energy methyl abstraction.

The R+O$_2$ PES for the higher energy methyl abstraction is given as Figure 5.18. In this figure the relative barriers to QOOH decomposition from the different QOOH radicals (88 kJ mol^{-1} and -55 kJ mol^{-1}), and the height of these QOOH radicals with respect to the RO$_2$ radical and the RO$_2$ to QOOH isomerization barriers, mean that only decomposition of the QOOH formed from the internal abstraction of an aldehydic proton had any influence on the MESMER simulations.

Energies in kJ/mol
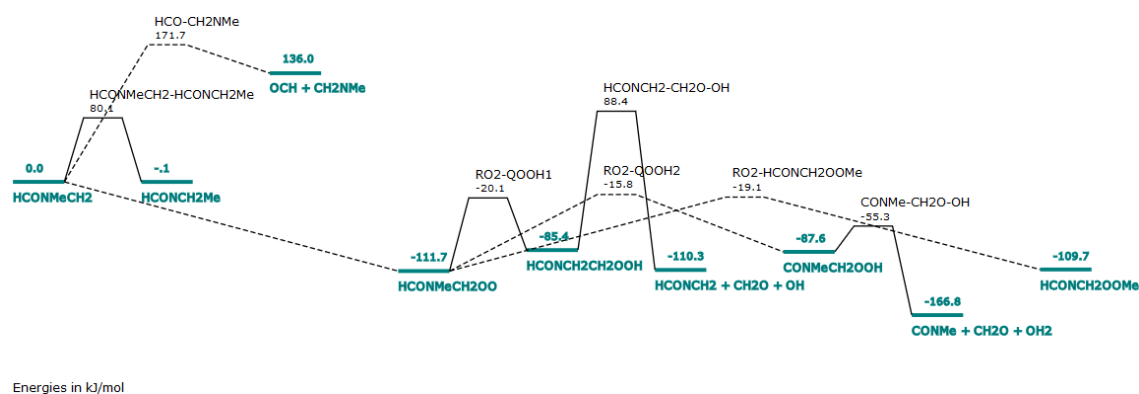
Figure 5.18 PES for the HCONMeCH$_2$ and O$_2$ reaction with CCSD(T)/CBS extrapolation for single point energies, with structures and frequencies at the MP2/6-311++g(3df,3pd) level, as used in section 5.3.1. There is a low energy route to OH regeneration, with a barrier to QOOH decomposition of -55.3 kJ mol^{-1}, and RO$_2$ to QOOH isomerization of -15.8 kJ mol^{-1}, compared to the energy of R+O$_2$.

The height of the RO$_2$ to QOOH internal abstraction (pseudo isomerization) barrier (15.8 kJ mol^{-1}) compared to the QO-OH decomposition barrier (-55.3 kJ mol^{-1}), and the relative heights of the QOOH and RO$_2$ wells (-111.7, -87.6 kJ mol^{-1}), meant that for this surface QOOH interception would not be efficient under most experimental conditions.

When compared to the CONMe$_2$ + O$_2$ surface, Figure 5.14, the barrier to internal abstraction is lower and the rate of this pseudo isomerization will be faster. This meant that when simulating the OH traces observed for DMF + OH, the methyl abstractions could potentially account for faster recycling of OH when compared with the CONMe$_2$ + O$_2$ surface.

Figure 5.19 gives the RO$_2$ surface, formed from the lowest energy pathway considering both methyl abstraction surfaces. It includes the energy for the rotational conformer change in the RO$_2$, the subsequent RO$_2$ to QOOH, and QOOH decomposition barriers. This was because the barrier for the QOOH formed directly from this RO$_2$ to decompose was 101 kJ mol^{-1} above the R+O$_2$ energy, 174 kJ mol^{-1} above

the QOOH radical. In addition, for the RO$_2$ rotamer the higher QOOH decomposition and its respective QOOH radical were also negated, because when simulations were performed on this part of the system, Figure 5.18, this channel had little influence on the simulated OH reformation eigenvalues. The R radical rotation was not included in this surface when used for MESMER simulation, as MESMER does not allow multiple reactions to lead to the same product, and at the high oxygen limit, this reaction will additionally be of minimal importance to the simulations.
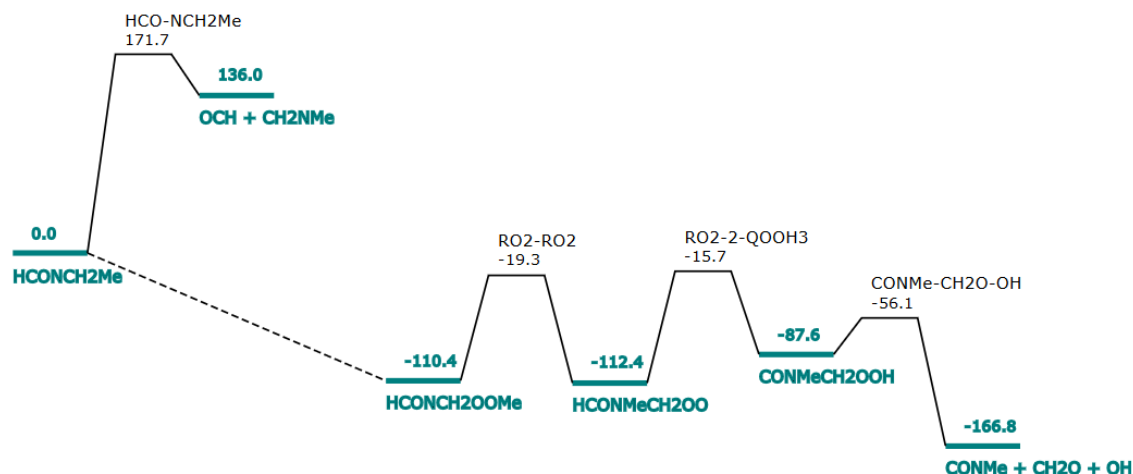
Energies in kJ/mol

Figure 5.19 Combines the lowest energy routes of the CCSD(T)CBS/MP2/6-311++g(3df,3pd) surfaces with respect to the HCONCH$_2$Me radical reacting with O$_2$. This surface provides a route to OH recycling with barriers of -19.3, -15.7 and -56.1 kJ mol^{-1} for the rotation, internal abstraction and decomposition reactions respectively, compared to the energyR+O$_2$.

When this surface was compared to the CONMe$_2$ + O$_2$ surface, Figure 5.14, the barriers to formation of the QOOH radical (91.1, 96.7 kJ mol^{-1} compared to their respective RO$_2$ species) on the methyl abstraction surface are both lower than that on the aldehydic abstraction surface (107 kJ mol^{-1} relative to the RO$_2$). Despite both the barriers being lower when this surface was simulated, the OH regeneration eigenvalue was lower than the equivalent simulation of the CONMe$_2$ + O$_2$ surface.

This may be the result of the requirement to pass over the rotational barrier between the respective RO$_2$ radicals. Although, this barrier was 19.3 kJ mol^{-1} below the entrance energy the imaginary frequency was 195 cm^{-1}, an order of magnitude lower than the typical imaginary frequency observed for an RO$_2$ QOOH isomerization. This can be

explained through the rotational barrier requiring the movement of multiple groups simultaneously whereas in a typical RO_2 – QOOH isomerization the predominant movement is only that of proton. In addition, the rotation in the transition between the RO_2s involves changing the bond order of the CN bond
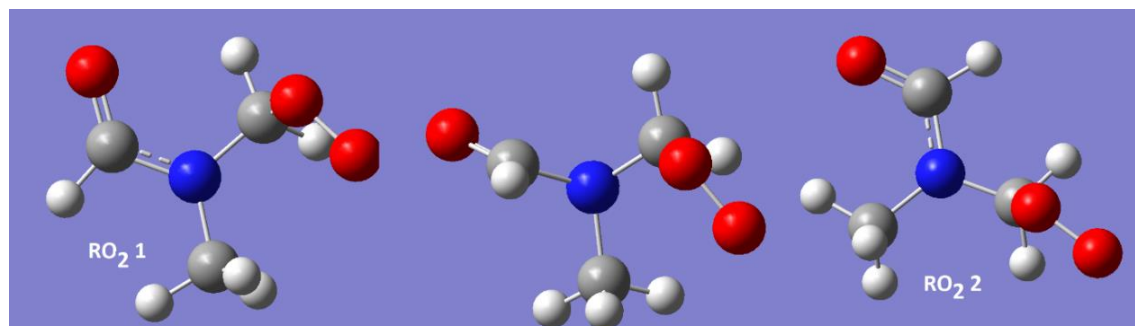
Figure 5.20 The structures calculated for the two methyl RO_2s, and the structure of the rotational barrier to interconversion. These structures were calculated at the MP2/6-311++g(3df,3pd) level in Gaussian 09.

When the methyl abstraction surfaces, Figures 5.18 and 5.19, were included in later direct trace analysis, they significantly increased the computational costs of the analysis and only provided slightly improved fits to the data. To assess if there was in fact a requirement to include them, a simple Arrhenius type RO_2 to OH reaction from the methyl channel was included. This again did not significantly improve the quality of the fits and as such a final test was carried out where the methyl channel was treated simply as a competing abstraction that did not lead to OH regeneration, for this the quality of the fits to the OH traces was not significantly improved. Although including the additional channels did not improve the quality of the fits, they did provide additional variable that made the system more flexible, which made it harder for the other parameters in the system to be defined. Therefore, in later analysis where OH regeneration eigenvalues from master equation simulations were fitted to experimentally obtained return rates, this was performed on only the $CONMe_2 + O_2$ surface.

5.4 Master equation calculations

The MESMER models of the dimethyl formamide (DMF) aldehydic R + O_2 system were based on CCSD(T)/CBS single point energies, with structures and frequencies generates at a lower level (M06-2X/ATZ, MP2/6-311++g(3df,3pd)). These MESMER models treated the collisional energy transfer properties (<ΔEdown>) of all

the wells as being a shared parameter, although this may not be accurate, within the bounds of the experimental and computational errors, this would have a minimal effect on the results. This conclusion was found after varying ΔE for R, RO_2 and QOOH between 125 and 300 cm^{-1} whilst holding the others at 150 cm^{-1} had little impact on the derived eigenvalues for the $CONMe_2 + O_2$ system. For all reactions that occurred via a transition state tunnelling corrections were made using a one dimensional Eckart model as described in (59).

5.4.1 CONC(CH$_3$)$_2$ + O$_2$ - MESMER analysis

Initial MESMER analyses were obtained by carrying out simulations of the PESs generated in section 5.3.1 (Figures 5.14, 5.15, 5.16), these simulations were carried out over a range of temperatures and pressures (290 – 650 K at 5, 50, 500, 1000, 1500 Torr). The eigenvalues generated from the MESMER simulations of the R + O_2 and QOOH + O_2 potential energy surface (Figure 5.16), showed that the rate coefficient for coming out of the RO_2 well, forming QOOH, was of a similar magnitude to the OH regeneration eigenvalue. This meant that this process was likely the rate-limiting step in the OH recycling process, and as such, MESMER analysis of the kinetics would not be able to define the QOOH interception rate effectively, as the surface was not sensitive to this step.

An additional issue for the attempts to determine the QOOH + O_2 rate coefficient was that there was a high degree of correlation between the QOOH + O_2 rate coefficient and the QO-OH decomposition barrier. It was not possible to selectively fix either of these processes. The QO-OH decomposition due to the differing barrier heights and vibration frequencies from the different calculations, and QOOH interception due to limited experimental data on similar QOOH radicals and oxygen reactions. It was therefore decided to simplify the system and treat only the R + O_2 surface for fitting to experimental data and any subsequent direct trace analysis.

When fitting the CCSD(T)/CBS/MP2 surface (Figure 5.14) to experimental eigenvalues (the return rate coefficients, k_b, in bi-exponential analytical fits to experimental traces), barriers on the surface were floated, the barriers to alkylhydroperoxy (QOOH) radical decomposition to regenerate OH were found to be sufficiently low with respect to the RO_2 to QOOH isomerization barrier that our data was not sensitive to it. When the RO_2 to QOOH pseudo-isomerization barrier was floated, it moved by 3.4 kJ mol^{-1}, to -29.8 ± 0.6 kJ mol^{-1} with respect to R+O_2 which is in good agreement with the

M06-2X/ATZ surface (Figure 5.16),and the CCSD(T)CBS//M06-2X/ATZ surface (Figure 5.15), and were still in reasonable agreement with the MP2 surface (Figure 5.14), which are given in Table 5-2.

The decrease in the isomerization barrier is not insignificant but this difference may be reduced by a more thorough treatment of the hindered rotors present, or by floating other parameters in the system. Hindered rotors are increasingly important when bond orders change between single to double and this was observed in this transition state. Therefore, this reduction in barrier height may be due to the simple, harmonic treatment of the vibrations, underestimating the density of states.

When calculated and experimental return rate values were plotted the correlation was close to 1 (1.08 ± 0.15). There was however, significant scatter about this line; such variation may be the result of temperature errors. As the temperature was assigned from the chemical thermometer of OH and methane, the assigned temperatures do have an error; typically, this was in the range of ± 5 K. The error in the assigned temperature from OH and methane calibration will have a non-random contribution from variations in the calibration error of the methane mass flow controllers. It is not possible to directly include temperatures with an error into the MESMER analysis, and a random error in this would have caused recycling to be over or underestimated in individual experiments but, in general, it should not have influenced the final values assigned to the barrier heights. A systematic difference in temperature assignment between experimental setups may cause a discrepancy between low and high-pressure measurements.

When other parameters were floated in these calculations, the additional floated parameters were the temperature dependence of the R radical reaction with oxygen (A, Ea, T^n), and the shared energy transfer parameter $<\Delta E_{down}>$. When the T^n parameter and $<\Delta E down>$ were floated along with the isomerization barrier, the MESMER fits to the experimental eigenvalues derived from this were equally as good as in the case where the barrier alone was floated.

In addition to those fits being equally good, the case where these were floated did not require the isomerization barrier to change significantly, -26.66 ± 0.58 kJ mol^{-1} for the experimentally floated value versus -26.4 kJ mol^{-1} from the CCSD(T) Gaussian extrapolation to the CBS limit. The results of this analysis are shown in Figure 5.21, and compared well to the results of later analysis performed on the CCSD(T)/CBS//M06-2X/ATZ surface.
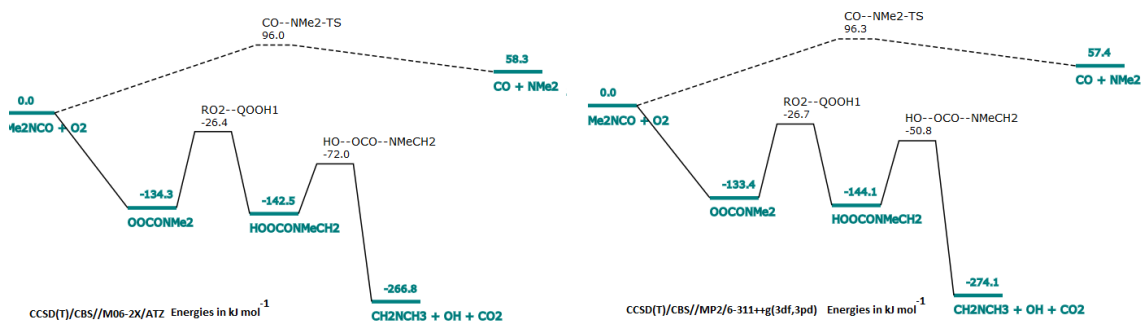
Figure 5.21: The PES produced by fitting the eigenvalue for OH regeneration to experimentally determined eigenvalues, for the CCSD(T)CBS//M06-2X/ATZ surface, on the left, and the CCSD(T)//MP2/6-311++g(3df,3pd) , on the right.

Using only the R + O_2 CCSD(T)/CBS//M06-2X/ATZ surface shown in Figure 5.15, MESMER was again used to fit the experimentally derived eigenvalues and this resulted in increase in the isomerisation barrier between RO_2 and QOOH, and an increase in the QOOH to OH barrier. Consequently barrier heights were adjusted to -26.40 ± 0.71 kJ mol^{-1} for RO_2 to QOOH and -72.0 ± 136.3 kJ mol^{-1} for QOOH to OH, in good agreement with the CCSD(T)/CBS//MP2 surface (Figure 5.14), the adjusted surfaces, are given as Figure 5.21.

5.4.2 Direct trace analysis

The direct trace analysis program wrote any parameters that were floated in the master equation calculations to the MESMER input files, called the execution of these input files and read in the resultant 'Bartis Widom' rate coefficients for all the experimental conditions. When used in MESMER analysis of the results from the master equation calculations, the term 'Bartis Widom' analysis refers to the solutions generated, to a matrix produced from the coupled differential equations that describe the reactive processes within the full master equation. This analysis relies on a separation of the reactive (chemically significant eigenvalues) processes and the collisional processes (internal energy relaxation eigenvalues).

These 'MESMER' rate coefficients were then coupled with any other processes that has been described in the program. The resultant simultaneous equations for the species were numerically integrated, the OH profiles that this produced for each trace were compared to the experimental data. The program then minimised the resulting differences using a Marquardt algorithm to minimise the χ squared, by varying the floated parameters.

175

One potential problem with this method could come from erroneous Bartis Widom rate coefficients being derived from the simulated species time profiles. To ensure that this had been accounted for, the Bartis Widom rate coefficients were routinely integrated, using the reaction scheme given to MESMER in Kintecus (a numerical integration package),(58) and the output of these species time profiles were compared to those in the paired output file. This was not observed to provide any significant issue in fitting the CCSD(T)/CBS//MP2/6-311++g(3df,3pd) surface to the experimental traces.

The program was initially used without any master equation simulations as a method of numerically integrating a scheme (based on modified Arrhenius descriptions for the methyl and aldehydic surfaces) and comparing the results to the experimental data. Using this description of the reaction system it was possible to generate excellent fits to the data with χ^2 of 1.4 - 1.8 per trace, each trace was pre-weighted by fitting to a multi-exponential decay curve so a perfect fit yields a χ^2 of 1.0 per trace. It was however, easy with this system to overparametrized the problem and as such many different sets of 'equally good fits' could be generated by fixing and floating different parameters.

Analysis was therefore moved forward to the next step where master equation simulations were coupled into the numerical simulation. In these simulations it was possible to modify any of the input however for the work carried out here only inputs to the ILT calculations, barrier heights and energy transfer parameters were modified. For the R + O$_2$ reactions the pre exponential and the temperature dependence were floated. For barriers the general practice was for barriers on the same surface to be moved in a linked manner, although some simulations were carried out where the QOOH barrier to OH and the RO$_2$ to QOOH barrier were manipulated independently for CONMe$_2$ +O$_2$.

Simulations were carried out with the methyl abstraction being described by two competing RO$_2$ loss processes described by modified Arrhenius equations, and where the methyl abstraction was described by a MESMER simulation of Figure 5.19, with the barrier heights fixed or floated. Where the competing modified Arrhenius model for the methyl abstractions was used, it was important to judiciously restrict the number of parameters that could float for this. In the same manner as for the simple fit initially carried out above, over parametrizing the fit could be achieved if too many parameters correlated parameters were floated too freely.

When fitting the CONMe$_2$ CCSD(T)/CBS//MP2/6-311++g(3df,3pd) surface, Figure 5.14, to the experimental data it was important to float several parameters that

were not included in the CONMe$_2$ R + O$_2$ surface. The initial OH reaction with DMF was floated, as was the branching ratio for this reaction, a 'local global' loss rate for the subsequently formed RO$_2$ radicals was also floated. These local global values were additionally used in some fits in place of a global DMF + OH reaction, where they were floated within the ranges determined for the bimolecular rate coefficients, derived from analytical fits carried out for the given set of conditions. Fits were performed where wider ranges for the DMF + OH bimolecular removal rates were allowed; these did not greatly improve the quality of the fits, but did provide greater ability to over parametrize the problem. The minor methyl abstraction channel was treated as two competing modified Arrhenius loss process leading to OH removal or recycling.
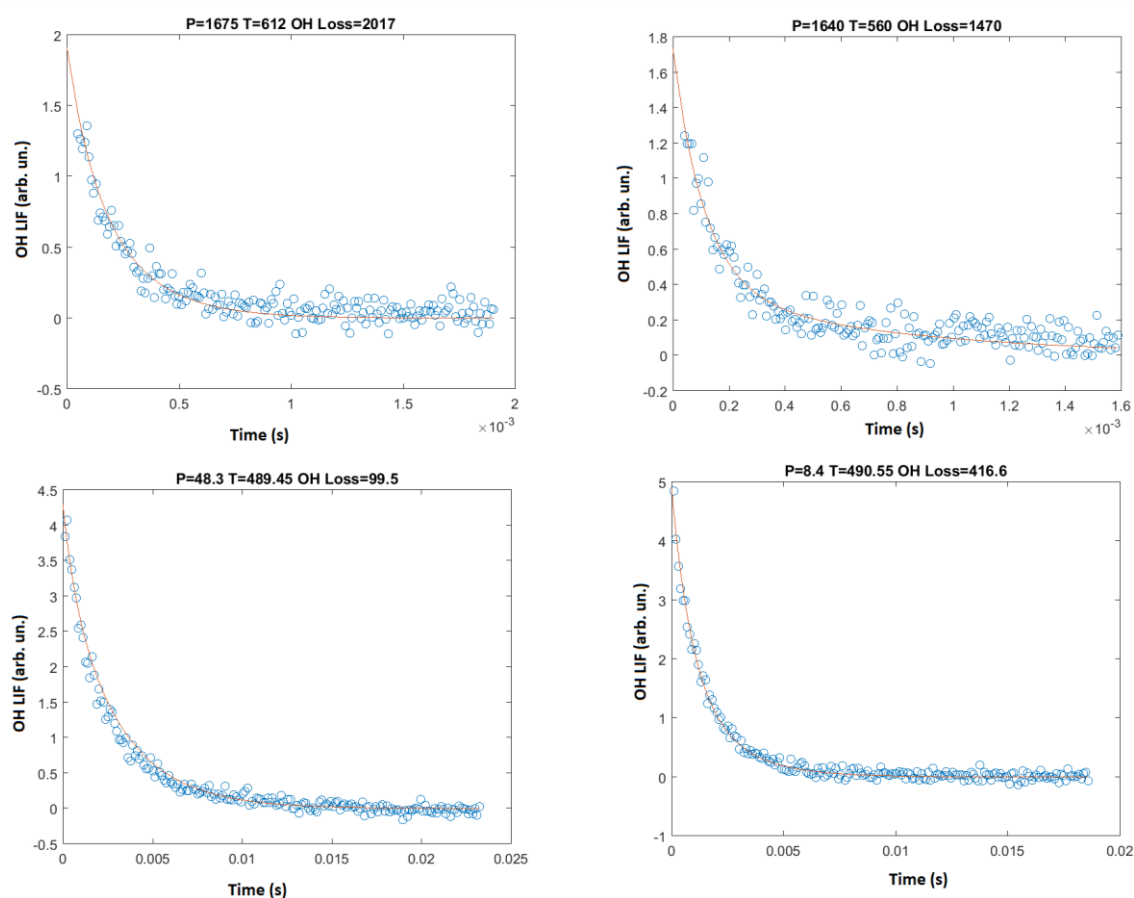
Figure 5.22 Are fits to the data generated from the direct trace analysis by fitting to the CCSD(T)/CBS//MP2/6-311++g(3df,3pd) surface, in general the OH recycling is well described as is shown by the excellent agreement between modelled and experimental traces.

This analysis allowed for the assignment of the route to OH recycling as predominantly coming thermally out of the CONMe$_2$ RO$_2$ well. Most OH recycling occurred before stabilisation into the QOOH well, for this system QOOH interception

177

is therefore not required to provide a good description of the observed OH traces. The majority of the methyl abstraction channel was shown to lead to OH reformation with a yield > 75 %. Four example fits are given as Figure 5.22, these led to the modified surface given as Figure 5.23. Where significant deviation between experimental and modelled OH traces was observed, in general these were when the either the concentration of oxygen or dimethyl formamide was subject to uncertainty. The oxygen concentrations were susceptible to being over and underestimated when there was not any 'added' oxygen present, where the oxygen concentration was proportional to the hydrogen peroxide flow and to the pressure of the reactor.

For elevated temperature measurements where pyrolysis of DMF was prolific, the DMF concentration was subject to large uncertainties. It should also be noted that the temperature assigned to an experiment was subject to an error of 5 K, and this was not accounted for well although this temperature error was assumed to be random and non-systematic with respect to individual experiments. That the temperature variation was random and not systematic was assumed, as it was for the earlier MESMER analysis and appears to be a valid.

Energies in kJ/mol
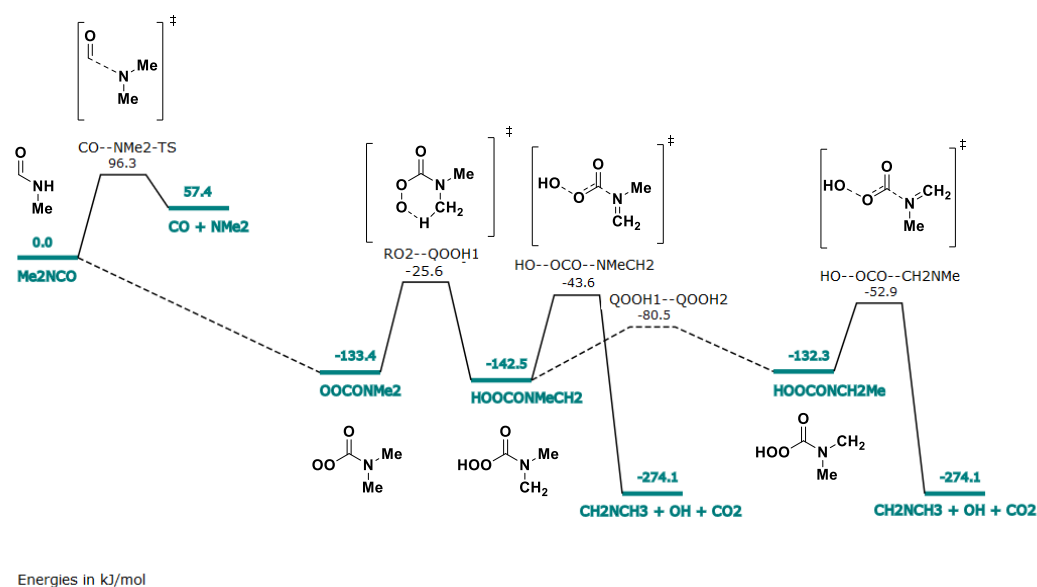
Figure 5.23 Is the surface for the reaction of the aldehydic R radical with oxygen following the reaction of OH and DMF where the methyl abstraction was treated using modified Arrhenius expressions. Where the initial CCSD(T)/CBS/MP2/6-311++g(3df,3pd) surface for CONMe$_2$ +O$_2$ was manipulated to reproduced experimental OH traces.

178

The PES, Figure 5.23, produced from this direct trace analysis gave a normalised χ^2 of 501 for 326 traces and the results were in excellent agreement with that initially calculated and close to that calculated at the CCSD(T)/CBS/MP2/6-311++g(3df,3pd) level. As discussed earlier a comparison of the χ^2 generated from a multi exponential fit to each trace was compared to the χ^2 generated from the model fit to the data the resultant normalised χ^2 returns one per trace for a perfect fit and the closer the total χ^2 is to the number of tracers in principle the better the fit of the model to the data. Where the initial barrier for RO_2 to QOOH isomerization was assigned as -25.6 kJ mol^{-1} with limits of this from the output files given as between -27.5 to -23.7 kJ mol^{-1}. ΔE_{down} for the RO_2 and QOOH radicals was assigned as 195 cm^{-1} (156 – 234 cm^{-1}) with a nitrogen bath gas.

Where both the methyl and the aldehydic surfaces were simulated, the barriers on both were treated as linked with each surface having an independent parameter. For both these surfaces an additional loss process of the RO_2 was included described as a modified Arrhenius process, due to the differing structures and the lack of any obvious competing loss reaction for the methyl RO_2 the two loss reactions were treated independently. The results of this analysis gave a χ^2 of 586 for 326, although this was an increase, this treatment was less flexible than the model that lead to Figure 5.23, and was therefore understandable. From this analysis the RO_2 to QOOH isomerization barrier for the aldehydic RO_2 was assigned as -25.3 $\pm$ 2.1 kJ mol^{-1}, with the majority abstraction being from the aldehydic site (68 $\pm$ 6 % at 298 K), and this ratio was temperature dependent, and was as high as 83 $\pm$ 7 % at 650 K, this surface is given as Figure 5.24.

Table 5-3 Summarizes the results of the RO2 to QOOH isomerization barrier both from calculations and evaluation of the OH recycling from OH and DMF.

Method	RO_2 QOOH isomerization barrier (kJ mol^{-1})	
	relative to R + O_2	relative to RO_2
CCSD(T)/CBS//M06-2X/ATZ	-30.2	104.1
CCSD(T)/CBS//MP2/6-311++g(3df,3pd)	-26.4	107.0
MESMER fit to eigenvalues (M06-2X TS)	-26.4 $\pm$ 0.7	107.9 $\pm$ 0.7
MESMER fit to eigenvalues (MP2 TS)	-26.7 $\pm$ 0.6	106.7 $\pm$ 0.6
Matlab/MESMER direct trace fitting 1 surface	-25.6 $\pm$ 1.8	107.8 $\pm$ 1.8
Matlab/MESMER direct trace fitting 2 surfaces	-25.3 $\pm$ 2.1	108.1 $\pm$ 2.1

The results of all the fitting exercises and the computational calculations for the aldehydic RO2 to QOOH barrier are summarized as Table 5-3, where the spread of the

resultant values allow this barrier to be assigned between -25 and -27 kJ mol⁻¹. With the experimental value of -25.3 ± 2.1 kJ mol⁻¹ (108.1 kJ mol⁻¹ relative to RO₂) is in excellent agreement with the CCSD(T)/CB//mp2/6-311++g(3df,3pd) value of -26.4 kJ mol⁻¹ (107 kJ mol⁻¹), and is within two σ of the CCSD(T)/CBS//M06-2X/ATZ barrier height relative to the RO2 well (104.1 kJ mol⁻¹), and just outside two σ relative to the entrance energy (-30.2 kJ mol⁻¹).
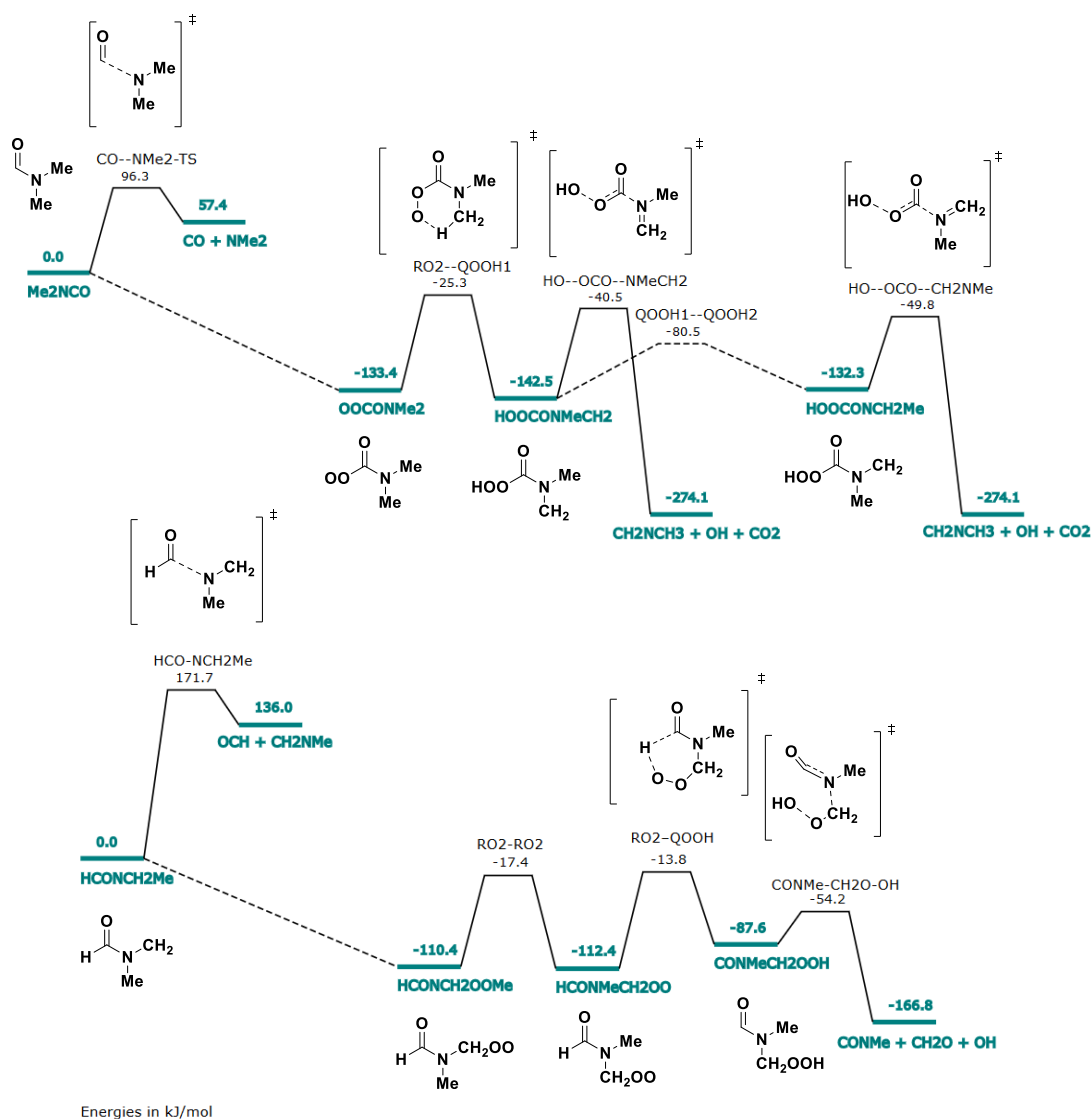
Figure 5.24 The two resultant R + O₂ potential energy surfaces generated when the barriers on both surfaces were floated during the MATLAB, Mesmer direct trace analysis. From this analysis the upper aldehydic surface was the majority abstraction process with the rate of OH reformation most sensitive to the RO₂ to QOOH barrier height.

5.5 Conclusion

This work has provided additional ambient temperature amide OH bimolecular rate coefficients for dimethyl formamide (DMF), $k_{DMF+OH,298\,K}= (1.30 \pm 0.12) \times 10^{-11} cm^3 s^{-1}$. Using a TOF-PTR-MS to measure the output of the reactor allowed for the concentration of added compound to be monitored, helping to ensure that a reliable bimolecular rate coefficient could be assigned even for a low vapour pressure compound.

Ambient temperature product branching ratios observed were not fully quantifiable. The TOF-PTR-MS data were in good agreement with previous published work of Bunkan *et al.*(20), Solignac *et al.*(18), and Borduas *et al.*(19). However, for DMF oxidation the PTR-MS was blind to the major product forming channel under ambient clean conditions, $Me_2N^.$. For the current setup, HO_2 yield information was heavily contaminated by photolysis of the amides themselves, so HO_2 yields provided little insight of significance to the branching ratios.

At elevated temperatures, the reaction of OH and DMF recycles OH, this OH recycling can be well described by abstraction from the aldehydic site followed by R + O_2, RO_2 QOOH isomerization and QO-OH decomposition processes. Fitting both the output of analytical fits and direct trace analysis gave reliable results showing that QO-OH fragmentation is a significant route to OH recycling for DMF and OH, in the presence of oxygen at elevated temperature (>450 K). Direct trace analysis where numerical integration was coupled to master equation calculations can define experimentally important barrier heights or well depths on a PES. However, the relative importance of QOOH interception and QOOH decomposition for OH recycling could not be well defined under the experimental conditions available. Coupling HO_2 to the system could allow for differentiation between OH recycling from QOOH and QO-OH, however this is not currently possible due to the complications from photolysis at 248 nm and 266 nm. Future work where photolysis initiates the OH reactions at longer wavelengths, for instance 280 nm, could potentially alleviate this and allow for the competition between QO-OH fragmentation and QOOH + O_2 interception to be assigned.

5.6 References

1. WEISSERMEL, K. *Industrial organic chemistry.* John Wiley & Sons, 2008.
2. NIELSEN, C.J., B. D'ANNA, C. DYE, M. GRAUS, M. KARL, S. KING, M.M. MAGUTO, M. MULLER, N. SCHMIDBAUER, Y. STENSTROM, A. WISTHALER and S. PEDERSEN. Atmospheric chemistry of 2-aminoethanol (MEA). *In:* J. GALE, C. HENDRIKS and W. TURKENBERG, eds. *10th International Conference on Greenhouse Gas Control Technologies.* Amsterdam: Elsevier Science Bv, 2011, pp.2245-2252.
3. PITTS, J.N., D. GROSJEAN, K. VANCAUWENBERGHE, J.P. SCHMID and D.R. FITZ. PHOTO-OXIDATION OF ALIPHATIC-AMINES UNDER SIMULATED ATMOSPHERIC CONDITIONS - FORMATION OF NITROSAMINES, NITRAMINES, AMIDES, AND PHOTO-CHEMICAL OXIDANT. *Environmental Science & Technology*, 1978, **12**(8), pp.946-953.
4. KARL, M. *Atmospheric degredation of amines (ADA): Amines in aerosol- A review.* N-110043. 2010.
5. NIELSEN, C.J., B. D´ANNA, R. BOSSI, A. JOAKIM, C. BUNKAN, L. DITHMER, M. GLASIUS, M. HALLQUIST, A. MARIA, K.HANSEN, A. LUTZ, K. SALO, M.M. MAGUTA, Q. NGUYEN, T. MIKOVINY, M. MÜLLER, H. SKOV, E. SARRASIN, Y. STENSTRØM, YIZHENTANG, J. WESTERLUND and A. WISTHALER. *Atmospheric Degradation of Amines (ADA): Summary report from atmospheric chemistry studies of amines, nitrosamines, nitramines and amides.* University of Oslo, 2012.
6. AL RASHIDI, M., A. EL MASRI, E. ROTH and A. CHAKIR. UV spectra and OH-oxidation kinetics of gaseous phase morpholinic compounds. *Atmospheric Environment*, 2014, **88**, pp.261-268.
7. BORDUAS, N., J.G. MURPHY, C. WANG, G. DA SILVA and J.P.D. ABBATT. Gas Phase Oxidation of Nicotine by OH Radicals: Kinetics, Mechanisms, and Formation of HNCO. *Environmental Science & Technology Letters*, 2016, **3**(9), pp.327-331.
8. RUSIN, A. and K. STOLECKA. An Analysis of Hazards Caused by Emissions of Amines from Carbon Dioxide Capture Installations. *Polish Journal of Environmental Studies*, 2016, **25**(3), pp.909-916.
9. SCHADE, G.W. and P.J. CRUTZEN. Emission of aliphatic amines from animal husbandry and their reactions: Potential source of N_2O and HCN. *Journal of Atmospheric Chemistry*, 1995, **22**(3), pp.319-346.
10. BARNES, I., G. SOLIGNAC, A. MELLOUKI and K.H. BECKER. Aspects of the Atmospheric Chemistry of Amides. *Chemphyschem*, 2010, **11**(18), pp.3844-3857.
11. MYERS, R.C. and B. BALLANTYNE. Comparative acute toxicity and primary irritancy of various classes of amines. *Toxic Substance Mechanisms*, 1997, **16**(2), pp.151-194.
12. WAGNER, E.D., J. OSIOL, W.A. MITCH and M.J. PLEWA. Comparative in Vitro Toxicity of Nitrosamines and Nitramines Associated with Amine-based Carbon Capture and Storage. *Environmental Science & Technology*, 2014, **48**(14), pp.8203-8211.
13. GROSJEAN, D. Atmospheric chemistry of toxic contaminants. 6. Nitrosamines: dialkyl nitrosamines and nitrosomorpholine. *Journal of the Air & Waste Management Association*, 1991, **41**(3), pp.306-311.
14. GJERNES, E., L.I. HELGESEN and Y. MAREE. Health and environmental impact of amine based post combustion CO2 capture. *Energy Procedia*, 2013, **37**, pp.735-742.

15. MAGUTA, M.M., M. AURSNES, A.J.C. BUNKAN, K. EDELEN, T. MIKOVINY, C.J. NIELSEN, Y. STENSTROM, Y.Z. TANG and A. WISTHALER. Atmospheric Fate of Nitramines: An Experimental and Theoretical Study of the OH Reactions with CH_3NHNO_2 and $(CH_3)_2NNO_2$. *Journal of Physical Chemistry A*, 2014, **118**(19), pp.3450-3462.

16. ONEL, L., M. BLITZ, M. DRYDEN, L. THONGER and P. SEAKINS. Branching Ratios in Reactions of OH Radicals with Methylamine, Dimethylamine, and Ethylamine. *Environmental Science & Technology*, 2014, **48**(16), pp.9935-9942.

17. MANZOOR, S., A. KORRE, S. DURUCAN and A. SIMPERLER. Atmospheric Chemistry Modelling of Amine Emissions from Post Combustion CO_2 Capture Technology. *Energy Procedia*, 2014, **63**, pp.822-829.

18. SOLIGNAC, G., A. MELLOUKI, G. LE BRAS, I. BARNES and T. BENTER. Kinetics of the OH and Cl reactions with N-methylformamide, N,N-dimethylformamide and N,N-dimethylacetamide. *Journal of Photochemistry and Photobiology A: Chemistry*, 2005, **176**(1–3), pp.136-142.

19. BORDUAS, N., G. DA SILVA, J.G. MURPHY and J.P.D. ABBATT. Experimental and Theoretical Understanding of the Gas Phase Oxidation of Atmospheric Amides with OH Radicals: Kinetics, Products, and Mechanisms. *The Journal of Physical Chemistry A*, 2015, **119**(19), pp.4298-4308.

20. BUNKAN, A.J.C., J. HETZLER, T. MIKOVINY, A. WISTHALER, C.J. NIELSEN and M. OLZMANN. The reactions of N-methylformamide and N,N-dimethylformamide with OH and their photo-oxidation under atmospheric conditions: experimental and theoretical studies. *Physical Chemistry Chemical Physics*, 2015, **17**(10), pp.7046-7059.

21. LINDLEY, C.R.C., J.G. CALVERT and J.H. SHAW. Rate studies of the reactions of the (CH3)2N radical with O_2, NO, and NO_2. *Chemical Physics Letters*, 1979, **67**(1), pp.57-62.

22. GE, X., A.S. WEXLER and S.L. CLEGG. Atmospheric amines – Part I. A review. *Atmospheric Environment*, 2011, **45**(3), pp.524-546.

23. CRITERIA, U.S.E.P.A., S.S. OFFICE, N.E.R. CENTER, U.S.E.P.A.O.O. RESEARCH and DEVELOPMENT. *Scientific and technical assessment report on nitrosamines*. U.S. Environmental Protection Agency, Office of Research and Development, 1977.

24. THITAKAMOL, B., A. VEAWAB and A. AROONWILAS. Environmental impacts of absorption-based CO_2 capture unit for post-combustion treatment of flue gas from coal-fired power plant. *International Journal of Greenhouse Gas Control*, 2007, **1**(3), pp.318-342.

25. NIELSEN, C.J., H. HERRMANN and C. WELLER. Atmospheric chemistry and environmental impact of the use of amines in carbon capture and storage (CCS). *Chemical Society Reviews*, 2012, **41**(19), pp.6684-6704.

26. VEGA, F., A. SANNA, B. NAVARRETE, M.M. MAROTO-VALER and V. CORTES. Degradation of amine-based solvents in CO_2 capture process by chemical absorption. *Greenhouse Gases-Science and Technology*, 2014, **4**(6), pp.707-733.

27. ONEL, L., M.A. BLITZ, J. BREEN, A.R. RICKARD and P.W. SEAKINS. Branching ratios for the reactions of OH with ethanol amines used in carbon capture and the potential impact on carcinogen formation in the emission plume from a carbon capture plant. *Physical Chemistry Chemical Physics*, 2015, **17**(38), pp.25342-25353.

28. KARL, M., T. SVENDBY, S.E. WALKER, A.S. VELKEN, N. CASTELL and S. SOLBERG. Modelling atmospheric oxidation of 2-aminoethanol (MEA)

emitted from post-combustion capture using WRF–Chem. *Science of the Total Environment*, 2015, **527–528**, pp.185-202.

29. BUGLER, J., K.P. SOMERS, E.J. SILKE and H.J. CURRAN. Revisiting the Kinetics and Thermodynamics of the Low-Temperature Oxidation Pathways of Alkanes: A Case Study of the Three Pentane Isomers. *The Journal of Physical Chemistry A*, 2015, **119**(28), pp.7510-7527.

30. GOLDSMITH, C.F., W.H. GREEN and S.J. KLIPPENSTEIN. Role of O_2 + QOOH in Low-Temperature Ignition of Propane. 1. Temperature and Pressure Dependent Rate Coefficients. *Journal of Physical Chemistry A*, 2012, **116**(13), pp.3325-3346.

31. JIAO, Y.G., F. ZHANG and T.S. DIBBLE. Quantum Chemical Study of Autoignition of Methyl Butanoate. *Journal of Physical Chemistry A*, 2015, **119**(28), pp.7282-7292.

32. SHA, Y. and T.S. DIBBLE. Tunneling effect in 1,5 H-migration of a prototypical OOQOOH. *Chemical Physics Letters*, 2016, **646**, pp.153-157.

33. MOHAMED, S.Y., L.M. CAI, F. KHALED, C. BANYON, Z.D. WANG, M.J. AL RASHIDI, H. PITSCH, H.J. CURRAN, A. FAROOQ and S.M. SARATHY. Modeling Ignition of a Heptane Isomer: Improved Thermodynamics, Reaction Pathways, Kinetics, and Rate Rule Optimizations for 2-Methylhexane. *Journal of Physical Chemistry A*, 2016, **120**(14), pp.2201-2217.

34. SHA, Y. and T.S. DIBBLE. Tunneling effect in 1,5 H-migration of a prototypical (center dot)OOQOOH. *Chemical Physics Letters*, 2016, **646**, pp.153-157.

35. WANG, Z.D., L.D. ZHANG, K. MOSHAMMER, D.M. POPOLAN-VAIDA, V.S.B. SHANKAR, A. LUCASSEN, C. HEMKEN, C.A. TAATJES, S.R. LEONE, K. KOHSE-HOINGHAUS, N. HANSEN, P. DAGAUT and S.M. SARATHY. Additional chain-branching pathways in the low-temperature oxidation of branched alkanes. *Combustion and Flame*, 2016, **164**, pp.386-396.

36. WALKER, R.W. and C. MORLEY. Chapter 1 Basic chemistry of combustion. *In:* M.J. PILLING, ed. *Comprehensive Chemical Kinetics*. Elsevier, 1997, pp.1-124.

37. ZÁDOR, J., C.A. TAATJES and R.X. FERNANDES. Kinetics of elementary reactions in low-temperature autoignition chemistry. *Progress in Energy and Combustion Science*, 2011, **37**(4), pp.371-421.

38. ZADOR, J., H. HUANG, O. WELZ, J. ZETTERBERG, D.L. OSBORN and C.A. TAATJES. Directly measuring reaction kinetics of [radical dot]QOOH - a crucial but elusive intermediate in hydrocarbon autoignition. *Physical Chemistry Chemical Physics*, 2013, **15**(26), pp.10753-10760.

39. FERNANDES, R.X., J. ZADOR, L.E. JUSINSKI, J.A. MILLER and C.A. TAATJES. Formally direct pathways and low-temperature chain branching in hydrocarbon autoignition: the cyclohexyl + O_2 reaction at high pressure. *Physical Chemistry Chemical Physics*, 2009, **11**(9), pp.1320-1327.

40. DESAIN, J.D., C.A. TAATJES, J.A. MILLER, S.J. KLIPPENSTEIN and D.K. HAHN. Infrared frequency-modulation probing of product formation in alkyl + O_2 reactions. Part IV. Reactions of propyl and butyl radicals with O_2. *Faraday Discussions*, 2002, **119**(0), pp.101-120.

41. SAVEE, J.D., E. PAPAJAK, B. ROTAVERA, H. HUANG, A.J. ESKOLA, O. WELZ, L. SHEPS, C.A. TAATJES, J. ZÁDOR and D.L. OSBORN. Direct observation and kinetics of a hydroperoxyalkyl radical (QOOH). *Science*, 2015, **347**(6222), pp.643-646.

42. GOPAL, R. and S.J.J.O.T.I.C.S. RIZVI. Vapour pressures of some mono-and di-alkyl substituted aliphatic amides at different temperatures. 1968, **45**(1), pp.13-&.

43. CHAKIR, A., G. SOLIGNAC, A. MELLOUKI and D. DAUMONT. Gas phase UV absorption cross-sections for a series of amides. *Chemical Physics Letters*, 2005, **404**(1), pp.74-78.

44. KELLER-RUDEK, H., G.K. MOORTGAT, R. SANDER and R. SÖRENSEN. The MPI-Mainz UV/VIS Spectral Atlas of Gaseous Molecules of Atmospheric Interest. *Earth Syst. Sci. Data*, 2013, **5**(2), pp.365-373.

45. BARNES, E.E. and W.T. SIMPSON. Correlations among Electronic Transitions for Carbonyl and for Carboxyl in the Vacuum Ultraviolet. 1963, **39**(3), pp.670-675.

46. DAVID R., G., L. CHI-HSIU, M. CHRISTOPHER, P. MICHAEL J. and R. STRUAN H. MESMER: An Open-Source Master Equation Solver for Multi-Energy Well Reactions. *The Journal of Physical Chemistry A*, 2012, **116**(38), pp.9545-9560.

47. *Gaussian 09, Revision D.01* M. J. Frisch, G. W. Trucks, H. B. Schlegel, G. E. Scuseria, M. A. Robb, J. R. Cheeseman, G. Scalmani, V. Barone, G. A. Petersson, H. Nakatsuji, X. Li, M. Caricato, A. Marenich, J. Bloino, B. G. Janesko, R. Gomperts, B. Mennucci, H. P. Hratchian, J. V. Ortiz, A. F. Izmaylov, J. L. Sonnenberg, D. Williams-Young, F. Ding, F. Lipparini, F. Egidi, J. Goings, B. Peng, A. Petrone, T. Henderson, D. Ranasinghe, V. G. Zakrzewski, J. Gao, N. Rega, G. Zheng, W. Liang, M. Hada, M. Ehara, K. Toyota, R. Fukuda, J. Hasegawa, M. Ishida, T. Nakajima, Y. Honda, O. Kitao, H. Nakai, T. Vreven, K. Throssell, J. A. Montgomery, Jr., J. E. Peralta, F. Ogliaro, M. Bearpark, J. J. Heyd, E. Brothers, K. N. Kudin, V. N. Staroverov, T. Keith, R. Kobayashi, J. Normand, K. Raghavachari, A. Rendell, J. C. Burant, S. S. Iyengar, J. Tomasi, M. Cossi, J. M. Millam, M. Klene, C. Adamo, R. Cammi, J. W. Ochterski, R. L. Martin, K. Morokuma, O. Farkas, J. B. Foresman, and D. J. Fox, Gaussian, Inc., Wallingford CT, 2009

48. ZHAO, Y. and D.G. TRUHLAR. The M06 suite of density functionals for main group thermochemistry, thermochemical kinetics, noncovalent interactions, excited states, and transition elements: two new functionals and systematic testing of four M06-class functionals and 12 other functionals. *Theoretical Chemistry Accounts*, 2008, **120**(1), pp.215-241.

49. JR., T.H.D. Gaussian basis sets for use in correlated molecular calculations. I. The atoms boron through neon and hydrogen. *The Journal of Chemical Physics*, 1989, **90**(2), pp.1007-1023.

50. III, G.D.P. and R.J. BARTLETT. A full coupled-cluster singles and doubles model: The inclusion of disconnected triples. *The Journal of Chemical Physics*, 1982, **76**(4), pp.1910-1918.

51. HALKIER, A., T. HELGAKER, P. JØRGENSEN, W. KLOPPER and J. OLSEN. Basis-set convergence of the energy in molecular Hartree–Fock calculations. *Chemical Physics Letters*, 1999, **302**(5), pp.437-446.

52. PETERSON, K.A., D.E. WOON and T.H.D. JR. Benchmark calculations with correlated molecular wave functions. IV. The classical barrier height of the $H+H_2 \rightarrow H_2+H$ reaction. *The Journal of Chemical Physics*, 1994, **100**(10), pp.7410-7415.

53. PAPAJAK, E., J. ZHENG, X. XU, H.R. LEVERENTZ and D.G. TRUHLAR. Perspectives on basis sets beautiful: seasonal plantings of diffuse basis functions. *Journal of chemical theory and computation*, 2011, **7**(10), pp.3027-3034.

54. PAPAJAK, E. and D.G. TRUHLAR. Convergent Partially Augmented Basis Sets for Post-Hartree−Fock Calculations of Molecular Properties and Reaction Barrier Heights. *Journal of chemical theory and computation*, 2011, **7**(1), pp.10-18.

55. HEAD-GORDON, M., J.A. POPLE and M.J. FRISCH. MP2 energy evaluation by direct methods. *Chemical Physics Letters*, 1988, **153**(6), pp.503-506.

56. PICCINI, G., M. ALESSIO and J. SAUER. Ab Initio Calculation of Rate Constants for Molecule–Surface Reactions with Chemical Accuracy. 2016, **55**(17), pp.5235-5237.

57. CRAMER, C.J. Essentials of Computational Chemistry: Theories and Models second edition. *In: Essentials of Computational Chemistry: Theories and Models second edition.* Wiley, 2004, pp.524-533.

58. IANNI, J.C. A comparison of the Bader-Deuflhard and the Cash-Karp Runge-Kutta integrators for the GRI-MECH 3.0 model based on the chemical kinetics code Kintecus. *Computational Fluid and Solid Mechanics*, 2003, pp.1368-1372.

59. MILLER, W.H. Tunneling Corrections to Unimolecular Rate Constants, with application to Formaldehyde. Journal American Chemical Society, 1979, 101(23): 6810-6814

6 The OH initiated oxidation of several nitrogen containing compounds

6.0 Overview of chapter 6

This work provides insights into minimising delivery problems that can arise when making OH kinetic measurements for low vapour pressure, and or basic compounds. This work focuses on three reactions: OH and tertiary butyl amine (tBuNH₂); OH and N-methyl-propane diamine (diamine); OH and methyl formamide (MF). For OH and MF, an ambient temperature bimolecular rate coefficient was assigned, $k_{OH+MF, 298K}= (1.03 \pm 0.23) \times 10^{-11}$ cm³ molecule⁻¹ s⁻¹. The temperature dependence of OH and tBuNH₂, using a modified Arrhenius equation, was given as $k_{OH+tBuNH2}= ((1.66 \pm 0.10)\times(T/298)^{-0.69\pm0.18}) \times 10^{-11}$ cm³ molecule⁻¹ s⁻¹ when the activation barrier was pinned to zero. For OH and the diamine, lower limits for the bimolecular removal rate could be assigned up to 350 K; the room temperature value was assigned as $k_{OH+Diamine,293K} = (7.09 \pm 0.22) \times 10^{-11}$ cm³ molecules⁻¹ s⁻¹ this is only a lower limit as there was still a potential for reaction between the amine and tBuOOH not being accounted for although efforts were made to minimise this.

6.1 Introduction

6.1.1 The reaction of OH and N-methyl formamide
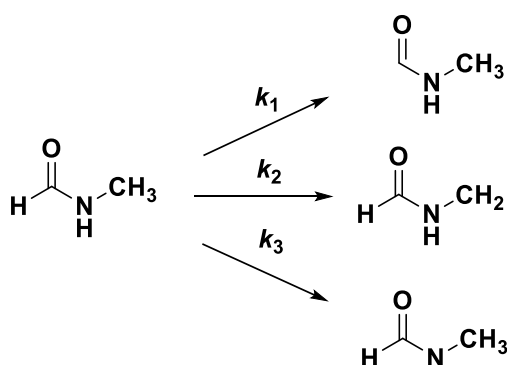
Scheme 6.1 The reaction of OH and N-methylformamide, shown on the left hand side, where the three OH abstractions reactions are given as, the aldehydic abstraction k_1, the methyl abstractions k_2, and the amino abstraction k_3. The initial radicals that would form following abstraction are shown on the right hand side.

Methyl formamide (MF) is a commodity chemical, used in the synthesis of methyl isocyanide (1) and in the place of formamide as a selective solvent for some hydrocarbons

in the oil industry.(2) In addition to the use of MF as an industrial solvent, MF can be formed from the atmospheric oxidation of dimethyl amine. (3)

There was limited literature work available on the rate for which N-methyl formamide (MF) reacts with OH. Previous work gave values of (1.01 ± 0.06) × 10^{-11} cm^3 molecule^{-1} s^{-1} from Borduas *at al.*,(4) (0.86±0.24) × 10^{-11} cm^3 molecule^{-1} s^{-1} from Solignac *et al.*,(5) both determined by the relative rate method, and (0.57±0.17) × 10^{-11} cm^3 molecule^{-1} s^{-1} by a direct kinetic study carried out by Bunkan *et al.*.(6) It was decided that this range of values was significant enough to merit being repeated. The ability to monitor reactant concentrations from the high-pressure system with a PTR-TOF-MS ensured that the concentration of MF had stabilized when kinetic measurements were made.

There are three distinct proton environments for OH abstraction in the reaction of OH and MF, shown in Scheme 6.1. From computational work performed at the CCSD(F12a)/aug-cc-pVTZ//M06-2X/aug-cc-pVTZ level, published by Bunkan *et al.*, (6)the barrier for the amino abstraction (k_3) is 12.6 kJ mol^{-1} above the entrance energy of OH and MF. The barriers for the other abstraction processes (k_1 and k_2) are comparable, and beneath the entrance energy at -7.7 kJ mol^{-1} for the aldehydic abstraction, and -9.6 kJ mol^{-1} for the methyl abstraction.(6) An additional potential energy surface (PES) for the OH abstraction reactions was calculated at the G3X-K level by Borduas *at al.*.(4)This surface had a significant barrier (16.9 kJ mol^{-1}) to the amino abstraction channel, with both the aldehydic and methyl abstraction channels again below the entrance energy. This surface gave the aldehydic abstraction (k_1) as -2.80 kJ mol^{-1} with a larger barrier than the methyl abstraction (k_2) -5.4 kJ mol^{-1}.

Considering both the surfaces given in the literature, there is agreement that abstraction will occur from the methyl and aldehydic sites. However, the barriers for these abstraction reactions are comparable, and with the errors present in even high-level calculations, this does not allow for differentiation of the expected branching ratio between k_1 and k_2. G3X-K and CCSD(F12a)/aug-cc-pVTZ//M06-2X/aug-cc-pVTZ are high level methods, with the expected errors in the calculated barrier heights being under 1 kcal mol^{-1}, or so called chemical accuracy. Both methods carry out high level single point energy calculations ,CCSD(T), carried out on M06-2X structures. The difference in these structures due to the basis sets used (6-31G(2df,p) verus aug-cc-pVTZ) are likely to be minor, and both the methods chosen give close to converged single point energies.

In addition to calculating surfaces, product studies on OH and methyl formamide have been carried out by Bunkan *et al.*, Barnes *et al.*, and Borduas *at al.*(4) The methyl isocyanate yield was given as 38 ± 2 % by Borduas *et al.* from PTR-MS measurements(4); this work states, however, that the methyl isocyanate measurements could also be well described by the model where the yield was fixed at 50 %. Barnes *et al.* (7) reported the methyl isocyanate yield as roughly 30 % and formyl formamide as 50 % using FTIR detection.(7) Bunkan *et al.*(6) gave the initial OH abstraction branching ratio of 0.83 k_1, 0.17 k_2,(6) which then led to 17 ± 3 % formylformamide formation, and 65 ± 3 % methyl isocyanate formation.

6.1.2 OH and t-Butylamine

In carbon capture and storage (CCS) by absorption in amine solutions, aminoethanol (MEA) is the benchmark standard to which other solvents are compared. However, because MEA has a relatively high binding energy with CO_2, sterically hindered amines can provide lower binding energies with greater or similar loading capacities to MEA. One of these sterically hindered amines is AMP (2-amino-2- methyl-1-propanol); direct OH study of AMP is complicated by a low vapour pressure [0.47 Torr at 25 °C,(8)], in addition to the general problems faced due to the reaction of amines with OH precursors.
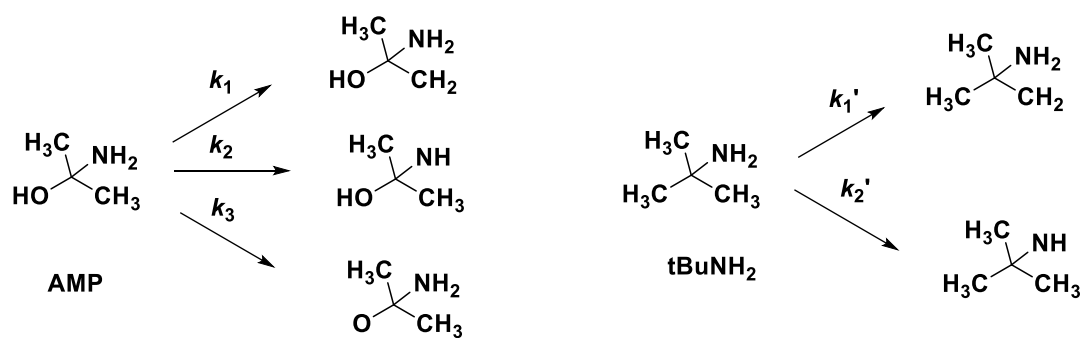
Scheme 6.2 Compares the OH oxidation of AMP to tBuNH$_2$, in general k_1' and k_2' may be expected to be similar to k_1 and k_2, if the hydroxy group is (as may be expected) a minor abstraction channel, and has a minimal influence on the beta methyl abstractions in AMP.

Tertiary butyl amine (tBuNH$_2$) differs from AMP only through the absence of the hydroxy group and as such, it may provide insight into the reactivity of sterically hindered amines towards OH reactions, as shown in Scheme 6.2. The importance of studying hindered amines is that that that their atmospheric loss processes are not as well understood as those of most primary amines. In the atmospheric oxidation of most

primary amines, the primary reactive loss of the radicals formed after reaction with OH, is HO_2 and imine formation. A fast route to imine formation is however not possible in amines such a $tBuNH_2$ due to the tertiary carbon adjacent to the NH_2 group.

The literature available on the reactivity of OH and $tBuNH_2$, when the work in this chapter was carried out, was a direct OH kinetic experiment performed by Koch *et al.*, (9) which gave $k_{OH+tBuNH2}=(1.2 \pm 0.12) \times 10^{-11}$ cm^3 molecule^{-1} s^{-1}. After the completion of both the experimental and computational work described in this chapter, a further experimental and theoretical paper on the reaction was published by Tan *et al.*(10) and gave $k_{OH+tBuNH2}=(0.84 \pm 0.17) \times 10^{-11}$ cm^3 molecule^{-1} s^{-1}. The work by Tan *et al.*(10) also provided a PES and product branching ratios, with the dominant channel being abstraction of an amino hydrogen. Formation of nitrogen centred radicals is problematic in that they are known to be gas phase sources of nitramines and nitrosamines. The reaction of nitrogen centred radicals with oxygen is well known to be slow, (11, 12) and therefore in environments with moderate to high NOx levels, the reaction with NO or NO_2 can be faster which leads to nitramines and nitrosamines formation. (13, 14)

In addition to being a proxy for studying OH and AMP, tertiary butyl amine is itself used in industry, in the vulcanization of rubber, and in the derivation of a variety of chemicals including pesticides. Its use in industrial processes and its volatility (measured as ≈ 6 Torr at 292 K) leads to losses to the atmosphere and OH initiated oxidation.

6.1.3 OH and N-methyl-propan-1,3-diamine

In CCS by absorption in amine solutions, the use of multi component amine based CO_2 absorption mixes has advantages over single component washes. One of the additives that is used in amine blends is N-methyl-propan-1,3-diamine (diamine).(15) The precise ratios and component amines used in the CCS industry are often classed as proprietary information, and the exact quantities of diamine used in CCS plants worldwide is not well known. Where this amine is used in CCS wash solutions it will be released to the atmosphere, but the atmospheric reaction of this amine with OH has not been studied in any detail.

6.2 Experimental results and discussions

The largest source of uncertainty in the kinetic measurements for these compounds was the error associated with defining the concentration of the reagent at the point that the kinetic measurements were being made. For methyl formamide, the vapour

pressure was insufficient (< 0.26 Torr), at 290 - 300 K (16) to allow accurate concentrations to be assigned to gas mixtures (measured with the baratron pressure gauges and mixing manifold available). As such, MF was added via the 'bubbler' method, where the ambient vapour above liquid MF was sampled by a backing flow of nitrogen; this method is described in greater detail in Chapter 2. The same method was used for the addition of N-methyl-propane diamine (diamine), because diamine was found to be lost when stored as a dilute mixture in cylinders. For tertiary butyl amine (tBuNH$_2$), known concentrations in nitrogen could be stored and used reliably, and the added concentrations were not reliant on vapour pressure calculations.

Delivered concentrations of methyl formamide (MF) were calculated from the Antoine equation, $\log(P/bar) = A - [B/(T/K + C)]$, using values of A = 4.99796, B = 2134.031, C = -45.071 (Heinrich *et al.*(17)) and these were measured over the range 369.6 - 472.4 K. For N-methyl-propan-1,3-diamine (diamine) no Antoine parameters were available from the literature, however a recent work on the enthalpy of vaporization carried out by Verevkin and Chernyak (18) gave $\Delta H_{vap} = (50.2 \pm 0.1)$ kJ mol^{-1} at 298 K. Using the enthalpy of vaporization, the boiling point 413 K(19) and the Clausius-Clapeyron equation, the vapour pressure was calculated for given temperatures. If better relationships between temperature dependences of the vapour pressures for MF or diamine become available in the future, the bimolecular rate coefficients given in this work should be summarily adjusted accordingly.

6.2.1 Room temperature OH and methyl formamide (MF)

The time taken to reach a stable concentration of added MF was notably slow and as such, the concentration was monitored by PTR-MS to ensure that it had stabilised before kinetic measurements were taken. By averaging the bimolecular plots collected at room temperature (293 – 300 K), the bimolecular rate coefficient k_{OH+MF} was assigned as $(1.03 \pm 0.23) \times 10^{-11}$ cm^3 molecule^{-1} s^{-1} where errors are given as 2 σ. Two example bimolecular plots are given as Figure 6.1, where different intercepts are apparent, this difference is due to the introduction of differing concentrations of H$_2$O$_2$.
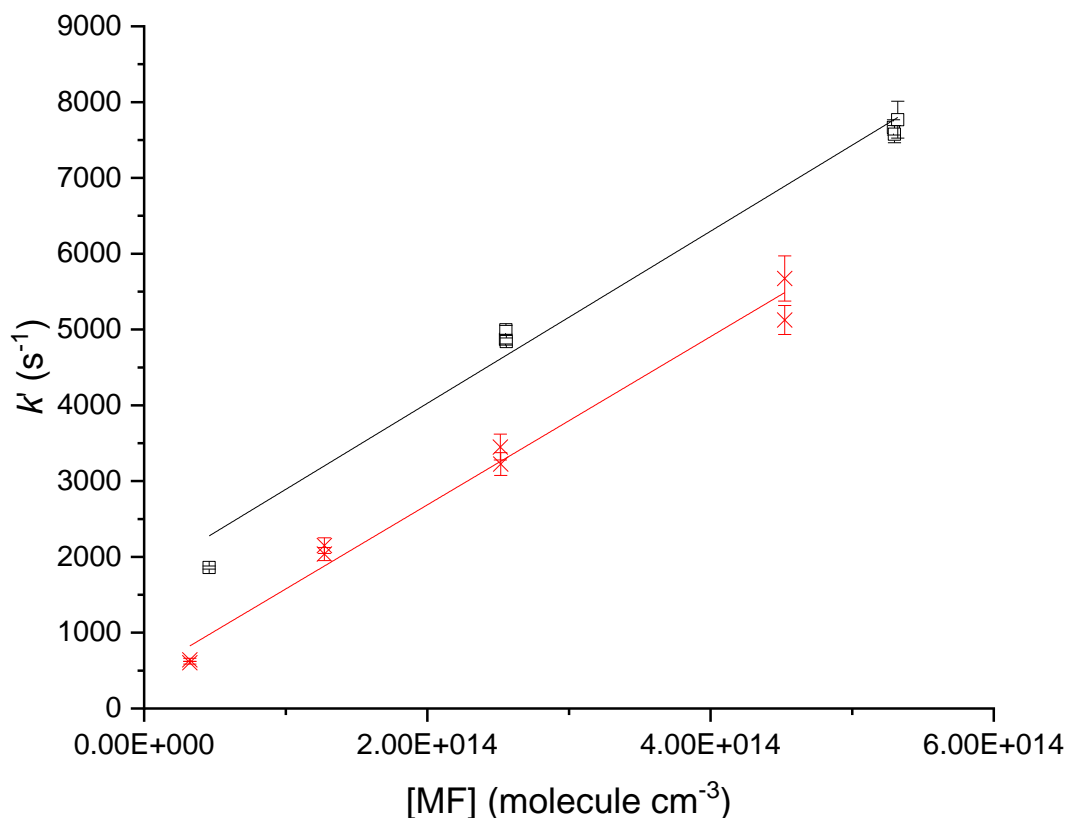
Figure 6.1 Two example bimolecular plots taken for MF and OH where H_2O_2 was photolysed at 248 nm and the concentration of MF was monitored via PTR-MS. The k_{OH+MF} values were assigned as $(1.14 \pm 0.12) \times 10^{-11}$ cm^3 molecule^{-1} s^{-1} and $(1.11 \pm 0.10) \times 10^{-11}$ cm^3 molecule^{-1} s^{-1}, with errors given as 2 σ.

TOF-PTR-MS spectra were analysed in order to assign product formation; from the experiments carried out at 5 Hz, the majority product observed was formylformamide (m/z 73 + 1 ($HCONHCHOH^+$) and 74 +1 its ^{13}C peak). Additional peaks from methyl isocyanate (m/z 76 ($CH_3NCOH_3O^+$)) and the peracid derivative of formylformamide (m/z 88 ($HCONCOOOH^+ -H_2O$)) were also observed. These are shown in Figure 6.2, where the dominance of abstraction from the methyl site (>65 %) can be clearly observed from the relative peak heights, when all amides and derivatives were assumed to have an equivalent PTR-MS response factor. This experiment was carried out under sufficiently low oxygen conditions (< 1×10^{18} molecule cm^{-3}) such that titration of any nitrogen centred radicals formed was not noticeably present.
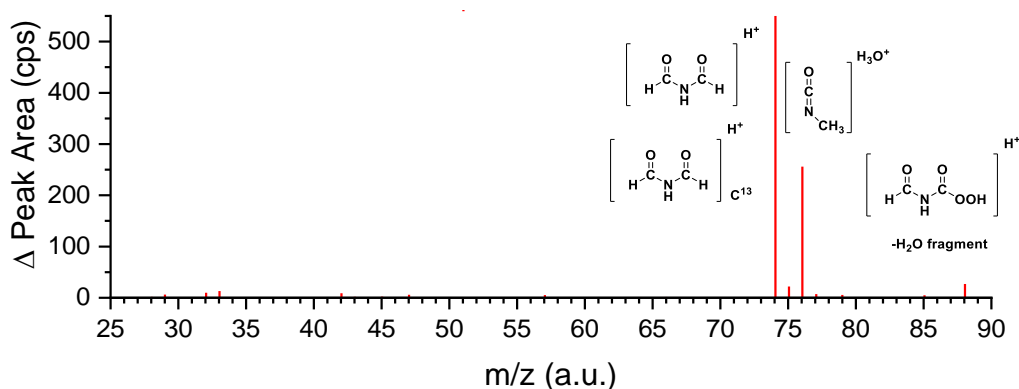
Figure 6.2 The TOF-PTR-MS product formation taken at 5 Hz with photolysis of H_2O_2 at 248 nm at 1530 Torr, $[O_2] \approx 3 \times 10^{16}$ molecule cm^{-3}. Dominant products observed at m/z 74 (a.u.) and m/z 76 (a.u.) and m/z 88 (a.u.).
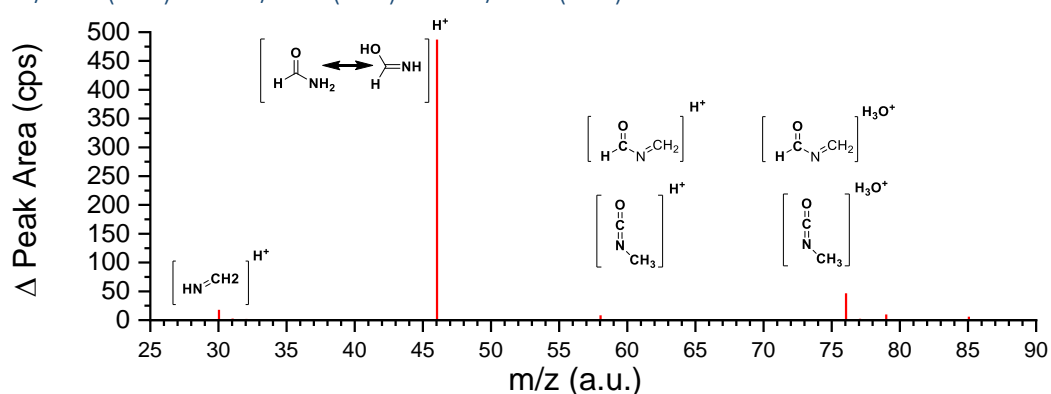
Figure 6.3 Change in peak areas for OH and MF observed at a repetition rate of 1Hz, with photolysis of H_2O_2 at 248 nm at 1530 Torr, $[O_2] = 1 \times 10^{18}$ molecule cm^{-3}. With lower radical concentrations, new products formed, with the majority product at m/z 46 (a.u.).

When the repetition rate was reduced to 1Hz, Figure 6.3, the product distribution changed with no observation of the formation of m/z 74 (73 + 1 ($HCONHCHOH^+$)). This can be assigned to the lower radical concentration present at the lower repetition rate. As these experiments were carried out under NOx free conditions, RO formation was dependant on RO_2-RO_2 reactions and was quadratically dependant on the radical concentration, and the radical concentration was itself dependant on the repetition rate. Under the lower radical concentrations the majority product was formamide or its alcohol tautomer (m/z 45 + 1), with methylimine formation (m/z 29 + 1) also observed from the aldehydic abstraction channel. The change in products can be explained by the dominance of internal isomerization chemistry for the RO_2 reactions. For the methyl abstraction, this allows the formation of HOCHNH, the tautomer of formamide that appeared at m/z (45 + 1).

Comparison of the products formed in both the 5 Hz and 1 Hz experiments was carried out. In the 5 Hz experiment, the ratio of the observed product yields were assigned as 66 ± 10 % formyl formamide, 30 ± 5 % methylisocyanate and 3 ± 5 % from the per-acid equivalent of formylformamide. The per-acid and methyl isocyanate was formed from the aldehydic channel and formyl formamide from the methyl abstractions. At 1 Hz 85 ± 10 % of the observed product formation was formamide, with methyl methylisocyanate accounting for 11 ± 5 %. It should be noted that the observed product yields were affected by losses of compounds to the walls before the PTR could sample the flow, and that the PTR was blind to any radicals which react too slowly with oxygen to form products. This would be expected to have impacted both the observation of isocyanates and the observation of imines. In the case of imines, this is a consequence of both their ability to polymerize, and their under representation due to inefficient titration by oxygen of the nitrogen-centred radicals.

The observed products formed at 5 Hz are in reasonable agreement with those observed by Barnes *et al.* (50 % formyl formamide 30% methyl isocyanate) (7) and by Borduas *et al.* (36 % methyl isocyanate) (4), and with the *ab initio* surfaces published in the work of Borduas *et al.* and Bunkan *et al.*(4, 6). As the temperature and pressure dependence of this reaction was not explored, master equation calculations were not required to fit the data. Additional computational calculations were not performed, given that high level surfaces were already available (CCSD(F12a)/aug-cc-pVTZ//M06-2X/aug-cc-pVTZ and G3X-K).

6.2.2 Tertiary butylamine OH photo-oxidation study.

Measurements were made on the kinetics of the reaction of OH and tertiary butyl amine ($tBuNH_2$), in both a conventional slow flow low-pressure reaction cell, and in the high-pressure system. Initial work in both setups showed that $tBuNH_2$ could be reliably stored as known concentrations in nitrogen, in both glass 'bulbs' and stainless steel 'scuba tanks'. Experiments carried out over multiple days showed little variation in the observed OH and $tBuNH_2$ values assigned at RT (293-300 K). Following this, experiments were carried out over a range of temperatures, 293 – 560 K, summarized in Table 6-1; an example elevated temperature bimolecular plot from this is shown as Figure 6.4.
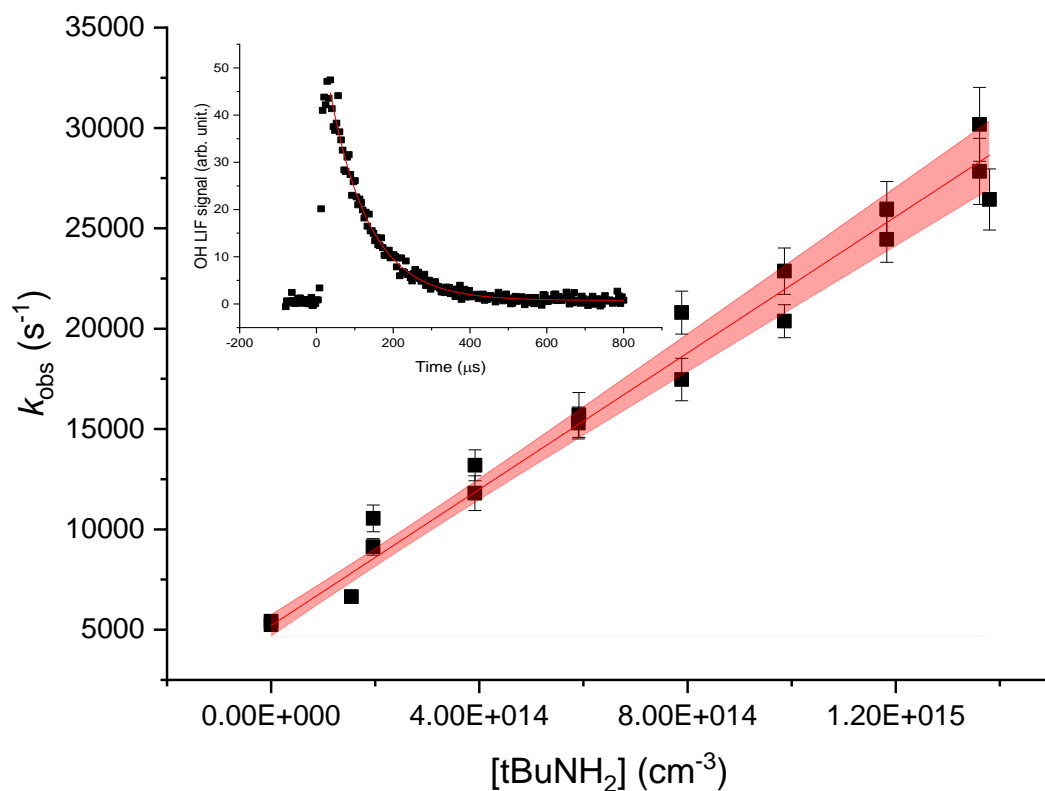
Figure 6.4 An OH and tBuNH$_2$ bimolecular plot used to generate $k_{OH+tBuNH2}$ at 303 K, 1478 Torr with tBuOOH as an OH precursor, with an apparent $k_{OH+tBuNH2}$ = (1.69 ± 0.07) × 10^{-11} cm^3 molecule^{-1} s^{-1}. Inset is an example OH fluorescence decay trace, used to generate the point at 1.5 × 10^{14} cm^{-3} tBuNH$_2$ on the bimolecular plot.

The experiments in the low-pressure and high-pressure reaction systems, were carried out using two different OH precursors, H$_2$O$_2$ and tBuOOH. It was noted that the removal rates appeared to be higher in the experiments carried out in the low-pressure apparatus with tBuOOH than in the high-pressure bay with H$_2$O$_2$. To assess whether this was due to the different OH precursors reacting with the amine at different rates before the gas mixtures reached the reaction region, tBuOOH was also used as the OH precursor for several room temperature measurements in the high-pressure system. The high-pressure measurements with tBuOOH as an OH precursor again returned the higher value observed in the low-pressure system. The resultant average ambient temperature bimolecular removal rate coefficient for tBuNH$_2$ and OH was assigned as $k_{OH+tBuNH2,298K}$ = (1.66 ± 0.14) × 10^{-11} cm^3 molecules^{-1} s^{-1}.

Table 6-1: Shows the rate coefficients for tBuNH$_2$ and OH measured both in the high-pressure reactor and in a conventional low-pressure cell. Two OH precursors were used, tBuOOH and H$_2$O$_2$. It is clear that where H$_2$O$_2$ was used, a lower rate coefficient was assigned.

Precursor	Temperature (K)			Pressure (Torr)			$10^{11} \times k_{OH+tBuNH2}$ (cm^3 molecule^{-1} s^{-1})		
HOOH	293	±	3	1250	±	75	1.27	±	0.03
HOOH	357	±	8	1251	±	75	1.39	±	0.02
HOOH	427	±	15	1253	±	75	1.40	±	0.02
HOOH	485	±	21	1270	±	75	1.42	±	0.05
HOOH	295	±	3	1297	±	75	1.29	±	0.03
HOOH	483	±	21	1488	±	75	1.36	±	0.03
HOOH	291	±	3	1371	±	75	1.30	±	0.02
HOOH	293	±	3	1287	±	75	1.36	±	0.03
tBuOOH	293	±	2	1350	±	75	1.69	±	0.11
tBuOOH	297	±	2	1377	±	75	1.67	±	0.04
tBuOOH	295	±	2	1260	±	75	1.70	±	0.07
tBuOOH	303	±	2	1478	±	75	1.69	±	0.07
tBuOOH	298	±	2	21	±	2	1.60	±	0.05
tBuOOH	298	±	2	21	±	2	1.66	±	0.06
tBuOOH	298	±	2	21	±	2	1.54	±	0.07
tBuOOH	298	±	2	21	±	2	1.63	±	0.07
tBuOOH	298	±	2	21	±	2	1.80	±	0.10
tBuOOH	350	±	5	51	±	2	1.43	±	0.05
tBuOOH	400	±	10	51	±	2	1.52	±	0.08
tBuOOH	450	±	15	51	±	2	1.22	±	0.06
tBuOOH	500	±	20	51	±	2	1.12	±	0.05
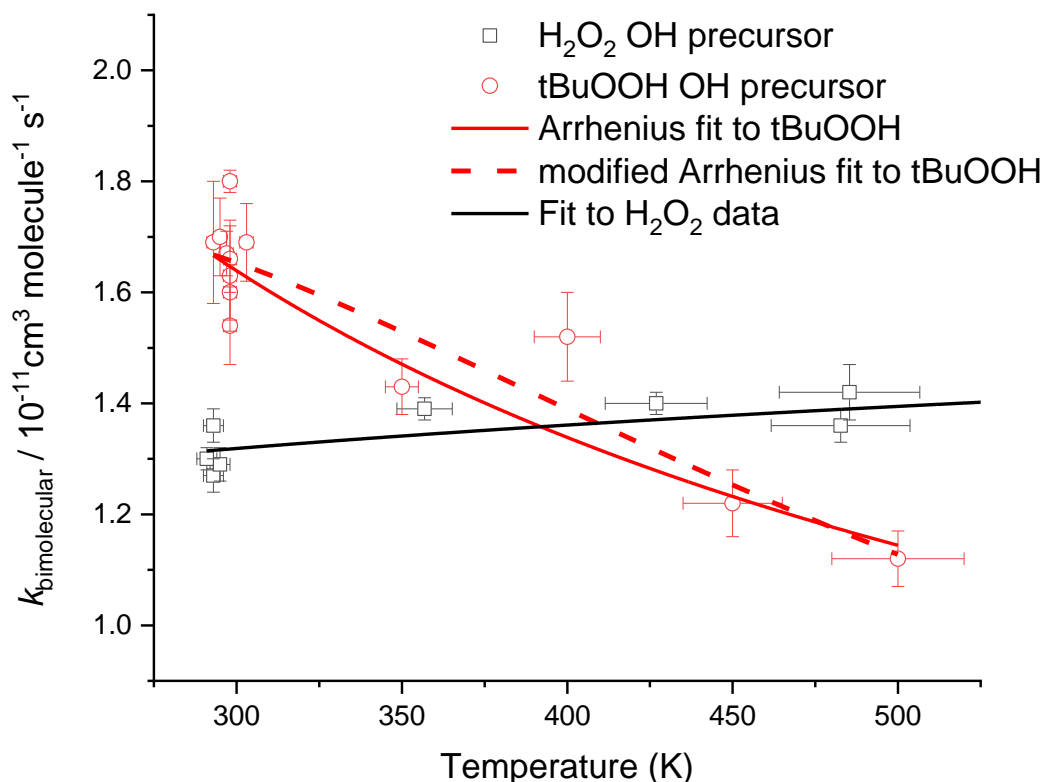
Figure 6.5 The observed temperature dependence of OH and tBuNH$_2$ where OH was formed through the photolysis of two different OH precursors, H$_2$O$_2$ and tBuOOH.

The rate coefficient is within a factor of two of the value calculated by relative rate in Tan *et al.*, $k_{OH+tBuNH2} = (0.84 \pm 0.17) \times 10^{-11}$cm^3 molecule^{-1} s^{-1} (10), and is in better agreement with a direct kinetic study by Koch *et al.,* k$_{OH+tBuNH2} = (1.20 \pm 0.12) \times 10^{-11}$ cm^3 molecule^{-1} s^{-1} at 298 K, measured by laser flash photolysis resonance fluorescence.(9) The value measured by Koch et al. (9) is however, in even better agreement with the average RT rate coefficient measured with H$_2$O$_2$ as the OH precursor indicating that perhaps that work was also influenced by precursor reaction with tertiary butyl amine.

Both the previous studies, Koch *et al.*(9)and Tan *et al.*(10) note the presence of issues in delivery of tBuNH$_2$, highlighting additional loss processes through reaction of the amine with both the OH precursors and walls. Tan *et al.* noted that a systematic error in accounting for the non-OH losses of the amine could have influenced their results.(10) Considering all these factors the apparent discrepancies between the previous works, and with those presented here is understandable. An estimate for the rate coefficient was generated by considering the removal rate of several simple amines was generated by considering the bimolecular rate coefficients and branching ratios for the reaction of OH and trimethylamine, methylamine, dimethyl amine and ethylamine from Onel *et al.* and

Carl *et al.* (20, 21), to work out a rate for the NH_2 group (1.14×10^{-11} cm^3 molecule^{-1} s^{-1}), and combining this with SAR values for the methyl protons from Kwok and Atkinson.(22) This method gave 1.19×10^{-11} cm^3 molecule^{-1} s^{-1} for OH and tBuNH$_2$ and 95.8 % amino abstraction, if the value for the amino protons (2.1×10^{-11} cm^3 molecule^{-1} s^{-1}) from the SAR analysis by Kwok and Atkinson (22) is instead used, a value of 2.15×10^{-11} cm^3 molecule^{-1} s^{-1} is produced with reaction being almost exclusively from the amino site (97.7 %). These estimations, however, neglect any possible influence of a pre reaction complex where if hydrogen bonding between the amino group and the OH radical exists abstractions rates from the methyl groups may be higher than that which would be estimated from the SAR analysis of Kwok and Atkinson.
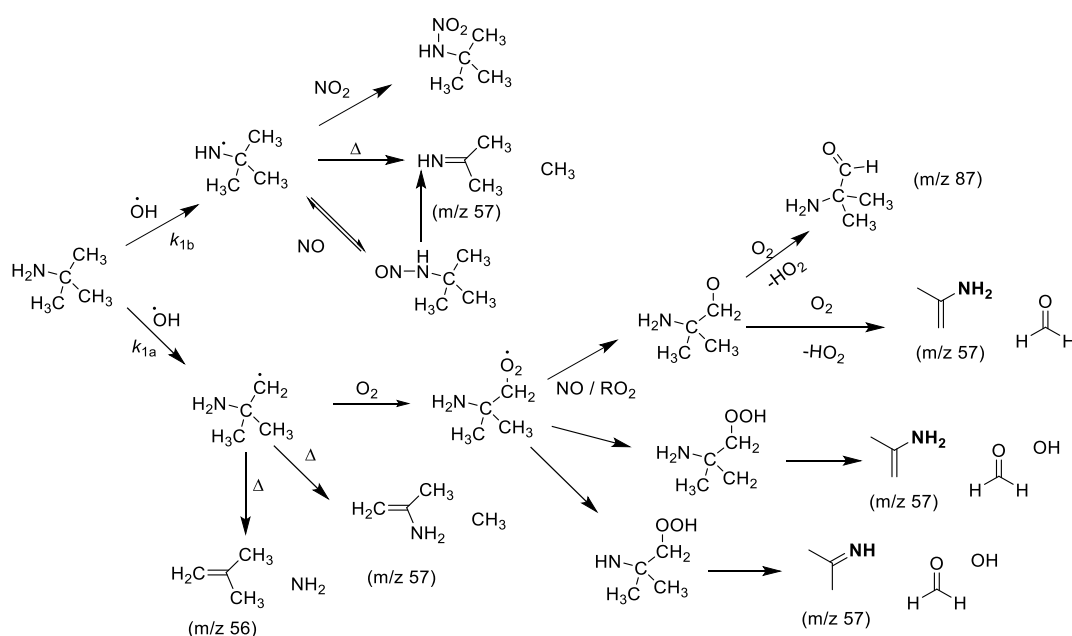
Scheme 6.3: Shows potential product formation pathways for tBuNH$_2$ and OH oxidation. The formation of an imine following amino abstraction has been verified by (10) with a route via the nitrosamine being indicated under ambient conditions.

To evaluate if there was any experimental evidence of OH recycling, from the route shown in Scheme 6.3, experiments were carried out over a variety of temperatures and pressures (21 – 1480 Torr, 293- 567 K), and the results in the high and low-pressure cells were in good agreement. The observed temperature dependence could be well described by a modified Arrhenius equation giving $k = ((9.0 \pm 35.0) \times (T/298)^{-2.07 \pm 5.16}) \times e^{((-4.20 \pm 9.70) \times 1000/RT)} \times 10^{-11}$ cm^3 molecule^{-1} s^{-1} (dashed red line in Figure 6.5); it was clear from this that there were insufficient high temperature points collected to define all three parameters. Therefore, a subsequent fit was performed where the activation energy was

pinned to zero. This visually improved the quality of the fit and allowed the other parameters to be defined as $k = ((1.66 \pm 0.10) \times (T/298)^{-0.69 \pm 0.18}) \times 10^{-11}$ cm^3 molecule^{-1} s^{-1} (solid red fit in Figure 6.5).

There was no evidence of non-exponential decays in experiments taken in either setup, even at elevated temperatures of 560 K. It may be that, although for the temperatures accessible with tertiary butyl hydroperoxide as an OH precursor there is no observable OH recycling, if a more thermally stable OH precursor were to be used for further experiments, at higher temperatures OH recycling may begin to occur.

When the OH and tBuNH$_2$ reactions were performed in the high-pressure system, the output was sampled by TOF-PTR-MS to provide end-product analysis. From the PTR-MS spectrum, Figure 6.6, there was observed product formation at m/z 58, 57, 88 and 46 a.u. The peak observed at m/z of 88 (87 +1, CH$_3$C(NH$_2$)(CH$_3$)CHOH$^+$), was due to the formation of 2-amino-2-methyl-propanal and is a minor product. The product observed at m/z 58 (57+1, C$_3$H$_7$NH$^+$) is the majority product and is due to the formation of 2-propanamine, and isopropenylamine. The peak at m/z 57 is due to the formation of isobutene (56 + 1, C$_4$H$_9^+$).

The imine and amine products can be formed by fragmentation of both the nitrogen centered and carbon centered radicals formed following the OH abstraction, (Scheme 6.3), and from the reactions of the RO$_2$ formed from oxygen addition to the methyl abstraction radical. As the majority product observed could be formed from both abstraction channels it did not alone allow for the abstraction branching ratio to be defined without further theoretical work.
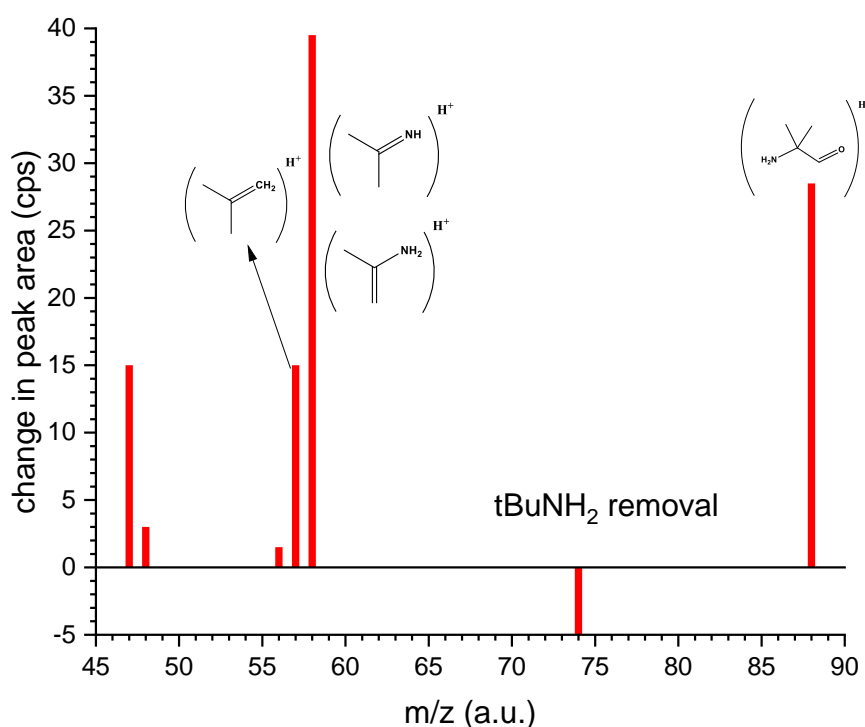
Figure 6.6 Changes in peak areas observed for OH and tBuNH$_2$ carried out at 1456 Torr and 293 K with hydrogen peroxide as an OH source and photolysis at 248 nm and 0.3 Hz. Changes in peak area were normalized to the loss of amine and only changes greater than 1 % of the loss of amine are displayed.

The likely fate of N centered radicals formed from the NH abstraction in the atmosphere will be reaction with NO$_2$ and NO to form nitra and nitrosomines, as the reaction with O$_2$ is slow (12). In clean (low NOx) environments it may be possible for the oxygen reaction to occur but it will be in competition with fragmentation of the aminyl radical, which forms the imine observed in the PTR-MS spectrum. The likely atmospheric fate of the carbon centered radicals will be reaction with O$_2$ to form RO$_2$ which can undergo further reactions (RO$_2$-RO$_2$ or RO$_2$ and NO, followed by reaction with oxygen) to form an aldehyde amine or undergo internal isomerization and fragmentation reactions to form an imine, both are seen in the PTR spectra, Figure 6.6.

To allow for further assignment of the products of tBuNH$_2$ OH initiated oxidation, *ab initio* calculations were carried out at the CCSD(T)/CBS//mp2/6-311++g(3df,3pd) level, and at the M06-2X/6-311++g(3df,3pd) level. The notation CCSD(T)/CBS//mp2/6-311++g(3df,3pd) is used to mean single point energies were calculated from a mixed Gaussian extrapolation of CCSD(T)/jun-cc-pvdz, tz, qz energies,

with structures and frequencies carried out at the MP2/6-311++g(3df,3pd) level, as described in Chapter 5.

These calculations provided PESs, which were evaluated for prompt routes to OH reformation and product formation. The relative barriers to a range of internal isomerizations were considered, and were generally in agreement with the previous scheme for the OH oxidation shown as Scheme 6.3.

For the initial OH abstraction reactions, the aminyl hydrogen abstraction occurs via a low energy pre reaction complex (PRC) of -11 kJ mol^{-1} followed by a slight barrier to abstraction of -6 kJ mol^{-1}. There are several competing methyl abstraction reactions; however only the lowest energy of these had a negative activation energy, as there is free rotation about the CN and CC bonds, only the lowest energy methyl abstraction will now be discussed; this occurs first through the formation of a deeper pre reaction complex of -30 kJ mol^{-1} before passing over a barrier of -4 kJ mol^{-1}. The reaction proceeding via abstraction reactions that occur over sunken barriers is in keeping with the observed negative temperature observed when tBuOOH was used as the OH precursor and is in opposition to the positive temperature dependence observed where H_2O_2 was used as the OH pre cursor. This provides further support that the measurements carried out with tBuOOH are more representative of the bimolecular removal rate coefficient for tBuNH$_2$ with OH.

A simple MESMER model of this system is shown as Figure 6.7; the results from this calculation at 300 K and 1600 Torr gave that the majority of the OH reaction occurred via NH abstraction (59 %), with the CH abstraction being the minor channel (41 %) In this model tunneling was accounted for using a one dimensional Eckart model. This result could over or underestimate the amino branching fraction, therefore further simulations were then carried out to evaluate the upper and lower limits of the amino branching fractions and these will now be described.
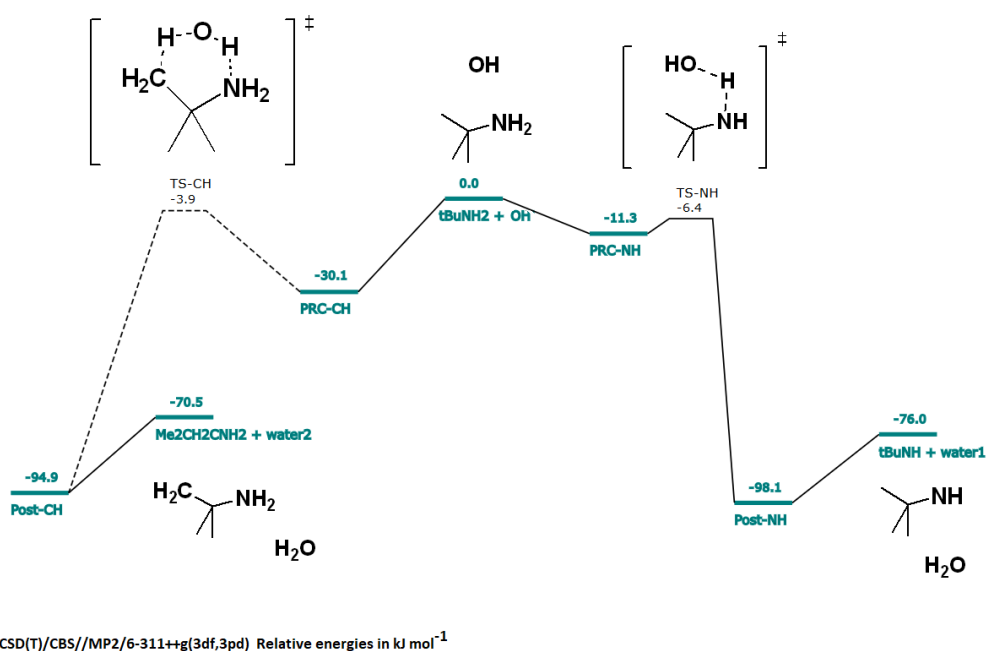
Figure 6.7 The PES surface for tBuNH$_2$ and OH at the CCSDT/CBS//MP2/6-311++g(3df,3pd) level. This surface begins in the centre with tBuNH$_2$ and OH and the LHS shows the methyl abstractions and the RHS the amino abstractions.

Because both abstraction reactions occur over submerged barriers from PRCs, the decision was made to also simulate the surface whilst treating the A factors of the two association reactions (forming the PRCs) statistically in the MESMER calculation (using a 3:1 ratio of the A factors for these processes). This treatment should provide an upper limit for the methyl abstraction branching fraction, and when this simulation was carried out, the dominant channel was abstraction from the methyls (62 %) leading to the carbon-centered radicals, and the minor channel would be the amino abstractions (38 %). This result (38 % amino abstraction) can be considered a lower limit to the amino branching fraction.

Although the NH abstraction transition state appears to occur via a different PRC to the methyl groups, there is a potential that in fact both abstractions occurred from the same (lower energy) pre reaction complex, when this was simulated the MESMER branching ratio at 300 K was 87 % amino and 13 % methyl abstraction. This result (87 % amino abstraction) can be considered to represent the upper limit for the amino branching fraction.

The energetics of the reaction of oxygen and the nitrogen centered aminyl radical agreed that this radical is relatively unreactive towards oxygen addition, with a well depth

of only 38 kJ mol^{-1} at the CCSD(T)/CBS//mp2/6-311++g(3df,3pd) level, and 31.8 kJ mol^{-1} below at the M06-2X/6-311++g(3df,3pd) level. Routes out of this RO$_2$ well, to form QOOH radicals through internal abstractions, all had barriers far above the entrance energies (> 65 kJ mol^{-1} from both CCSD(T)//MP2 and M06-2X calculations) and as such, were not relevant to any observed product formation.

The energy barrier to fragmentation of the nitrogen centered aminyl radical via C-C bond scission in order to form a CH$_3$ radical and imine was + 99.7 kJ mol^{-1} from the CCSD(T)/CBS//mp2-6-311++g(3df,3pd) calculations. The decomposition of this radical was then simulated for a range of temperatures and pressures using MESMER.

The OH and tBuNH$_2$ reaction leading to the N centered R radical is 78 kJ mol^{-1} exothermic. This coupled with the low reactivity of the aminyl radicals towards oxygen means that in very low NOx environments ([NOx] < 5 × 10^6 cm^{-3}), imine formation will be the major sink for this radical, for higher NOx concentration reactions fragmentation will be a minor channel however (< 1 % at 280 K). From the MESMER simulations at 280 K and 760 Torr, the reaction of NO with tBuNH was competitive with imine formation for even moderately low concentrations of NO ([NO] > 5.5 × 10^7 cm^{-3}), and the reaction with NO$_2$ was competitive at even lower concentrations of NO$_2$ ([NO$_2$] > 6.1 × 10^6 cm^{-3}). Although, the rate of fragmentation increased by a factor of 20 by 300 K, reaction with NOx can still be expected to be the majority product formed in urban and rural environments. These results were calculated using an assumption of a reaction rate coefficient for tBuNH with NO of 1 × 10^{-13} cm^3 s^{-1}, and a rate coefficient for tBuNH with NO$_2$ of 9 × 10^{-13} cm^3 s^{-1}, with 3 × 10^{-13} cm^3 s^{-1} of this forming nitramine; rural NO concentrations were treated as [NO] = 3 × 10^9 cm^{-3} and NO$_2$ was treated as [NO$_2$] = 6 × 10^{10} cm^{-3}. Reducing the barrier to fragmentation by 10 kJ mol^{-1} lead to fragmentation being under a 1 % channel with respect to reaction with NO$_2$ at 280 K, and this was still less than 9 % at 300 K. Under the experimental conditions in this work (NOx free), the fragmentation of the aminyl radical leading to imine will have been the only product formed following abstraction from the amino position.

For the methyl abstraction surface, only the initial RO$_2$ well depth and R radical decomposition had been calculated at the CCSD(T)/CBS//MP2/6-311++g(3df,3pd) level. The remaining calculations were performed at the M06-2X/6-311++g(3df,3pd) level. From the CCSD(T) calculation the RO$_2$ well depth was assigned as 151.3 kJ mol^{-1} relative to the energies of the R and oxygen, and the R decomposition to form imine and

a methyl was assigned a barrier of 114.3 kJ mol^{-1} above. An additional R fragmentation channel was available for this radical through the loss of NH$_2$ to form isobutene; the barrier to this process was 98.3 kJ mol^{-1}. This reaction will be the predominant fragmentation following abstraction of a methyl proton.

The respective M06-2X/6-311++g(3df,3pd) energies for the R decompositions and the RO$_2$ well depth were comparable to the CCSD(T)/MP2 calculations with: a well depth of 149.6 kJ mol^{-1}, a R decomposition barrier via loss of a methyl of 122.0 kJ mol^{-1}, and a barrier to the decomposition through the loss of NH$_2$ of 105.1 kJ mol^{-1}. Considering the respective well depth and decomposition barrier, it can be reasonably assumed that a stable RO$_2$ radical will be formed and that the subsequent chemistry of this RO$_2$ will be important under atmospheric conditions. However, at elevated temperatures with low oxygen the decomposition of the R radical to form isobutene will become significant, akin to the behavior of tertiary butanol.

$(CH_3)_2C(NH_2)CH_2$ $\rightarrow$ $CH_2C(CH_3)_2$ + NH$_2$ ΔH = + 82.3 kJ mol^{-1} (R6.1)

$(CH_3)_2C(NH_2)CH_2$ + O$_2$ $\rightarrow$ $(CH_3)_2C(NH_2)CH_2OO$ ΔH = -151.3 kJ mol^{-1} (R6.2)
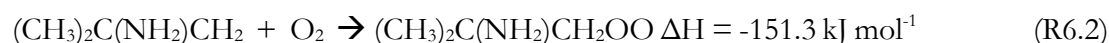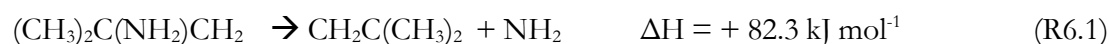
Following formation of an RO$_2$ radical there are two internal abstractions that can lead to formation of a QOOH species: abstraction of an aminyl proton, and abstraction from a methyl. At the M06-2X/6-311++g(3df,3pd) level, these barriers were both below the entrance energy of the R + O$_2$ reaction at –56.4 kJ mol^{-1} for the aminyl proton and -38.9 for abstraction of a methyl proton.

Only abstraction from the aminyl site leads to formation of a QOOH radical that can decompose to regenerate OH. This reaction is a two-stage process where the C-C bond cleaves to leave imine and a quasi-stable formyl OH complex, which then decomposed to yield an OH radical and formaldehyde. The barrier to this OH regeneration reaction is 18.4 kJ mol^{-1} below the R+O$_2$ energy, and at elevated temperatures and at low enough pressure, this route will allow for OH recycling. The full R+O$_2$ surface for the methyl abstraction channel is summarized as Figure 6.8.
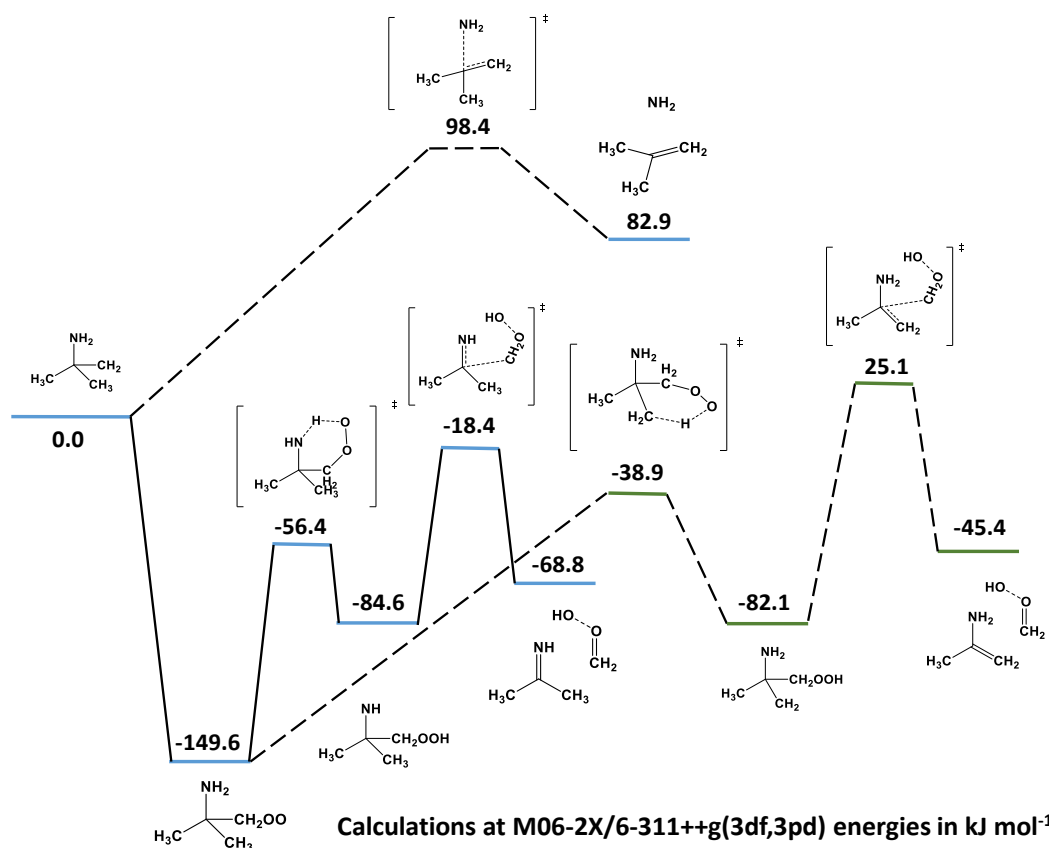
Figure 6.8. The R + O$_2$ surface calculated at the M0-62X/6-311++g (3df, 3pd) level for the radical formed following abstraction of a methyl proton from tertiary butyl amine.

When MESMER simulations of this surface (Figure 6.8) were performed, OH recycling only began to occur on the experimental timescale for the OH kinetic measurements (1-100 ms) at temperatures above 550 K. The MESMER simulations did support the hypothesis that OH recycling will occur at higher temperatures than those accessed in this work using tBuOOH as an OH precursor. From the MESMER simulation at room temperature (300 K) pressure dependent, OH recycling (well skipping OH) would not have been observed, as this only became an available route for pressures less than 0.5 Torr.

The principle decomposition reaction for the methyl abstraction is loss of NH$_2$ to form isobutene, and OH recycling route were not available; therefore, the majority product observed in the TOF-PTR-MS spectra at m/z 58 can be attributed to OH abstraction of an amino proton. It should be noted however, that the decomposition processes will be only a minor channel (< 0.2 %) under atmospheric conditions, when compared to reaction with O$_2$. Where the PTR response of the amines and the amino

aldehydes were assumed to be the same, the yield of m/z 58 was 36 % (28 – 51 %), and the yield of the amino aldehyde was 26 % (20 – 37 %), and the formation of isobutene was 14 % (8 – 20 %). An observation of 36 % abstraction from the amino position and > 50 % abstraction from the methyl positions is in line with the lower limit simulations for the amino abstraction from the MESMER analysis of the abstraction potential energy surface. The MESMER analysis where the A factors were weighted statistically gave 38 % amino and 62 % methyl abstraction. Within the limits of the experimental data and the computational work performed, the branching ratio for methyl abstraction can be assigned between 0.4 and 0.6 with the remainder being the amino abstraction channel. Even with the value for the amino abstraction close to the lower limit for the MESMER simulations, the potential for the formation of Nitramines and Nitrosamines is significant (40 – 60 %) under atmospheric conditions.

Further work on this reaction could aid in defining the branching fraction, this could be carried out by the introduction of a small additional flow of NO_2 to titrate any nitrogen-centered radicals to nitramines. This is important as there is the potential that the amino branching fraction has been underestimated in the current work. Carrying out both the PTR analysis and OH measurements over a greater range of temperatures (> 550 K) where OH recycling may begin to occur would also allow for better assignment of the branching ratios for the initial OH abstraction reactions; in a manner similar to the work carried out on n-butanol oxidation discussed in chapter 4.

6.2.3 N-methyl-propane diamine OH photo-oxidation work:

Work on N-methyl-1,3-diaminopropane (diamine) was more complex than that carried out on $tBuNH_2$ and MF. The diamine reacted readily with hydrogen peroxide before it reached the high-pressure reactor in the delivery line and could not be delivered consistently from cylinders. The diamine also reacted readily with air, releasing a gaseous product and the amine changed colour to yellow from being colourless. The early work that was carried out on this compound resulted in non-reproducible results due to inconsistent delivery of the diamine.
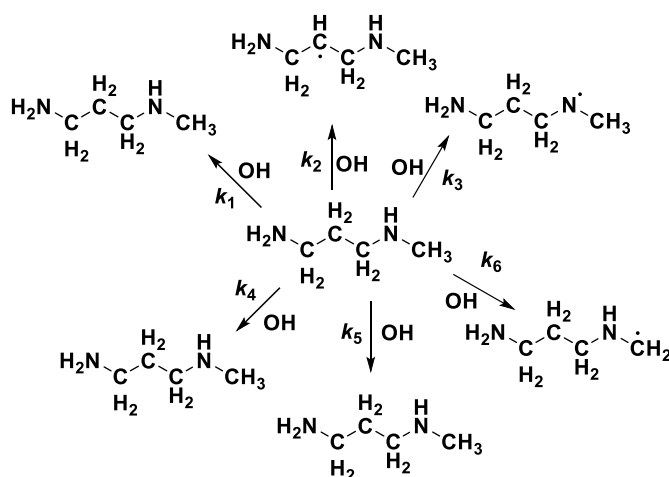
Scheme 6.4: Shows all six different abstractions available for the diamine each of these will lead to different product formation leading to a complex mix of products that along with high background counts makes product analysis complex.

To minimize reagent and precursor reactions the minimum peroxide flow that produced sufficient OH signal for precise rate coefficients to be assigned was used for experiments with diamine. Where hydrogen peroxide was used linear bimolecular plots were not possible, when tertiary butyl hydro peroxide was used it was possible to generate linear plots; however, where the diamine was delivered from a cylinder these experiments were still not reproducible.

By delivering the amine under nitrogen from a bubbler, combined with using a minimal flow of tertbutlyhydroperoxide as the OH precursor, reproducible and linear results were obtained. These measurements gave $k_{298\text{ K}} = (7.09 \pm 0.45) \times 10^{-11}$ cm^3 molecule^{-1} s^{-1} which should be considered a lower limit for the room temperature removal rate as it is probable that some of the diamine was still lost through reaction with the precursor. One of the linear bimolecular plots generated using a bubbler to deliver the diamine and tBuOOH as an OH precursor is shown in Figure 6.9. A summary of all the OH kinetic work carried out with tBuOOH as an OH precursor and diamine addition from a bubbler are given in Table 6-2, and are plotted as Figure 6.10, and were collected over a temperature range of 293-500 K.
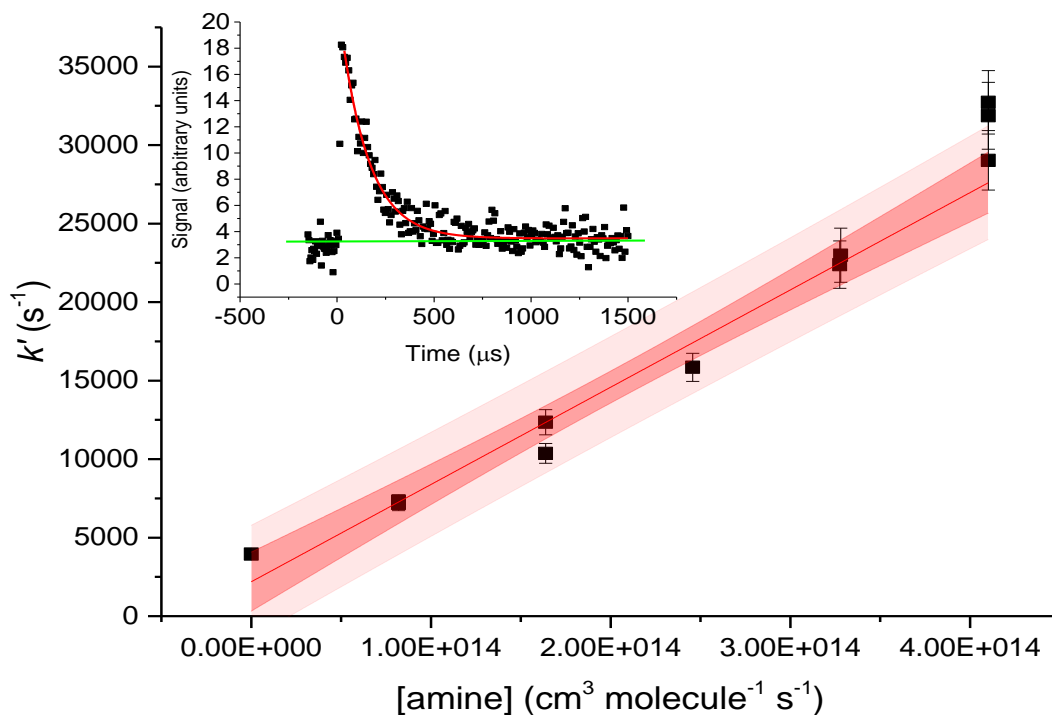
Figure 6.9 An example bimolecular plot for the diamine delivered by a bubbler using tBuOOH as an OH precursor at 100 °C.

Table 6-2: Shows the rate coefficients collected for N-methyl-1,3-diaminopropane and OH using tBuOOH as the precursor.

Temperature (K)	$10^{11} \times k_{\text{OH+Diamine}}$ (cm^3 molecule^{-1} s^{-1})	Pressure (Torr)	OH precursor
293	7.07 ± 0.32	1500 ± 30	tBuOOH
293	6.54 ± 0.27	1550 ± 30	tBuOOH
293	7.60 ± 0.52	1610 ± 30	tBuOOH
293	7.16 ± 0.08	1550 ± 30	tBuOOH
353	7.61 ± 0.20	1596 ± 30	tBuOOH
353	6.20 ± 0.33	1600 ± 30	tBuOOH
353	6.86 ± 0.29	1608 ± 30	tBuOOH
421	4.40 ± 0.22	1610 ± 30	tBuOOH
432	2.38 ± 0.18	1370 ± 30	tBuOOH
489	2.20 ± 0.16	1600 ± 30	tBuOOH
496	1.38 ± 0.22	1380 ± 30	tBuOOH

TOF-PTR-MS spectra were collected during the experiments carried out on the high-pressure system. For the experiments carried out with hydrogen peroxide as the OH precursor there was no observation of the amine reaching the TOF-PTR-MS. In the absence of an OH precursor there was a parent mass peak at m/z 89 (88+1); however, this peak did not respond linearly to changes in the bubbler flow. When the amine was flowed in the presence of tBuOOH, again a mass was observed at m/z 89, and again this peak did not respond linearly to the flow through the bubbler; the observed removal rate however did respond linearly. That linear responses were not observed was likely caused by losses within the PTR-MS sampling system.
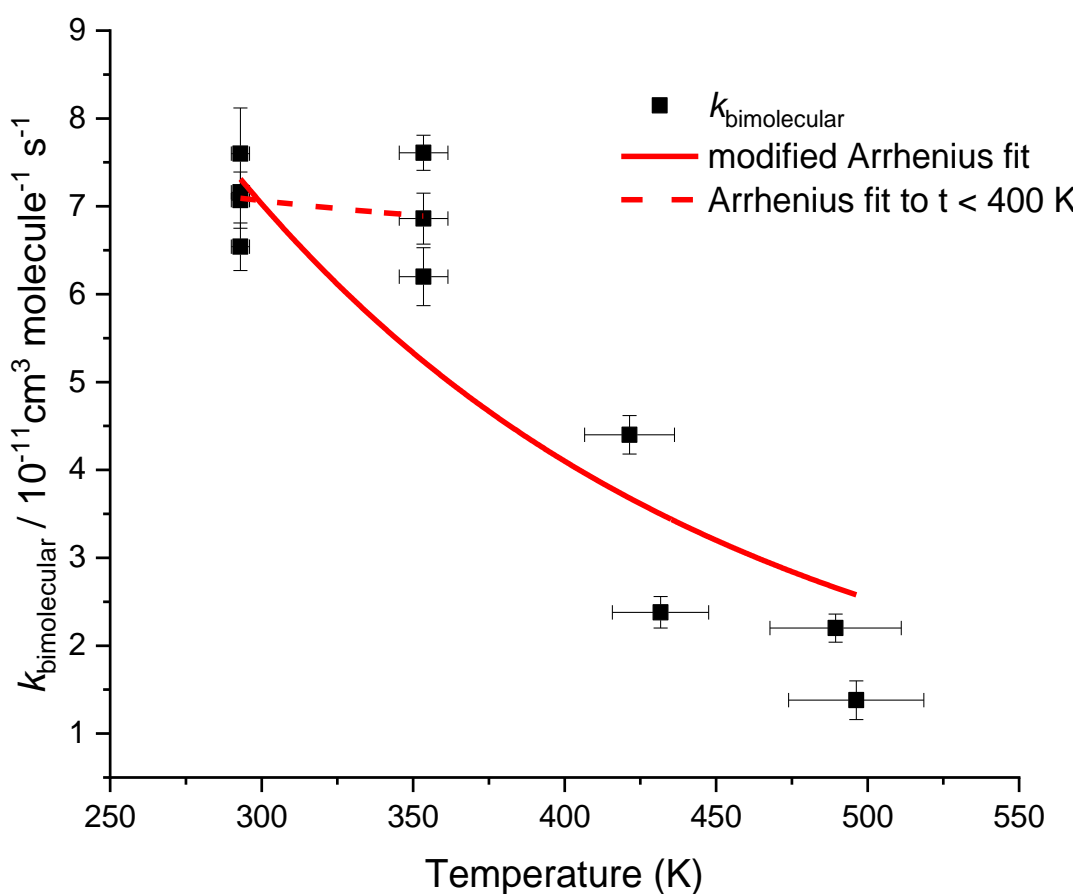
Figure 6.10 The observed temperature dependence for OH and N-methyl propane diamine the apparent strong temperature dependence observed was likely due to wall induced pyrolysis of the amine at elevated temperatures.

From the work summarized in Table 6-2, and shown in Figure 6.10, the reaction appears to have a strongly negative temperature dependence, which is consistent with a fast gas phase abstraction reaction with a negative activation energy. However, the change in observed bimolecular removal rate with temperature was exacerbated due to the

diamine having low thermal stability. The reduced observed rates were a consequence of less of the compound reaching the sampled region of the high-pressure system. This is supported by the weaker change in rate coefficient between 290 and 370 K compared with 370 to 500 K. From the two point fit between 290 and 370 K, the temperature dependence was given as $k = ((6.0 \pm 2.0) \times e^{((-0.41 \pm 0.09) \times 1000/RT)}) \times 10^{-11}$ cm^3 molecule^{-1} s^{-1}.

It was not possible to quantify the degree to which the lower observed bimolecular removal rates was due to pyrolysis. This was because the PTR-MS peak response was non-linear. As a result, the decision was made to not include any measurements made at over 400 K in the temperature dependence given earlier. Improvements to the work carried out here could be made by measuring the amine concentration *in situ* by UV absorption. This technique has previously been used successfully to quantify the amine concentration delivered to conventional quasi-static cells.

6.3 Summary

This work has provided additional ambient temperature OH bimolecular rate coefficients for methyl formamide (MF), $k_{OH+MF,298K} = (1.03 \pm 0.23) \times 10^{-11}$ cm^3 molecules^{-1} s^{-1}, tertiarybutyl amine (tBuNH$_2$), $k_{OH+tBuNH2,298K} = (1.66 \pm 0.20) \times 10^{-11}$ cm^3 molecules^{-1} s^{-1}, for N-methyl-propanediamine, $k_{OH+Diamine,293K} = (7.09 \pm 0.22) \times 10^{-11}$ cm^3 molecules^{-1} s^{-1}. The use of a TOF-PTR-MS to measure the output of the reactor allowed for the concentration of added compound to be monitored. This helped to ensure that a reliable bimolecular rate coefficient could be assigned, even for such a low vapour pressure compound as methyl formamide.

The measured k_{OH+MF} is in excellent agreement with the published value of $k_{OH+MF,298K} = (1.0 \pm 0.60) \times 10^{-11}$ cm^3 molecules^{-1} s^{-1} from Borduas *et al.*(4) which was measured by relative rate, and is within error of the value $k_{OH+MF,298K} = (0.86 \pm 0.24) \times 10^{-11}$ cm^3 molecules^{-1} s^{-1} from Solignac *et al.*(5) The value in this work was however a factor of 2 higher the value from Bunkan et al of $(0.57 \pm 0.17) \times 10^{-11}$ cm^3 molecules^{-1} s^{-1}; this value was calculated in a direct study and as such any issues with delivering MF would have lead to an underestimation of the removal rate.

Ambient temperature product branching ratios observed for OH and MF were not fully quantifiable. When quantification was attempted, the PTR response of isocyanates and amides were treated as equivalent. The observed products for MF oxidation were 66 $\pm$ 10 % formyl formamide (FF), and 30 $\pm$ 5 % methylisocyanate

(MI). These results were in good agreement with previous published work of Barnes *et al.* (50 % FF, 30 % MI),(7) and Borduas *et al.*(28 % MI).(4) Bunkan *et al.*(6) assigned the product yields as 65 % MI and 17 % FF which seems in disagreement with the results of this work. If the calibration factors used by Bunkan *et al.*(6) for these products differs strongly from the assumption of equivalency used to generate the results presented here, then the discrepancy with the results of Bunkan *et al.*(6) may be explained.

The calculated surface for OH and tertiary butyl amine is in very good agreement with a surface presented in the SI for a recent paper on this reaction published by Tan *et al.*.(10) The OH removal rate measured in this study $k_{OH+tBuNH2,298K} = (1.66 \pm 0.20) \times 10^{-11}$ cm^3 molecules^{-1} s^{-1}, was higher than that presented in Tan *et al.* $(k_{OH+tBuNH2} = (0.84 \pm 0.17) \times 10^{-11}$ cm^3 molecule^{-1} s^{-1}) which was measured by relative rate. (10) The value in this work was however in better agreement with previous work published by Koch *et al.* $k_{OH+tBuNH2} = (1.20 \pm 0.12) \times 10^{-11}$ cm^3 molecule^{-1} s^{-1} at 298 K, measured by laser flash photolysis resonance fluorescence.(9) The amino abstraction branching fraction from the surface was calculated to be 0.59, with this in reasonable agreement with the product formation observed by TOF-PTR-MS. Even if a lower limit for the amino branching fraction of 0.4 is used, the potential for the formation of nitramines and nitrosamines is still significant for the atmospheric oxidation of tBuNH$_2$.

Repeatable kinetics for OH and n-methyl propane diamine were observed for measurements made where the amine was delivered in a backing flow of nitrogen, and OH was generated from photolysis of tertiary butyl hydroperoxide. These measurements gave a lower limit for the OH removal rate coefficient at room temperature and 350 K.

6.4 References

1. R. E. SCHUSTER, J.E.S., AND JOSEPH CASANOVA, JR. METHYL ISOCYANIDE. *Organic Syntheses*, 1966, **46**(75).
2. HANSJÖRG BIPP, H.K. Formamides. *In: Ullmann's Encyclopedia of Industrial Chemistry*. 2011.
3. NIELSEN, C.J., H. HERRMANN and C. WELLER. Atmospheric chemistry and environmental impact of the use of amines in carbon capture and storage (CCS). *Chemical Society Reviews*, 2012, **41**(19), pp.6684-6704.
4. BORDUAS, N., G. DA SILVA, J.G. MURPHY and J.P.D. ABBATT. Experimental and Theoretical Understanding of the Gas Phase Oxidation of Atmospheric Amides with OH Radicals: Kinetics, Products, and Mechanisms. *The Journal of Physical Chemistry A*, 2015, **119**(19), pp.4298-4308.
5. SOLIGNAC, G., A. MELLOUKI, G. LE BRAS, I. BARNES and T. BENTER. Kinetics of the OH and Cl reactions with N-methylformamide, N,N-dimethylformamide and N,N-dimethylacetamide. *Journal of Photochemistry and Photobiology A: Chemistry*, 2005, **176**(1–3), pp.136-142.
6. BUNKAN, A.J.C., J. HETZLER, T. MIKOVINY, A. WISTHALER, C.J. NIELSEN and M. OLZMANN. The reactions of N-methylformamide and N,N-dimethylformamide with OH and their photo-oxidation under atmospheric conditions: experimental and theoretical studies. *Physical Chemistry Chemical Physics*, 2015, **17**(10), pp.7046-7059.
7. BARNES, I., G. SOLIGNAC, A. MELLOUKI and K.H. BECKER. Aspects of the Atmospheric Chemistry of Amides. *Chemphyschem*, 2010, **11**(18), pp.3844-3857.
8. KLEPÁCOVÁ, K., P.J. HUTTENHUIS, P.W. DERKS, G.F.J.J.O.C. VERSTEEG and E. DATA. Vapor pressures of several commercially used alkanolamines. 2011, **56**(5), pp.2242-2248.
9. KOCH, R., H.U. KRÜGER, M. ELEND, W.U. PALM and C. ZETZSCH. Rate constants for the gas-phase reaction of OH with amines: tert-Butyl amine, 2,2,2-Trifluoroethyl amine, and 1,4-Diazabicyclo[2.2.2] octane. *International Journal of Chemical Kinetics*, 1996, **28**(11), pp.807-815.
10. TAN, W., L. ZHU, T. MIKOVINY, C.J. NIELSEN, A. WISTHALER, P. EICHLER, M. MÜLLER, B. D'ANNA, N.J. FARREN, J.F. HAMILTON, J.B.C. PETTERSSON, M. HALLQUIST, S. ANTONSEN and Y. STENSTRØM. Theoretical and Experimental Study on the Reaction of tert-Butylamine with OH Radicals in the Atmosphere. *The Journal of Physical Chemistry A*, 2018, **122**(18), pp.4470-4480.
11. GROSJEAN, D. Atmospheric chemistry of toxic contaminants. 6. Nitrosamines: dialkyl nitrosamines and nitrosomorpholine. *Journal of the Air & Waste Management Association*, 1991, **41**(3), pp.306-311.
12. LINDLEY, C.R.C., J.G. CALVERT and J.H. SHAW. Rate studies of the reactions of the $(CH_3)_2N$ radical with O_2, NO, and NO_2. *Chemical Physics Letters*, 1979, **67**(1), pp.57-62.
13. GE, X., A.S. WEXLER and S.L. CLEGG. Atmospheric amines – Part I. A review. *Atmospheric Environment*, 2011, **45**(3), pp.524-546.
14. MANZOOR, S., A. KORRE, S. DURUCAN and A. SIMPERLER. Atmospheric Chemistry Modelling of Amine Emissions from Post Combustion CO_2 Capture Technology. *Energy Procedia*, 2014, **63**, pp.822-829.
15. GARCIA, M., H.K. KNUUTILA and S.J.E.P. GU. Determination of kinetics of CO_2 absorption in unloaded and loaded DEEA+ MAPA blend. 2017, **114**, pp.1772-1784.

16. DAUBERT, T.E.J.D.I.F.P.P.D. Physical and thermodynamic properties of pure chemicals: data compilation. 1989.

17. HEINRICH, J., J. ILOVSKY and J.J.C.Z. SUROVY. Abhängigkeit des Dampfdrucks des N-Methylformamids von der Temperatur. Flüssigkeit-Dampf-Gleichgewicht des Systems N-Methylformamid-Wasser. 1961, **15**, pp.414-418.

18. VEREVKIN, S.P. and Y. CHERNYAK. Vapor pressure and enthalpy of vaporization of aliphatic propanediamines. *The Journal of Chemical Thermodynamics*, 2012, **47**, pp.328-334.

19. ALDRICH, S. *N-Methyl-1,3-diaminopropane* [online]. 2019. [Accessed 16-04-2019]. Available from: https://www.sigmaaldrich.com/catalog/product/aldrich/127027?lang=en&region=GB.

20. ONEL, L., M. BLITZ, M. DRYDEN, L. THONGER and P. SEAKINS. Branching Ratios in Reactions of OH Radicals with Methylamine, Dimethylamine, and Ethylamine. *Environmental Science & Technology*, 2014, **48**(16), pp.9935-9942.

21. CARL, S.A. and J.N. CROWLEY. Sequential Two (Blue) Photon Absorption by NO2 in the Presence of H_2 as a Source of OH in Pulsed Photolysis Kinetic Studies: Rate Constants for Reaction of OH with CH3NH2, $(CH_3)_2NH$, $(CH_3)_3N$, and $C_2H_5NH_2$ at 295 K. *The Journal of Physical Chemistry A*, 1998, **102**(42), pp.8131-8141.

22. KWOK, E.S.C. and R. ATKINSON. Estimation of hydroxyl radical reaction rate constants for gas-phase organic compounds using a structure-reactivity relationship: An update. *Atmospheric Environment*, 1995, **29**(14), pp.1685-1695.

7 PTR-TOF-MS studies of OH initiated isoprene and TMB oxidation.

7.0 Overview of chapter 7

A variety of OH reactions have been studied using the Leeds KORE TOF-PTR-MS. This instrument has been used to make these measurements from a variety of different reactors (chamber experiments, flow cells), and a comparison of the results from different setups helped evaluate systematic issues associated with different wall chemistry and NOx conditions.

Relative-rate measurements were performed in HIRAC and in EUPHORE for OH and TMB versus OH and isoprene, and the results were in good agreement (k_{TMB}/k_{ISO} = 0.574 – 0.580). From the results of these experiments a bimolecular removal rate for OH and TMB to be assigned as $(5.77 \pm 0.05) \times 10^{-11}$ cm^3 molecule^{-1} s^{-1}.

For OH and isoprene oxidation measured in: HIRAC, the high pressure system, and a quartz reactor, the abstraction reaction was assigned as 5 ± 2 % at 293 K. The abstraction reaction increases with temperature and can be a significant loss process at high temperatures. (1) The measurements carried out in EUPHORE, the high-pressure system, and the quartz reactor, found that the MVK and methacrolein yield was > 70 %, which is in good agreement with Sprengnether *et al.* *(2)*

7.1 Introduction

Understanding the mechanism of OH initiated isoprene oxidation is required to deduce the source of the gap between modelled and observed OH detected in remote regions with high isoprene concentrations.(3) Many methods have been employed to detect isoprene oxidation products to help elucidate the details of the mechanism. A wide variety of techniques have been utilised in chamber studies to monitor both kinetics and product formation; these techniques include: FAGE - LIF, FTIR, GC-MS, PTR-MS, SIFT-MS, and a variety of traps. (4-6)

The use of PTR-TOF-MS for the analysis of oxidation products is well established and proton transfer is a relatively low energy ionisation method. PTR-TOF-MS can provide time resolved observation of a wide variety of volatile organic compounds. The University of Leeds KORE TOF-PTR-MS has been modified to allow sampling from reduced pressures, in addition to sampling from atmospheric pressure and above. This

allows the same instrument to measure reactions under a wide range of experimental conditions.

In the work that will follow isoprene oxidation was examined in a variety of environments. The PTR has been coupled to conventional slow flow low-pressure cells (40-200 mbar), HIRAC (highly instrumented reactor for atmospheric chemistry, 1000 mbar), the Leeds high pressure kinetic reactor ($1000 - 3000$ mbar), a quartz photoreactor (1000 mbar), and the EUPHORE chamber (EUropean PHOtoREactor, 1000 mbar). The reactions observed in the low-pressure and high-pressure reactors occurred under pseudo first order conditions, where the OH was removed on the millisecond timescale, ensuring that any products observed were primary oxidation products. The measurements carried out in chamber studies (HIRAC, EUPHORE) allowed for longer timescales of the reaction to be observed, but were subject to the formation of secondary products.

HIRAC is a low NOx chamber where the levels of NOx are usually kept below 1 ppbv.(6, 7) Reactions performed in the high-pressure and low-pressure reactors are NOx free due to the use of hydrogen peroxide as the OH source, and the absence of any heterogeneous sources of NOx. Therefore, in both HIRAC and the pulsed laser photolysis systems, RO_2-NOx chemistry will have no influence on the observed products. In the low pressure and high-pressure reactors, the timescale for the reactions and the flow rates ensured that the potential for heterogeneous chemistry to influence the observed products was minimised.

Comparing the observations from EUPHORE and HIRAC allowed for the influence of differing heterogeneous chemistry and photolysis effects. This influence could be observed for both the relative rate experiments and for the subsequent product studies. In EUPHORE and in HIRAC, OH initiated isoprene oxidations were performed. Where these were carried out in the presence of TMB, the well understood rate coefficient of isoprene and OH provided a reliable reference reaction for a relative rate study.

7.2 Experimental results

The near universal nature of PTR-TOF-MS for both product studies and for kinetic measurements lead to a wide range of different measurements. These will include relative rate studies of the OH reactions with isoprene and a range of compounds, which will allow the comparison of different chambers for measuring the same reaction. Product studies included for isoprene will again compare only OH initiated chemistry.

7.2.1 OH with trimethylbenzene (TMB) and Isoprene relative rate studies

Relative rate experiments provide a reliable method for assigning the rate of reaction to unknown VOCs, the derivation of the relative rate method has been described in detail earlier in chapter 1.3. The method is highly accurate if all non-reactive losses can be accounted for, and the reaction rate with the reference compound is well defined. The advantage of this method, over direct measurements, is that the exact concentration of the compounds are not required to define the bimolecular reaction rate coefficients. This means that even for compounds with high wall loss rates or low vapour pressures, where knowing the exact concentration is complex, so long as dark reactions and precursor free photolysis rates can be assigned, an accurate bimolecular rate coefficient can still be measured.

PTR-TOF-MS studies carried out in the EUPHORE and in HIRAC chambers both involved relative rate measurements of the hydroxyl (OH) radical and isoprene and 1,3,5-trimethyl benzene (TMB). For both studies hydrogen peroxide (HOOH) was used as the photolytic OH source, in HIRAC this was achieved by photolysis by black lamps with output centred at 254 nm, in EUPHORE ambient sunlight was used as the photolysis source.

The difference in photolysis source meant that in EUPHORE, photolysis of isoprene and TMB was assumed to be negligible, whereas in HIRAC it was known that photolysis of TMB was significant (lamps peak output at 254 nm, but additionally, the lamps in HIRAC had non-negligible output at wavelengths as low as 185 nm). TMB has a significant absorption cross-section between 240 and 290 nm ($7 \times 10^{-19} - 6 \times 10^{-20}$ cm^2 molecule^{-1}; values were taken from the MAINZ spectral atlas,(8) calculated from the data of Etzkorn *et al.*(9)). As such, more care had to be taken to account for photolytic loss of TMB in HIRAC than in EUPHORE. Isoprene has a smaller absorption cross section at 254 nm ($< 1 \times 10^{-20}$ cm^2 molecule^{-1}, value taken from the MAINZ spectral atlas,(8) calculated from the data of Martins *et al.* (10)), photolysis of isoprene was not significant in either chamber. Although, any photolysis of isoprene was still accounted for in HIRAC, where the precursor-less loss rates were assigned.

In EUPHORE, no experimental measurements were carried out with the chamber open to allow photolysis of the contents, in the absence of hydrogen peroxide. Dark chemistry, involving reactive or diffusive loss to the walls of the chamber for both TMB and isoprene were measured. A relative rate plot, Figure 7.1, plots the relative loss

of TMB against the isoprene reference both when dark loss processes were, and were not accounted for.
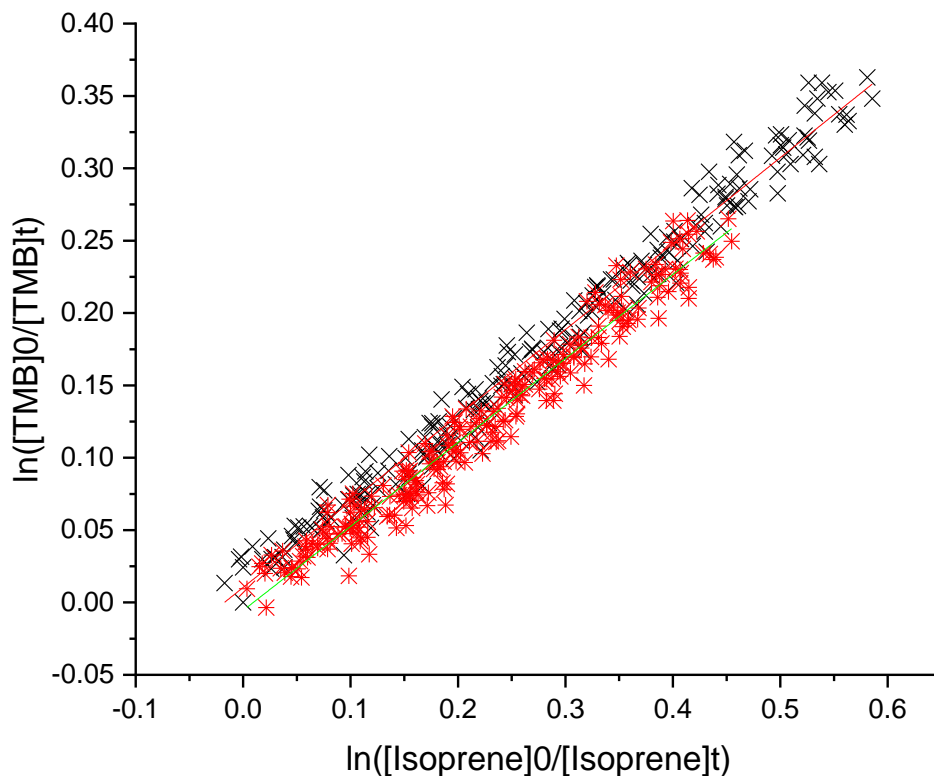
Figure 7.1 Plots the relative losses of TMB and the isoprene reference for reaction with OH, carried out in EUPHORE at 1000 mbar with OH generated by photolysis of hydrogen peroxide by ambient light. Black crosses gave $k1/k2 = 0.594 \pm 0.012$ and are uncorrected for wall losses, red stars gave $k1/k2 = 0.580 \pm 0.014$ when wall losses were accounted for.

The unadjusted relative rate of isoprene and TMB removal in EUPHORE, plotted in Figure 7.1, gave $k_{TMB}/k_{ISO} = 0.594 \pm 0.012$ (2 σ error), with $k_{OH+Isoprene} = 1.0 \times 10^{-10}$ cm^3 molecule^{-1} s^{-1}, (1, 11) this leads to a bimolecular rate coefficient for OH and TMS of $k_{OH+TMB} = (5.9 \pm 0.1) \times 10^{-11}$ cm^3 molecule^{-1} s^{-1}. This was in good agreement with the experimental work of Bohn *et al.* $k_{OH+TMB} = (5.95 \pm 0.20) \times 10^{-11}$ cm^3 molecule^{-1} s^{-1}. (12)

When wall loss rates and dilution effects in EUPHORE were accounted for, using the dark portion of the experiment, there was little change observed to the relative rate result, and $k_{TMB}/k_{ISO} = 0.580 \pm 0.014$ was obtained. This ratio lead to a bimolecular rate coefficient for OH and TMS of $k_{OH+TMB} = (5.8 \pm 0.1) \times 10^{-11}$ cm^3 molecule^{-1} s^{-1}, again in excellent agreement with Bohn *et al.* (12) and this was also in better agreement with the

literature values of Atkinson *et al.* and Paulson *et al.* of $(5.75 \pm 0.92) \times 10^{-11}$ cm^3 molecule^{-1} s^{-1} and $(5.73 \pm 0.53) \times 10^{-11}$ cm^3 molecule^{-1} s^{-1}. (13, 14)

The excellent agreement with the literature showed that for experiments carried out with TMB and isoprene in EUPHORE, neglecting photolysis was only a minor source of error. Additionally, the small differences between the wall loss corrected and uncorrected rates (< 5 %) shows that the large surface to volume, and Teflon walls, allow for only minor errors being attributed to this if the wall loss rates are neglected entirely.
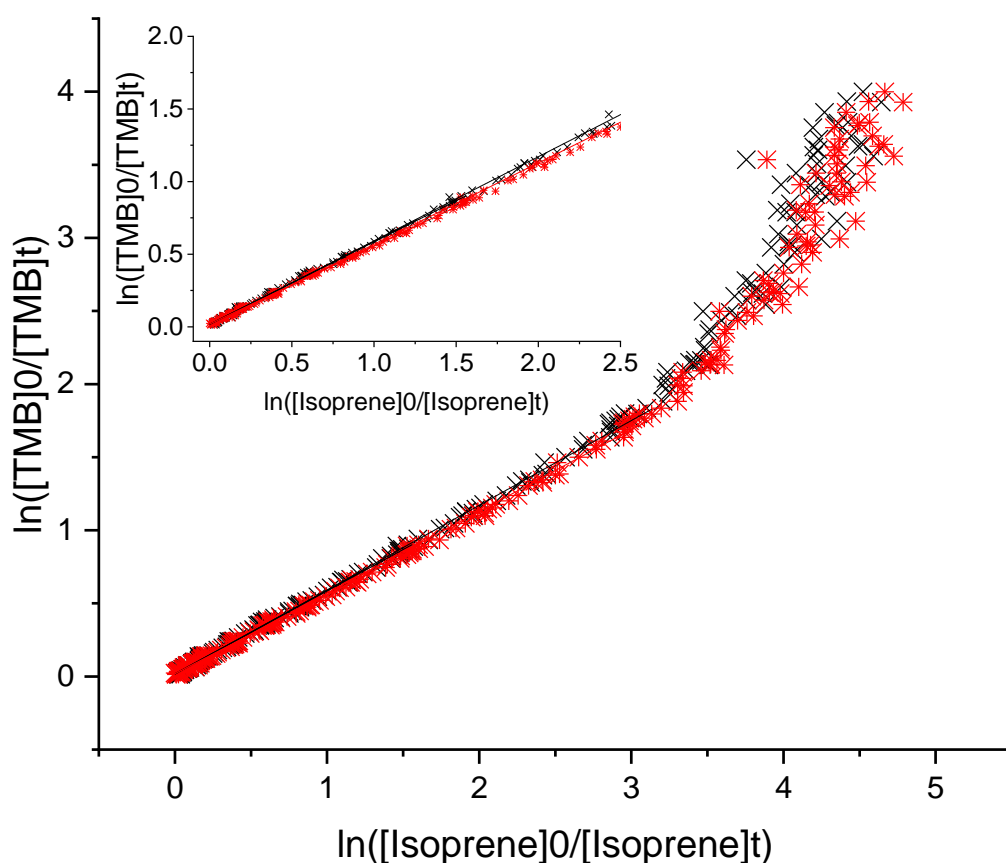
Figure 7.2 A relative rate plot for OH reaction with 1,3,5-trimethyl benzene, against isoprene as a reference compound, carried out at 293 K and 1000 mbar in HIRAC with VOC decays monitored by PTR-TOF-MS. OH was generated by photolysis of hydrogen peroxide at 254nm. The non-reactive loss of isoprene was accounted for in the black crosses, for the red points this was neglected. The inset shows the linear portion of the plot used to assign the gradient, for the fully correct, black, plot $k_1/k_2 = 0.574 \pm 0.020$ was assigned.

In HIRAC, photolysis of the compounds, and wall losses and dilution effects, were corrected for in the absence of the OH precursor. When these were accounted for, a relative rate of isoprene and TMB was plotted as Figure 2; the gradient from this plot

was $k_{TMB}/k_{ISO} = 0.574 \pm 0.020$ (2 σ error), giving a bimolecular rate coefficient k_{OH+TMB} of $(5.74 \pm 0.20) \times 10^{-11}$ cm^3 molecule^{-1} s^{-1}, which is in good agreement with the literature value of Atkinson et al. and Paulson et al. of $(5.75 \pm 0.92) \times 10^{-11}$ cm^3 molecule^{-1} s^{-1}, $(5.73 \pm 0.53) \times 10^{-11}$ cm^3 molecule^{-1} s^{-1}. (13, 14). Where photolysis and wall losses of isoprene were not accounted for, $k_{TMB}/k_{ISO} = 0.571 \pm 0.016$ was assigned, indicating that wall losses and photolysis were minimal for isoprene in this experiment. The experimental values calculated in EUPHORE and HIRAC differ marginally, and this difference has been assigned as a truer representation of the experimental precision errors; however, this may be evidence that photolysis losses in EUPHORE were not negligible.

Considering the values derived from these experiments in was concluded that for OH and TMB the bimolecular rate coefficient can be given as $k_{OH+TMB,293K} = (5.74 \pm 0.20) \times 10^{-11}$ cm^3 molecule^{-1} s^{-1}. And that for large volume chambers such as EUPHORE and HIRAC wall losses can provide minimal influences to observed chemical losses, even for compounds with low vapour pressure such as TMB (2.3 mbar at 293 K). (15)

7.2.2 Isoprene and OH oxidation products
OH and isoprene in the high-pressure system

In addition to monitoring the loss of the added VOCs (volatile organic compounds) using a TOF-PTR-MS also gave information on the product formation for these reactions. Under the conditions available in the laboratory-based studies, sampling the high-pressure system it was possible to observe how the product ratios of the primary oxidation species changed with temperature. One channel of interest in this was the product formed from the minor abstraction reaction, the product of this is an aldehyde (2-methylene-3-buteneal) with a PTR-MS m/z of 83 a.u. corresponding to $(CHCH(CH_2O)CH_2CH_2)H^+$, observation of this mass in previous chamber studies (16-20) has often been attributed to the formation of 3-methyl furan (3MF). From Atkinson *et al.* this peak in the GC-MS had a retention time corresponding to 3MF and there was a peak in the FT-IR spectrum that could be assigned as 3MF. (17)

The mass 83 species was observed in experiments, Figure 7.3, carried out in the high-pressure reactor, under conditions where 3-methyl furan formation was unlikely, and where the abstraction was known to be occurring. (1) Formation of mass 83 where furan formation was not possible is supported by the earlier work of Sprengnether *et al.* (2) where a flow reactor monitored by FTIR showed that furan formation does not occur as

a primary product channel in isoprene oxidation, but that an unassigned carbonyl species was formed.
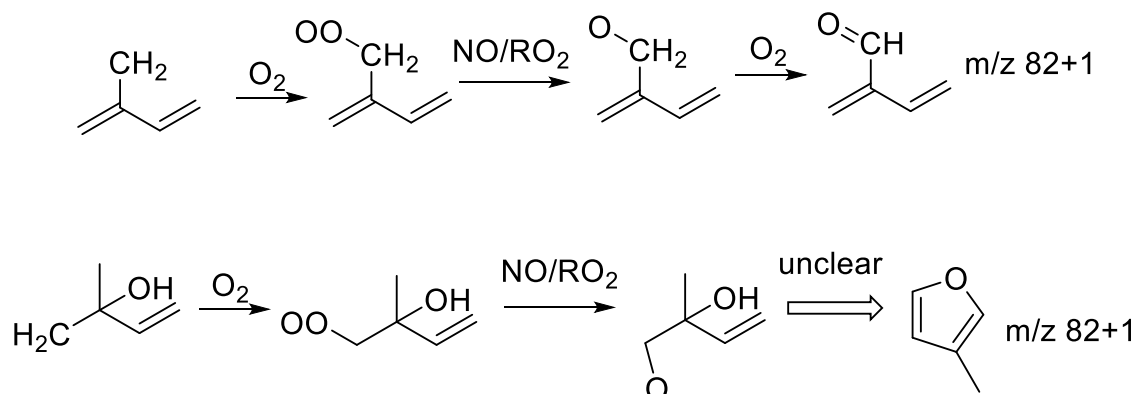
Scheme 7.1 Potential route to the formation of m/z 83. The upper shows the route to the formation of an aldehyde following the methyl abstraction from isoprene. The lower route shows a hypothetical route to the formation of 3-MF following OH addition.

M/z 83 can be attributed as the product of the OH abstraction from the methyl position of isoprene, Scheme 7.1. It is not unreasonable however to suggest that this mass spectral observation in chamber studies is of 3-methyl furan, not observation of the abstraction channel. It may be possible that at longer timescales, with the availability of heterogeneous process, elaborate isomerizations could lead to the formation of furans from isoprene, as is shown as the lower channel in Scheme 7.1. Heterogeneous processes can allow for the promotion of rearrangements that may appear unlikely in gas phase chemistry. We therefore compared the experimentally observed m/z 83 product formation to that expected from other work on isoprene oxidation that was performed in clean environments.
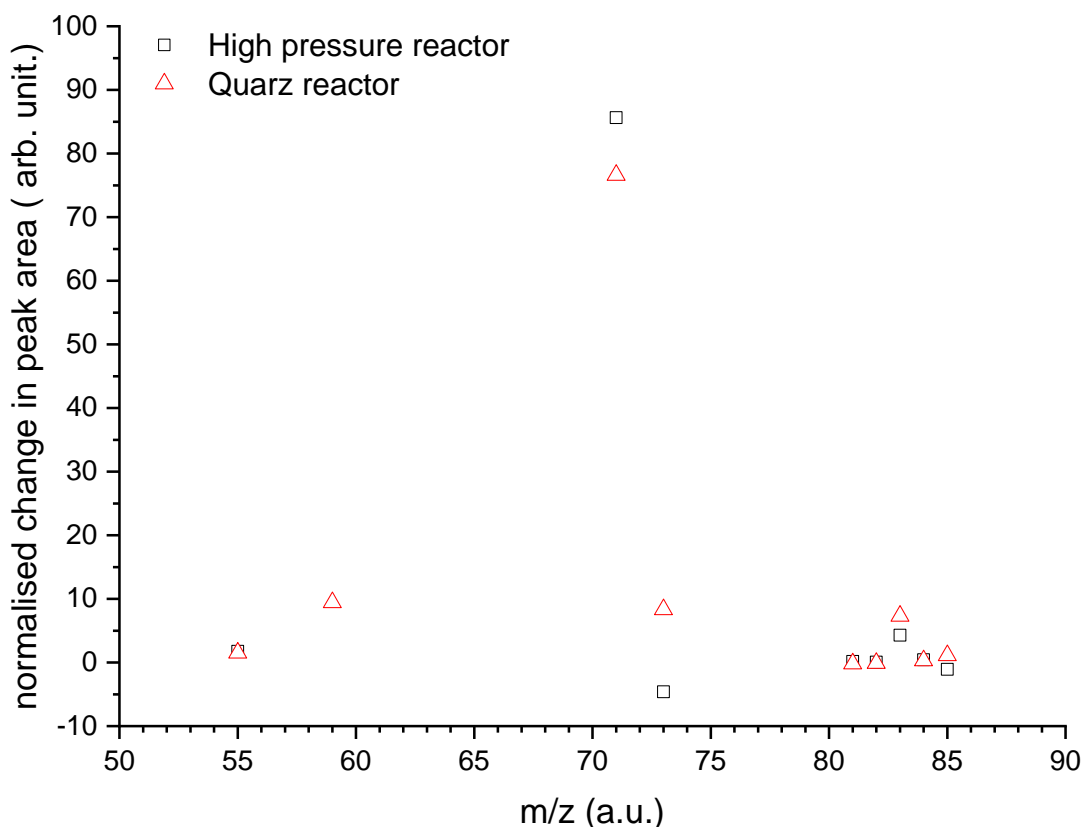
Figure 7.3 Changes in selected PTR-MS concentrations normalised to the loss of isoprene. Red triangles were for experiments carried out in the quarz reactor with photolysis at 10 Hz, black squares were carried out in the high-pressure system at 1 Hz. Both experiments were carried out at 1000 mbar and 293 K.

The yield of m/z 83 observed in the high-pressure reactor was 7.3 %. As this reaction was carried out in the high-pressure system it could also be measured at elevated temperatures. Both the yield of m/z 83 and the abstraction fraction required to fit OH kinetic traces increased with temperature, as would be expected from the temperature dependence of abstraction branching ratios of other similar reactions e.g. OH and ethylene. This leads to the reasonable assumption that m/z 83 observed in chamber studies is not an artefact of chamber studies but is evidence of the minor but observable OH abstraction from isoprene.

A series of subsequent experiments were also carried out where the gas flow was passed through a quartz absorption cell situated in the path of the photolysis laser instead of through the high-pressure reactor. The quartz absorption cell had a volume of 8.2 cm^3 with dimensions of 4, 2, 1 cm^3, this cell could be illuminated at 10 Hz with a flow rate of 5 SLM with the gas passing through only experiencing 1 photolysis event. Here the yield of m/z 83 was assigned as 4.3 %.

The results of monitoring several key peak areas for OH + isoprene in both these systems is shown as Figure 7.3; from this the yield for MVK and methacrolein was similar in both experiments (Quartz 86 % and high-pressure 77 %) and both were higher but in reasonable agreement with the yield measured by Sprengnether *et al.* of 72 ± 7 %. (2) PTR-TOF-MS detection cannot separate MVK and methacrolein as these species are isobaric, the yield given from the peak area therfore represents the sum of MVK and methocrolein (and any other non sufficiently resolved species). Other detection methods (FTIR, SIFT-MS, GC) can separate these species and as such some other works give indivdual yields for MVK and methacrolein.

There was no observation of m/z 85 from ($C_5H_8OH^+$) during the reactions carried out in the quartz reactor. For the reactions carried out in the high-pressure reactor, the yield was 1.1 %. This product is the minor channel from the reaction of oxygen with the ROH species formed following OH addition. A yield of 1.1 % is at the lowest limit to which products can begin to be reliably assigned from the flash photolysis PTR-MS experiments and as such it is understandable that it was not detected in both cells.

That the yield of m/z 83 appears increased in the stainless steel high-pressure reactor compared to the quartz reaction cell, means it is possible that wall chemistry can increase the observed yield of m/z 83. The route to this could be the stainless steel walls leading to faster RO formation from the post abstraction RO_2 radical, or due to the walls catalysing a rearrangement to form 3-MF. However, it is also reasonable to assume that the difference, 4.3 % versus 7.3 %, is merely the precision error with which yields could be detected using the TOF-PTR-MS coupled to photolysis cells in this manner. From this assumption the estimation of the OH isoprene abstraction branching fraction from these experiments was 5 ± 2 % at 1000 mbar and 293 K.

Isoprene and OH carried out in EUPHORE
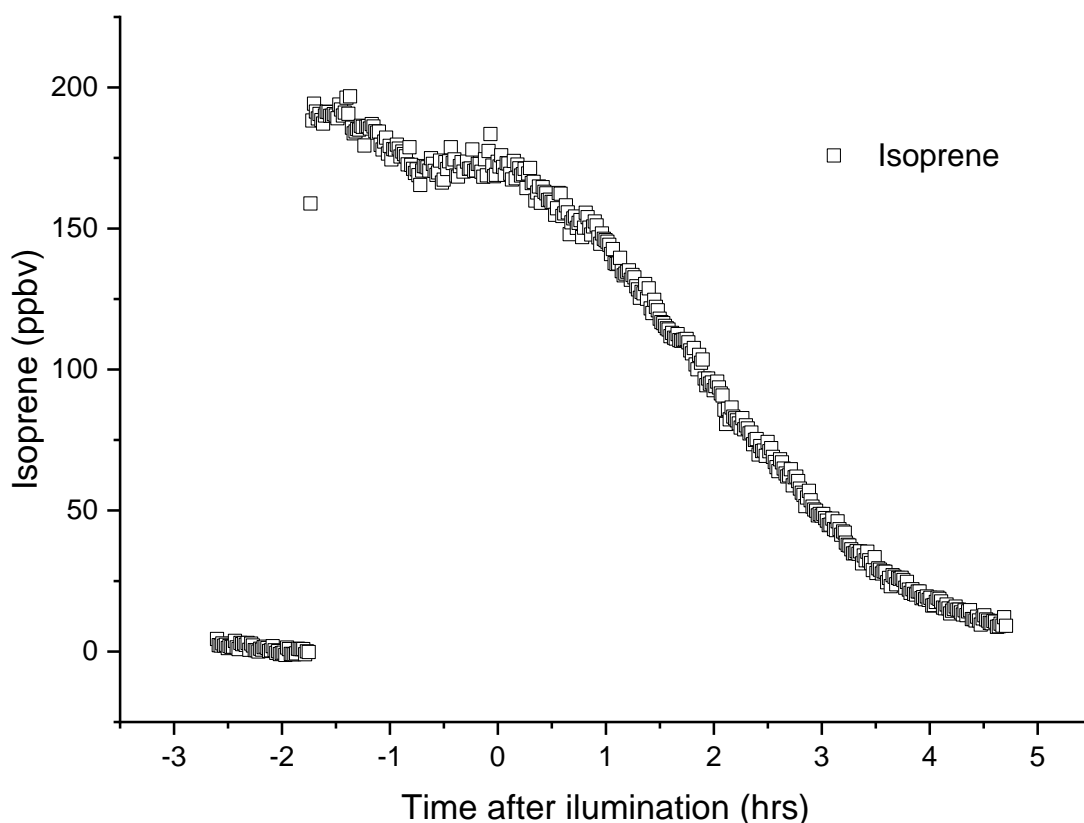
Figure 7.4 The time evolution of the isoprene mixing ratio, measured by PTR-TOF-MS, during an OH initiated photo-oxidation experiment carried out in EUPHORE. Time is given in hours after the chamber was opened to allow illumination by natural light.

The time evolution of the calibrated isoprene mixing ratio during an OH initiated, oxidation experiment carried out during the EUROCHAMP OVOCS (oxidated volatile organic compounds) campaign at EUPHORE is given as Figure 7.4. The initial signature (t= -1.6 to -1.1) of the isoprene concentration could potentially be an artefact of the location of the sampling port, the sampling port was adjacent to the port for the addition of VOCs, but was more likely to have been the result of changes in the relative humidity within the chamber. This signal displayed in Figure 7.5 is that obtained once the chamber response from isoprene had stabilized, timings are normalized to time zero as the point at which the chamber was opened to allow illumination.
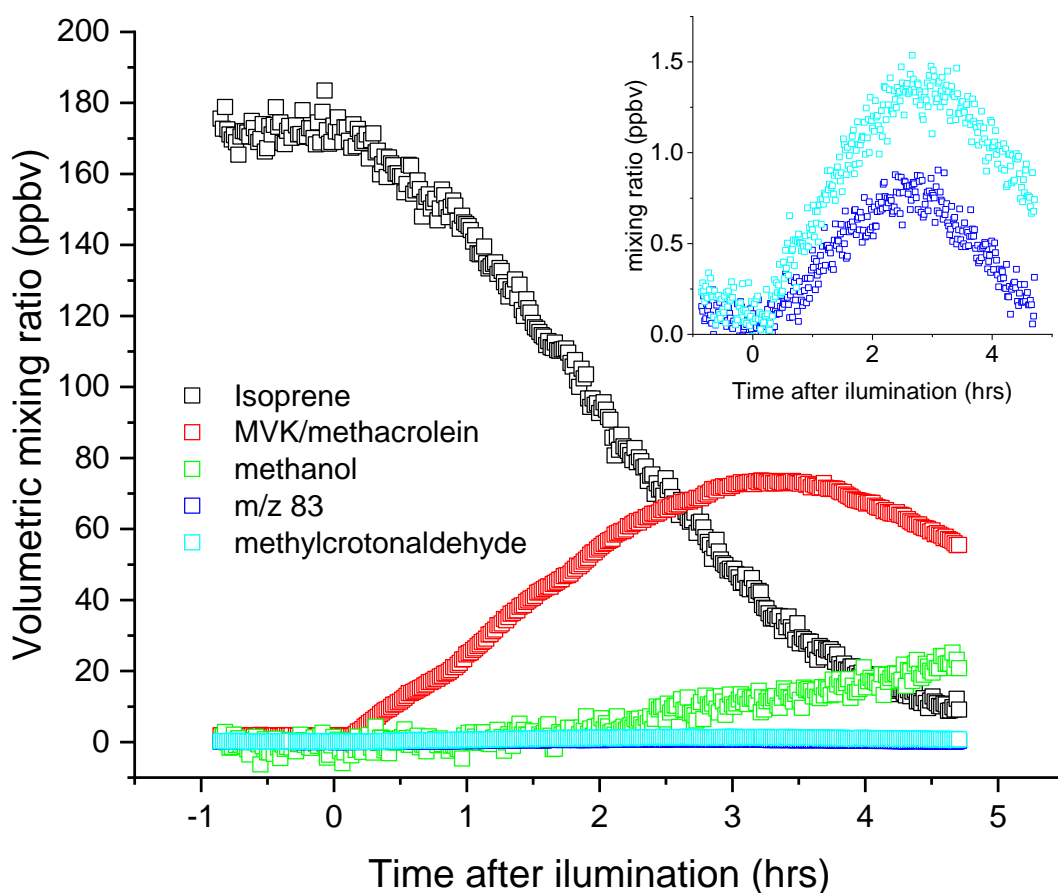
Figure 7.5 Shows product formation from the OH oxidation of Isoprene carried out in EUPHORE during the EUROCHAMPS OVOCS campaign. MVK and methacrolein can be seen as primary products of isoprene oxidation, where methanol as a secondary product appears at later times (> 2 hrs). The inset shows m/z 83 formation is as a primary product.

Once the chamber was opened to allow photolysis of hydrogen peroxide to initiate the OH chemistry, the decay of isoprene mixing ratio is accompanied by product formation. The majority product at early times is MVK and methacrolein, at later times in the study MVK and methacrolein were themselves consumed via reaction with OH causing the PTR signals to plateau then decrease, where the early times average yield of MVK and methacrolein was (72 ± 3) % at t= 0 – t= 1.5 hrs. At long times the observed yield was reduced due to (33 ± 1) % at t= 4.7 hrs, with an average value over the whole study of 52 ± 19 %.

At longer reaction times (> 1.5 hrs) formation of methanol is observed as a secondary product following additional oxidation of the primary oxidation products (3 % at t= 1.5 hrs, (15 ± 1) % at t= 4.7 hrs). The setup of the TOF PTR MS for this experiment meant that it was not sensitive to the formation of formaldehyde nor acetone, glyoxal and

methyl glyoxal, this was due to interference and water concentrations present in the PTR reactor, however they should be responsible for the bulk of the unattributed oxidation products.

Differences in the observed fractional yield of methyl vinyl ketone (MVK) and methacrolein to loss of isoprene, observed from chamber studies and our high-pressure reactor, are due to the differing environments under which the chemistry is occurring. It is well known that the NO concentration and the exposure to metal surfaces can change the observed MVK and methacrolein yields.[21, 22] Comparing the average yield of MVK and methacrolein to the literature showed good agreement with the product yields from Tuazon *et al.* of 54 ± 9 %,[20] Paulson *et al.* 61 ± 5 %,[19] and Miyoshi *et al.* 54 ± 5 %.[23] When only the early time points before secondary chemistry became significant, the yield of (72 ± 3) % was in excellent agreement the flow tube study of Sprengnether *et al* which gave a value of (72 ± 7) %. [2]

From this experiment shown in the inset of Figure 7.5, the yield of the mass 83 aldehyde abstraction product was assigned as 1.04 ± 0.35 % at 292 K, as with MVK and methacrolein, m/z 83 was consumed by secondary reactions at times beyond t=1.5 hrs. As discussed earlier, estimates of the ambient temperature abstraction branching ratio for OH and isoprene have predicted a value in line with the experimentally assigned fraction of 1 % for m/z 83.[24] The observed yield is somewhat lower than the quoted yields for 3 methyl furan observed in Tuazon *et al.* (4.8 ± 0.6 %)[20] and Paulson *et al.* (4 ± 2 %)[19]but still in reasonable agreement.

In addition to the products observed above, that could be quantified, additional masses were observed, and these included m/z 117, which corresponded to C_5-HPALD. However due to the highly oxygenated nature of HPALD, fragmentation of this mass was significant, leading to multiple different fragments.

Isoprene and OH carried out in HIRAC
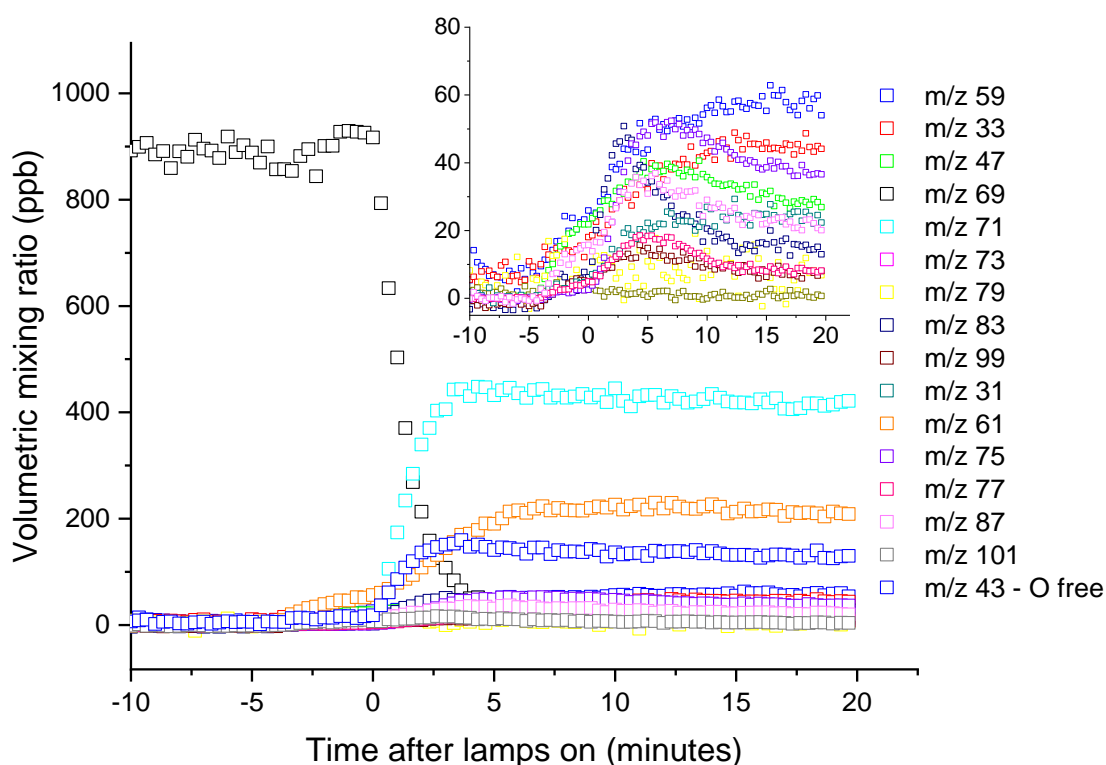
Figure 7.6 Plots PTR-MS mixing ratios observed during an OH initiated oxidation of Isoprene, carried out in HIRAC with 800 mbar of nitrogen and 200 mbar of oxygen at 293 K with OH generation from the photolysis of hydrogen peroxide at 254 nm. All products with a yield greater than 1 % are included.

When the reaction was performed in HIRAC at room temperature and 1000 mbar, Figure 7.6, the dominant observed product were MVK, methacrolein, glycoaldehyde and propene. Where product formation is given as a fraction of loss of the loss of isoprene the yields were: 50 ± 4 % MVK + methacrolein, 25.9 ± 1.4 % glycoaldehyde, 19 ± 1 % propene. The observed yields for all of these will have systematic errors in their assignments, where fragmentation within the PTR either leads to over or underestimation of their masses. However, the observation of MVK and methacrolein as 50 ± 4 % is in good agreement with the average value over the whole reaction time, recovered from experiments in EUPHORE.

Comparing the MVK and methacrolein yields to the literature shows good agreement with the product yields from Tuazon *et al.* of 54 ± 9 %,(20) Paulson *et al.* 61 ± 5 %,(19) and Miyoshi *et al.* 54 ± 5 %,(23) but were in some disagreement with the flow tube study of Sprengnether *et al.* which gave a higher value of 72 ± 7 %. (2) For this

experiment the much faster reaction timescale both between OH and isoprene and OH and the oxidation products, when compared to the experiment performed in EUPHORE, meant that it was not possible to separate the MVK and methacrolein early time yield in the same manner.
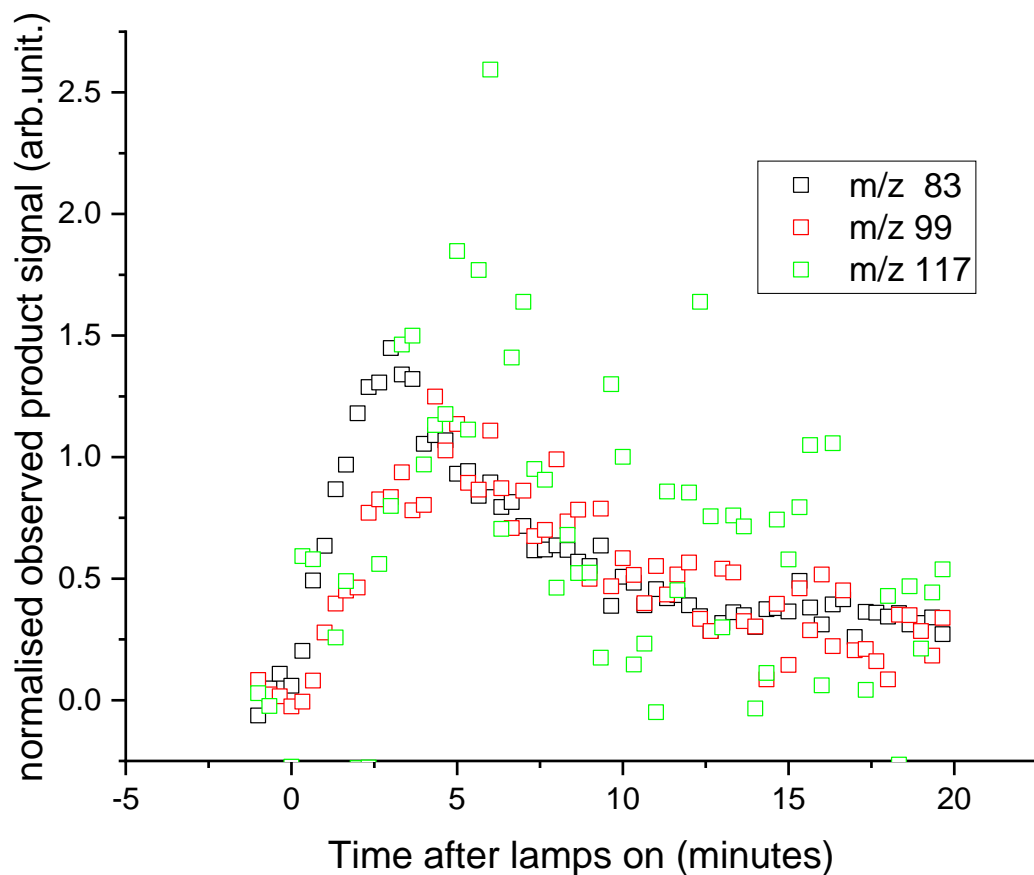
Figure 7.7 Plots of normalised observed product peaks for m/z 117 (green), 99 (red) and 83 (black), where signals were normalised to an observed peak height at 1.3 minutes after photolysis began. The early time shape (< 2.5 minutes) of the black squares shows that m/z 83 is not a signature of HPALD formation.

With respect to the observed formation of the abstraction product (2-methylene-3-buteneal) or 3MF (3-methyl-furan), a much higher yield was shown in HIRAC when compared with EUPHORE. The observed yield was (6 ± 2) %, due to the surface to volume ratio differences and the presence of exclusively stainless steel walls in HIRAC, it is entirely possible that here wall chemistry occurs on a much larger scale. If heterogeneous chemistry is leading to much higher observed yields at m/z 83 it may be that this mass is both 3MF and the abstraction product. The higher yield of (6 ± 2) % is

in better agreement with Tuazon *et al.* (4.8 ± 0.6 %) (20) and Paulson *et al.* (4 ± 2 %) (19) than the lower yield observed from the EUPHORE experiment.

Methyl glyoxal was observed as a minor product from the reaction carried out in HIRAC with a yield of (4.0 ± 0.5) %. One route to methyl glyoxal formation is from the decomposition pathway of di-HPCARP, di-HPCARP is one of the species predicted to be a route to regeneration of OH from isoprene oxidation. Peaks observed at m/z 99 and m/z 117 were highly correlated with a ratio of 1:1.03 these peaks are assigned as protonated HPALD and the loss of water from protonated HPALD. When peroxides are protonated in the PTR they can lose both water and hydrogen peroxides for HPALD this would lead to observed masses at m/z 177, 99 and 83, the mass observed at m/z 83 was not well correlated with m/z 117 from a simple correlation plot. When the initial raw mass peaks were normalised for the signal at a given time after photolysis began a plot, Figure 7.7, was generated and there was by eye, a similarity in the shape of the observed masses. The early time signature however does differ and therefore confidence was given to the assignment of the early time yields of m/z 83 as not being from HPALD. Future work integrating FTIR analysis in HIRAC should allow for the observation of the presence or absence of 3-MF, and the timescale of 3-MF formation with respect to MVK and methacrolein if it is observed.

7.3 Conclusion

Comparison of relative rate experiments in EUPHORE and HIRAC showed that there is negligible photolysis of isoprene by both the 254 nm black lamps and by sunlight over the experimental timescales. For TMB there was significant removal via photolysis by 254 nm black lamps but not via sunlight, when photolysis was accounted for the OH and TMB rate coefficient could be assigned as $(5.77 \pm 0.05) \times 10^{-11}$ cm^3 molecule^{-1} s^{-1}.

Coupling direct OH kinetic measurements carried out under pseudo first order conditions to end-product analysis by TOF-PTR-MS can provide additional information on branching ratios. Under pseudo first order conditions, there is minimal further oxidation of any products reducing the influence of secondary chemistry on the observed branching ratios.

For OH and isoprene, the measurements carried out in a quartz reactor the high-pressure system and HIRAC were in good agreement on the yield of m/z 83, and it can be assigned as 3 – 7 % at room temperature. This yield matched well with the expected

OH abstraction branching ratio at RT from work carried out on high temperature OH isoprene oxidation by Medeiros *et al.* (1)

For OH and isoprene the measurements carried out in a quartz reactor the high pressure system and EUPHORE the yields of MVK and Methacrolein were in good agreement and were in agreement with the literature value of 72 ± 7 % from Sprengnether *et al.*.(2) The returned value from the chamber experiments made in HIRAC was lower; however, this can be attributed to the faster removal rate due to higher OH concentrations making separation of the product yields before removal via reaction with OH influenced the MVK and methacrolein yield.

7.4 References

1. MEDEIROS, D.J., M.A. BLITZ, L. JAMES, T.H. SPEAK and P.W. SEAKINS. Kinetics of the Reaction of OH with Isoprene over a Wide Range of Temperature and Pressure Including Direct Observation of Equilibrium with the OH Adducts. *The Journal of Physical Chemistry A*, 2018.

2. SPRENGNETHER, M., K.L. DEMERJIAN, N.M. DONAHUE and J.G. ANDERSON. Product analysis of the OH oxidation of isoprene and 1,3-butadiene in the presence of NO. *Journal of Geophysical Research: Atmospheres*, 2002, **107**(D15), pp.ACH 8-1-ACH 8-13.

3. STONE, D., L.K. WHALLEY and D.E. HEARD. Tropospheric OH and HO_2 radicals: field measurements and model comparisons. *Chemical Society Reviews*, 2012, **41**(19), pp.6348-6404.

4. HIDY, G.M. Atmospheric Chemistry in a Box or a Bag. Atmosphere, 2019, **10**, 401.

5. ONEL, L., A. BRENNAN, M. GIANELLA, G. RONNIE, A. LAWRY AGUILA, G. HANCOCK, L. WHALLEY, P.W. SEAKINS, G.A. RITCHIE and D.E. HEARD. An intercomparison of HO_2 measurements by fluorescence assay by gas expansion and cavity ring-down spectroscopy within HIRAC (Highly Instrumented Reactor for Atmospheric Chemistry). *Atmospheric Measurement Techniques*, 2017, **10**(12), pp.4877-4894.

6. WINIBERG, F., S. SMITH, I. BEJAN, C. BRUMBY, T. INGHAM, T. MALKIN, S. ORR, D. HEARD and P. SEAKINS. Pressure-dependent calibration of the OH and HO_2 channels of a FAGE HOx instrument using the Highly Instrumented Reactor for Atmospheric Chemistry (HIRAC). *Atmospheric Measurement Techniques*, 2015, **8**(2), pp.523-540.

7. WINIBERG, F.A.F. *Characterisation of FAGE apparatus for HOx detection and application in an environmental chamber.* thesis, University of Leeds, 2014.

8. KELLER-RUDEK, H., G.K. MOORTGAT, R. SANDER and R. SÖRENSEN. The MPI-Mainz UV/VIS Spectral Atlas of Gaseous Molecules of Atmospheric Interest. *Earth Syst. Sci. Data*, 2013, **5**(2), pp.365-373.

9. ETZKORN, T., B. KLOTZ, S. SØRENSEN, I.V. PATROESCU, I. BARNES, K.H. BECKER and U. PLATT. Gas-phase absorption cross sections of 24 monocyclic aromatic hydrocarbons in the UV and IR spectral ranges. *Atmospheric Environment*, 1999, **33**(4), pp.525-540.

10. MARTINS, G., A.M. FERREIRA-RODRIGUES, F.N. RODRIGUES, G.G.B. DE SOUZA, N.J. MASON, S. EDEN, D. DUFLOT, J.P. FLAMENT, S.V. HOFFMANN, J. DELWICHE, M.J. HUBIN-FRANSKIN and P. LIMÃO-VIEIRA. Valence shell electronic spectroscopy of isoprene studied by theoretical calculations and by electron scattering, photoelectron, and absolute photoabsorption measurements. *Physical Chemistry Chemical Physics*, 2009, **11**(47), pp.11219-11231.

11. ATKINSON, R. Kinetics and mechanisms of the gas-phase reactions of the hydroxyl radical with organic compounds under atmospheric conditions. *Chemical reviews*, 1986, **86**(1), pp.69-201.

12. BOHN, B. and C. ZETZSCH. Kinetics and mechanism of the reaction of OH with the trimethylbenzenes–experimental evidence for the formation of adduct isomers. *Physical Chemistry Chemical Physics*, 2012, **14**(40), pp.13933-13948.

13. KRAMP, F. and S.E. PAULSON. On the uncertainties in the rate coefficients for OH reactions with hydrocarbons, and the rate coefficients of the 1, 3, 5-

trimethylbenzene and m-xylene reactions with OH radicals in the gas phase. *The Journal of Physical Chemistry A*, 1998, **102**(16), pp.2685-2690.

14. ATKINSON, R. and S.M. ASCHMANN. Rate constants for the gas-phase reactions of the OH radical with a series of aromatic hydrocarbons at 296±2 K. *International Journal of Chemical Kinetics*, 1989, **21**(5), pp.355-365.

15. FORZIATI, A.F., W.R. NORRIS and F.D. ROSSINI. Vapor Pressures and Boiling Points of 60-API-NBS Hydrocarbons. *Journal of Research of the National Bureau of Standards*, 1949, **43**(6), pp.555-563.

16. NAVARRO, M.A., S. DUSANTER, R.A. HITES and P.S. STEVENS. Radical Dependence of the Yields of Methacrolein and Methyl Vinyl Ketone from the OH-Initiated Oxidation of Isoprene under NOx-Free Conditions. *Environmental Science & Technology*, 2011, **45**(3), pp.923-929.

17. ATKINSON, R., S.M. ASCHMANN, E.C. TUAZON, J. AREY and B. ZIELINSKA. Formation of 3-Methylfuran from the gas-phase reaction of OH radicals with isoprene and the rate constant for its reaction with the OH radical. *International Journal of Chemical Kinetics*, 1989, **21**(7), pp.593-604.

18. PAULOT, F., J. CROUNSE, H. KJAERGAARD, J. KROLL, J. SEINFELD and P. WENNBERG. Isoprene photooxidation: new insights into the production of acids and organic nitrates. *Atmospheric Chemistry and Physics*, 2009, **9**(4), pp.1479-1501.

19. PAULSON, S.E. and J.H. SEINFELD. Development and evaluation of a photooxidation mechanism for isoprene. *Journal of Geophysical Research: Atmospheres*, 1992, **97**(D18), pp.20703-20715.

20. TUAZON, E.C. and R. ATKINSON. A product study of the gas-phase reaction of Isoprene with the OH radical in the presence of NOx. *International Journal of Chemical Kinetics*, 1990, **22**(12), pp.1221-1236.

21. BERNHAMMER, A.-K., M. BREITENLECHNER, F.N. KEUTSCH, A.J.A.C. HANSEL and PHYSICS. Conversion of isoprene hydroxy hydroperoxides (ISOPOOHs) on metal environmental simulation chamber walls. *Atmospheric Chemistry and Physics*, 2017, **17**(6), pp.4053-4062.

22. LIU, Y., I. HERDLINGER-BLATT, K. MCKINNEY and S. MARTIN. Production of methyl vinyl ketone and methacrolein via the hydroperoxyl pathway of isoprene oxidation. *Atmospheric Chemistry and Physics*, 2013, **13**(11), pp.5715-5730.

23. MIYOSHI, A., S. HATAKEYAMA and N. WASHIDA. OH radical- initiated photooxidation of isoprene: An estimate of global CO production. *Journal of Geophysical Research: Atmospheres*, 1994, **99**(D9), pp.18779-18787.

24. JENKIN, M., S. SAUNDERS, V. WAGNER and M. PILLING. Protocol for the development of the Master Chemical Mechanism, MCM v3 (Part B): tropospheric degradation of aromatic volatile organic compounds. *Atmospheric Chemistry and Physics*, 2003, **3**(1), pp.181-193.

8 Summary and future directions

The FAGE sampled high-pressure (500 – 4000 mbar) reactor for time resolved OH measurements and HO_2 yield detection,[1] has been validated for both the measurement of accurate and precise OH kinetics, and HO_2 yields. The reaction of OH and ethylene validated that where OH LIF measurements were performed in the 'jetting gas' the kinetics recovered were linear with added ethylene up to 150,000 s^{-1}; with the bimolecular rate coefficient recovered $k_{OH+C2H4} = (8.33 \pm 0.16) \times 10^{-12}$ cm^3 molecule$^{-1}s^{-1}$ (2σ errors) was in excellent agreement of the high-pressure limit value from Tully of $k^{\infty} = (8.47 \pm 0.24) \times 10^{-12}$ cm^3 s^1.[2]

The ability to detect precise and accurate HO_2 yields was demonstrated through comparing the internal calibration of OH and H_2O_2 to the reaction of OH with methanol under both high (6×10^{18} cm^{-3}) and low oxygen conditions ($<1 \times 10^{16}$ cm^{-3}). Under high oxygen conditions the HO_2 yield of OH and methanol is 100 %, under the low oxygen conditions only the alpha branching fraction will lead to HO_2 formation under the experimental time frame and as such the expected HO_2 yield was (85 ± 8) %.[3] These expected values were well reproduced with measured yields of (87 ± 5) % with low oxygen, and (99 ± 2 %) with high oxygen (1σ errors).

When this system was used to study the reaction of OH and n-butanol, it allowed for the evaluation of the α and β branching fractions. Abstraction from the σ position led to the formation of an R radical that in the presence of oxygen rapidly yielded HO_2; the HO_2 yield was assigned as the σ branching fraction, with $\alpha = (0.57 \pm 0.06)$ at 293 K, and (0.54 ± 0.04) at 616 K. At elevated temperatures the radical formed following abstraction from the β position recycled OH; the OH recycling yield could therefore be assigned as the β branching fraction and the recovered value was $\beta = 0.24 \pm 0.04$ (616 – 640 K). The ratio between the α and β branching fractions is more important than the rate of reaction of n-butanol with OH for the modelling of the ignition delay time of n-butanol.[4]

This ability to observed and assign OH recycling kinetics, and measure HO_2 yield under the same experimental conditions can be applied to many other low-temperature combustion systems (Fuel + OH at elevated temperatures at high pressure with high oxygen concentrations, $> 1 \times 10^{18}$ cm^{-3}). Where HO_2 yields, may provide information on the presence of different routes to OH recycling (from OOQOOH vs QOOH), or provide information on the ratio of chain terminating reactions (OOQOOH $\rightarrow$ HO_2, QOOH $\rightarrow$ HO_2, R$\rightarrow$ HO_2).[5] Reactions of particular interest to study could be OH

with methyl furans, and OH with ethers, compounds that could be important biofuels in a move towards a low carbon economy.(6)

Reactions of OH with amines and amides were carried out in the novel high-pressure reactor (500 – 4000 mbar), with some additional experiments carried out in a conventional slow-flow reactor (< 500 mbar). High-level computational calculations (M06-2X/aug-cc-pVTZ, MP2/6-311++g(3df,3pd), with single point energies calculated at the CCSD(T)/CBS level from an extrapolation of a series of correlation consistent basis sets) were carried out to support the experimental work. These were used to explain the source of OH recycling observed (for DMF) and to help assign the product formation observed.

For OH and methyl formamide (MF) the bimolecular removal rate coefficient, $k_{OH+MF, 298K}$= (1.03 ± 0.23) × 10^{-11} cm^3 s^{-1} was assigned which was in good agreement with that observed by Borduas et al.,(7) $k_{OH+MF,298K}$=(1.0 ± 0.60) × 10^{-11}cm^3 s^{-1}, and $k_{OH+MF,298K}$= (0.86 ± 0.24) × 10^{-11} cm^3 s^{-1} from Solignac et al.(8) these studies were carried out by relative rate. This value was however, a factor of two higher than that observed by Bunkan et al. of (0.57 ± 0.17) × 10^{-11} cm^3 s^{-1} measured in a direct kinetic study,(9) MF has a low vapour pressure and took a long time to fully stabilize between changes in concentration (> 45 minutes), this was compounded with the method of delivery which relied on estimating the vapour pressure sampled, and could be the cause of this apparent discrepancy.

The reaction between OH and dimethyl formamide (DMF) was carried out over a wide range of temperatures (300 - 650 K) and pressure (12 – 2400 mbar). From this work the temperature dependence of the OH reaction was assigned as k_{OH+DMF}=(1.317± 0.117)×$10^{-11}(\frac{T}{298})^{-0.5}e^{37.16/RT}$cm^3 s^{-1}, with an ambient temperature value of k_{298K} = (1.30 ± 0.12) × 10^{-11} cm^3 s^{-1}. This value was in agreement with that derived the by relative rate method, with several different reference compounds, by Solignac et al. as (1.4 ± 0.3) × 10^{-11} cm^3 s^{-1} (8), but was in discrepancy with a direct measurements as (0.80 ±0 .26) x 10^{-11} cm^{3}molecule^{-1}s^{-1} , by Bunkan et al. (9) Direct methods are highly dependent on the understanding of the added concentration, this could explain the slightly lower value recovered here versus Solignac et al.. The discrepancy between the result here and that presented in Bunkan et al. may be due to how the vapour pressure delivered was defined, where the temperature dependence of

the Arrhenius parameters used in this work were sometimes extrapolated outside the range over which they were measured (303 – 363 K).

Where OH recycling was observed (> 450 K) this was not observed to be pressure dependent (12 – 2400 mbar) and as such was primarily not the result of chemically activated processes. The recycled OH was shown to be primarily from the RO_2 radical formed following abstraction of the aldehydic proton (60 – 80 %), with a minor contribution from the methyl abstraction (≈20 %). The dominance of the aldehydic abstraction is of environmental importance, where at low temperatures this route generally leads to the formation of a nitrogen centred radical, which can lead to the formation of dimethyl nitramine and dimethyl nitrosamine. (10) Nitramines and nitrosamines are potent carcinogenic compounds. (11) The experimental assignment of this dominance was supported by the CCSD(T)/CBS/MP2/6-311++g(3df,3pd) surface, which when simulated in MESMER showed 60 – 99 % aldehydic abstraction at 298 K and 1000 mbar.

The ambient temperature bimolecular removal rate coefficient for OH and tertiary butyl amine ($tBuNH_2$) measured in this study $k_{OH+tBuNH2,298K}$= (1.66 ± 0.20) × 10^{-11} cm^3 s^{-1}, was in slight disagreement with a previous work published by Koch et $al.$ $k_{OH+tBuNH2}$ = (1.20 ± 0.12) × 10^{-11} cm^3 s^{-1} at 298 K, measured by laser flash photolysis resonance fluorescence.(12) Which was itself significantly higher than that presented in Tan et $al.$ ($k_{OH+tBuNH2}$ = (0.84 ± 0.17) × 10^{-11}cm^3 molecule^{-1} s^{-1}) which was measured by relative rate. (13) The apparent disagreement between these results and that presented here may be due to the reaction between $tBuNH_2$ and the OH precursors, it is noticeable that the value recovered with H_2O_2 as an OH precursor was in perfect agreement with that of Koch et $al.$.(12) The calculated surface for OH and tertiary butyl amine is in very good agreement with a surface presented in the SI for a recent paper on this reaction published by Tan et $al.$.(13) The potential for formation of nitramines and nitrosamines could be significant (40 - 60 %), with the majority OH abstraction channel being assigned to the amino position; this will then lead to the formation of nitramines or nitrosamines under most atmospheric conditions.

Repeatable kinetics for OH and n-methyl propane diamine were observed for measurements made where the amine was delivered in a backing flow of nitrogen, and OH was generated from photolysis of tertiary butyl hydroperoxide. These measurements gave a lower limit for the OH removal rate coefficient at room temperature and 350 K

$k=((5.99 \pm 2.0) \times e^{((-0.41\pm0.09)\times1000/RT}\times 10^{-11}$ cm^3 s^{-1}., with a room temperature value of $k_{298 K} = (7.09\pm 0.45) \times 10^{-11}$ cm^3 s^{-1}. Further measurement with this compound and with other amines may be improved by the use of a different source of OH generation, potentially through photolysis of ozone, which will not undergo acid base reactions with the amines pre delivery to the region of study. In addition, further work could be carried out using UV absorption to assign the concentration of the amines in situ.

Where PTR-TOF-MS studies of VOCs were carried out, it was possible to examine the difference in product ratios that are observed under a variety of different conditions. These allowed for the study of primary oxidation products where an atmospheric pressure quartz reactor was used, and the high-pressure reaction cell with photolysis of the OH precursor achieved via pulsed laser photolysis. When large atmospheric simulation chambers were used (HIRAC and EUPHORE) photolysis of the OH precursor was achieved through either UV lamps or ambient light, allowing the progression of the reaction to be monitored over an extended time period (over minutes or hours) where secondary reaction products become apparent.

Applied to the relative rate study of OH and 1,3,5-tri methyl benzene (TMB) versus OH and Isoprene in both EUPHORE and HIRAC the ratio of k_1/k_2 recovered were in excellent agreement. In EUPHORE k_1/k_2 = 0.594 ± 0.012 was observed, in HIRAC k_1/k_2 = 0.574 ± 0.020 (2 σ errors) was assigned, these led to the assignment of the bimolecular rate coefficient for OH and TMB as k_{OH+TMB}= (5.77 ± 0.05) × 10^{-11} cm^3 molecule^{-1} s^{-1}.

The significance of the OH abstraction reaction from the methyl position of isoprene has been previously described in the high temperature study of the OH isoprene equilibrium by Medeiros *et al.*(14) In the product studies of OH and isoprene carried out here the product observed at m/z 83 has been identified as being the product of this channel (2-methylene-3-butenal). Where this product was observed from both the high-pressure reactor and the quartz reactor it is not immediately apparent how this mass could be assigned to the observation of 3-methyl furan as this requires heterogeneous process or secondary chemistry to be formed.(15) From the reactions monitored in these reactors and in HIRAC the abstraction channel has been assigned as 3 – 7 % at room temperature and 1000 mbar. In EUPHORE the apparent yield at m/z 83 was lower (≈ 1 %), either differing humidity levels may have affected the observed PTR response factor or overlap of product formation and removal by reaction with OH may have caused this to be under

represented. Future Work in HIRAC integrating simultaneous FTIR and PTR-TOF-MS analysis should provide verification of the presence or absence of 3-MF as a product of isoprene oxidation. If 3-MF is observed the FTIR analysis should provide the timescale for formation, and this would allow for 3-MF to be deconvoluted from the isobaric abstraction product at m/z 83.

Where the PTR -TOF -MS was used to monitor the VOC concentrations from the high-pressure system this allowed for a better understanding of the time taken for the concentrations of low volatility compounds (methyl and dimethyl formamide) to become stable. This system also allowed for the assignment of the reaction of hydrogen peroxide with tertiary butyl amine that was causing erroneously low bimolecular removal rates to be observed.

Future work with the PTR-TOF-MS will involve the study of OH initiated VOC oxidation reactions in HIRAC. Here, the monitoring of VOC decay profiles for compounds with well-known OH removal rate coefficients can be used to *in situ* calibrate the concentration of OH observed from HIRAC by FAGE. Coupling this system to HIRAC will also allow for further observation of oxygenated reaction products, and where these signals can be calibrated accurate reaction branching ratios may be defined. Modifying the ionization reagent in the system to use N_2^+, O_2^+ or Ar^+ can allow for the observation of other species, where Ar^+ is used the instrument can be used to monitor the loss of SO_2, which can potentially be used to study the atmospherically important reaction of OH with SO_2. (16-18)

References

1. SPEAK, T.H., M.A. BLITZ, D. STONE and P.W. SEAKINS. A New Instrument for Time Resolved Measurement of HO$_2$ Radicals. *Atmos. Meas. Tech. Discuss.*, 2019, **2019**, pp.1-30.
2. TULLY, F.P. Laser photolysis/laser-induced fluorescence study of the reaction of hydroxyl radical with ethylene. *Chemical Physics Letters*, 1983, **96**(2), pp.148-153.
3. MCCAULLEY, J., N. KELLY, M. GOLDE and F.J.T.J.O.P.C. KAUFMAN. Kinetic studies of the reactions of atomic fluorine and hydroxyl radical with methanol. 1989, **93**(3), pp.1014-1018.
4. AGBRO, E. and A. TOMLIN. Low temperature oxidation of n-butanol: Key uncertainties and constraints in kinetics. *Fuel*, 2017, **207**, pp.776-789.
5. KNEPP, A.M., G. MELONI, L.E. JUSINSKI, C.A. TAATJES, C. CAVALLOTTI and S.J. KLIPPENSTEIN. Theory, measurements, and modeling of OH and HO$_2$ formation in the reaction of cyclohexyl radicals with O$_2$. *Physical Chemistry Chemical Physics*, 2007, **9**(31), pp.4315-4331.
6. ELDEEB, M. and B. AKIH-KUMGEH. Recent trends in the production, combustion and modeling of furan-based fuels. *Energies*, 2018, **11**(3), p.512.
7. BORDUAS, N., G. DA SILVA, J.G. MURPHY and J.P.D. ABBATT. Experimental and Theoretical Understanding of the Gas Phase Oxidation of Atmospheric Amides with OH Radicals: Kinetics, Products, and Mechanisms. *The Journal of Physical Chemistry A*, 2015, **119**(19), pp.4298-4308.
8. SOLIGNAC, G., A. MELLOUKI, G. LE BRAS, I. BARNES and T. BENTER. Kinetics of the OH and Cl reactions with N-methylformamide, N,N-dimethylformamide and N,N-dimethylacetamide. *Journal of Photochemistry and Photobiology A: Chemistry*, 2005, **176**(1–3), pp.136-142.
9. BUNKAN, A.J.C., J. HETZLER, T. MIKOVINY, A. WISTHALER, C.J. NIELSEN and M. OLZMANN. The reactions of N-methylformamide and N,N-dimethylformamide with OH and their photo-oxidation under atmospheric conditions: experimental and theoretical studies. *Physical Chemistry Chemical Physics*, 2015, **17**(10), pp.7046-7059.
10. LINDLEY, C.R.C., J.G. CALVERT and J.H. SHAW. Rate studies of the reactions of the (CH3)2N radical with O$_2$, NO, and NO$_2$. *Chemical Physics Letters*, 1979, **67**(1), pp.57-62.
11. WAGNER, E.D., J. OSIOL, W.A. MITCH and M.J. PLEWA. Comparative in Vitro Toxicity of Nitrosamines and Nitramines Associated with Amine-based Carbon Capture and Storage. *Environmental Science & Technology*, 2014, **48**(14), pp.8203-8211.
12. KOCH, R., H.U. KRÜGER, M. ELEND, W.U. PALM and C. ZETZSCH. Rate constants for the gas-phase reaction of OH with amines: tert-Butyl amine, 2,2,2-Trifluoroethyl amine, and 1,4-Diazabicyclo[2.2.2] octane. *International Journal of Chemical Kinetics*, 1996, **28**(11), pp.807-815.
13. TAN, W., L. ZHU, T. MIKOVINY, C.J. NIELSEN, A. WISTHALER, P. EICHLER, M. MÜLLER, B. D'ANNA, N.J. FARREN, J.F. HAMILTON, J.B.C. PETTERSSON, M. HALLQUIST, S. ANTONSEN and Y. STENSTRØM. Theoretical and Experimental Study on the Reaction of tert-Butylamine with OH Radicals in the Atmosphere. *The Journal of Physical Chemistry A*, 2018, **122**(18), pp.4470-4480.
14. MEDEIROS, D.J., M.A. BLITZ, L. JAMES, T.H. SPEAK and P.W. SEAKINS. Kinetics of the Reaction of OH with Isoprene over a Wide Range of Temperature

and Pressure Including Direct Observation of Equilibrium with the OH Adducts. *The Journal of Physical Chemistry A*, 2018.

15. SPRENGNETHER, M., K.L. DEMERJIAN, N.M. DONAHUE and J.G. ANDERSON. Product analysis of the OH oxidation of isoprene and 1,3-butadiene in the presence of NO. *Journal of Geophysical Research: Atmospheres*, 2002, **107**(D15), pp.ACH 8-1-ACH 8-13.

16. BLITZ, M.A., R.J. SALTER, D.E. HEARD and P.W. SEAKINS. An Experimental and Master Equation Study of the Kinetics of OH/OD + SO$_2$: The Limiting High-Pressure Rate Coefficients. *The Journal of Physical Chemistry A*, 2017, **121**(17), pp.3184-3191.

17. MEDEIROS, D.J., M.A. BLITZ and P.W. SEAKINS. Exploring the features on the OH + SO$_2$ potential energy surface using theory and testing its accuracy by comparison to experimental data. *Physical Chemistry Chemical Physics*, 2018, **20**(13), pp.8984-8990.

18. LONG, B., J.L. BAO and D.G. TRUHLAR. Reaction of SO$_2$ with OH in the atmosphere. *Physical Chemistry Chemical Physics*, 2017, **19**(11), pp.8091-8100.